

University  
of  
St Andrews

**The Assembly of Molecular Networks at  
Surfaces: Towards Novel  
Enantioselective Heterogeneous Catalysts**

Sean Jensen

**A thesis submitted in accordance with the requirements of the University of  
St. Andrews for the degree of Doctor of Philosophy**

August 2010

**THE ASSEMBLY OF MOLECULAR NETWORKS AT SURFACES:  
TOWARDS NOVEL ENANTIOSELECTIVE HETEROGENEOUS  
CATALYSTS**

**Sean Jensen**

**A Thesis Submitted for the Degree of PhD  
at the  
University of St Andrews**



**2010**

**Full metadata for this item is available in  
Research@StAndrews:FullText  
at:**

**<http://research-repository.st-andrews.ac.uk/>**

**Please use this identifier to cite or link to this item:**

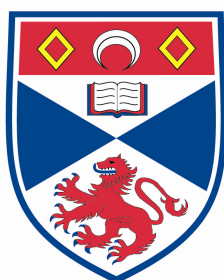
**<http://hdl.handle.net/10023/2153>**

**This item is protected by original copyright**

Funded by the EPSRC Basic Technology Grant (EP/DO48761/1)  
Supramolecular self-assembly of 1-10nm templates for biofunctional  
surfaces, quantum information processing and nanoelectronics

Under the supervision of Dr. C. J. Baddeley

**EPSRC**



University  
of  
St Andrews



The Edinburgh and St Andrews  
Research School of Chemistry

## Declaration

I, Sean Jensen, hereby certify that this thesis, which is approximately 62000 words in length, has been written by me, that it is the record of work carried out by me and that it has not been submitted in any previous application for a higher degree.

I was admitted as a research student in October 2006 and as a candidate for the degree of Ph.D in October 2006; the higher study for which this is a record was carried out in the University of St Andrews between 2006 and 2010.

Date:                      Signature of candidate:

I, Dr. C. J. Baddeley, hereby certify that the candidate has fulfilled the conditions of the Resolution and Regulations appropriate for the degree of Ph. D. in the University of St Andrews and that the candidate is qualified to submit this thesis in application for that degree.

Date:                      Signature of supervisor:

In submitting this thesis to the University of St Andrews we understand that we are giving permission for it to be made available for use in accordance with the regulations of the University Library for the time being in force, subject to any copyright vested in the work not being affected thereby. We also understand that the title and the abstract will be published, and that a copy of the work may be made and supplied to any bona fide library or research worker, that my thesis will be electronically accessible for personal or research use unless exempt by award of an embargo as requested below, and that the library has the right to migrate my thesis into new electronic forms as required to ensure continued access to the thesis. We have obtained any third-party copyright permissions that may be required in order to allow such access and migration, or have requested the appropriate embargo below.

The following is an agreed request by candidate and supervisor regarding the electronic publication of this thesis:

Embargo on both all or part of printed copy and electronic copy for the same fixed period of 1 year on the grounds that publication would preclude future publications.

Date:                      Signature of candidate:

Signature of supervisor:

## Abstract

Understanding the supramolecular interactions governing the self-assembly of molecular building blocks upon surfaces is fundamental to the design of new devices such as sensors or catalysts. Successful heterogeneous enantioselective catalysts have relied upon the adsorption of ‘chiral modifiers’, usually chiral amino acids, onto reactive metal surfaces. One of the most researched examples is the hydrogenation of  $\beta$ -ketoesters using nickel-based catalysts. The stability of the chiral modifiers upon catalyst surfaces is a major obstacle to the industrial scale-up of this reaction. In this study, the replacement of conventional modifiers with porous, chiral and functionalised self-assembled networks is investigated.

Perylene-3,4,9,10-tetracarboxylic diimide (PTCDI) and melamine (1,3,5-triazine,-2,4,6-triamine) have been shown to form hydrogen bonded networks on Ag-Si(111) $\sqrt{3}\times\sqrt{3}R30^\circ$  in ultra-high vacuum (UHV) and Au(111) substrates in UHV and ambient conditions, these networks are capable of hosting guest molecules. These networks are investigated further in this study. In UHV, the behaviour of the components and network formation on Ni(111) is probed using scanning tunnelling microscopy (STM) and temperature-programmed desorption (TPD). The stability of the PTCDI-melamine network on Au(111) was analysed using TPD. Metal coordination interactions between each of the network components and nickel upon the Au(111) surface were examined by STM before testing the ability of the network to act as a template for metal growth.

Finally, a number of polymerisation reactions are investigated with a view to replacing chiral modifiers with porous, chiral, functionalised covalent networks. Periodic covalent networks should possess the greater chemical and thermal stability required for more widespread use. In UHV and ambient conditions, STM is used to monitor the progress of surface-confined reactions on Au(111) and characterise the resultant covalent structures.

## Acknowledgements

I would like to express gratitude to my supervisor, Dr Chris Baddeley, for allowing me the opportunity to work on this project and for his advice throughout. His knowledge and enthusiasm have been a constant inspiration during my time in St Andrews.

I am indebted to Dr Tim Jones and Dr Aoife Trant for the time and patience they kindly afforded in teaching me how to operate the apparatus used over the course of this project. I would also like to thank Dr Steve Francis and Dr Federico Grillo for sharing their considerable expertise. I am grateful to Dr Herbert Früchtl for the computational theory work he performed.

I am grateful to the EPSRC for funding my study. I would like to acknowledge the contribution of the other members of the Basic Technology collaboration in the University of Nottingham, University of Oxford and King's College London and locally, in St Andrews. The knowledge and advice shared at the regular consortium meetings were of great use. I am grateful to Dr Manfred Buck, Dr Minna Räisänen and Dr Rafael Madueño for their helpful discussions and allowing me to borrow chemicals.

The friendliness of everyone I encountered in the St Andrews Surface Science Group, and particularly those in my own research group; Andrew Haire, Karen Wilson, Nicola Toma and John Greenwood; is much very much appreciated.

Finally, I am most thankful to my family, their continued support and encouragement has allowed me many privileges. Their kindness, selflessness and understanding have made my studies at first, the University of Edinburgh and now, the University of St. Andrews considerably easier and more enjoyable.

## List of Publications

Formation of PTCDI-Based Metal Organic Structures on a Au(111) Surface Modified by 2-D Ni Clusters

S. Jensen and C.J. Baddeley, *Journal of Physical Chemistry C*, **2008**, *112*, 15439

Coupling of triamines with diisocyanates on Au(111) leads to the formation of polyurea networks

S. Jensen, H. Früchtl and C.J. Baddeley, *Journal of American Chemical Society*, **2009**, *131*, 16706

Improved templates for metal growth on surfaces: A comparative study of hydrogen bonded and covalent networks

S. Jensen and C.J. Baddeley (in preparation)

STM investigation of polyamide network formation by surface-confined polymerization

S. Jensen, J. Greenwood and C.J. Baddeley (in preparation)

## List of Acronyms

1,3-PDI	1,3-phenylene diisocyanate
1,4-PDI	1,4-phenylene diisocyanate
1,6-HDI	1,6-hexamethylene diisocyanate
AES	Auger Electron Spectroscopy
bcc	Body-centred cubic
BTA	Benzene-1,3,5-tryl-tribenzoic acid
DAH	1,6-diaminohexane
DMF	Dimethylformamide
fcc	Face-centred cubic
hcp	Hexagonal close-packed
HOMO	Highest Occupied Molecular Orbital
IUPAC	International Union of Pure and Applied Chemistry
LEED	Low Energy Electron Diffraction
LUMO	Lowest Unoccupied Molecular Orbital
PTCDA	Perylene-3,4,9,10-tetracarboxylic dianhydride
PTCDI	Perylene-3,4,9,10-tetracarboxylic diimide
RAIRS	Reflection Absorption Infrared Spectroscopy
STM	Scanning Tunnelling Microscopy
TAPB	Tris-1,3,5-(4-aminophenyl)-benzene
THF	Tetrahydrofuran
TPD	Temperature-Programmed Desorption
UHV	Ultra-high Vacuum

## List of Units

Å	Ångström
amu	Atomic Mass Unit
cm	Centimetre
eV	Electron volt
K	Kelvin
$\text{kJ mol}^{-1}$	Kilojoule per mole
kV	Kilovolt
L	Langmuir
mm	Millimetre
mM	Millimolar
nA	Nanoampere
nm	Nanometre
s	Second
V	Volt

## Table of Contents

Declaration.....	iii
Abstract.....	iv
Acknowledgements.....	v
List of Publications.....	vi
List of Acronyms.....	vii
List of Symbols.....	viii

## Chapter 1 Introduction

Introduction.....	1
1.1 Self-Assembly .....	1
1.1.1 Hydrogen bonding .....	2
1.1.2 Metal-Organic Co-ordination Networks.....	15
1.1.3 Van der Waals Forces.....	18
1.2 Chiral Catalysis .....	20
1.3 Surface Self-Assembly in Relation to Heterogeneous Chiral Catalysis .....	25
1.4 References .....	27

## Chapter 2 Experimental Methodology

Introduction.....	35
2.1 Ultra High Vacuum .....	35
2.2 Temperature-Programmed Desorption .....	38
2.3 Auger Electron Spectroscopy.....	42
2.4 Low Energy Electron Diffraction.....	44
2.5 Scanning Tunnelling Microscopy .....	47
2.6 References.....	51

### 3 Self-Assembly on a Nickel Surface

Introduction.....	52
3.1 Self-assembly on the Ni(111) surface .....	52
3.2 Experimental.....	54
3.3 Results and Discussion .....	56
3.3.1 PTCDI on Ni(111) .....	56
3.3.1.1 TPD of PTCDI from Ni(111).....	56
3.3.1.2 STM analysis of PTCDI on Ni(111).....	72
3.3.1.3 Summary .....	79
3.3.2 Melamine on Ni(111).....	80
3.3.2.1 TPD of melamine from Ni(111).....	80
3.3.2.2 STM analysis of melamine on Ni(111).....	85
3.3.2.3 Summary .....	89
3.3.3 Co-deposition of PTCDI and melamine on Ni(111) .....	90
3.4 Conclusion .....	92
3.5 References.....	93

### 4 PTCDI- and Melamine-based Metal-Organic Structures on Au(111)

Introduction.....	95
4.1 Au(111) Surface Reconstruction.....	95
4.2 Metal-organic networks on Au(111) .....	96
4.3 Experimental.....	97
4.4 Results and Discussion .....	98
4.4.1 PTCDI on Au(111) .....	98

4.4.2 PTCDI Deposition onto Au(111) Surfaces Modified by 2-D Ni Clusters.....	100
4.4.3 Nickel Deposition onto Au(111) Surfaces Bearing PTCDI Islands.....	118
4.4.4 Melamine Deposition onto Au(111).....	125
4.4.5 Melamine Deposition onto Au(111) Surfaces Modified by 2-D Ni Clusters .....	127
4.5 Conclusions.....	134
4.5.1 Interaction of PTCDI and Ni on Au(111) .....	134
4.5.2 Interaction of Melamine and Ni on Au(111).....	135
4.6 References.....	136

## 5 PTCDI and Melamine Bicomponent Networks

Introduction.....	140
5.1 Self-assembled Organic Monolayers Hosting Metal Adatoms.....	141
5.2 PTCDI-Melamine Hydrogen Bonding Network on Au(111).....	142
5.3 Experimental .....	144
5.4 Results and Discussion .....	145
5.4.1 TPD of PTCDI from Au(111) .....	145
5.4.2 TPD of Melamine from Au(111).....	157
5.4.3 TPD of co-deposited PTCDI and Melamine from Au(111) .....	164
5.4.4 STM of Nickel Deposition into PTCDI and Melamine Phases on Au(111).....	169
5.4.4.1 Mixed Phase.....	170
5.4.4.2 Parallelogram Phase .....	180
5.4.4.3 Hexagonal Phase .....	185
5.5 Conclusions.....	194
5.6 References.....	197

## 6 Covalent Self-assembly

Introduction.....	199
6.1 Surface-confined Covalent Reactions .....	200
6.2 Experimental.....	202
6.2.1 Ambient Conditions.....	202
6.2.2 UHV Conditions.....	202
6.2.3 Computational Theory .....	203
6.3 Formation of Surface-Supported Polyurea Networks .....	203
6.3.1 Melamine and 1,4-phenylene diisocyanate.....	204
6.3.2 1,3,5-tris-(4-aminophenyl)-benzene and 1,4-phenylene diisocyanate...	232
6.3.3 Melamine and 1,3-phenylene diisocyanate.....	236
6.3.4 Melamine and 1,6-hexamethylene diisocyanate .....	241
6.3.5 1,4-phenylene diisocyanate and 1,6-diaminohexane.....	245
6.3.6 1,3-phenylene diisocyanate and 1,6-diaminohexane.....	249
6.4 Formation of Surface-Supported Polyamide Networks .....	251
6.4.1 1,4-phenylene diisocyanate and Benzene-1,3,5-triyl-tribenzoic acid....	252
6.4.2 Melamine and Trimesoyl Chloride.....	264
6.5 Conclusions.....	275
6.6 References.....	277

## 7 Conclusions and Future Outlook

Summary.....	281
7.1 Conclusions.....	281
7.2 Future Work.....	283
7.3 References.....	285

## 1 Introduction

Supramolecular chemistry<sup>1-3</sup> has developed as the study of molecular systems where components are held together by weak, reversible interactions, not covalent bonds. The potential applications of nanometre-scale molecular arrays have stimulated significant research in the self-assembly of molecules upon surfaces. The ability to tailor surfaces of well-defined landscapes and functionality offers itself to opportunities in the fabrication of environmental and biological sensors, gas storage devices, purposely-tuned catalysts as well as many other devices.

Molecules, themselves, are built of atoms held together by precise chemical bonds. They can be synthesised to a huge range of specifications. However, the major challenge is controlling the organisation of appropriate molecules into structures relevant to their intended future applications.

This work forms part of ongoing research into chiral heterogeneous catalysis and examines how systems of self-assembled molecules could be applied to metal substrates in the design of heterogeneous catalysts for chiral reactions.

### 1.1 Self-Assembly

Whitesides<sup>4</sup> states that ‘molecular self-assembly is the spontaneous association of molecules under equilibrium conditions into stable, structurally well-defined aggregates joined by non-covalent bonds’. Sequential covalent synthesis is clearly very important; it can be used to generate molecules of well-defined composition, connectivity and shape. Although, in principle, it can be used to synthesise very large molecules, the production of true macromolecules ( $10^4 - 10^7$  amu) is very difficult. Polymerisation techniques, whereby molecules are reacted with

themselves, can generate larger units but only limited control over their final structure is possible.

In designing supramolecular structures, covalent chemistry is still of major importance; self-assembly into supramolecular structures takes place between functional molecules. Functional molecules are those which possess the necessary groups to allow interaction with other molecules, for example, groups which promote H-bond formation, in non-covalent binding events. Of course, covalent chemistry is vital to impart such functionality into the component molecules of the intended supramolecular structures.

Generally, covalent bond formation takes place under kinetic control. In contrast, self-assembling systems are part of a reversible and dynamic equilibrium. Thus the thermodynamically most stable structure is almost always obtained. If approaching structural units are incompatible or wrongly positioned, they are rejected in the dynamic equilibrium assembly. Binding sites remain unoccupied until associations that represent the thermodynamic minimum are achieved. The molecules undergo a process of self-organising and the resultant structures are therefore self-healing as reconfiguration takes place to amend defects and stabilisation through uniformity. Many weak non-covalent bonds, comprising hydrogen bonding, metal-ligand bonds, ion-ion attractions, dipole-dipole interactions and van der Waals interactions may contribute to the final conformation of supramolecular structures.

### **1.1.1 Hydrogen bonding**

Weak interactions between molecules containing hydroxyl groups were noted by Nernst in 1892. These interactions were labelled ‘hydrogen bonds’ in 1936 when the understanding of these phenomena became clearer. It was realised that the interaction energies between molecules containing polar X-H bonds and those

containing an electronegative atom bearing non-bonding electron pairs are relatively high<sup>5,6</sup>. The energy of a H-bond is typically in the range 8-80 kJ mol<sup>-1</sup>, which is much weaker than a covalent bond (the bond dissociation energy of a C-C bond<sup>7</sup> is typically 368 kJ mol<sup>-1</sup>, a C-H bond<sup>7</sup> is typically 435 kJ mol<sup>-1</sup>) but considerably larger than van der Waals forces (<8 kJ mol<sup>-1</sup>).

Self-assembly is ubiquitous in nature, it plays a huge part in daily life, especially in biological systems. Processes such as recognition in DNA base pairings, ligand binding to receptor sites, enzyme catalysis and  $\alpha$ -helix and  $\beta$ -sheet formation rely upon a host of supramolecular interactions to take place. In many of these cases, combinations of supramolecular interactions are necessary to fulfil these tasks, but hydrogen bonding is very important for the determination of the conformations of resulting structures.

In the study of supramolecular structures, <sup>1</sup>H NMR spectroscopy, vibrational spectroscopy, X-ray and neutron diffraction, mass spectrometry and quantum mechanical calculations can be used to determine binding orientations and the strength of the interactions, but analysis by scanning tunnelling microscopy (STM)<sup>8</sup> of species deposited on surfaces allows direct visualisation of some of the complexes that can form.

Through hydrogen bonding of organic functionalities, molecules may assemble into H-bonded dimers. Homodimer assemblies may be formed by, for example, alcohols, carboxylic acids, amines, amides, imides, ureas and heterodimers based on mixtures of hydrogen bonding compounds, such as those listed, can also form. The number of H-bonds and the sequence in which they occur within assemblies determine the strength of the complexes formed. The secondary interactions in the sequence of H-bonds can be highly influential; additional stabilisation can be gained from electrostatic attraction between positively and negatively polarised atoms in adjacent H-bonds, in the same way, repulsion is created by two

positively or negatively polarised atoms. The polar X-H bond is referred to as the donor, D, whilst the electronegative atom with which it forms a H-bond is known as the acceptor, A. Although dimeric complexes may be formed from the same number of hydrogen bonds, their stability can vary, for example, in figure 1.1, the two complexes are formed by the creation of three hydrogen bonds, but their association constants (measure of interaction strengths) are significantly different<sup>9,10</sup>, which in this case can mainly be attributed to the sequence of donors and acceptors on the participating molecules leading to non-complementary secondary interactions.

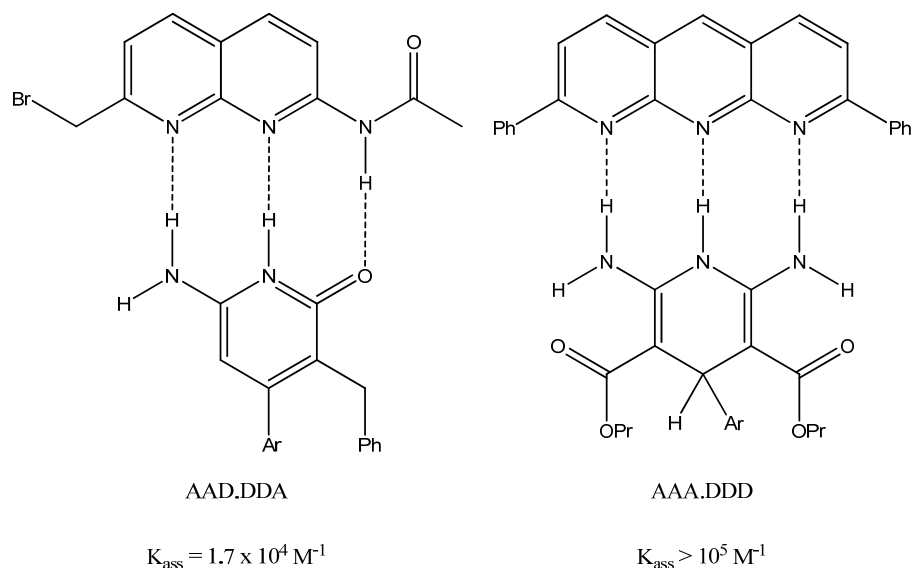


**Figure 1.1 Comparative stabilities of two H-bonded complexes, in terms of  $K_{\text{ass}}$  (association constants). There stabilities are dependent on the sequence of H-bond donors and acceptors and the effect of secondary interactions<sup>9,10</sup>**

The position of the H-bonds also plays a significant role in determining the nature of the complexes formed. Compounds may possess self-complementary H-bonding capabilities which limit self-assembly to the formation of small complexes. For example, two like compounds which feature rigidly linked 2-pyridone units were found to form quite different assemblies (figure 1.2), one compound forms stable dimers in  $\text{CHCl}_3$  whereas the other forms flexible polymeric aggregates as its hydrogen bonding sites have to be fulfilled by more than one partner<sup>11</sup>.

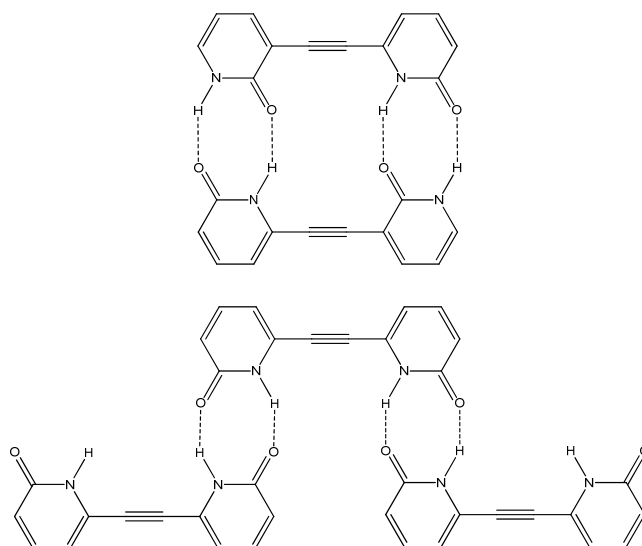


**Figure 1.2 Demonstration of complementary (above) and non-complementary (below) H-bonding junctions with resulting bimolecular complex or H-bonded polymer respectively<sup>11</sup>**

Following on, if appropriate functionalities exist on more than one side of the molecule, H-bonded assemblies of multiple units can form. Benzene-1,3,5-tricarboxylic acid (trimesic acid) has a three-fold symmetry that results in the assembly of a hexagonal lattice, shown in figure 1.3, based on the formation of two O-H...O H-bonds with three neighbouring molecules<sup>12</sup>. This system has been observed via STM following self-assembly on single crystal surfaces after deposition from vapour and solution in ultra-high vacuum (UHV)<sup>13,14</sup> and ambient conditions<sup>14-17</sup>. Similarly, using the same H-bonding motif, larger analogues of trimesic acid can self-assemble into hexagonal networks under appropriate conditions<sup>18</sup>.

Multiuunit assemblies based on H-bonded junctions can form from mixtures of species, for example, networks based on three H-bond junctions are observed from melamine and cyanuric acid (figure 1.4). The keto-tautomer of cyanuric acid possesses ADA H-bond capabilities along each of its edges, these are complementary with the DAD sides of melamine, resulting in an infinite 2-D hexagonal lattice of cyanuric acid and melamine units, as confirmed by X-ray crystallography<sup>19</sup>.

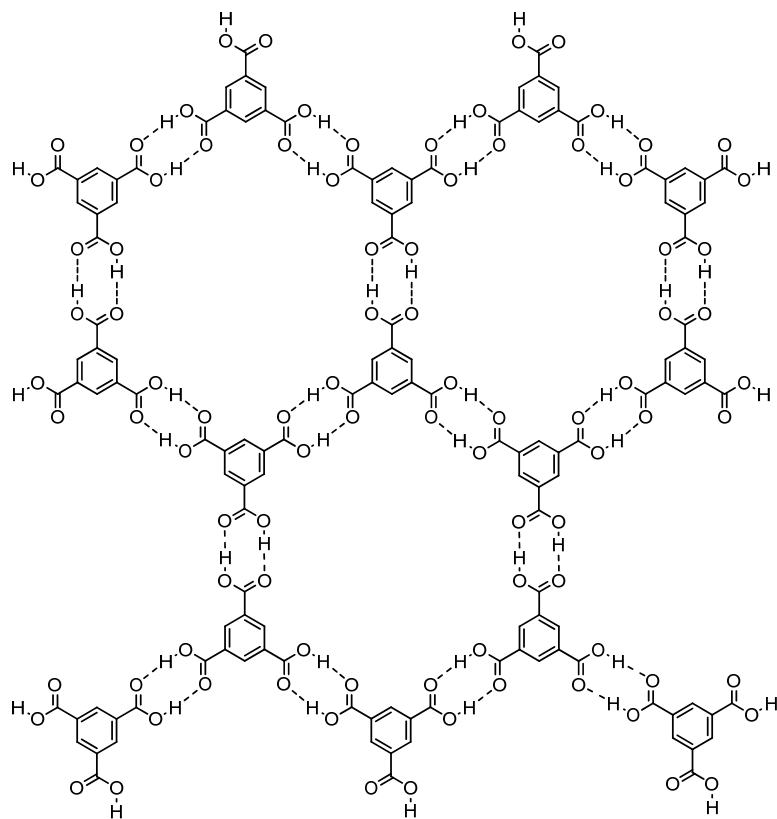


Figure 1.3 Two-dimensional array formed by trimesic acid due to hydrogen bonding<sup>13</sup>

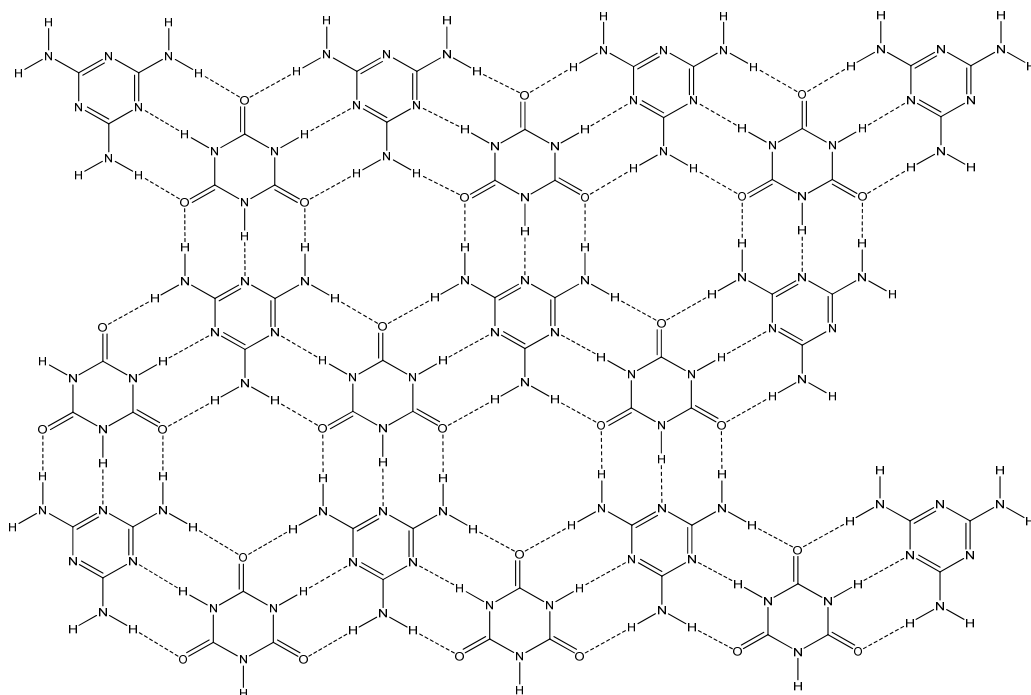


Figure 1.4 Two-dimensional array of cyanuric acid and melamine formed by hydrogen bonding<sup>20</sup>

Lehn and Whitesides have studied this system in depth, confining the growth of the assemblies to ‘rosettes’<sup>20</sup> (single hexamers) and ‘tapes’<sup>21-23</sup> (chains of alternating components) can be achieved by blocking off the functionalities of either component down specific edges (figure 1.5). Whitesides has shown that by covalently linking components to form compounds of multiple melamine or multiple isocyanuric analogues, self-assembly could be extended into three-dimensions<sup>24,25</sup>. In some systems, the formation of polymeric nanorods (figure 1.6) can be observed by transmission electron microscopy<sup>25</sup>.

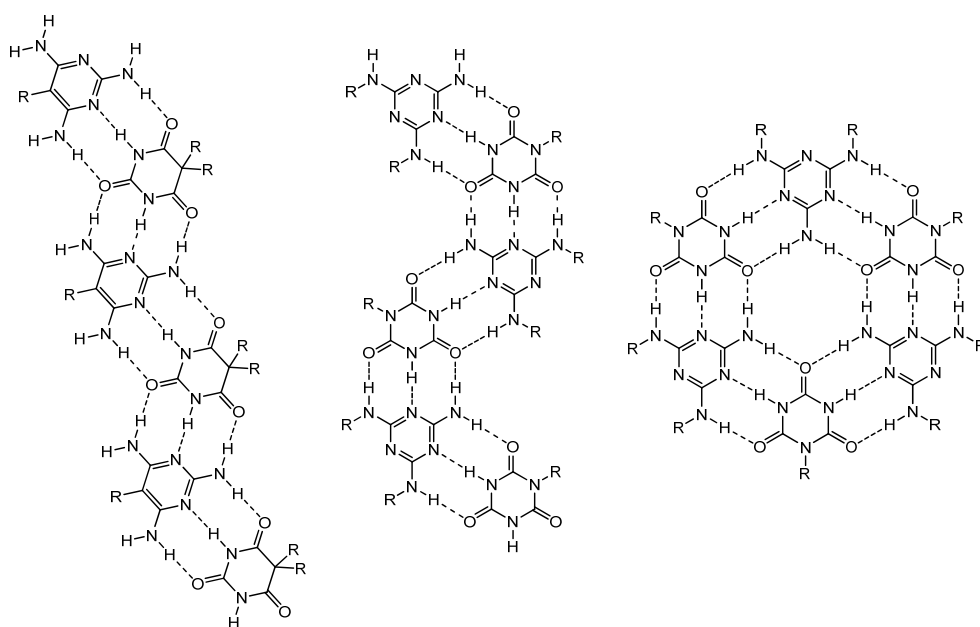


Figure 1.5 Two types of 'tape' and a 'rosette' motif that can be formed by blocking off specific hydrogen bonding sites<sup>5</sup>

As with trimesic acid, cyanuric acid and melamine self-assemble on surfaces when deposited from vapour (or solution). Similarly, the molecules of this system can be replaced with the retention of the H-bond motif; of particular interest, is the example of 3,4,9,10-perylene-3,4,9,10-tetracarboxylic-diimide (PTCDI) and melamine<sup>26</sup>.

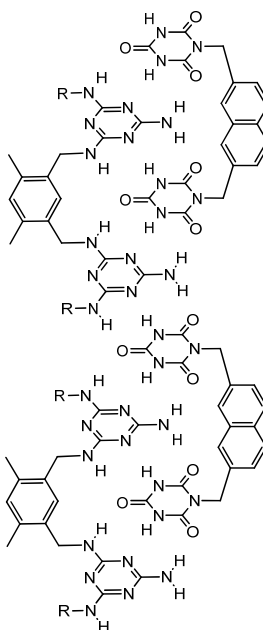


Figure 1.6 Schematic showing how linked melamine units and linked cyanuric acid units can be combined to form 3-D self-assembled aggregates<sup>25</sup>

### 1.1.1.1 PTCDI-melamine H-bonded networks

PTCDI is a rigid, aromatic molecule which, by virtue of its head and tail imide groups, possesses the same ADA hydrogen bonding capabilities as one edge of cyanuric acid.

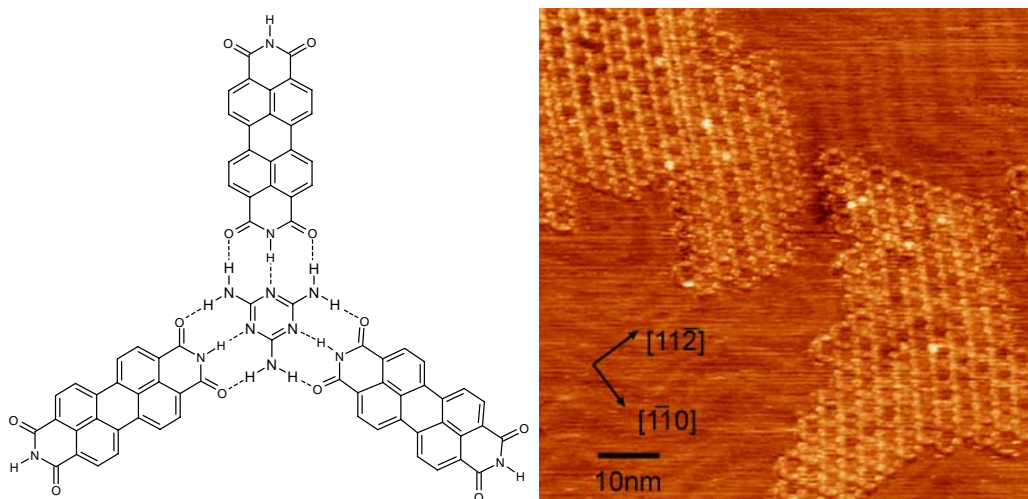
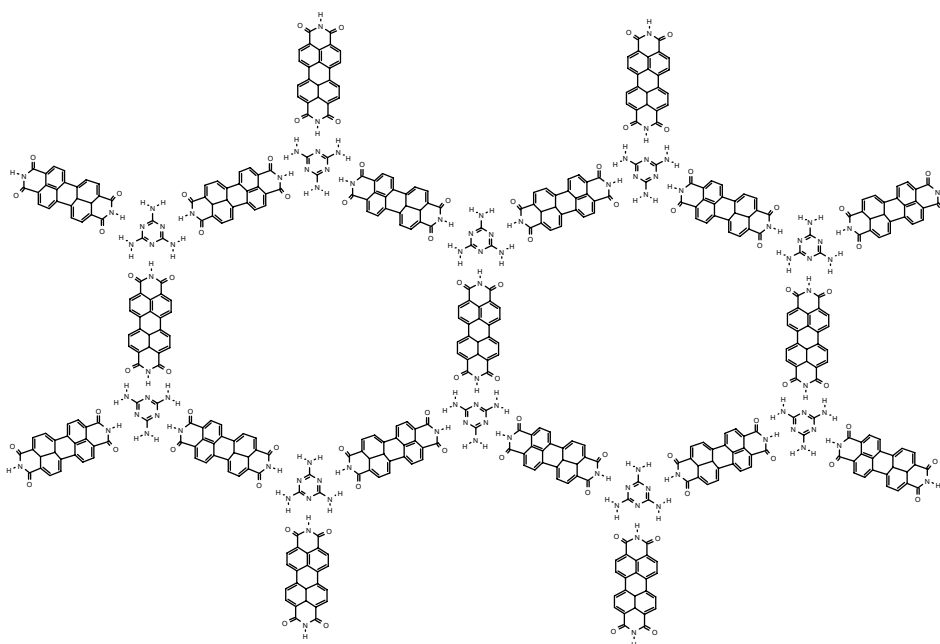


Figure 1.7 PTCDI and melamine and an example of the networks formed on surfaces (an STM image of PTCDI and melamine on Au(111) surface)

On a silver-terminated silicon surface, in UHV, co-adsorbed PTCDI and melamine molecules assemble into a hexagonal network that is stabilised by hydrogen bonding<sup>26</sup>. The network can form either by simultaneous deposition or by sequential deposition of both components before annealing to 100°C. Annealing provides sufficient thermal energy to allow PTCDI and melamine molecules to detach from monocomponent domains first formed after deposition onto the surface, diffuse across the surface and to intermix and form uniform, porous arrangements. The Ag-Si(111)- $\sqrt{3}\times\sqrt{3}R30^\circ$  substrate<sup>27</sup> interaction with the molecules is minimal, this allows the molecules to move around freely and form the most stable arrangements. There are three hydrogen bonds between melamine and each PTCDI at every junction in the network. These are formed at the expense of the two hydrogen bond junctions that exist in both monocomponent surface assemblies (figure 1.7).



**Figure 1.8 Hexagonal network stabilised by hydrogen bonding between PTCDI and melamine<sup>26</sup>**

Melamine forms the vertices whilst PTCDI constitutes the straight edges of the network, shown in figure 1.8, which has a periodicity of 34.6 Å and pores of approximately 30 Å. The ability to trap guest species in the pores of the hydrogen-bonded network represents great potential for future applications. Adsorbed C<sub>60</sub>

and  $C_{84}$  fullerenes<sup>26,28</sup> have been shown to be captured in the pores of the honeycomb network upon  $Ag-Si(111)-\sqrt{3} \times \sqrt{3}R30^\circ$ .

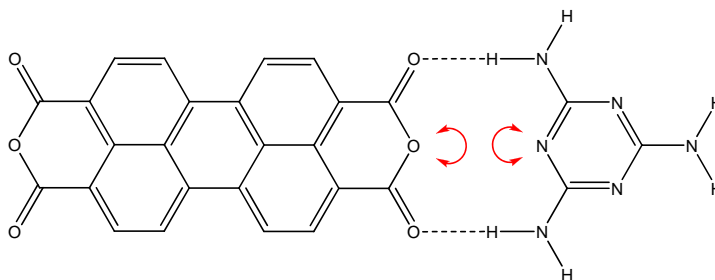


**Figure 1.9** Only two hydrogen bonds form at the junction between PTCDA and melamine<sup>29</sup>. A repulsive electrostatic interaction is formed at the centre of face-on junction whereas PTCDI forms three hydrogen bonds with melamine in the analogous situation.

An analogous system using PTCDA and melamine has been tested<sup>29</sup>. Hexagonal networks are only observed over small areas as alternative assemblies are formed to minimise the impact of the electrostatic repulsion at the centre of the AAA.DAD fully-aligned PTCDA-melamine junction (figure 1.9). A ‘double row’ arrangement which preserves many melamine-melamine H-bonds and does not involve face-on anhydride-melamine junctions is observed. A similar bicomponent system of PTCDA and tetraaminobenzene, figure (1.10), omits the repulsive interaction and a stable assembly of alternate rows of each component is observed<sup>30</sup>.

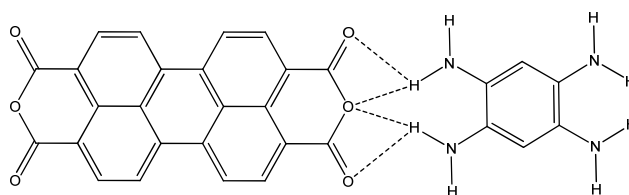


**Figure 1.10** PTCDA and 1,2,4,5-tetraaminobenzene form hydrogen bonds which lead to the arrangement of alternate rows of each species on the  $Ag-Si(111)-\sqrt{3} \times \sqrt{3}R30^\circ$  surface<sup>30</sup>.

PTCDI and melamine have been observed to assemble into a hexagonal network on the  $Au(111)$  surface<sup>31</sup>. The ability to form the network on  $Au(111)$  increases the viability of its use in various applications given the instability of the  $Ag-Si(111)-\sqrt{3} \times \sqrt{3}R30^\circ$  surface outside UHV conditions. The limited substrate-adsorbate interactions upon  $Au(111)$  affords both components the same mobility experienced upon  $Ag-Si(111)-\sqrt{3} \times \sqrt{3}R30^\circ$  and after annealing, hexagonal

networks can be formed. Networks capable of hosting C<sub>60</sub> fullerenes and decanethiol in UHV have been reported. Buck and co-workers have shown that the PTCDI-melamine network can be formed after deposition onto Au(111) from solution in ambient conditions and have also used to the networks to control the deposition of thiols<sup>32</sup> and subsequently, copper via electrodeposition<sup>33,34</sup>.

### 1.1.1.2 PTCDI

PTCDI can be synthesised from PTCDA by refluxing perylene tetracarboxylic dianhydride (PTCDA) in concentrated ammonia<sup>35</sup>. PTCDI has been investigated for its potential use as a dye and in organic semiconductor devices.

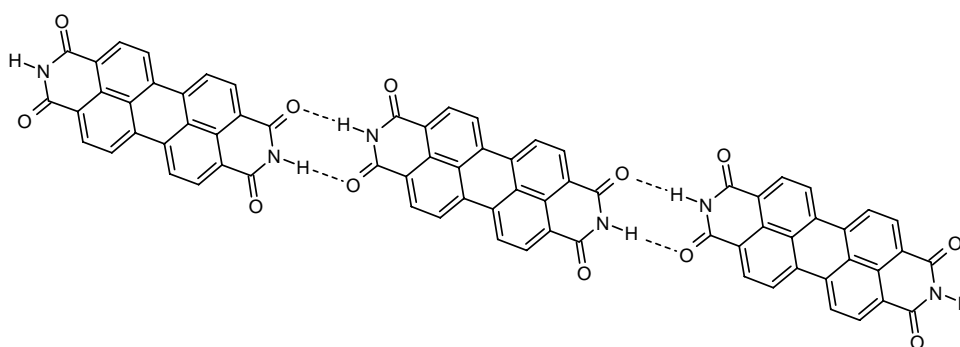


**Figure 1.11 Formation of a 1-D chain of PTCDI molecules stabilised by two intermolecular hydrogen bonds between adjacent molecules<sup>36</sup>**

The number of reports of adsorption of PTCDI onto metal substrates are relatively limited, one such example is its adsorption on Pt(100)<sup>37</sup>. However, its adsorption was also studied separately as part of the wider research into the formation of the PTCDI-melamine network on silver-terminated silicon surfaces<sup>36</sup>. On the Ag-Si(111)- $\sqrt{3}\times\sqrt{3}R30^\circ$  surface, the formation of two N-H...O hydrogen bonds between the terminal diimide groups control the arrangement of PTCDI molecules. At very low coverages (<0.02 ML), molecules are either isolated across the surface or part of single molecule wide rows. Surface defects and step edges act as nucleation sites for single molecules and the growth of 1-D rows (figure 1.11). Molecules are ordered in a head-to-tail fashion within these rows,

and stabilised by hydrogen bonding between terminal functional groups. At greater coverages, 2-D islands are observed, similar to the 1-D rows, hydrogen bonding occurs between the ends of molecules. The rows are tilted with respect to each other to allow interlocking and formation of close-packed domains (figure 1.12). Likewise, the formation of PTCDI arrangements is observed on Au(111) prior to conversion to bicomponent supramolecular networks after deposition of melamine and annealing steps.

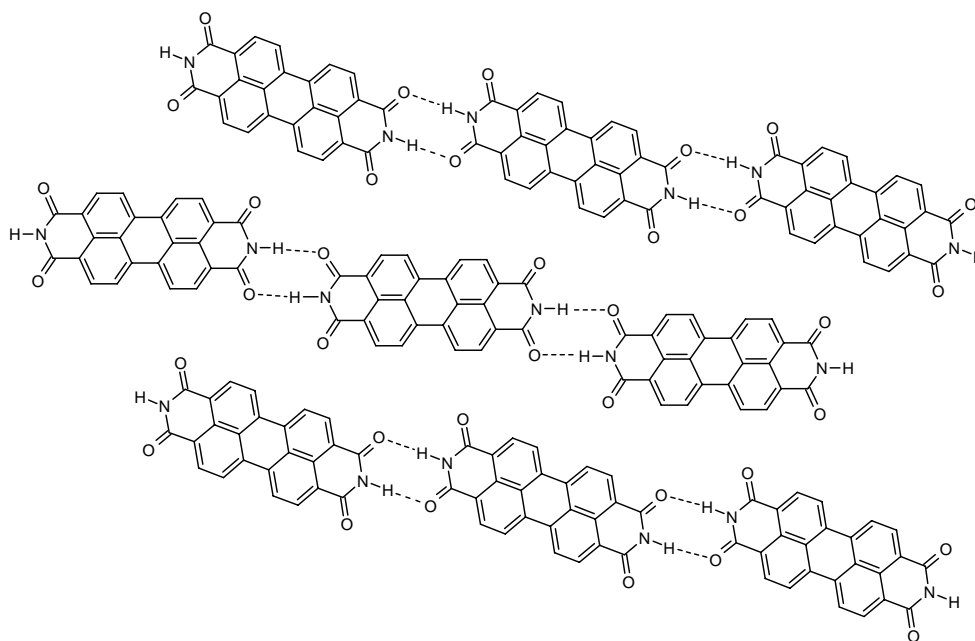


Figure 1.12 Schematic diagram of how 1-D chains of PTCDI molecules would interlock to form a larger 2-D island<sup>36</sup>

### 1.1.1.3 Melamine

Melamine is commercially produced from urea, it can also be generated by heating other nitrogen containing compounds such as cyanamide, dicyandiamide, guanidine or biguanide to induce conversion<sup>38</sup>. The generation of melamine from the reaction of cyanuric acid chloride and ammonia is an example of conversion of triazine compounds to melamine which is another possible synthetic route. Melamine is a colourless solid which sublimates at 300°C under reduced pressure and melts with decomposition at 350°C. It is mainly used in the production of high-pressure laminates for home furniture (via the formation of

melamine/formaldehyde resins) and in the production of fire retardant material (for example, in combustion-modified flexible polyurethane foams).

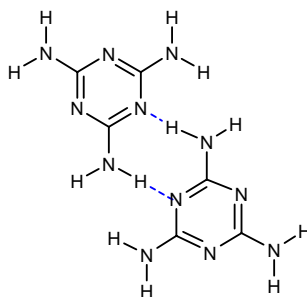


Figure 1.13 Schematic showing the formation of two hydrogen bonds between adjacent molecules<sup>31</sup>

The self-assembly of melamine on Au(111) was studied by Silly et al<sup>39</sup>, but previous to this, the monolayer arrays of melamine had been observed during bicomponent studies with cyanuric acid on Ag-Si(111)- $\sqrt{3} \times \sqrt{3} R30^{040}$  and Au(111)<sup>25,41-43</sup>, PTCDI on Au(111)<sup>31</sup> and NTCDI on Ag-Si(111)- $\sqrt{3} \times \sqrt{3} R30^{044}$ . Upon these surfaces, melamine forms a characteristic hexagonal arrangement. Two N-H...N H-bonds are formed between pairs of melamine molecules between the triazine N atoms and the N-H bonds of amine groups (figure 1.13), this can be extended due to the three-fold symmetry of melamine and hexagonal arrangements result (figure 1.14).

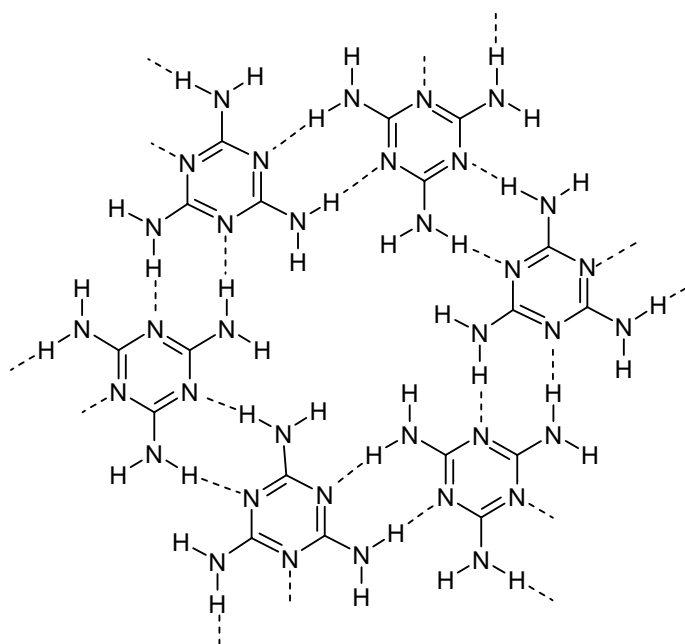


Figure 1.14 Schematic diagram illustrating how the symmetry of melamine results in hexagonal arrangements<sup>31</sup>

#### **1.1.1.4 Further Imide-Diaminotriazine Couplings in 2-D Self-Assembly on Surfaces**

As the retention of the stabilising three H-bond motif of the cyanuric acid-melamine system despite the replacement of one of the component species has proved successful in the PTCDI-melamine network, other studies have looked at altering the dimensions of the resulting networks by further modifications to the component units.

The group of Beton, who have led the research on the PTCDI-melamine system, also experimented with NTCDI and melamine on Ag-Si(111)- $\sqrt{3}\times\sqrt{3}R30^\circ$  in UHV<sup>45</sup>. NTCDI is a smaller analogue of PTCDI, featuring an aromatic core of only two fused rings. Previous studies had shown that NTCDI behaves similarly to PTCDI with the formation of 1-D rows and islands of interlocking rows<sup>46</sup>, nevertheless, a range of bi-component assemblies other than the hexagonal networks are reported when NTCDI is co-deposited with melamine. The three H-bond array is still formed between NTCDI and melamine at junctions, however, substrate-adsorbate interactions are thought to influence the composition of the final assemblies and several networks whose stoichiometry is weighted towards melamine are observed.

By reducing the symmetry of the melamine component, different shaped arrays are formed. Replacing the melamine unit with a molecule of two-fold symmetry featuring two melamine molecules covalently jointed by an aromatic linker results in the formation of ‘1-D bimolecular wires’ (rows of alternating species) and ‘2-D ribbons’ (closely-packed domains of aligned wires) on the Au(111) surface in UHV<sup>47</sup>.

The group of de Feyter have also utilised the imide-diaminotriazine coupling in their studies of self-assembled systems at the liquid-solid interface<sup>48-52</sup>. PTCDI

derivatives and NTCDI derivatives have been combined with melamine derivatives to form hydrogen bonded hetero-complexes of several units upon HOPG after deposition from solution, usually 1-phenyloctane. The derivatives usually incorporate longer alkyl or aromatic linker chains to aid adsorption to the substrate and ordering via van der Waals interactions.

Hexagonal networks were also observed when melamine are deposited with bisuracyl-functionalised linear aromatic species from 1,2,4-trichlorobenzene solutions onto graphite surface by Palma and co-workers<sup>53</sup>.

### 1.1.2 Metal-Organic Co-ordination Networks

Metal coordination complexes have been in use since the beginning of chemistry but it was in 1892 that they began to be understood and defined with the proposal by Alfred Werner that such inorganic compounds consisted of metal centres surrounded by a specific number of ligands in a symmetrical geometric arrangement<sup>54</sup>. X-ray crystallography and spectroscopic techniques including UV-visible spectroscopy, electron-spin resonance spectroscopy, cyclic voltammetry and other techniques can be used to characterise these compounds.

Coordination complexes may be built up into larger networks by the use of polytopic ligands, those which contain more than one binding site thus can link metal centres. A wide range of metal-ligand interactions are possible thus it is possible to use the inherent symmetry of available metal orbitals and the spatial organisation of donor atoms on specifically chosen ligands to produce one-, two- or three-dimensional networks of high order. A wide range of supramolecular architectures such as polygonal clusters, polyhedra, cages and porous frameworks<sup>55-63</sup> have been reported.

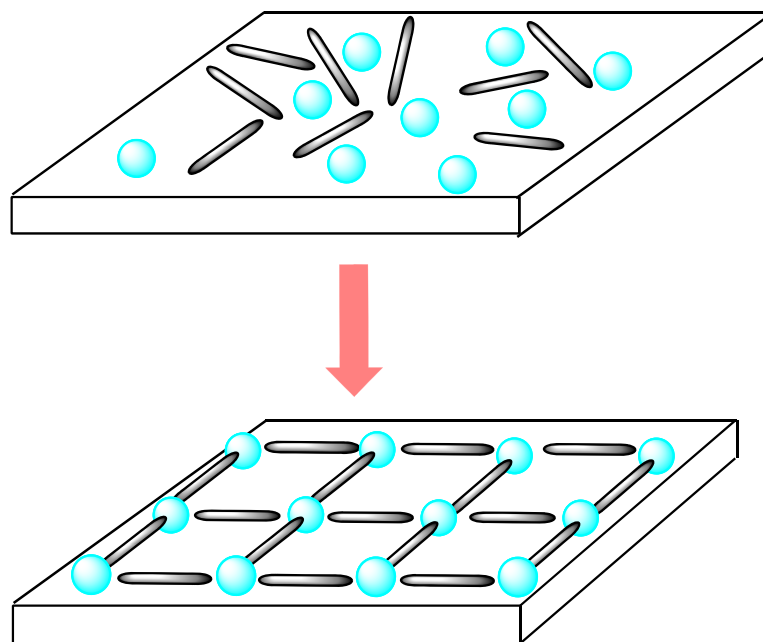


**Figure 1.15** Schematic showing how metal-organic coordination networks may assemble from components adsorbed upon a surface. Organic linker molecules are represented by grey lozenges whilst metal adatoms are represented by blue spheres.

As with hydrogen bonding networks, surfaces represent a platform upon which metal coordination architectures may be built, this is illustrated in figure 1.15. Surface adatoms are those which sit atop the crystal surface<sup>64</sup>. They may be of the native crystal species or they may be introduced from external sources. Adatoms obviously behave differently from atoms of the bulk crystal lattice, they possess unsaturated coordination sites; these sites may be satisfied by other surface adsorbates, namely, organic molecules which incorporate functional groups capable of binding. Scanning tunnelling microscopy (STM) allows direct visualisation of the metal-organic arrangements on surfaces. Other surface science techniques may give insight into their orientation on the surface or the nature of the bonding involved.

Ultra-high vacuum (UHV) allows the study of the supramolecular components, the metal centres and the organic linkers, with each other and the surface in isolation. In general, metal-organic coordination complexes or networks can be formed directly following the adsorption of both components onto the surface

from evaporators within the UHV apparatus. Similar to three-dimensional supramolecular metal-organic structures, the electronic structure, magnetic properties and the chemical function of the network may be altered by choice of metal centre, the binding sites of the ligand are key to the nature of the linkage to metal centres and the coordination motif. The strength and geometry of the linkage also determines the subsequent availability and role of the metal centres. Organic linker molecules featuring functional groups such as carboxylic acids<sup>65-74</sup>, biphenols<sup>75</sup>, pyridines<sup>75-77</sup> and carbonitriles<sup>78-81</sup> have been shown to form metal-organic complexes on a variety of surfaces with a range of metal adatom centres.

The formation of porous networks is of particular interest; achievement of an ordered monolayer arrangements may permit the growth outwards from the surface into three-dimensional structures either through co-ordination of linker molecules to remaining outwards facing co-ordination sites on the metal centres or through deposition of further adsorbates into network pores.

Organic linker molecules are central to the design of network structures. The size of the linker molecules can determine pore size and their structure is responsible for imparting functionality into pore walls. Schlickum et al demonstrated the ability to change the cavity size of a 2-D hexagonal Co-based metal-organic coordination network on the Ag(111) surface,  $\text{N}\equiv\text{C}-\text{Ph}_n-\text{C}\equiv\text{N}$  linkers (where  $n = 3, 4, 5$  and  $6$ ) yielded stable networks of increasing pore size<sup>79</sup>. Similarly, using carboxylic acid linker molecules of longer or shorter aromatic cores, the pore sizes of the 2-D grid network formed by coordination to Fe on Cu(100) can be changed<sup>67</sup>. The coordination motif of these networks is still retained when an analogue of these molecules featuring a carboxylic acid branch is used in their place, this functional group is therefore in place within the network pores and available for follow-on applications. With changing linker molecules, these networks capture varying numbers of  $\text{C}_{60}$  fullerenes. Along with being able to control the deposition of  $\text{C}_{60}$  fullerenes<sup>74</sup>, some networks have been shown capable of ordering metal adatoms<sup>80</sup>.

Metal-organic coordination interactions have also been exploited as a tool of supramolecular architecture at the solid-liquid interface and in ambient conditions<sup>54</sup>. Formation of metal-organic complexes can take place via a number of methods. The most simple, and that which parallels the UHV strategy most closely, involves the deposition of organic linker molecules from solution prior to addition of a metal complex solution to the sample. For example, De Feyter and co-workers showed that arrays of 2,2'-bipyridine-functionalised molecules upon a graphite surface could be altered by the subsequent addition of Pd(OAc)<sub>2</sub> from a phenyloctane solution<sup>48,82</sup>. The formation of metal-organic structure via this method is thought to involve the desorption of the ligands from the initial monolayer on the surface. Subsequent self-assembly with the complexed metal centres in solution occurs before deposition of the metal-organic coordination network upon the surface. Other methods such as deposition of the metal structures under potential control from an electrolytic solution may also be employed, this method was used successfully to impart a templating effect upon the metal-organic networks by alteration of the surface substrate via prior adsorption of chloride anions to a Cu(100) surface<sup>83</sup>.

### 1.1.3 Van der Waals Forces

Van der Waals forces encompass a range of weak intermolecular interactions. They are named after Johannes Diderik van der Waals who proposed the existence of non-covalent interactions between atoms and molecules. The term is sometimes used rather indiscriminately and, in some instances, this description might envelop both interactions between molecules with or without permanent dipoles<sup>6,84</sup>.

All bonds between unlike atoms will result in permanent dipoles being created, thus electrostatic attractions between dipoles on nearby molecules may be formed and be crucial in their assembly relative to each other. Hydrogen bonding is the extreme case of dipole-dipole interactions. In hydrogen bonds, the difference in the electronegativities of the two atoms in the polar covalent bond (the X-H bond

where X = N, O, F) gives a better defined dipole that can interact more strongly with an electronegative atom on an adjacent molecule. It is because of this increased strength and conferred directionality that hydrogen bonds are considered separately from typical dipole-dipole interactions.

London dispersion forces are weak interactions that exist between temporary dipoles in atom and molecules, they also act between non-polar molecules. As electron density moves around an atom or a molecule, momentary dipoles will be created due to the unevenness in distribution. When considering molecules, the greater a molecule is in size, the greater this effect will be and, along with the incorporated polar bonds, a more substantial multipole will exist.

As van der Waals forces are weak and, generally, active in all directions, their use in design of self-assembly systems is limited, but, clearly, since all of these systems consist of atoms and molecules, these forces are still present. With respect to the PTCDI-melamine hydrogen bonded network upon Ag-Si(111)- $\sqrt{3}\times\sqrt{3}R30^\circ$  and Au(111) surfaces, the interplay between hydrogen bonding and van der Waals forces has been investigated using Kinetic Monte Carlo simulations<sup>85</sup>. These simulations predict the temperature range at which the hexagonal network (as previously discussed in section 1.1.1.1) is stable. A compact phase and disordered components are observed based on calculated interaction strengths for combinations of PTCDI and melamine in a range of orientations that correspond to hydrogen bonding or solely van der Waals configurations. The simulations can also be used to predict the size of the molecules for which the hexagonal hydrogen bonding motif (that based on the initial cyanuric acid-melamine system) becomes strongly compromised by van der Waals forces.

Instances of surface self-assembly controlled exclusively by van der Waals forces are usually limited to systems where alkyl chain interdigitation<sup>86-88</sup> is possible. De

Feyter and co-workers present an example of how the weakness of these forces may be used to an advantage with the accommodation of guest molecules into a previously ordered surface array<sup>89</sup>. After the formation of ordered monolayer arrangements from dihydrobenzo[12]annulene derivatives featuring long alkyl side-chains, coronene and similar guest molecules, could be added to the samples and accommodated within the surface monolayer. The weak intermolecular interactions present in the initial arrangement allow disruption and re-assembly with the inclusion of the guest species.

## 1.2 Chiral Catalysis

Chirality refers to the property by which the mirror image of a geometrical figure is not superimposable upon itself<sup>90</sup>. Molecules having chirality, or chiral molecules, exist in two forms, enantiomers, each being the mirror image of the other. Despite having the same chemical composition, the two enantiomers, labelled (R) and (S) using the Cahn-Ingold-Prelog convention, of a chiral molecule often have different chemical and physical properties.

Chirality is of fundamental importance to the pharmaceutical industry because there are numerous examples where opposite enantiomers of the same compound can have very different effects upon its consumers. Ibuprofen is a widely used anti-inflammatory drug sold over the counter in capsules as a racemic mixture (a product containing both enantiomers in their natural abundance). However, only the (S)-enantiomer is pharmacologically active, whilst a portion of the (R)-enantiomer is converted to the (S)-enantiomer, the remainder is excreted, unchanged, without exerting any effect upon the body<sup>91</sup>. The difference in physiological properties between enantiomers can be much more critical, and the ineffective enantiomer, with respect to treatment, can have seriously detrimental effects. Hence an understanding of enantioselective metabolic processes must be

attained and the production of only a single enantiomer may be a strict requirement.

Controlling the reaction pathway to yield only one enantiomeric product is difficult due to the fact that both isolated enantiomers in non-modified processes have identical Gibbs energies. However, enantioselective homogeneous catalysts have been developed for a wide range of reactions in recent years. Knowles, Noyori and Sharpless were awarded the Nobel Chemistry Prize in 2001 for development of catalysts used in industrial scale production of chiral molecules<sup>92</sup>. The majority of these types of catalyst are organometallic complexes featuring chiral ligands. Enantioselectivity arises through limiting the access of prochiral reagent via the steric hindrance of bulky ligands; as a result, reagents adopt a specific geometry for reaction that results in the preferential production of only one enantiomer.

There are very few examples of chiral heterogeneous catalytic reactions. Two series of such reactions – Pt-catalysed hydrogenation of  $\alpha$ -keto esters and Ni-catalysed hydrogenation of  $\beta$ -keto esters - have received particular attention and much work has been carried out with the aim of understanding the mechanisms of these reactions and to define the attributes of these reactions which make them successful in order that they can be extrapolated, with enhancement, to further reaction series<sup>93</sup>.

The key step in the production of enantioselective catalysts for the above processes is the alteration of metal substrates via the adsorption of a chiral modifier prior to reaction<sup>93</sup>. A heterogeneous catalyst can become chiral by the adsorption of a chiral species, “a modifier”; the metal substrate is then described as “chirally modified”. There appear to be two main requirements of the chiral modifier species: firstly, modifier species must contain a functional group that allows adsorption to the surface of the catalyst substrate, and secondly, the

modifiers must contain a functional group that is free to interact with the reactant molecules.

After Orito and co-workers reported the hydrogenation of methyl pyruvate, a simple  $\alpha$ -ketoester, over a Pt/carbon catalyst modified by adsorption of chiral alkaloids, cinchonidine or cinchonine, from solution resulted in the formation of (R)-methyl lactate or (S)-methyl lactate, respectively; numerous theories were proposed to account for the enantioselective behaviour<sup>93</sup> (figure 1.16).

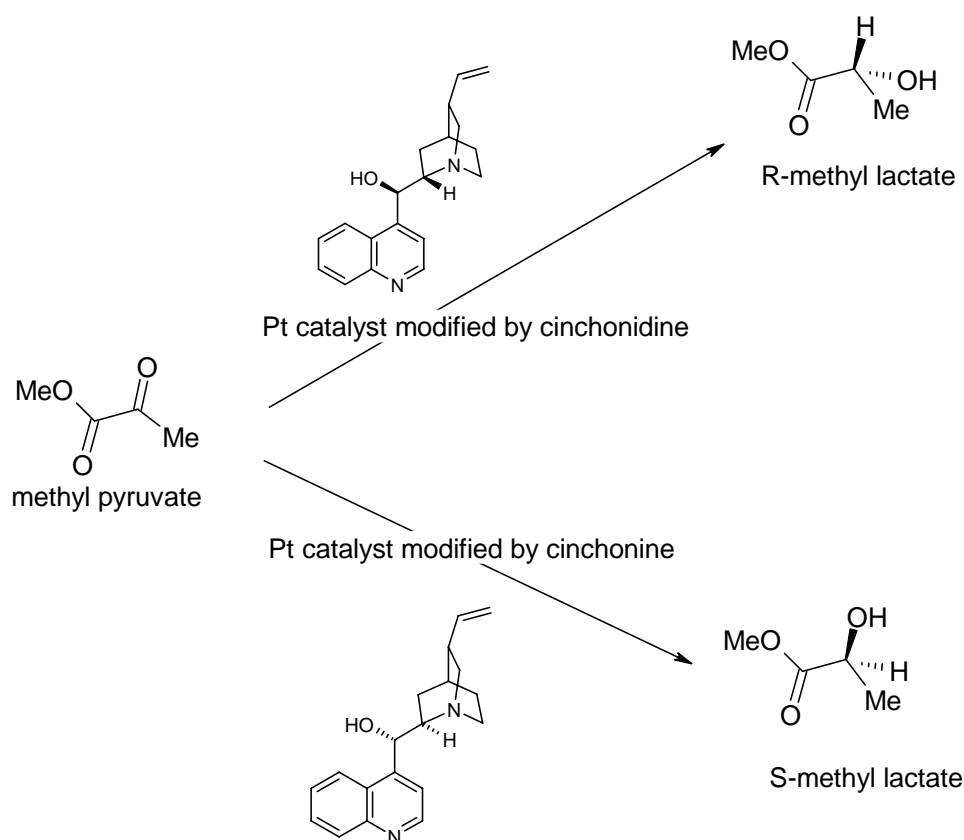
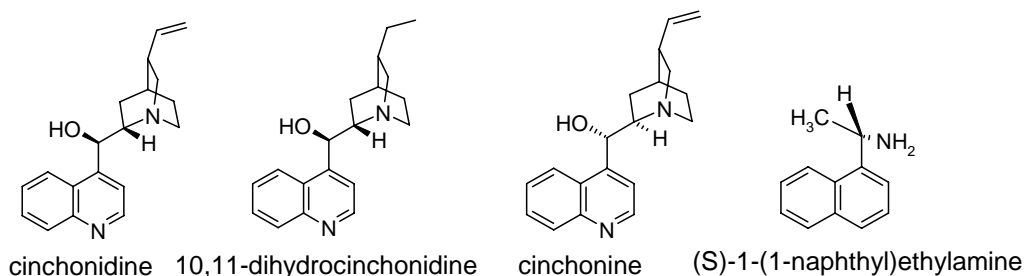


Figure 1.16 Schematic diagram illustrating the differing results when carrying out the hydrogenation of methyl pyruvate over catalysts modified by the adsorption of different alkaloid species<sup>93</sup>.

A “template model” was proposed to explain enantioselective catalysis of the hydrogenation of methyl pyruvate to form (R)-(+)-methyl lactate by a Pt substrate<sup>94</sup>. It was suggested that the formation of ordered 2-D porous arrays of chiral modifiers on the catalyst surface would leave a chiral ensemble of metal

atoms to which adsorption of reactant molecules via a particular enantioface would be favoured. If all of the reactant molecules are adsorbed in a specific orientation, it is then expected that the reaction will occur enantioselectively, as the same face of the reactant molecules will be always be presented towards incoming H atoms which are thought to attack the from below the molecular plane.

With relation to the creation of chiral spaces, Ortega Lorenzo et al demonstrated via STM the formation of ordered monolayers on the Cu(110) surface specific to the enantiomers of tartaric acid<sup>95</sup>; (R,R)-tartaric acid was observed to form a phase which is the mirror image of the phase formed by (S,S)-tartaric acid under similar deposition and sample preparation conditions. The molecules are seen to order into rows of clusters which contain three molecules; should such a structure exist upon a chirally modified catalyst, the channels between the molecular features would represent the adsorption sites for reactant molecules described by the template model.



**Figure 1.17 Structures of modifier species for Pt-based enantioselective catalytic reactions**

Nevertheless, the template model was discounted for the Pt-based system when it was shown by LEED studies of dihydrocinchonidine<sup>96</sup> and STM studies of a synthetic analogue, (S)-1-(naphthyl)ethylamine<sup>97</sup> that no ordered array is formed on Pt(111); the structures of these modifiers are shown in figure 1.17. In its place, a one-to-one mechanism has been elucidated, unlike the template model, bonding interactions between modifier and reactant molecules are said to occur. Constraining the geometry of the reactant molecules through hydrogen bonding to

modifiers is believed to be sufficient to ensure one face of the reactant was more susceptible to hydrogenation thus yield an enantiomeric excess. Evidence of a 1:1 docking interaction between (S)-1-(naphthyl)ethylamine and methyl pyruvate (the prochiral reagent)<sup>97</sup> has been obtained by STM images although it is impossible to obtain conformational information from such images and debate exists over how the cinchonidine modifier hydrogen bonds to the reactant molecules.

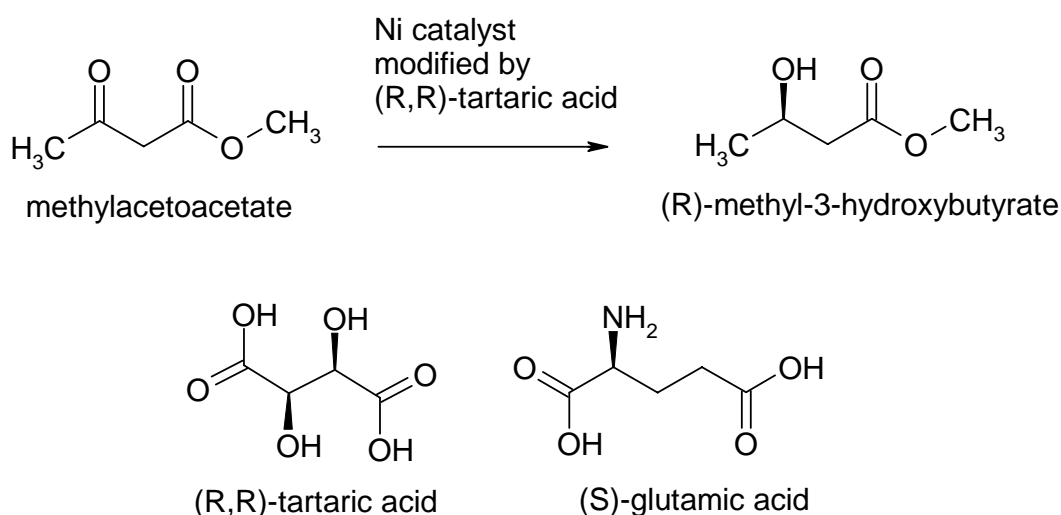


**Figure 1.18** Enantioselective hydrogenation of a  $\beta$ -ketoester, methylacetoacetate, over a modified Ni catalyst. Adsorption of (R,R)-tartaric acid to the catalyst leads to (R)-form of the product<sup>93</sup>. The structures of chiral modifiers, (R,R)-tartaric acid and (S)-glutamic acid are also shown.

The one-to-one mechanism is thought to operate in the Ni-based series but ordered arrangements of chiral modifiers, usually amino acids, such as (R,R)-tartaric acid<sup>98</sup> and (S)-glutamic acid<sup>99</sup> are only observed at very high coverages where they co-exist with dense amorphous arrays. In such arrangements, reactant molecules cannot be accommodated; in UHV, the observed sticking probabilities of the methyl acetoacetate (a prochiral reactant) to Ni surfaces bearing high coverages are very low. After adsorbing methyl acetoacetate onto a Ni(111) surface bearing an intermediate coverage of (R,R)-tartaric acid modifier, hydrogen bonded networks of 1:1 stoichiometry between modifier and reactant are observed<sup>100</sup>. Formation of an ordered network requires all of the prochiral reactants to be orientated identically, thus if reaction was to be carried out, an enantiomeric excess of the hydrogenated product would be expected. So far, few of the well-established reactions using catalysts modified by the adsorption of

chiral molecules have been employed industrially. The major drawback is the stability of chiral modifiers upon catalyst surfaces during the reaction process. By definition, a catalyst should remain unchanged at the end of the reaction and it should be re-usable. However, loss of chiral modifiers from the surface during catalyst preparation procedures and reaction process leads to the generation of unmodified sites upon the surface. At achiral sites, the reaction will proceed racemically.

Various proposals have been suggested as mechanisms for specific reactions but, in short, it seems the ability of the adsorbed chiral modifiers to interact with the prochiral reagents through hydrogen bonding is very important to the catalytic series studied. The dependence on the modifier coverage of the adsorption of the reactant and the idea of creating regular arrays of well-defined spaces above active sites are aspects which must also be considered when designing a modifier overlayer for a catalytic surface. The robustness of the modifier layer is clearly very important, with a view to utilising surfaces studied in UHV in catalytic processes in ambient conditions at the solid-liquid interface. The behaviour of some of these substrate/modifier systems have been analysed in ambient conditions where modifiers and prochiral reactants have been deposited upon catalyst substrates from solution and various parameters including adsorption temperature and solution pH<sup>101-107</sup> can significantly alter the operation of the catalyst, whilst the potential loss of modifier from the surface during catalyst preparation and the reaction is also a factor that must be protected against.

### 1.3 Surface Self-Assembly in Relation to Heterogeneous Chiral Catalysis

As effective chiral surface modifiers show, existing adsorbates can have a marked effect on the arrangement of subsequent adsorbates. Likewise, certain self-assembled supramolecular networks can determine the spatial distribution of further adsorbed molecules. Logically, it follows that some self-assembled

networks could be used, with appropriate adaptations, to control the distribution and orientation of prochiral reagents thus serve as efficient chiral modifiers. This approach would require the creation of networks that are reliably assembled on surfaces that are catalytically active towards the desired reaction. Furthermore, the network must be stable throughout reactions, thus be tolerant of reaction conditions (solvent, temperature, pressure, etc.). Appropriate functionalisation must be incorporated into the network structure, some porous network systems reported have merely been shown to control the spatial distribution of guest molecules. However, the overall orientation of prochiral reagents is vital to chiral reactions thus side groups capable of influencing this, through hydrogen bonding or similar, are desirable.

Towards this end, the PTCDI-melamine network presents itself as a suitable candidate to investigate. As previously discussed, it was first observed upon the Ag-Si(111)- $\sqrt{3}\times\sqrt{3}R30^\circ$  surface. However, further study showed it could be formed on Au(111) in UHV<sup>31</sup> and then in ambient conditions<sup>32</sup>. Scope for functionalisation of the network pores via addition of substituents to the aromatic backbone of PTCDI components may help meet the criteria of chiral modifiers and offer the possibility of tuning the network to specific tasks. Addition of functional groups in these positions should leave the imide-diaminotriazine hydrogen bonding motif intact. Functionalised PTCDI derivatives have previously been used to form thin films and supramolecular aggregates through combination with diaminotriazine or diaminopyridine derivatives<sup>108-114</sup>. More relevantly, hexagonal networks consisting of functionalised derivatives of PTCDI with melamine have been reported on Ag-Si(111)- $\sqrt{3}\times\sqrt{3}R30^\circ$  surface<sup>115</sup>. The Br<sub>2</sub>-PTCDI-melamine and the di(propylthio)-PTCDI-melamine network are both capable of trapping C<sub>60</sub> fullerenes but by different quantities.

Initial work in this study examines the behaviour of both PTCDI and melamine on a nickel substrate, a Ni(111) single crystal surface, with a view to forming well-defined porous networks on nickel catalyst surfaces. The interaction of PTCDI

and melamine with nickel adatoms in absence of a strong adsorbate-substrate influence is investigated by analysing the co-deposition of each species with nickel upon Au(111). Nickel typically forms ordered arrays of clusters on the Au(111) substrate<sup>116</sup> and the effect of the presence of each network component has upon these is examined with a view to creating nickel clusters of controlled dimensions on Au(111) using hydrogen bonding networks as templates. Construction of the PTCDI-melamine network on Au(111) is probed using scanning tunnelling microscopy and temperature-programmed desorption spectroscopy. Both techniques allow the stability of the PTCDI-melamine networks to be gauged; the reliability with which the porous hydrogen bonding networks assemble can be observed visually using STM whilst TPD gives a greater insight into the thermal stability of each of the network components upon the surface. Upon formation, the ability of PTCDI-melamine networks to control the distribution of nickel particles and template cluster growth is tested. Finally, an alternative approach to the surface assembly of molecular components is considered by investigating surface-confined covalent reactions which produce functionalised polymers – potentially leading to the development of a new class of chiral modifiers.

## 1.4 References

- (1) Lehn, J. M. *Proceedings of the National Academy of Sciences of the United States of America* **2002**, *99*, 4763.
- (2) Lehn, J. M. *Chemical Society Reviews* **2007**, *36*, 151.
- (3) Lehn, J. M. *Science* **1993**, *260*, 1762.
- (4) Whitesides, G. M.; Mathias, J. P.; Seto, C. T. *Science* **1991**, *254*, 1312.
- (5) Prins, L. J.; Reinhoudt, D. N.; Timmerman, P. *Angewandte Chemie-International Edition* **2001**, *40*, 2383.
- (6) Lindoy, L. F.; Atkinson, I. M. *Self-assembly in Supramolecular Systems*; Royal Society of Chemistry: Cambridge, 2000.

- (7) Atkins, P.; de Paula, J. *Physical Chemistry*, 7th ed.; Oxford University Press: Oxford, 2002.
- (8) Binnig, G.; Rohrer, H. *IBM Journal of Research and Development* **2000**, *44*, 279.
- (9) Fenlon, E. E.; Murray, T. J.; Baloga, M. H.; Zimmerman, S. C. *Journal of Organic Chemistry* **1993**, *58*, 6625.
- (10) Murray, T. J.; Zimmerman, S. C. *Journal of the American Chemical Society* **1992**, *114*, 4010.
- (11) Boucher, E.; Simard, M.; Wuest, J. D. *Journal of Organic Chemistry* **1995**, *60*, 1408.
- (12) Duchamp, D. J.; Marsh, R. E. *Acta Crystallographica Section B-Structural Science* **1969**, *25*, 5.
- (13) Dmitriev, A.; Lin, N.; Weckesser, J.; Barth, J. V.; Kern, K. *Journal of Physical Chemistry B* **2002**, *106*, 6907.
- (14) Sheerin, G.; Cafolla, A. A. *Surface Science* **2005**, *577*, 211.
- (15) Griessl, S. J. H.; Lackinger, M.; Jamitzky, F.; Markert, T.; Hietschold, M.; Heckl, W. A. *Langmuir* **2004**, *20*, 9403.
- (16) Ishikawa, Y.; Ohira, A.; Sakata, M.; Hirayama, C.; Kunitake, M. *Chemical Communications* **2002**, 2652.
- (17) Lackinger, M.; Griessl, S.; Heckl, W. A.; Hietschold, M.; Flynn, G. W. *Langmuir* **2005**, *21*, 4984.
- (18) Ruben, M.; Payer, D.; Landa, A.; Comisso, A.; Gattinoni, C.; Lin, N.; Collin, J. P.; Sauvage, J. P.; De Vita, A.; Kern, K. *Journal of the American Chemical Society* **2006**, *128*, 15644.
- (19) Ranganathan, A.; Pedireddi, V. R.; Rao, C. N. R. *Journal of the American Chemical Society* **1999**, *121*, 1752.
- (20) Seto, C. T.; Whitesides, G. M. *Journal of the American Chemical Society* **1990**, *112*, 6409.
- (21) Lehn, J.-M.; Mascal, M.; DeCian, A.; Fischer, J. *Journal of the Chemical Society, Chemical Communications* **1990**, 479.
- (22) Zerkowski, J. A.; Seto, C. T.; Wierda, D. A.; Whitesides, G. M. *Journal of the American Chemical Society* **1990**, *112*, 9025.

- (23) Zerkowski, J. A.; Seto, C. T.; Whitesides, G. M. *Journal of the American Chemical Society* **1992**, *114*, 5473.
- (24) Mathias, J. P.; Seto, C. T.; Simanek, E. E.; Whitesides, G. M. *Journal of the American Chemical Society* **1994**, *116*, 1725.
- (25) Choi, I. S.; Li, X. H.; Simanek, E. E.; Akaba, R.; Whitesides, G. M. *Chemistry of Materials* **1999**, *11*, 684.
- (26) Theobald, J. A.; Oxtoby, N. S.; Phillips, M. A.; Champness, N. R.; Beton, P. H. *Nature* **2003**, *424*, 1029.
- (27) Wan, K. J.; Lin, X. F.; Nogami, J. *Physical Review B* **1993**, *47*, 13700.
- (28) Theobald, J. A.; Oxtoby, N. S.; Champness, N. R.; Beton, P. H.; Dennis, T. J. S. *Langmuir* **2005**, *21*, 2038.
- (29) Swarbrick, J. C.; Rogers, B. L.; Champness, N. R.; Beton, P. H. *Journal of Physical Chemistry B* **2006**, *110*, 6110.
- (30) Ma, J.; Rogers, B. L.; Humphry, M. J.; Ring, D. J.; Goretzki, G.; Champness, N. R.; Beton, P. H. *Journal of Physical Chemistry B* **2006**, *110*, 12207.
- (31) Perdigao, L. M. A.; Perkins, E. W.; Ma, J.; Staniec, P. A.; Rogers, B. L.; Champness, N. R.; Beton, P. H. *Journal of Physical Chemistry B* **2006**, *110*, 12539.
- (32) Madueno, R.; Raisanen, M. T.; Silien, C.; Buck, M. *Nature* **2008**, *454*, 618.
- (33) Silien, C.; Raisanen, M. T.; Buck, M. *Angewandte Chemie-International Edition* **2009**, *48*, 3349.
- (34) Silien, C.; Raisanen, M. T.; Buck, M. *Small* **2009** *6*, 391.
- (35) Aviram, A.; Ratner, M. A. *Chemical Physics Letters* **1974**, *29*, 277.
- (36) Swarbrick, J. C.; Ma, J.; Theobald, J. A.; Oxtoby, N. S.; O'Shea, J. N.; Champness, N. R.; Beton, P. H. *Journal of Physical Chemistry B* **2005**, *109*, 12167.
- (37) Guillermet, O.; Glachant, A.; Hoarau, J. Y.; Mossoyan, J. C.; Mossoyan, M. *Surface Science* **2004**, *548*, 129.
- (38) Smolin, E. M.; Rapoport, L. *s-Triazines and Derivatives*; Interscience Publishers Inc., New York, 1959.

- (39) Silly, F.; Shaw, A. Q.; Castell, M. R.; Briggs, G. A. D.; Mura, M.; Martinsovich, N.; Kantorovich, L. *Journal of Physical Chemistry C* **2008**, *112*, 11476.
- (40) Perdigao, L. M. A.; Champness, N. R.; Beton, P. H. *Chemical Communications* **2006**, 538.
- (41) Staniec, P. A.; Perdigao, L. M. A.; Rogers, B. L.; Champness, N. R.; Beton, P. H. *Journal of Physical Chemistry C* **2007**, *111*, 886.
- (42) Xu, W.; Dong, M. D.; Gersen, H.; Rauls, E.; Vazquez-Campos, S.; Crego-Calama, M.; Reinhoudt, D. N.; Stensgaard, I.; Laegsgaard, E.; Linderoth, T. R.; Besenbacher, F. *Small* **2007**, *3*, 854.
- (43) Zhang, H. M.; Xie, Z. X.; Long, L. S.; Zhong, H. P.; Zhao, W.; Mao, B. W.; Xu, X.; Zheng, L. S. *Journal of Physical Chemistry C* **2008**, *112*, 4209.
- (44) Perdigao, L. M. A.; Fontes, G. N.; Rogers, B. L.; Oxtoby, N. S.; Goretzki, G.; Champness, N. R.; Beton, P. H. **2008**.
- (45) Perdigao, L. M. A.; Fontes, G. N.; Rogers, B. L.; Oxtoby, N. S.; Goretzki, G.; Champness, N. R.; Beton, P. H. *Physical Review B* **2007**, *76*, 6.
- (46) Keeling, D. L.; Oxtoby, N. S.; Wilson, C.; Humphry, M. J.; Champness, N. R.; Beton, P. H. *Nano Letters* **2003**, *3*, 9.
- (47) Canas-Ventura, M. E.; Xiao, W.; Wasserfallen, D.; Mullen, K.; Brune, H.; Barth, J. V.; Fasel, R. *Angewandte Chemie-International Edition* **2007**, *46*, 1814.
- (48) Abdel-Mottaleb, M. M. S.; Schuurmans, N.; De Feyter, S.; Van Esch, J.; Feringa, B. L.; De Schryver, F. C. *Chemical Communications* **2002**, 1894.
- (49) De Cat, I.; Roger, C.; Lee, C. C.; Hoeben, F. J. M.; Pouderoijen, M. J.; Schenning, A.; Wurthner, F.; De Feyter, S. *Chemical Communications* **2008**, 5496.
- (50) De Feyter, S.; Miura, A.; Yao, S.; Chen, Z.; Wurthner, F.; Jonkheijm, P.; Schenning, A.; Meijer, E. W.; De Schryver, F. C. *Nano Letters* **2005**, *5*, 77.
- (51) Hoeben, F. J. M.; Zhang, J.; Lee, C. C.; Pouderoijen, M. J.; Wolffs, M.; Wurthner, F.; Schenning, A.; Meijer, E. W.; De Feyter, S. *Chemistry-a European Journal* **2008**, *14*, 8579.
- (52) Thalacker, C.; Miura, A.; De Feyter, S.; De Schryver, F. C.; Wurthner, F. *Organic & Biomolecular Chemistry* **2005**, *3*, 414.

- (53) Palma, C. A.; Bonini, M.; Llanes-Pallas, A.; Breiner, T.; Prato, M.; Bonifazi, D.; Samori, P. *Chemical Communications* **2008**, 5289.
- (54) Lin, N.; Stepanow, S.; Ruben, M.; Barth, J. V. Surface-Confined Supramolecular Coordination Chemistry. In *Templates in Chemistry Iii*; Springer-Verlag Berlin: Berlin, 2009; Vol. 287; pp 1.
- (55) Cheetham, A. K.; Ferey, G.; Loiseau, T. *Angewandte Chemie-International Edition* **1999**, 38, 3268.
- (56) Janiak, C. *Dalton Transactions* **2003**, 2781.
- (57) Fujita, M.; Umemoto, K.; Yoshizawa, M.; Fujita, N.; Kusukawa, T.; Biradha, K. *Chemical Communications* **2001**, 509.
- (58) Kitagawa, S.; Kitaura, R.; Noro, S. *Angewandte Chemie-International Edition* **2004**, 43, 2334.
- (59) Swiegers, G. F.; Malefetse, T. J. *Chemical Reviews* **2000**, 100, 3483.
- (60) Hosseini, M. W. *Accounts of Chemical Research* **2005**, 38, 313.
- (61) Moulton, B.; Zaworotko, M. J. *Chemical Reviews* **2001**, 101, 1629.
- (62) Leininger, S.; Olenyuk, B.; Stang, P. J. *Chemical Reviews* **2000**, 100, 853.
- (63) Lawrence, D. S.; Jiang, T.; Levett, M. *Chemical Reviews* **1995**, 95, 2229.
- (64) Kolasinski, K. W. *Surface Science: Foundations of Catalysis and Nanoscience*; John Wiley & Sons Ltd.: Chichester, 2008.
- (65) Lingenfelder, M. A.; Spillmann, H.; Dmitriev, A.; Stepanow, S.; Lin, N.; Barth, J. V.; Kern, K. *Chemistry-a European Journal* **2004**, 10, 1913.
- (66) Stepanow, S.; Lin, N.; Barth, J. V.; Kern, K. *Journal of Physical Chemistry B* **2006**, 110, 23472.
- (67) Stepanow, S.; Lingenfelder, M.; Dmitriev, A.; Spillman, H.; Delvigne, E.; Lin, N.; Deng, X.; Cai, C.; Barth, J. V.; Kern, K. *Nature Materials* **2004**, 3, 229.
- (68) Clair, S.; Pons, S.; Fabris, S.; Baroni, S.; Brune, H.; Kern, K.; Barth, J. V. *Journal of Physical Chemistry B* **2006**, 110, 5627.
- (69) Lin, N.; Stepanow, S.; Vidal, F.; Barth, J. V.; Kern, K. *Chemical Communications* **2005**, 1681.
- (70) Lin, N.; Stepanow, S.; Vidal, F.; Kern, K.; Alam, M. S.; Stromsdorfer, S.; Dremov, V.; Muller, P.; Landa, A.; Ruben, M. *Dalton Transactions* **2006**, 2794.
- (71) Dmitriev, A.; Spillmann, H.; Lin, N.; Barth, J. V.; Kern, K. *Angewandte Chemie-International Edition* **2003**, 42, 2670.

- (72) Dmitriev, A.; Spillmann, H.; Lingenfelder, M.; Lin, N.; Barth, J. V.; Kern, K. *Langmuir* **2004**, *20*, 4799.
- (73) Zhang, Y. F.; Zhu, N.; Komeda, T. *Surface Science* **2008**, *602*, 614.
- (74) Zhang, Y. F.; Zhu, N.; Komeda, T. *Journal of Physical Chemistry C* **2007**, *111*, 16946.
- (75) Tait, S. L.; Langner, A.; Lin, N.; Stepanow, S.; Rajadurai, C.; Ruben, M.; Kern, K. *Journal of Physical Chemistry C* **2007**, *111*, 10982.
- (76) Auwarter, W.; Klappenberger, F.; Weber-Bargioni, A.; Schiffrin, A.; Strunskus, T.; Woll, C.; Pennec, Y.; Riemann, A.; Barth, J. V. *Journal of the American Chemical Society* **2007**, *129*, 11279.
- (77) Langner, A.; Tait, S. L.; Lin, N.; Chandrasekar, R.; Ruben, M.; Kern, K. *Angewandte Chemie-International Edition* **2008**, *47*, 8835.
- (78) Stepanow, S.; Lin, N.; Payer, D.; Schlickum, U.; Klappenberger, F.; Zoppellaro, G.; Ruben, M.; Brune, H.; Barth, J. V.; Kern, K. *Angewandte Chemie-International Edition* **2007**, *46*, 710.
- (79) Schlickum, U.; Decker, R.; Klappenberger, F.; Zoppellaro, G.; Klyatskaya, S.; Ruben, M.; Silanes, I.; Arnau, A.; Kern, K.; Brune, H.; Barth, J. V. *Nano Letters* **2007**, *7*, 3813.
- (80) Decker, R.; Schlickum, U.; Klappenberger, F.; Zoppellaro, G.; Klyatskaya, S.; Ruben, M.; Barth, J. V.; Brune, H. *Applied Physics Letters* **2008**, *93*, 3.
- (81) Kuhne, D.; Klappenberger, F.; Decker, R.; Schlickum, U.; Brune, H.; Klyatskaya, S.; Ruben, M.; Barth, J. V. *Journal of the American Chemical Society* **2009**, *131*, 3881.
- (82) De Feyter, S.; Abdel-Mottaleb, M. M. S.; Schuurmans, N.; Verkuijl, B. J. V.; van Esch, J. H.; Feringa, B. L.; De Schryver, F. C. *Chemistry-a European Journal* **2004**, *10*, 1124.
- (83) Safarowsky, C.; Merz, L.; Rang, A.; Broekmann, P.; Hermann, B. A.; Schalley, C. A. *Angewandte Chemie-International Edition* **2004**, *43*, 1291.
- (84) Steed, J. W.; Atwood, J. L. *Supramolecular Chemistry, Second Edition*; John Wiley & Sons Ltd.: Chichester, 2009.
- (85) Weber, U. K.; Burlakov, V. M.; Perdigao, L. M. A.; Fawcett, R. H. J.; Beton, P. H.; Champness, N. R.; Jefferson, J. H.; Briggs, G. A. D.; Pettifor, D. G. *Physical Review Letters* **2008**, *100*, 156101.

- (86) Keg, P.; Lohani, A.; Fichou, D.; Lam, Y. M.; Wu, Y. L.; Ong, B. S.; Mhaisalkar, S. G. *Macromolecular Rapid Communications* **2008**, *29*, 1197.
- (87) Grevin, B.; Rannou, P.; Payerne, R.; Pron, A.; Travers, J. P. *Journal of Chemical Physics* **2003**, *118*, 7097.
- (88) Popoff, A.; Fichou, D. *Colloids and Surfaces B-Biointerfaces* **2008**, *63*, 153.
- (89) Furukawa, S.; Tahara, K.; De Schryver, F. C.; Van der Auweraer, M.; Tobe, Y.; De Feyter, S. *Angewandte Chemie-International Edition* **2007**, *46*, 2831.
- (90) Roma, F.; Stacchiola, D.; Tysoe, W. T.; Zgrablich, G. *Physica A: Statistical Mechanics and its Applications* **2004**, *338*, 493.
- (91) Buser, H.-R.; Poiger, T.; Muller, M. D. *Environmental Science and Technology* **1999**, *33*, 2529.
- (92) Lohray, B. B. *Current Science* **2001**, *81*, 1519.
- (93) Baddeley, C. J. *Topics in Catalysis* **2003**, *25*, 17.
- (94) Sutherland, I. M.; Ibbotson, A.; Moyes, R. B.; Wells, P. B. *Journal of Catalysis* **1990**, *125*, 77.
- (95) Ortega Lorenzo, M.; Baddeley, C. J.; Muryn, C.; Raval, R. *Nature* **2000**, *404*, 376.
- (96) Carley, A. F.; Rajumon, M. K.; Roberts, M. W.; Wells, P. B. *Journal of the Chemical Society-Faraday Transactions* **1995**, *91*, 2167.
- (97) Bonello, J. M.; Williams, F. J.; Lambert, R. M. *Journal of the American Chemical Society* **2003**, *125*, 2723.
- (98) Jones, T. E.; Baddeley, C. J. *Surface Science* **2002**, *513*, 453.
- (99) Jones, T. E.; Urquhart, M. E.; Baddeley, C. J. *Surface Science* **2005**, *587*, 69.
- (100) Jones, T. E.; Baddeley, C. J. *Surface Science* **2002**, *519*, 237.
- (101) Izumi, Y. *Advances in Catalysis* **1983**, *32*, 215.
- (102) *Chiral Catalyst Immobilization and Recycling*; De Vos, D. E.; Vankelecom, I. F. J.; Jacobs, P. A., Eds.; Wiley-VCH: Weinheim, 2000.
- (103) Tai, A.; Harada, T. Asymmetrically Modified Nickel Catalysts. In *Tailored Metal Catalysts*; Iwasawa, I., Ed.; D. Reidel Publishing Company: Dordrecht, 1986.

- (104) Keane, M. A. *Catalysis Letters* **1993**, *19*, 197.
- (105) Jones, T. E.; Baddeley, C. J. *Journal of Physical Chemistry C* **2007**, *111*, 17558.
- (106) Jones, T. E.; Rekasas, A. E.; Baddeley, C. J. *Journal of Physical Chemistry C* **2007**, *111*, 5500.
- (107) Wilson, K. E.; Baddeley, C. J. *Journal of Physical Chemistry C* **2009**, *113*, 10706.
- (108) Beckers, E. H. A.; Chen, Z. J.; Meskers, S. C. J.; Jonkheijm, P.; Schenning, A.; Li, X. Q.; Osswald, P.; Wurthner, F.; Janssen, R. A. J. *Journal of Physical Chemistry B* **2006**, *110*, 16967.
- (109) Liu, Y.; Xiao, S. Q.; Li, H. M.; Li, Y. L.; Liu, H. B.; Lu, F. S.; Zhuang, J. P.; Zhu, D. B. *Journal of Physical Chemistry B* **2004**, *108*, 6256.
- (110) Liu, Y.; Zhuang, J. P.; Liu, H. B.; Li, Y. L.; Lu, F. S.; Gan, H. Y.; Jiu, T. G.; Wang, N.; He, X. R.; Zhu, D. B. *Chemphyschem* **2004**, *5*, 1210.
- (111) Wurthner, F.; Chen, Z. J.; Hoeben, F. J. M.; Osswald, P.; You, C. C.; Jonkheijm, P.; von Herrikhuyzen, J.; Schenning, A.; van der Schoot, P.; Meijer, E. W.; Beckers, E. H. A.; Meskers, S. C. J.; Janssen, R. A. J. *Journal of the American Chemical Society* **2004**, *126*, 10611.
- (112) Wurthner, F.; Thalacker, C.; Sautter, A. *Advanced Materials* **1999**, *11*, 754.
- (113) Wurthner, F.; Thalacker, C.; Sautter, A.; Schartl, W.; Ibach, W.; Hollricher, O. *Chemistry-a European Journal* **2000**, *6*, 3871.
- (114) Schenning, A.; von Herrikhuyzen, J.; Jonkheijm, P.; Chen, Z.; Wurthner, F.; Meijer, E. W. *Journal of the American Chemical Society* **2002**, *124*, 10252.
- (115) Perdigao, L. M. A.; Saywell, A.; Fontes, G. N.; Staniec, P. A.; Goretzki, G.; Phillips, A. G.; Champness, N. R.; Beton, P. H. *Chemistry-a European Journal* **2008**, *14*, 7600.
- (116) Chambliss, D. D.; Wilson, R. J.; Chiang, S. *Physical Review Letters* **1991**, *66*, 1721.

## **2 Experimental Methodology**

The fundamental aim of all surface science experiments is to gain insight on atomic and electronic structure and composition of surfaces, and the nature of adsorption and reactivity of atomic and molecular species upon them. With the evolution of a range of surface spectroscopies, ultra-high vacuum techniques and the innovation of scanning probe microscopies, systems may be characterised in great detail.

Scanning tunnelling microscopy, used predominantly in UHV, is the principal analytical tool employed in this study; it allows direct visualisation of the electronic structure of surfaces. From this information, spatial distribution of adsorbates can be measured and their intermolecular interactions interpreted. Temperature-programmed desorption (TPD) is also employed to determine the stability of the molecular components in the systems of interest. The theoretical principles and the experimental details of the techniques used to prepare, test and characterise the surface self-assemblies created in this study are detailed in this Chapter.

### **2.1 Ultra High Vacuum**

Many surface science experiments take place in ultra high vacuum (UHV). There is no definitive pressure that constitutes UHV although pressures of  $<10^{-9}$  mbar are widely considered to be UHV. These conditions allow surfaces to be maintained in an almost contamination-free state for the duration of experiments and create the most reproducible surfaces for series of experiments. Although these conditions may be far removed from the operating conditions of the processes studied or the devices being manufactured, they allow the examination of individual components in isolation with surfaces.

UHV conditions are also needed for the use of valuable low energy electron and ion-based analytical techniques without excessive interference from gas phase scattering. To achieve and maintain UHV conditions, a high pumping speed is essential; this can be achieved by fitting the system with powerful turbomolecular and rotary pumps. It is also important to minimise the surface area in the chamber and that it be constructed from low outgassing materials such as certain stainless steels.

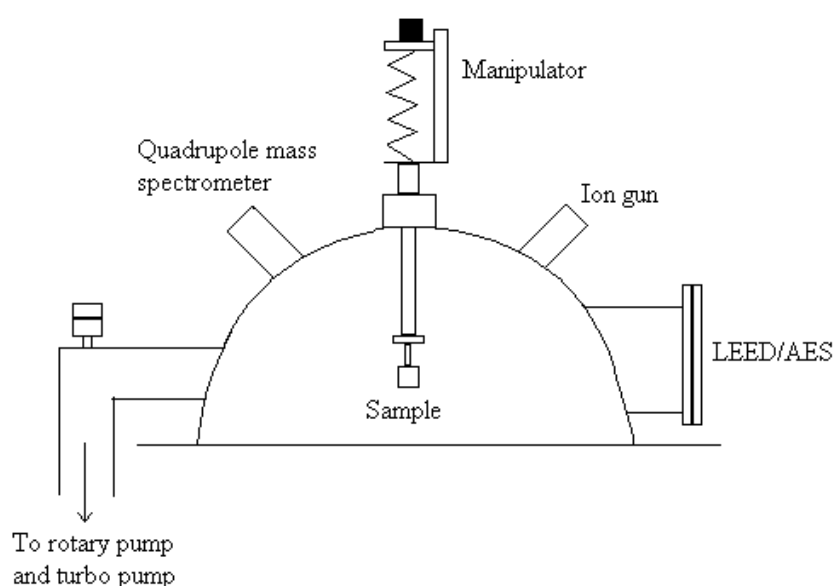


**Figure 2.1 Schematic diagram of Chamber 1 used for TPD experiments**

The UHV chambers used in this study can sustain a base pressure of around  $1 \times 10^{-10}$  mbar. Within the chamber, the sample is mounted onto a manipulator, a thermocouple is used to determine the temperature of the sample, and this may be attached directly to the sample or the manipulator depending on the experimental setup. Figure 2.1 shows a diagram of Chamber 1, used in this study for TPD experiments. The manipulator allows the movement of the sample in three dimensions as well as rotation of the sample such that it can be positioned for cleaning, dosing or characterisation with the analytical facilities installed within the chamber. After mounting the sample, the rotary pump is used to reduce the pressure in the chamber from atmospheric to around  $1 \times 10^{-2}$  mbar before activating

the turbomolecular pump to attain pressures of around  $1 \times 10^{-7}$  mbar. To achieve UHV, it is necessary to bake the chamber at temperatures of around  $150^\circ\text{C}$  whilst the system is being continuously pumped to remove traces of water, hydrocarbons and other species adsorbed to the walls of the chamber. Filaments of instrumentation installed within the chamber and the sample itself also have to be degassed by heating to reduce the pressure and eliminate contaminants before any experimentation. The pressure inside the chamber is measured by an ionisation gauge and the composition of the species within the chamber can be monitored in real-time using quadrupole mass spectrometry.

Before any experiments, the sample is cleaned via  $\text{Ar}^+$  sputtering using the ion gun to deliver ion energy typically below 1.5 kV and a sample drain current of around  $20 \mu\text{A}$ . This method of cleaning relies upon physically impacting the surface with argon ions thereby desorbing adsorbed species and substrate atoms. As a result, the surface becomes very rough and requires annealing to achieve a flat surface before any experiments are carried out. The sample cleanliness can be checked by Auger electron spectroscopy (AES) and low energy electron diffraction (LEED).

Organic compounds which are solid at room temperature can be dosed into the vacuum chamber after being packed tightly into a glass capillary tube doser, provided that they do not thermally decompose within the doser. At one end of the tube, wire gauze, which allows gaseous molecules to pass, is inserted; the other end is sealed by a thermocouple unit. A heating wire is coiled around the outside of the tube, which is then mounted onto the chamber. The compound of interest is sublimed into the chamber by heating to a temperature sufficiently high to generate a substantial vapour pressure; the pressure within in the chamber is controlled by the valve which is used to leak in the gas phase compound. Liquid compounds may be dosed from container reservoirs fitted onto the system. Freeze-pump-thaw cycles of liquid compounds removes volatile impurities, the gas lines are then filled with pure vapours and leaked into the chamber via a high-precision leak valve.

## 2.2 Temperature-Programmed Desorption

Temperature-programmed desorption (TPD) is a method used to study surface reactions and kinetics of molecular desorption processes. The technique may be used to study surface coverage and the bonding energies of adsorbates to surfaces.

In a TPD experiment, a sample surface is exposed to one or more molecular species at a particular temperature in order to obtain a specific coverage. The sample is then heated in a controlled manner, usually a linear temperature ramp is desirable, to desorb species from the surface. The gas pressure above the surface is monitored as the surface is heated. Small quadrupole mass-spectrometers are the most commonly used detectors; a large number of evolved products can be monitored simultaneously. TPD experiments were carried out in Chamber 1, vacuum chamber with base pressure of  $1 \times 10^{-10}$  mbar. The chamber is fitted with a quadrupole mass spectrometer, facilities for low energy electron diffraction (LEED) and Auger electron spectroscopy (AES) and sample cleaning via argon ion sputtering. A schematic of the chamber is shown above in figure 2.1

Spectra can be generated that display the partial pressure variations of each recorded mass fragment as a function of temperature. The competition between molecules entering the gas phase volume and leaving the volume through pumping of the experimental chamber creates a TPD spectrum with shapes that are often characteristic of the nature of the adsorbed species, the surface under investigation, adsorption temperature or surface coverage.

TPD data can also be used to estimate the activation energy of desorption,  $E_d$ , of a compound from a given surface<sup>1</sup>. The rate of desorption as the temperature ramp is applied to the sample can be expressed as follows:

$$-\frac{d\theta}{dt} = k_d N^m \quad \text{Equation (2.1)}$$

where  $\theta$  is the surface coverage,  $N$  is the adsorbed number of molecules and  $m$  is the order of desorption.

Desorption is known to follow Arrhenius-type kinetics, thus the rate constant for the desorption process,  $k_d$  may be expressed in terms of temperature,  $T$ , the pre-exponential factor,  $\nu$ , the activation energy of desorption,  $E_d$ , and the gas constant,  $R$ :

$$k_d = \nu \exp\left(-\frac{E_d}{RT}\right) \quad \text{Equation (2.2)}$$

The rate of desorption can be re-written as:

$$\frac{d\theta}{dt} = \frac{d\theta}{dT} \times \frac{dT}{dt} = \frac{d\theta}{dT} \beta \quad \text{Equation (2.3)}$$

where  $\beta = \frac{dT}{dt}$  (the heating rate). This can then be substituted into the equation 2.1 to give:

$$-\frac{d\theta}{dT} = \frac{k_d}{\beta} N^m \quad \text{Equation (2.4)}$$

Subsequent substitution for  $k_d$  yields:

$$-\frac{dN}{dT} = \frac{\nu}{\beta} m \theta^{m-1} \exp\left(-\frac{E_d}{RT}\right) \quad \text{Equation (2.5)}$$

The vacuum chamber in which the experiment takes place is pumped constantly, thus the temperature at which maximum desorption occurs ( $T_{max}$ ) must also correspond to the temperature of maximum desorption rate. At  $T = T_{max}$ ,  $\frac{d^2N}{dT^2} = 0$ . Therefore the following expression can be derived:

$$\frac{E_d}{RT_{max}^2} = \frac{\nu}{\beta} m \theta^{m-1} \exp\left(-\frac{E_d}{RT_{max}}\right) \quad \text{Equation (2.6)}$$

The method of analyzing TPD spectra depends on the information required by the investigation in question: the TPD might only be used to determine a temperature range at which an adsorbate may be stable on a certain surface or it may be used

to extract more quantitative information such as activation energies of desorption. Desorption curves may be indicative of the order of the desorption,  $m$ .

### *Zero order desorption*

If  $m = 0$ , Equation 2.1 and 2.6 may be written as:

$$-\frac{d\theta}{dt} = \frac{\nu}{\beta} \exp\left(-\frac{E_d}{RT_{max}}\right) \quad \text{Equation (2.7)}$$

Desorption rate in zero order processes is independent of coverage and rises exponentially with increasing temperature. Desorption peaks for these processes tend to have a common leading edge rising to the desorption maximum before a sharp decrease.

### *First order desorption*

Molecules at submonolayer coverages commonly desorb via a first order process ( $m = 1$ ). This occurs when the rate of desorption depends only on the concentration of one desorbing species.

$$-\frac{d\theta}{dt} = \frac{\nu}{\beta} \theta \exp\left(-\frac{E_d}{RT_{max}}\right) \quad \text{Equation (2.8)}$$

First order desorption events typically produce an asymmetric peak shape, with a longer leading edge which sharply decreases after the desorption maximum. Based on the observed linear relationship between  $E_d$  and  $T_{max}$  when  $\frac{\nu}{\beta}$  is between  $10^8$  and  $10^{13} \text{ K}^{-1}$ , the Redhead equation<sup>1,2</sup> may be used to estimate  $E_d$  in first order processes to good accuracy assuming a constant heating rate and  $\nu = 10^{13} \text{ s}^{-1}$ :

$$E_d = RT_{max} \left[ \ln\left(\frac{AT_{max}}{\beta}\right) - 3.46 \right] \quad \text{Equation (2.9)}$$

**Second order desorption**

Second order desorption ( $m = 2$ ) typically arises from a recombinative event between two species before desorption. Peaks are characteristically broader and symmetric about  $T_{max}$ . The desorption rate is given by:

$$-\frac{d\theta}{dt} = \frac{\nu}{\beta} \theta^2 \exp\left(-\frac{E_d}{RT_{max}}\right) \quad \text{Equation (2.10)}$$

As described, peak shapes may provide information on the order of the desorption process. However, this may be obscured by lateral interactions between adsorbate molecules, significant adsorbate-adsorbate interactions may change the peak shape or position. Repulsive interactions between molecules may be expected to lower the value of  $E_d$  with desorption occurring at lower temperature with increasing coverage. This study examines self-assembled systems which would otherwise not exist without attractive interactions (H-bonding), it is thought that this may significantly alter desorption spectra by raising the activation energy of desorption of molecules by the magnitude of the stabilization received from all lateral supramolecular interactions:

$$E_d = E_{ads-sub} + xS_1 + yS_2 \quad \text{Equation (2.11)}$$

where  $E_{ads-sub}$  is the adsorption energy between a molecule and the surface,  $S_1$  and  $S_2$  are adsorbate-adsorbate interaction energies and  $x$  and  $y$  are the respective numbers of each interaction formed<sup>3</sup>. Depending on the system being analysed or the method,  $S_1$  and  $S_2$  might be used to represent the interaction of a molecule with its nearest neighbour and its next-nearest neighbour or in this case, the adsorbate-adsorbate interactions experienced from each of the two lateral dimensions.

The TPD spectra may also be made up of more than one peak or overlapping peaks<sup>4</sup>, this may occur if there are multiple adsorption sites or states. These may be related to different environments on the surface, different bonding configurations or different sites within the adsorbate overlayer.

The speed of the pumping in the vacuum chamber and the sample heating rate may have a bearing upon the shape of TPD spectra, thus the method of analysis employed in Chapters 3 and 5 uses observed pumping speed plots (certain species may be pumped from the chamber quicker than others) and sample heating rate curves specific to the adsorbates and sample substrates used in the local vacuum chamber to gauge empirically activation energies of desorption for various adsorption states and better understand their nature.

### 2.3 Auger Electron Spectroscopy

Auger electron spectroscopy (AES) can be used to obtain quantitative information on surface composition and is also useful for monitoring the cleanliness of sample surfaces.

The first stage of the Auger process is initiated by expulsion of an electron from a low-lying orbital after irradiation of the sample with a beam of high energy electrons (usually, in Auger spectroscopy, an electron beam of energy in the 1-5 keV range is used rather than electromagnetic radiation)<sup>5</sup>. An excited atom relaxes by filling the vacancy in its core shell with an electron from a higher shell (an electron of lower binding energy). This 'down' transition results in either the generation of radiation, which is called x-ray fluorescence, or by the ejection of another electron, which is the Auger effect.

In the Auger effect, an electron from an upper level falls in to the vacancy created in the low-lying orbital. The energy released in this transition is sufficient to expel a second electron from an upper level orbital (figure 2.2). Auger emissions are described in terms of the orbital transitions involved in the production of an Auger electron<sup>1</sup>. For example, initial expulsion of a K electron, followed by transition of an L<sub>1</sub> electron and simultaneous emission of a second electron from the L<sub>2,3</sub> level would be classified as a KL<sub>1</sub>L<sub>2,3</sub> Auger emission.

The kinetic energy of the Auger electron is dependent on the energy available to the Auger electron (generated by the transition of the ‘down’ electron) and the energy required to overcome the barrier to emission from the atom. The kinetic energy,  $E_{kin}$ , of the Auger electron in the example of figure 2.2 is given by:

$$E_{kin} = E_K - E_{L_1} - E_{L_{2,3}} - \Phi \quad \text{Equation (2.12)}$$

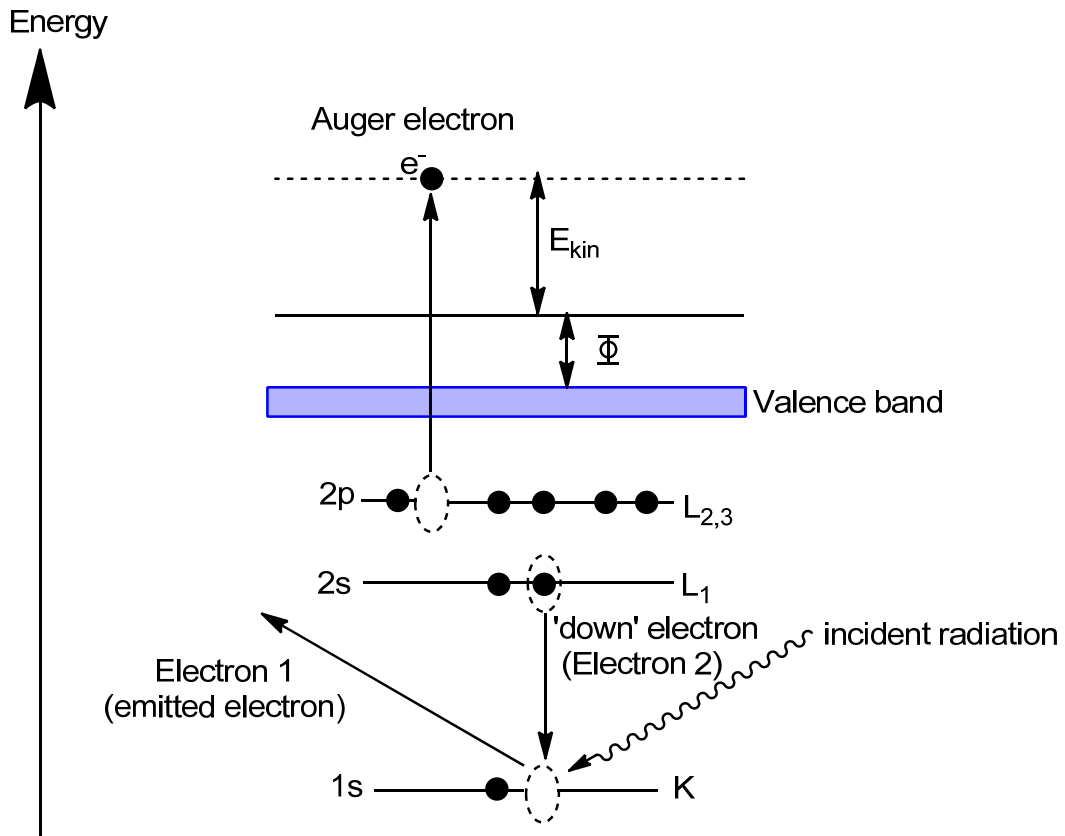


**Figure 2.2** A schematic of the Auger effect<sup>1</sup>. An incident beam of electrons causes the ejection of Electron 1 from the core. The core hole is filled by a transition of Electron 2 from a level of lower binding energy. Energy is liberated from the atom either as a photon or in the emission of an Auger electron.

The kinetic energy of the Auger electrons is independent of the incident radiation causing the initial vacancy in the core shell. The kinetic energy of the Auger electrons is characteristic of the binding energies of the orbitals within the atoms present. Detection of Auger electrons can therefore provide an accurate elemental analysis of the near surface region of a sample.

Using standard Auger spectra (available for most elements), surface composition or sample cleanliness can be determined. The number of electrons with a given kinetic energy  $N(E)$  is measured across a wide range of kinetic energy,  $E_{kin}$ , (usually 0-1000 eV). The kinetic energies of the intense peaks present in the spectrum are compared with elemental values to determine the elements present. Auger spectra are often used in differentiated form. This offers greater sensitivity by removing most of the background contribution.

In determining the elemental composition of a surface, the area under an Auger peak is directly proportional to surface concentration. The change in the intensity of a principal peak can be related to the concentration of the species present using equation 2.13. For a metal surface bearing a metal overlayer of thickness,  $d$ , the intensity of a substrate Auger peak,  $I$ , can be expressed as:

$$I = I_0 \exp\left(-\frac{d}{\lambda \cos \theta}\right) \quad \text{Equation (2.13)}$$

where  $I_0$  is the peak intensity for the clean metal surface,  $\lambda$  is the mean free path of electrons in the adsorbate metal and  $\theta$  is the angle between the detector and the surface normal.

In this study, Auger spectroscopy was used mainly to determine the cleanliness of the Au(111) and Ni(111) surfaces prior to TPD experiments. Au Auger peaks of 69 eV and Ni Auger peaks of 61 eV and 848 eV were used to monitor surface cleanliness or composition during experiments involving bimetallic surfaces.

## 2.4 Low Energy Electron Diffraction

Low energy electron diffraction (LEED) is a technique which allows the determination of the atomic arrangement close to a sample surface.

The LEED apparatus consists of an electron gun which emits electrons of energy typically in the range 10-200 eV, a series of energy-filtering grids and a phosphor screen<sup>5</sup>.

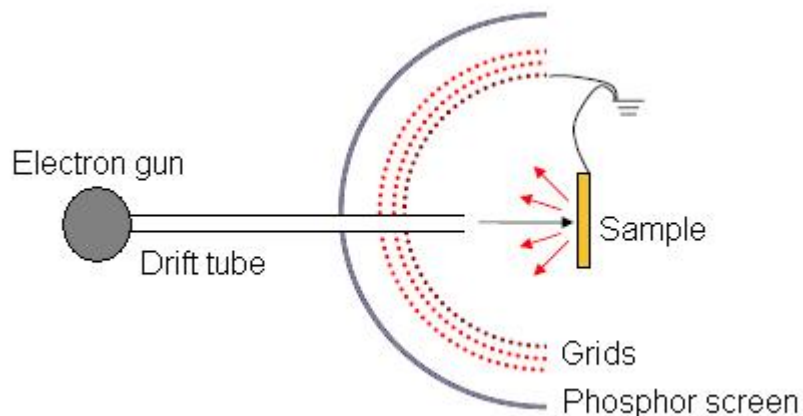


Figure 2.3 Schematic diagram of LEED apparatus

Periodic surface structures (e.g. a monocrystalline or adsorbate-covered surface with long-range order) can act as a conventional diffraction grating (figure 2.4). The beam of electrons can be considered a succession of plane waves of de Broglie wavelength,  $\lambda$ , at normal incidence to the sample if it is positioned sufficiently far from the beam source.

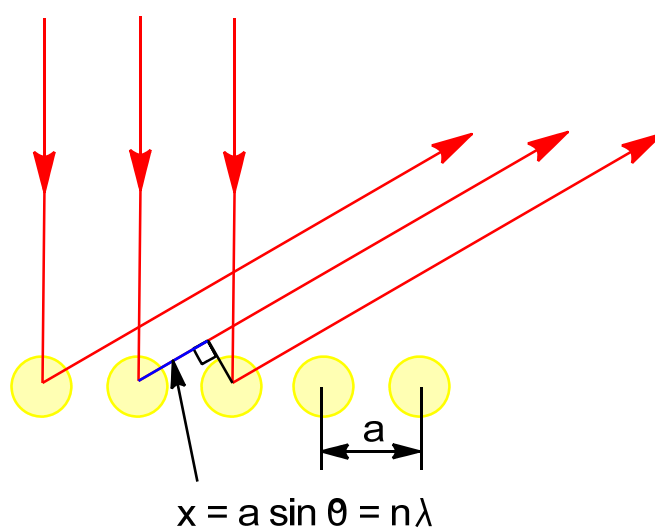


Figure 2.4 Diffraction by surface atoms

If the beam backscatters from surface atoms at an angle  $\theta$  to the surface normal, the distance each beam has to travel to the screen will be separated by path length,  $x$ . For constructive interference to occur, the difference in path length must be equal to an integral number of wavelengths.

The equation of figure 2.4 can be expressed as:

$$\sin \theta = 2\pi n/ka \quad \text{Equation (2.14)}$$

where  $n$  is the order of diffraction. The quantity  $k = 2\pi/\lambda$  is known as the wave number and can be related directly to the momentum of the wave.

Positions of constructive interference will show up as bright spots on the fluorescent phosphor LEED screen. The equation 2.14 implies that when  $n = 0$ , the scattering angle,  $\theta$ , must also equal zero, this results in zero order or specular diffraction which produces the bright spot that appears in the centre of LEED patterns. By the above equation, when  $\frac{n\lambda}{a}$  is greater than 1, diffraction is no longer possible.

The spacing between diffraction spots is inversely proportional to the lattice parameter,  $a$ , of the overlayer structure. Hence the LEED pattern on the screen is actually the reciprocal of the real periodicity of the surface. The spacing of the spots can allow surface unit cell size and symmetry to be determined.

In this study, LEED was used mostly for monitoring the sample cleanliness and surface order before experiments. A clean, well-ordered surface is the most reproducible surface and is necessary to ensure experimental fairness and allow just comparison of results. A pattern consisting of sharp spots on the screen indicates a well-ordered surface. A diffuse series of spots could indicate a poorly

ordered surface or the presence of impurities; in either case, further annealing or a sputter and annealing cycle would be required.

## 2.5 Scanning Tunnelling Microscopy

Developed in 1981, scanning tunnelling microscopy (STM)<sup>6</sup> is a non-optical microscopy technique that allows atomic scale imaging and measurement of surfaces by specific probing of individual atoms and molecules in contrast to traditional surface science techniques that collect and average measurement across a large area. The underlying physical basis of STM operation is electron tunnelling. Electron tunnelling can occur between two conductors that are separated by a thin insulating barrier, which may be vacuum, liquid or gas.

In STM operation, an atomically sharp tip, commonly Pt-Ir, Pt-Rh or W, is brought close to a conducting surface and a bias voltage of between a few millivolts and a few volts is applied between them. As the tip approaches to within a few nanometres of the surface, its quantum mechanical wavefunctions overlap with those of the sample and electrons are shared between them. The movement of electrons across the barrier is known as ‘tunnelling’, this phenomenon violates the laws of classical dynamics which disallow such an interaction as the electrons possess insufficient kinetic energy to overcome a potential barrier of this magnitude.

A tunnelling current,  $I_t$ , is typically established at tip-surface separations of 3-7 Å, it can be described as:

$$I_t \propto \exp\left(-kd\phi^{\frac{1}{2}}\right) \quad \text{Equation (2.15)}$$

where  $k$  is a constant,  $\phi$  is the barrier height and  $d$  is the tip-sample separation<sup>7</sup>. The exponential dependence of  $I_t$  on the tip-sample separation implies that STM exhibits high vertical resolution, an increase of 1 Å in  $d$  can result in a corresponding decrease of  $I_t$  by around an order of magnitude. This relationship also means that the atom at the apex of the tip is the one through which the majority of the electrons tunnel. Likewise, electrons will only tunnel into the closest sample atom, thus during scanning, the tunnelling current is confined to a filament between the apex of the tip and the surface; for a particularly pointed tip – where a single atom exists at the apex – the dimension of this filament is reduced to atomic dimensions and high resolution images can be acquired.

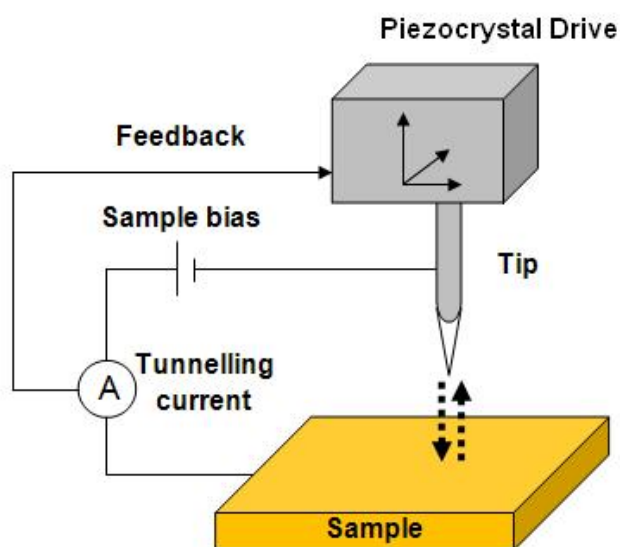


Figure 2.5 Schematic representation of STM apparatus<sup>6</sup>

The scanner consists of a piezoelectric actuator upon which the tip is mounted; piezoelectric materials change length upon a voltage being applied, the position of the tip can be controlled accurately in the  $x$ -,  $y$ - and  $z$ - directions<sup>6-8</sup>(figure 2.5). The actuator and the sample are both contained within a unit atop a vibrationally isolated stage.

The tip first approaches the sample in ‘coarse’ steps by a control unit motor, before precision positioning by piezoelectrics. Figure 2.6 schematically shows the stages of electron tunnelling that takes place<sup>6</sup>. Initially, the tip and the sample are independent of each other and separated by a macroscopic distance; the wavefunctions of both the tip and the sample decay exponentially into the vacuum. A potential difference is applied between the tip and the sample and once brought within close proximity, electrons will tunnel between overlapping wavefunctions of the tip and the sample.

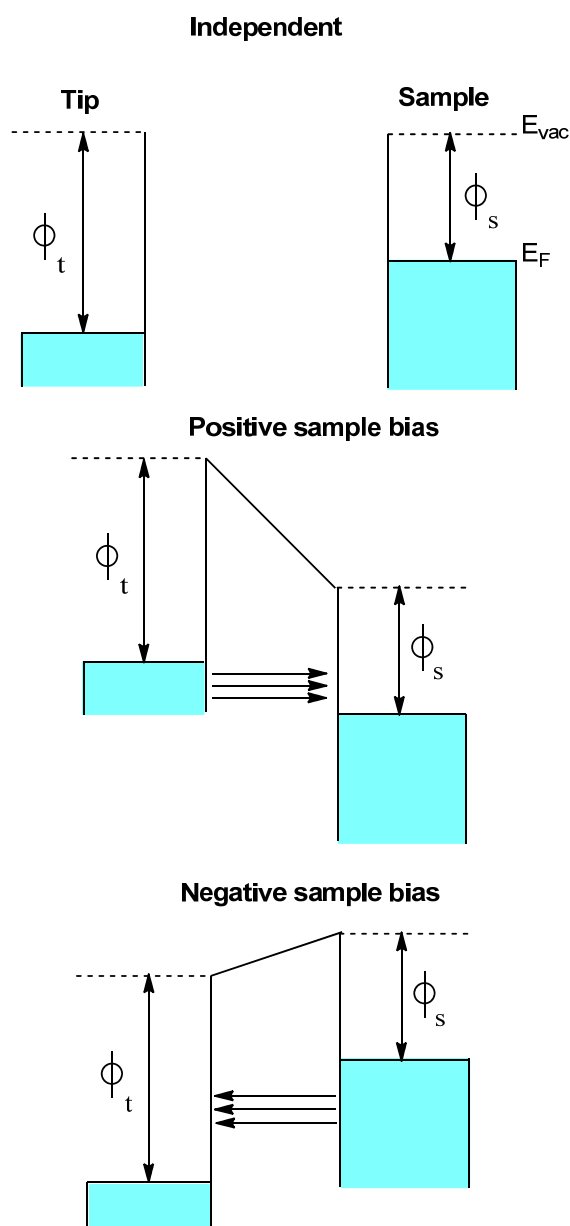


Figure 2.6 Schematic representation of electron tunnelling between the tip and the surface<sup>7</sup>

The sign of the bias voltage determines the direction in which the current flows. If the sample is biased by a positive voltage,  $V_s$ , with respect to the tip, then the energy levels of the tip will increase by  $eV_s$ . Electrons tunnel from the filled tip states into empty sample states and a dc tunnel current is established. By biasing the sample negatively with respect to the tip, the tunnelling current flows in the opposite direction.

Once a tunnelling current is established, the tip can be raster scanned across a chosen sample area to allow an image of the surface to be generated. Scanning may be carried out in two modes: constant current or constant height<sup>6,8</sup>. In constant current, the tunnelling current is fixed by the user. As scanning progresses changes to the chosen current are corrected by feedback signals controlling the  $z$ -piezodrive. A record of the height of the tip (the retraction and the extension of the piezodrive) at points in the  $xy$  plane is used to generate an image of a specific area of the surface. In constant height mode, the tip is scanned in the  $xy$  plane at a fixed height from the surface. The tunnelling current is recorded as a function of lateral position and used to create the STM image. The computer converts the data acquired into pictures or maps where apparently high areas are bright and low areas are dark, image processing software allows measurements or improvements such as contrast adjustment or noise removal. In general, constant current mode results in slower scanning of the surface but it also limits the risk of the tip crashing into the surface. Surface roughness is important in deciding which mode is most suitable; if scanning a large area of the sample, where many surface terraces may be expected, constant current mode offers more stable scanning whereas upon a small, atomically flat areas, constant height mode yields images of better resolution.

The tunnelling current depends not only upon the distance between the tip and the surface but upon the electronic structure of both the tip and the sample<sup>8</sup>. Careful analysis of STM images is required to distinguish between features that are due to changes in topography or to the local density of electronic states across the surface. STM images are therefore maps of the electronic structure of the surface

and not merely steric representations. Interpretation may not be as simple as relating regions of brightness or darkness to high and low points on a surface, and gaining data on actual atomic positions or their chemical nature may also be difficult. With the knowledge of typical or anticipated chemical behaviour, computer modelling and possibly, in combination, with other surface science techniques, STM images may be interpreted to give an accurate understanding of the processes occurring on the surface. The unique visualisation of the surface offered by STM makes it an invaluable surface science tool.

## 2.6 References

- (1) Attard, G.; Barnes, C. *Surfaces*; Oxford University Press: Oxford, 1998.
- (2) Woodruff, D. P.; Delchar, T. A. *Modern Techniques of Surface Science*; Cambridge University Press: Cambridge, 1986.
- (3) Sales, J. L.; Zgrablich, G. *Physical Review B* **1987**, *35*, 9520.
- (4) Spinicci, R. *Thermochimica Acta* **1997**, *296*, 87.
- (5) Atkins, P.; de Paula, J. *Physical Chemistry*, 7th ed.; Oxford University Press: Oxford, 2002.
- (6) Davies, P. R.; Roberts, M. W. *Atom Resolved Surface Reactions: Nanocatalysis*; RSC: Cambridge, 2007.
- (7) Vickerman, J. C., *Surface Analysis – The Principal Techniques*; John Wiley & Sons: Chichester, 1997.
- (8) Kirkland, A. I.; Hutchinson, J. L. *Nanocharacterisation*; RSC: Cambridge, 2007.

### 3 Self-assembly on a Nickel Surface

Controlling the assembly of adsorbate molecules on a reactive metal surface is fundamental to the design of effective enantioselective heterogeneous catalysts. The formation of chiral, functionalised and porous molecular networks upon a reactive metal surface is most desirable for applications in catalysis. Systems of molecules which reliably self-assemble into two-dimensional networks present themselves as ideal candidates to combine with surfaces of relevant catalytic properties. Once the ability to form supramolecular networks is established, organic synthesis may then be used to confer functionality into the component molecules and tailor the networks to specific chemical reactions.

The aim of the experiments carried out in this chapter is to assess the possibility of growing a hydrogen bonded network from PTCDI and melamine, which are known to reliably form regular supramolecular structures on Ag-Si(111)- $\sqrt{3}\times\sqrt{3}R30^\circ$ <sup>1</sup> and Au(111)<sup>2</sup> substrates, atop a nickel substrate. The surface behaviour of PTCDI and melamine may be probed directly using scanning tunnelling microscopy (STM) to determine the viability of this approach whilst temperature-programmed desorption (TPD) is also used to further the understanding of the energetic interactions of each of these components with the substrate. The TPD experiments may be used to determine the stability of PTCDI and melamine on a reactive metal substrate and estimate quantitative values for comparison with those derived from experiments on Au(111).

#### 3.1 Self-assembly on the Ni(111) Surface

The asymmetric hydrogenation of  $\beta$ -ketoesters has been observed over modified nickel catalysts<sup>3,4</sup>. The mechanism of the reaction is thought to involve attack by H atoms on the C=O bond (or the C=C bond where the reagents are present in the enol tautomeric form). This results in a newly formed chiral centre with a C-OH

bond pointing away from the surface<sup>5</sup>. The prochiral  $\beta$ -ketoesters reagents (for example, methylacetoacetate) are initially close to planar and they adsorb with their molecular plane parallel to the nickel surface<sup>6,7</sup>, thus the chirality of the product is determined by the particular enantiotopic face that interacts with the surface. For an unmodified surface, both faces of the prochiral reagent should be adsorbed with the same probability resulting in both enantiomers being produced in equal quantity.

The adsorption of a specific molecular overlayer prior to the reagents is one way in which the surface could be modified such that the prochiral reagent is directed into adsorption to the surface through only one of its two enantiotopic faces.

Single crystal surfaces, often in UHV, are typically used to study the adsorption of chiral modifiers and prochiral molecules. These surfaces are good models of the facets of metal nanoparticles that exist upon real catalyst surfaces. The Ni(111) surface has been selected as a suitable substrate for investigation of the PTCDI-melamine network. Its flat surface parallels those where network assembly has already been observed, Ag-Si(111)- $\sqrt{3}\times\sqrt{3}R30^\circ$ <sup>1</sup> and Au(111)<sup>2</sup>. Upon the Ni(111) surface, ordered supramolecular arrangements have been observed at high coverages of chiral modifier species, such as (R,R)-tartaric acid<sup>8</sup> and (S)-glutamic acid<sup>9</sup>, but under these conditions little space is available for the adsorption of prochiral reactants. The potential formation of a network such as the hexagonal PTCDI-melamine hydrogen bonded (with further functionalisation) may offer both an ordered overlayer capable of interacting with a prochiral reagent in an exclusive configuration<sup>10,11</sup> but also grant the necessary space on the surface (within the pores) for adsorption to the catalyst surface.

Previous studies have indicated that aromatic molecules tend to adsorb to surfaces with their ring systems parallel to the surface in order to maximise interaction of the  $\pi$ -systems<sup>12,13</sup>. Several studies have examined the interaction of aromatic molecules on Ni(111) but very little evidence of ordered arrangements has been

discovered. The simplest of systems; benzene on Ni(111); seems to represent typical behaviour on nickel surfaces. Benzene is reported to adsorb parallel to the Ni(111) surface but ordered arrangements are only observed when present at high coverages with added stabilisation from co-adsorbed CO or at low temperatures<sup>14,15</sup>. Fink et al<sup>16</sup> report that naphthalene-3,4,7,8-tetracarboxylic dianhydride (NTCDA) does not form ordered monolayers on Ni(111) after annealing the substrate in the range 300 K to 320 K. They suggest that the formation of strong local bonds between the surface and the NTCDA  $\pi$ -system and anhydride groups causes the molecules to 'hit and stick'. Naphthalene-3,4-dicarboxylic anhydride (NDCA) behaves slightly differently on Ni(111)<sup>17</sup>: at low coverages (<0.7 ML), molecules are orientated parallel to the surface and ordered arrangements are observed, however, molecular dissociation occurs as the surface temperature approaches 350 K. At higher coverages (0.7-1.0 ML), NDCA does not adsorb parallel to the surface. PTCDA and PTCDI have both been analysed by near edge X-ray adsorption fine structure (NEXAFS) on Ni(111)<sup>18</sup>. An average tilt angle of 29° of the PTCDI plane with respect to the surface was found: this could either indicate flat-lying molecules alongside a minority of randomly oriented molecules or domains of molecules which are tilted by about 30°.

As well as investigating the possibility of granting mobility to network components and forcing assembly into an organised network via annealing conditions, STM could also be used to determine which of the two possible outcomes suggested in the above study of PTCDI on Ni(111) takes place<sup>18</sup>.

## 3.2 Experimental

TPD experiments were carried out in Chamber 1, a PSP Vacuum Technologies UHV system with a base pressure of  $1 \times 10^{-10}$  mbar. The system is described in Section 2.1. The Ni(111) sample was prepared by cycles of argon ion bombardment (1 kV) and annealing to 900 K until a sharp (1x1) LEED pattern and no surface impurities were detected by Auger electron spectroscopy (AES).

Clean samples were allowed to cool to room temperature before exposure to the species being examined. PTCDI and melamine were sublimed into the chamber from dosers isolated from the main chamber by gate valves, as described in Section 2.1, after heating to 638 K and 363 K, respectively. After exposure, the pressure is allowed to return to base level before carrying out the temperature-programmed desorption experiment. In some cases, the sample is annealed prior to performing the experiment; this allows for the adsorbate layer to become more ordered; when this step is taken, the sample is allowed to cool to room temperature before proceeding. The temperature-programmed desorption experiment is carried out by positioning the sample in close proximity to the quadrupole mass spectrometer. The sample is heated at  $4 \text{ K s}^{-1}$  through heating wires that are used to mount the sample onto the manipulator. The mass spectrometer is used to measure desorbed species throughout the duration of the temperature ramp. The characteristic mass fragment  $m/z = 69$  is used to monitor PTCDI, whilst fragments  $m/z = 43, 68, 83, 85$  and the molecular ion  $m/z = 126$  can be used to monitor melamine. The choice of which of these fragments to use in this study is limited by the  $m/z$  range of the mass spectrometer ( $m/z = 0-300$ ) and its sensitivity; the molecular ion for PTCDI ( $m/z = 390$ ) lies outside the range of detectable  $m/z$  hence  $m/z = 69$  is used, whereas  $m/z = 43$  lies within the most sensitive  $m/z$  range for this instrument and is used, the other fragments, however, are used to establish whether molecular desorption occurs or if the molecule dissociates before desorption.

STM experiments were carried out in Chamber 2, an Omicron UHV system with a base pressure of  $1 \times 10^{-10}$  mbar. The system consists of three linked chambers: a preparation chamber with facilities for argon ion sputtering, AES and LEED and the dosing of molecular species and two analysis chambers for reflection adsorption infrared spectroscopy (RAIRS) and STM. Sample cleaning and dosing of PTCDI and melamine is carried out as in the TPD experiments in the preparation chamber before images of the surface were acquired by transferring under UHV conditions to the STM chamber where data were taken in constant current mode using an electrochemically etched W tip. All STM images were

acquired at room temperature. STM images were processed using WSxM software<sup>19</sup>.

## 3.3 Results and Discussion

### 3.3.1 PTCDI on Ni(111)

#### 3.3.1.1 TPD of PTCDI from Ni(111)

Temperature-programmed desorption spectra of PTCDI from Ni(111) are somewhat disorganised, no trend could be obtained despite following the same sample preparation, deposition and analysis procedures for every level of PTCDI exposure administered to the surface (figure 3.1). The amplitude of the desorption spectra should be dependent on the dose delivered into the chamber. For example, the spectrum generated after the 200 L dose should feature peaks greater in amplitude than those observed in the 1 L spectrum. The discrepancy may be attributed to the PTCDI dosers. In the experimental setup, the open end of the doser is pointed towards the sample so that the adsorbate, in this case, PTCDI, is sprayed onto the sample. The intensity of the PTCDI ‘beam’ delivered to the sample may vary between TPD experiments due to the packing of material within the doser. As more material is sublimed from the doser, the packing within the doser changes and it can be difficult to maintain the same pressure for the duration of each dose. The thermocouple reading from within the doser may also complicate matters. The thermocouple is inserted within the doser and the chemical of interest is packed around it in order to measure the temperature of the material being dosed. As sublimation occurs, the contact between the thermocouple and the dosing species will be constantly changing, this could lead to inaccurate temperature readings as the doser empties. As a precaution, the partial pressure of PTCDI was often monitored by the mass spectrometer whilst dosing to ensure sublimation was occurring, but it must be noted that there will be a discrepancy between the localised partial pressure of PTCDI at the sample

surface and the mass spectrometer due to the intensity of the ‘beam’ from the doser.

A low temperature peak is observed around 310 K for the majority of the desorption spectra. This type of peak is usually associated with multilayer desorption or can be explained as an artefact created by desorption from the sample mounting. The spectra are obtained by monitoring the  $m/z = 69$  mass fragment; this fragment is consistently observed in the mass spectrum analysis of PTCDI. The  $m/z = 69$  fragment is also observed in the mass spectrum of perylene so this fragment will most likely be generated from the aromatic core of PTCDI molecules. Analysis of the surface by AES after the TPD experiment indicated a clean Ni surface.

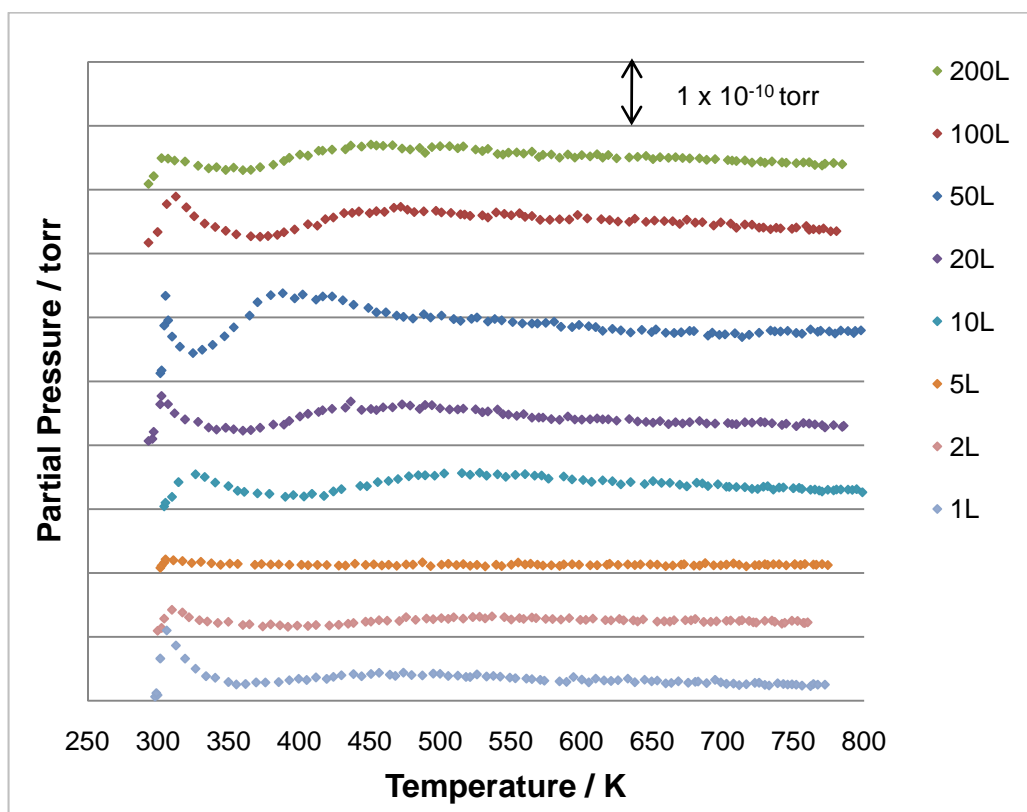


Figure 3.1 TPD of PTCDI from Ni(111) for a range of initial exposures to the sample at 300 K. Desorption spectra are based upon the  $m/z=69$  fragment.

Pre-annealing samples prior to the actual TPD experiment seems to generate more consistency in the results of the experiments shown in figure 3.2. The surface

coverage in these spectra acquired after either 5 L and 10 L doses is thought to be close to 1 ML. A range of  $T_{max}$  values roughly around 450 K, are observed. The spectra are still not typical of zero, first or second order desorption kinetics. The low temperature peak was not removed via the pre-annealing step which suggests that the pre-annealing step may be too short or at too low a temperature or that the feature is generated by some surface process that is regenerative. The long pressure decay after the second peak needs further attention as TPD experiments usually result in sharp peaks over short temperature ranges. The peaks in the PTCDI TPD experiments sprawl over the range 300 K to 800 K with a very slow pressure decay after the main peaks at around 310 K and 450 K.

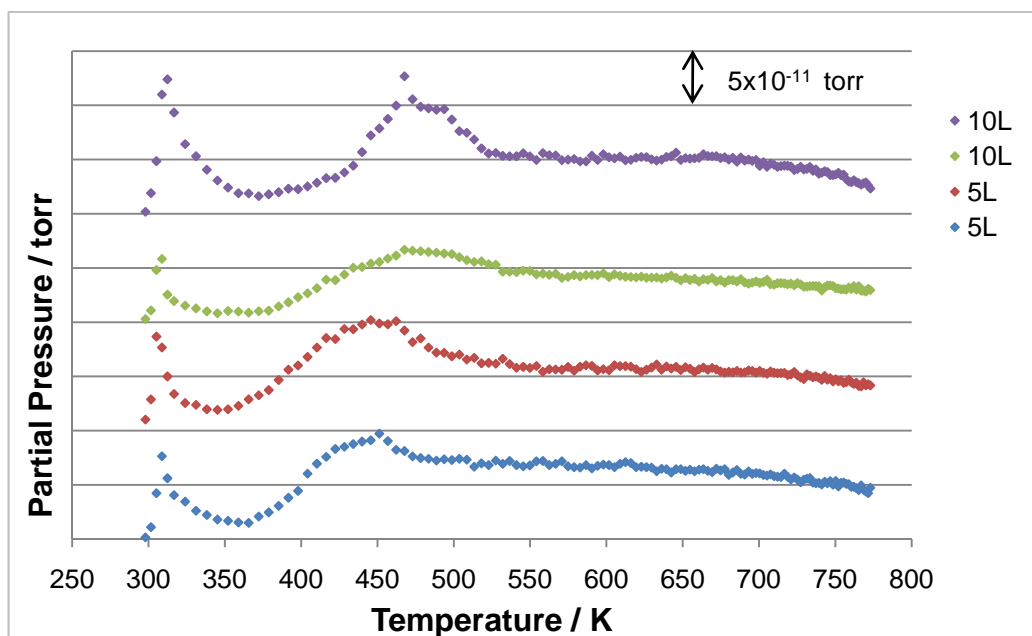


Figure 3.2 TPD of PTCDI from Ni(111) where pre-annealing treatment of flashing to 313 K is used. Initial exposures of 5 L and 10 L to PTCDI occurs whilst the sample is held at 300 K. Desorption spectra acquired after monitoring  $m/z=69$  ion. TPD experiments were repeated for both initial exposure levels.

The temperature of  $T_{max}$ , around 450 K, is less than the temperature the solid doser must be heated to, around 638 K, in order to sublime PTCDI into the chamber. This may imply that the PTCDI-PTCDI interaction strength in the 3-D bulk crystal formation is greater than the interaction of PTCDI with the Ni(111) surface. If this is the case, then it may be expected that multilayer, rather than monolayer, formation on the surface might be more favourable. If multilayer formation is occurring, a characteristic tall, sharp peak, might be observed in the

TPD spectra for molecular desorption. As the desorption spectra in figure 3.2, for 5 L and 10 L doses, are nearly equal in amplitude and similar in shape, near monolayer coverage is assumed. Presumably, for this to occur, the sample has to be sprayed evenly only to monolayer coverages and an energy barrier towards multilayer formation prevents reorganisation. Doses of up to 3 L are used to achieve the coverages (up to  $\sim 0.5$  ML) in the range of STM images, shown in Section 3.3.1.2, where monolayer formations are observed. Although it is impossible to confirm that molecular desorption does indeed take place, it must be noted that the  $m/z = 69$  fragment is observed in the mass spectrum of PTCDI (recorded using EI-MS by the Mass Spectrometry Service in the School of Chemistry) and whilst recording the pumping speed plot, when no surface upon which dissociation might occur, is involved. If dissociation of PTCDI does occur upon heating the surface, then the observed  $m/z = 69$  fragment must therefore be a fragment of a fragment. Umbach et al<sup>18</sup> declare that the bonding between PTCDI and the Ni(111) surface leaves the molecule intact although no information is provided on this interaction upon heating.

Factors such as extensive supramolecular interactions and pumping speed (the removal of PTCDI from the vacuum chamber) may be significant in the shape of the desorption spectra obtained. The position of each peak in TPD spectra will depend on the activation energy of desorption,  $E_d$ , of the molecules from which it is derived. The activation energy of desorption will be determined by the strength of the interaction of the molecules with the metal surface and may also contain contributions from intermolecular interactions. If a range of intermolecular adsorption geometries exist, then a number of different  $E_d$  values, and therefore peaks in the TPD spectrum, would be anticipated. If adsorption states of similar  $E_d$  are present, as may be the case if the differences in the desorption states are caused by the number of weak supramolecular interactions each state experiences, then a single desorption peak may be broadened because it incorporates molecules desorbed from a variety of sites and is formed from the overlap of a several desorption peaks. Transitions between desorption sites as desorption progresses may also have an influence. Furthermore, if the peak is derived from just one adsorption site (or a few low population adsorption sites close in  $E_d$ ), then it

would be expected to be sharper than a peak which encompassed many adsorption sites of a wider range of  $E_d$ . The desorption process taking place at the surface is not entirely responsible for the temperature-programmed desorption spectra; if desorbed molecules are not removed from the chamber, the pressure they exert will continue to be measured and incorporated in the TPD spectra long after the desorption occurs.

The pumping speed plot is obtained separate from the desorption experiments; it is carried out by allowing the chamber to fill to an arbitrary but significant pressure (notionally  $1 \times 10^{-8}$  mbar throughout pumping speed calibration tests) via leaking of PTCDI vapour before monitoring its decay as a function of time after the doser valve is closed. The pumping speed plot for PTCDI in the UHV system used for the TPD experiments is shown in figure 3.3, it has a shape similar to an exponential decay.

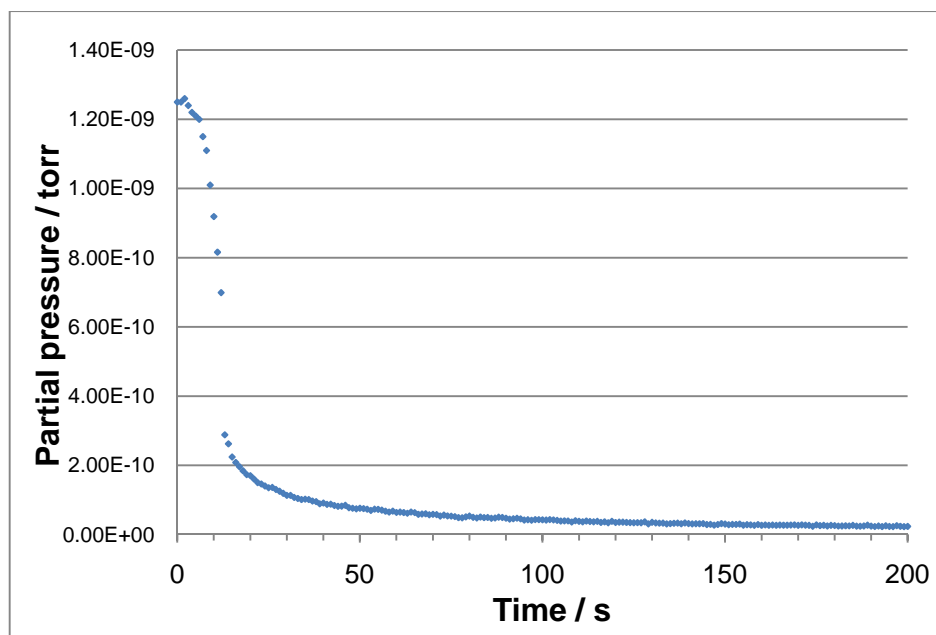


Figure 3.3 Pumping speed plot for an exposure of PTCDI to the vacuum chamber. The partial pressure is again monitored using the  $m/z=69$  fragment. The pressure in the chamber was  $3 \times 10^{-9}$  torr at  $t=0$  when the gate valve to the PTCDI doser was closed.

A two step process can be used to describe the process by which a PTCDI molecule on the Ni(111) surface reaches the pump and influences the pressure measured at the sensor:



The pressure,  $p$ , exerted by the gas phase inside the chamber is caused by the number of molecules desorbing from the surface and those molecules not yet removed from the chamber via pumping.

An Arrhenius-type relationship can be used to predict how many molecules of those present will be desorbed at a given  $T$ , as has been discussed in Chapter 2. Assuming a first order desorption process, the change in pressure inside the chamber should reflect the change in surface coverage,  $\theta$ :

$$\frac{dp}{dt} = k_d \theta = \gamma \theta \exp\left(-\frac{E_d}{RT}\right) \quad \text{Equation (3.1)}$$

A number of molecules on the surface at a given temperature,  $N_T$ , can be used to replace the surface coverage,  $\theta$ , and using the above, the number of molecules desorbed at a given temperature,  $N_d$ , can be represented as:

$$N_d = \gamma N_T \exp\left(-\frac{E_d}{RT}\right) \quad \text{Equation (3.2)}$$

Simple subtraction takes into account the number of molecules lost over a temperature increment:

$$N_T = N_{T-1} - N_d \quad \text{Equation (3.3)}$$

Using a spreadsheet, a simulated desorption spectrum can be generated by plotting the number of molecules desorbed with temperature,  $N_d$ , versus  $T$ , using equations 3.2 and 3.3, if values are inputted for  $\gamma$  and  $E_d$  and a large stock of molecules are inputted ( $8 \times 10^{13}$ ) as being present at the beginning of the heating ramp,  $N_T$  at  $T = 300$  K (room temperature, when heating ramp is started). The number of molecules incorporated into the initial stock is close to the typical number present in 1 ML coverage of a  $1 \text{ cm}^2$  area of Ni(111) surface.

By altering the value of  $E_d$ , the simulated spectra can be aligned with the experimental spectra, the upper 5 L desorption spectrum from figure 3.2 is used, and it should match it fairly well if the removal of the desorbed species from the vacuum chamber during the experiment is sufficiently rapid. An  $E_d$  value of 112 kJ mol<sup>-1</sup> is used to roughly align the simulated spectra based on  $N_d$  versus  $T$  against the experimental result in figure 3.4.

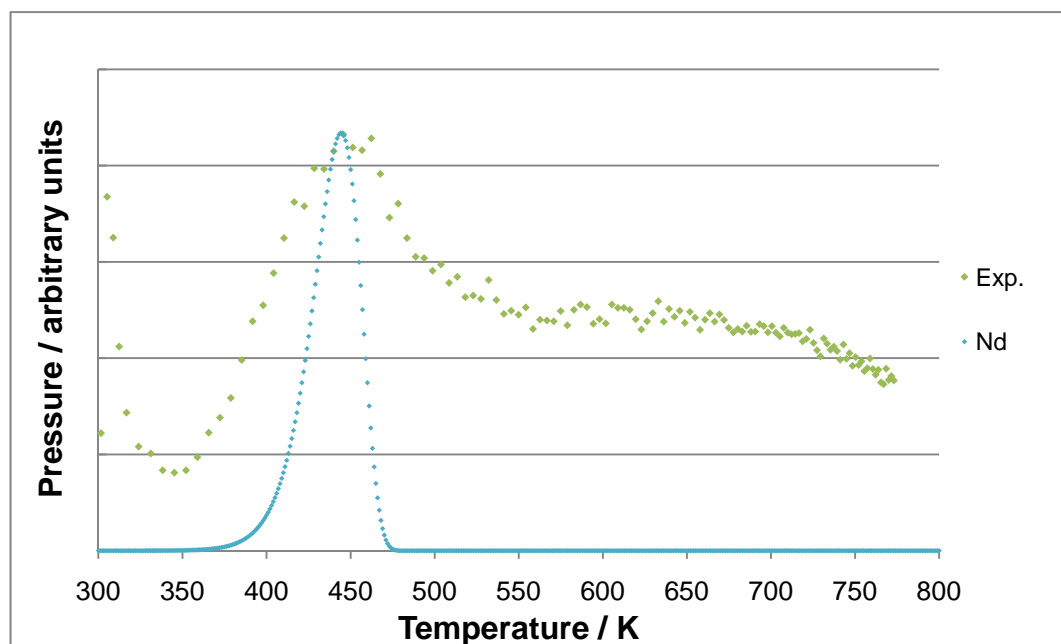


Figure 3.4 By varying the  $E_d$  value the main peak of the simulated spectrum based on  $N_d$  can be aligned with that of the experimentally obtained TPD spectrum (the upper 5 L spectrum in figure 3.2). A value of 112 kJ mol<sup>-1</sup> is used as  $E_d$  to obtain the fit above.

Although the main peak position can be matched using this simple method, the peak shapes are vastly different and, as alluded, the removal of PTCDI from the chamber by pumping and also the possibility of multiple adsorption sites may be responsible for the unusual shape of the TPD spectra obtained. The observed spectra show peaks that do not return to the baseline after the main desorption peak and as such, attempts to simulate this have to be made by taking into account environmental factors (those which relate to the experimental apparatus) as well as the processes happening at the solid-gas interface involving desorption.

PTCDI removal rate from the chamber and detection by the mass spectrometer sensor may be treated as one and incorporated into the model spectra using data

from the pumping speed plot (figure 3.3). Although the overall graph was recorded after exposing the chamber to a pressure of  $1 \times 10^{-8}$  mbar, the chamber pressure during TPD experiments is much smaller since desorption of a monolayer of PTCDI molecules from a sample of surface area of  $\sim 1 \text{ cm}^2$  does not generate equivalent pressures. To enable the simulation of PTCDI TPD spectra, only the pressure range of pumping speed plots that are on the same order of magnitude of the pressure generated during desorption is considered and early points corresponding to higher pressures are ignored, a first order exponential decay equation can be closely fitted to this section using Microsoft Excel.

If the predicted number of molecules desorbing,  $N_d$ , is multiplied by a constant to reduce them to the same order of magnitude as the pressures observed during the TPD experiment, the adjusted  $N_d$  pressure generated after the first temperature increment as the heating ramp begins can be matched to a time on the pressure versus time pumping speed plot.

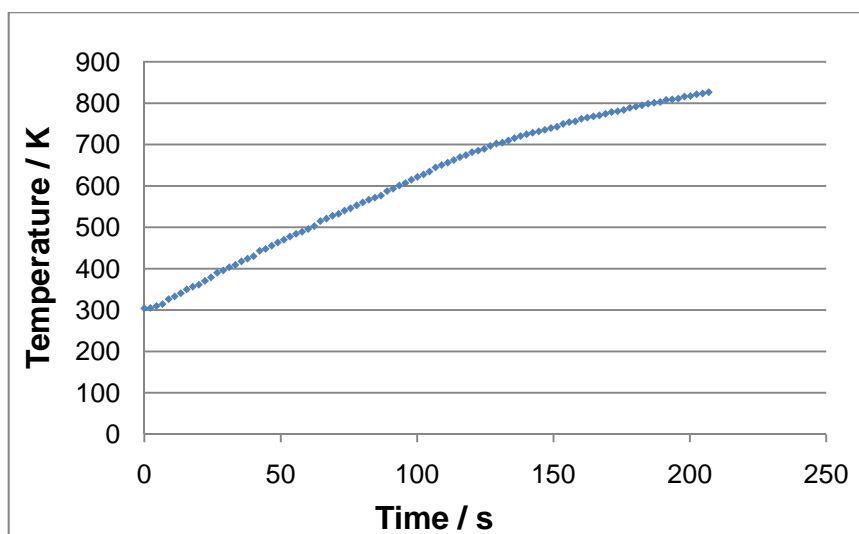


Figure 3.5 Ni(111) sample heating curve, an equation of  $T=294+3.25t-0.006t^2$  was found to be the best fit for this curve using a spreadsheet programme

During TPD experiments, the sample is heated by passing a current through it; this current is chosen so as to give a linear temperature increase. However, the rate of temperature increase decreases gradually as the temperature rises (figure

3.5). Using Microcal Origin spreadsheet software, an equation can be fitted to the heating curve that relates the temperature,  $T$ , to the time on the heating ramp,  $t$ .

$$T = 294 + 3.25t - 0.006t^2 \quad \text{Equation (3.4)}$$

The instantaneous heating rate at each temperature can be determined by differentiating the equation fitted to the experimental heating curve,  $\frac{dT}{dt} = 3.25 - 0.012t$ . As illustrated in figure 3.6, by relating the heating rate to the sample temperature, the duration of temperature increments (1 K) can be deduced for every temperature in the range studied, this duration is important for deducing the number of molecules (the pressure) that can be removed during these increments if the starting pressure and relationship between the pressure decrease and time is known.

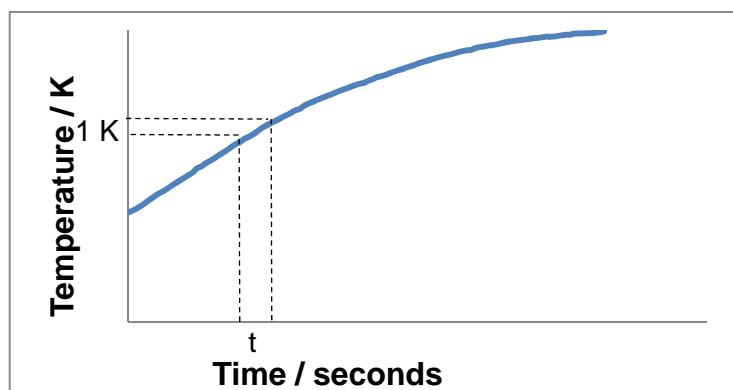


Figure 3.6 Example of a sample heating curve and how it can be used to determine how long a model T increment lasts.

The pressure at the start of a temperature increment can be given as  $N_d (N_D)$  and subsequently, the number of molecules in the chamber,  $N_S$  (see below), and this can be related to a time on the pressure versus time pumping speed plot. The pumping speed plot was acquired after monitoring the decay after the pressure to reach  $3 \times 10^{-9}$  torr inside Chamber 1, but the pressure generated during TPD experiments never equals this. A satisfactory relationship that fits the complete pumping speed plot was not found but a satisfactory first order decay relationship could be matched to a low pressure section of the plot. Assuming  $t = 0$  where the partial pressure  $p = 1 \times 10^{-10}$  torr, the equation:

$$p = -1.89 \times 10^{-18} + 1.0098 \times 10^{-11} \exp\left(-\frac{t}{144.11}\right) \quad \text{Equation (3.5)}$$

was obtained from a Microcal Origin spreadsheet to fit the pressure decay trend. This equation allows any pressure, as represented by the number of molecules desorbing,  $N_d$ , and subsequently, the number of molecules at the sensor,  $N_s$ , to be related to a time on the low pressure section of the pumping speed plot, the low pressure section can be used as an effective pressure decay calibration plot (figure 3.7). The time that a temperature increment lasts can be used to obtain a value for the size of the pressure decay that would occur during it by using the equation that defines the pressure calibration plot to acquire pressure values at the beginning and end of a temperature increment.

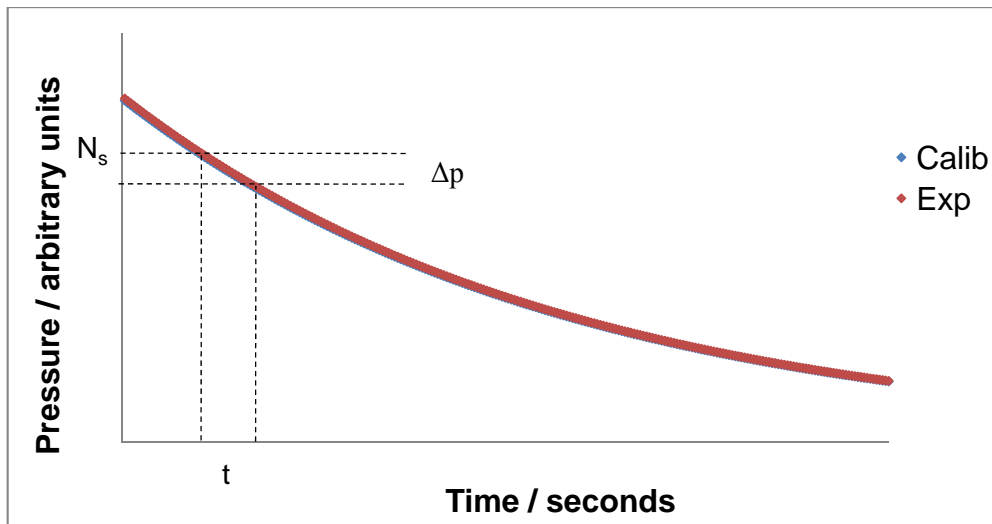


Figure 3.7 Low pressure section of plot from figure 3.3 and how it can be used to determine the quantity of molecules removed during a T increment. In the above section, which may be considered as a pressure calibration plot,  $t=0$  is where taken to be at partial pressure of  $1 \times 10^{-10}$  torr, a first order decay relationship of  $p = -1.89 \times 10^{-18} + 1.0098 \times 10^{-11} [\exp(-t/144.110)]$  across this pressure/time range was given using Microcal Origin. The calibration plot fits the experimental data almost perfectly.

Following on, after the first temperature increment, the number of molecules in the chamber (detected by the sensor),  $N_s$  at  $T_0$  will simply be  $N_d$  at  $T_0$ . After the next temperature increment, the number of the molecules in the chamber will be the sum of the number of molecules desorbed during that temperature increment,  $N_d$ , and the number of molecules that were desorbed during the previous

temperature increment but not pumped from the chamber over the subsequent temperature increment.

With temperature increments of 1 K and the starting temperature,  $T_0$ , of 300 K:

At 300 K,

$$N_s = N_d(T = 300 \text{ K})$$

At 301 K,

$$N_s = N_d(T = 301 \text{ K}) + N_s(T = 300 \text{ K}) - \Delta p_{(p_0 = N_s(T = 300 \text{ K}))}$$

At 302 K,

$$N_s = N_d(T = 302 \text{ K}) + N_s(T = 301 \text{ K}) - \Delta p_{(p_0 = N_s(T = 301 \text{ K}))}$$

Scheme 3.1

Scheme 3.1 can be extended to produce a spectrum, plotting  $N_s$  versus  $T$ , that has a much longer decay than the desorption spectrum produced by plotting  $N_d$  versus  $T$ .

Producing a value for  $\Delta p$  relies upon use of the pressure decay calibration curve and the sample heating rate curve. The relationship produced used to fit the decay curve can be arranged to give a time,  $t$ , on the curve for a specific pressure. The pressure, in this case, is  $N_d$ , and subsequently,  $N_s$ , the number of desorbed molecules detected at the sensor.

$$t = 144.11 \ln \left( \frac{N_s + 1.89 \times 10^{-18}}{1.0098 \times 10^{-11}} \right) \quad \text{Equation (3.6)}$$

$N_d$  and  $N_s$  are simulated values, ranging from 0 to  $8 \times 10^{13}$ , or the total number of molecules chosen to stock the surface; these may be related to pressures on the calibration curve by multiplying by a constant. A value for the pressure change,  $\Delta p$ , over a 1 K temperature increment may be obtained from the difference in

pressure between two values of  $t$  on the pressure calibration plot,  $t$  and  $t + \frac{dt}{dT}$ . Equation 3.6 is used to obtain  $t$ , and  $t + \frac{dt}{dT}$ , which represents the time on the pressure calibration plot after a 1 K temperature increment, is derived from the heating rate curve.

$$\Delta p = \left( -1.89 \times 10^{-18} + 1.0098 \times 10^{-11} \exp \left( -\frac{t}{144.11} \right) \right) - \left( -1.89 \times 10^{-18} + 1.0098 \times 10^{-11} \exp \left( -\frac{t + \frac{dt}{dT}}{144.11} \right) \right)$$

Equation (3.7)

If the observed desorption spectrum is considered as being made up of only one peak,  $E_d$  can be varied to move the simulated curves to match the position of the peak to that in the experimentally observed spectra, below in figure 3.8, a value of 106.5 kJ mol<sup>-1</sup> is used to match the spectrum based on  $N_s$  versus  $T$  (red) with the experimental result (green). The curve of  $N_s$  versus  $T$ , plotting the number of molecules desorbing from the surface with temperature, is also shown (blue). The amplitude of this curve is much smaller than that based on  $N_s$  due to the slow removal rate of PTCDI from the chamber. By Scheme 3.1,  $N_d$  should never be greater than  $N_s$ , and if  $\Delta p$  is very small, the number of molecules desorbing,  $N_d$ , may be much smaller than the number of molecules detected by the sensor,  $N_s$ , during a  $T$  increment. Since  $\Delta p$  is small, there is also a lag in peak position in the plot based on  $N_s$  relative to that based on  $N_d$  between the two plots;  $N_s$  peaks around 17 K higher than  $N_d$ ; ideally,  $T_{max}$  should represent the temperature at which the rate of desorption is highest, but in this case, the slow removal of PTCDI from the chamber causes this information to be obscured.

After adding in the effect of the pumping speed to the spectrum in figure 3.8, a mismatch still exists between the experimental and the simulated spectra. Concentrating on the main desorption peak at 450 K, the mismatch in the region above 450 K indicates the likelihood of adsorption sites of more than one  $E_d$  being present.

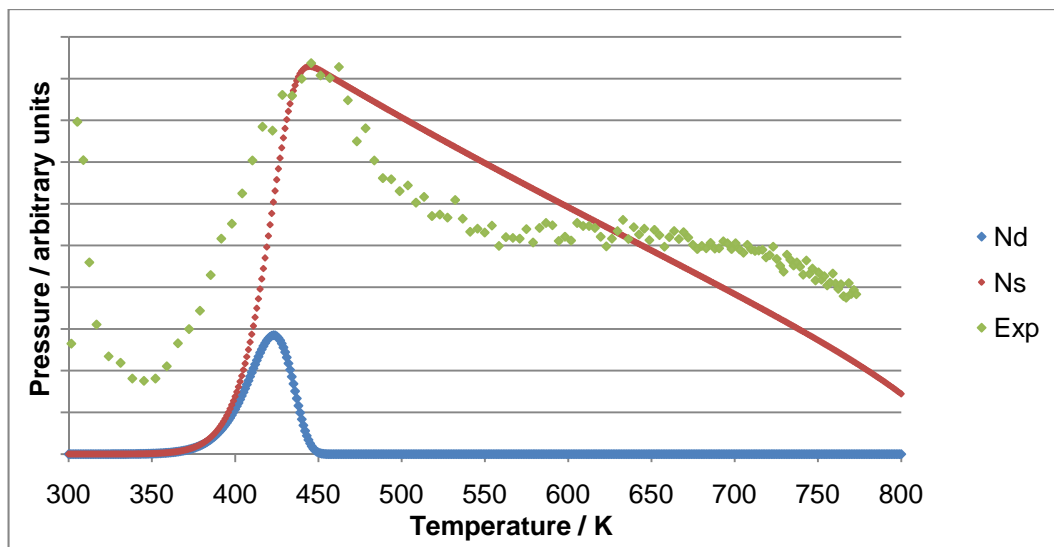


Figure 3.8 Comparison of simulated TPD spectra based on  $N_d$  and  $N_s$  versus temperature with the experimental result (the upper 5 L desorption spectrum taken from figure 3.2). The red plot takes into account a delayed removal of PTCDI molecules after desorption, whilst the blue plot, based solely on the number of molecules desorbing at a given temperature, returns to the baseline soon after  $T_{max}$ .

The TPD spectra acquired for PTCDI from Ni(111) each have two peaks, the low temperature peak at 310 K and the broad desorption with  $T_{max}$  at 450 K. TPD studies where the adsorbate exists in two or multiple adsorption sites generally result in spectra of two or more peaks, molecules in a site of a lower activation energy of desorption will desorb first at lower temperatures before more strongly held molecules desorb at higher temperatures. The number of molecules desorbing,  $N_D$ , during each temperature increment will be a sum of the number desorbing,  $N_d$ , from each site:

$$N_D = \sum_{site\ 1}^{site\ n} N_d \quad \text{Equation (3.8)}$$

Figure 3.9 shows examples of simulated TPD spectra based on number of molecules desorbing with temperature if equal numbers of molecules are placed in two desorption sites of differing desorption energies for a hypothetical adsorbate-substrate system. Peaks can be separate from each other if the difference in  $E_d$  between adsorption sites is vast enough or overlap if the difference is smaller.

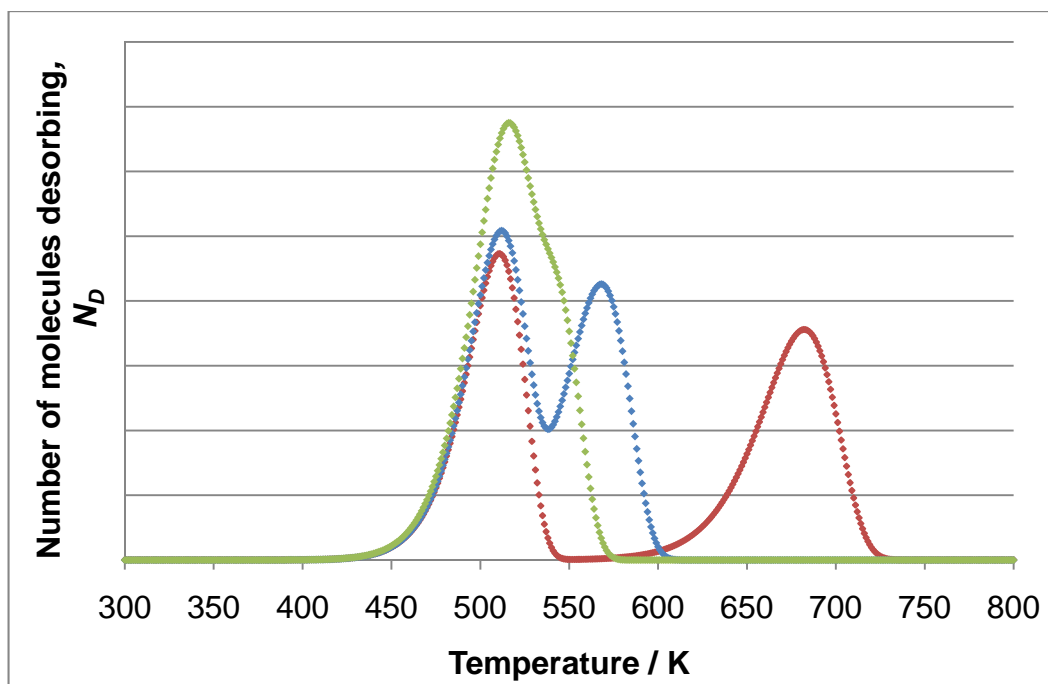


Figure 3.9 Model TPD spectra showing desorption from two sites of differing  $E_d$  where molecules cannot transfer between sites. The green spectrum represents desorption from two sites of close in  $E_d$  ( $129.3 \text{ kJ mol}^{-1}$  and  $136.8 \text{ kJ mol}^{-1}$ ), the blue spectrum represents desorption from sites further apart in  $E_d$  ( $129.3 \text{ kJ mol}^{-1}$  and  $144.3 \text{ kJ mol}^{-1}$ ), and the red spectrum represents desorption from two sites of very different  $E_d$  ( $129.3 \text{ kJ mol}^{-1}$  and  $174.3 \text{ kJ mol}^{-1}$ ).

After taking account of the effect of pumping speed, the TPD spectrum of PTCDI from Ni(111) can best be matched if it is considered as three different regions, the low temperature peak, the broader main peak and the long plateau on the decay from the main peak and these will be related to features observed by STM (see Section 3.3.1.2). As seen before, the position of the main peak can be matched by the inclusion of four sites of similar  $E_d$  (ranging  $99\text{-}120 \text{ kJ mol}^{-1}$ ) into the simulation of figure 3.10, the main peak can be broadened out. The narrow range of  $E_d$  may be caused by substrate-adsorbate interactions of different strengths; however, the variation is sufficiently small to be adsorbates being under the influence of relatively weak supramolecular interactions (e.g. van der Waals interactions). One of the possible outcomes suggested by the NEXAFS study<sup>18</sup> is that most of the molecules lie flat upon the surface alongside a minority of more randomly orientated molecules, thus the bulk of main peak may represent desorption of molecules lying parallel to the surface, the lowest of the  $E_d$  sites incorporated into this peak may encompass molecules oriented to the surface. In contrast to the simulated spectrum of figure 3.8, which demonstrates the effect of

the pumping speed on the pressure decay after desorption from a single site with  $E_d$  of  $112 \text{ kJ mol}^{-1}$ , the experimental spectrum features a pressure plateau from 500 K to 700 K before decaying.

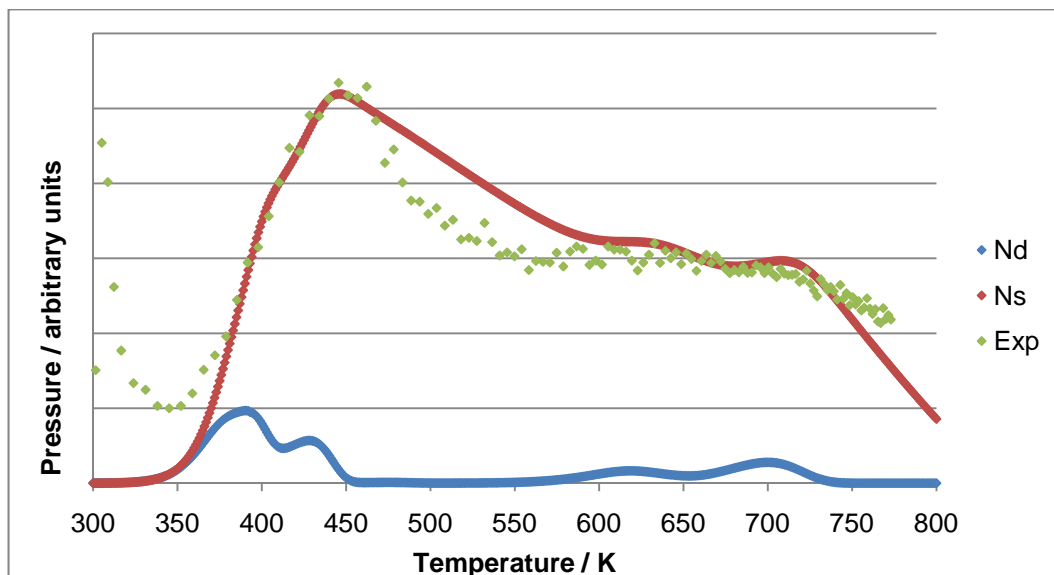


Figure 3.10 Simulated TPD spectrum based on  $N_s$ , accounting for pumping speed and incorporating multiple adsorption sites for PTCDI on Ni(111), red, and comparison with the experimentally obtained TPD spectrum, green (the upper 5 L spectrum from figure 3.2).

In order to incorporate a plateau into the pressure decay from this main peak, adsorption sites of high  $E_d$  ( $138 \text{ kJ mol}^{-1}$ ,  $155 \text{ kJ mol}^{-1}$  and  $175 \text{ kJ mol}^{-1}$ ) are inputted into the final simulated TPD spectrum (figure 3.10). The number of molecules used to fill them initially is around a third of the starting stocks of the main adsorption site. From the spectra in figure 3.10, it appears that due to the slow removal rate of PTCDI from the chamber, only a relatively small number of molecules in each of these high  $E_d$  sites is required to perturb the decay from the main peak and create a plateau. The high  $E_d$  values of these sites may be indicative of the formation of metal-organic interactions; the STM images of Section 3.3.1.2 suggest that a considerable proportion of the PTCDI molecules may coordinate to surface adatoms. This approach matches the main desorption peak and its decay reasonably although there is a discrepancy between the pressure decays in the simulated and the experimental spectra between 450 and 550 K which may be associated with trying to apply a universal pressure decay calibration curve to a specific experiment given that the background pressure of PTCDI in the chamber will vary from experiment to experiment.

The low temperature desorption peak at 310 K, if caused by the desorption of weakly adsorbed molecules from the Ni(111) surface, may be so sharp this because the heating rate in the first 10 seconds of the temperature ramp during the experiment is slower thus the number of molecules that can be pumped away in the duration of these temperature increments is much greater compared to faster temperature increments throughout the rest of the experiment. Furthermore, if the peak is only responsible for one adsorption site (or a few low population adsorption sites close in  $E_d$ ), then it would be expected to be sharper than a peak which encompassed many adsorption sites of a wider range of  $E_d$ . However, this peak could not be matched sufficiently closely using the sample heating rate and pumping speed calibration relationships obtained empirically and has been omitted from the simulated TPD in figure 3.10. This may indicate that this peak is generated through desorption of molecules from the sample heating wires, of course, the heating wires will heat at a different rate from the Ni(111) sample.

By varying the number of adsorption sites, the desorption energies of these sites and the proportion of molecules which populate them, these relatively simple spreadsheet models allow qualitative understanding of the behaviour of PTCDI on the Ni(111) surface that can complement the STM analysis (Section 3.3.1.2). A more sophisticated set of calculations would be required to fit the data properly; the values used in the simulated TPD spectrum of figure 3.10 may not match the real values exactly and the number of adsorption sites may be underestimated. Nevertheless, this empirical spreadsheet exercise demonstrates that there are mostly likely two different categories of PTCDI adsorbate on the Ni(111) surface; the main group of molecules on the surface existing in a few adsorption sites of  $E_d$  in the range  $99 \text{ kJ mol}^{-1}$  to  $120 \text{ kJ mol}^{-1}$ , the lowest  $E_d$  sites in this range may consist of molecules not lying parallel to the surface, and a smaller number of molecules of higher  $E_d$  values of up to  $175 \text{ kJ mol}^{-1}$  and these may be caused by the formation of some stronger metal-organic interactions (see Section 3.3.1.2).

### 3.3.1.2 STM analysis of PTCDI on Ni(111)

Analysis of PTCDI on the Ni(111) surface by STM provides visual evidence that the substrate-adsorbate interaction is the major factor in controlling the distribution across the surface as opposed to lateral supramolecular interactions between PTCDI molecules.

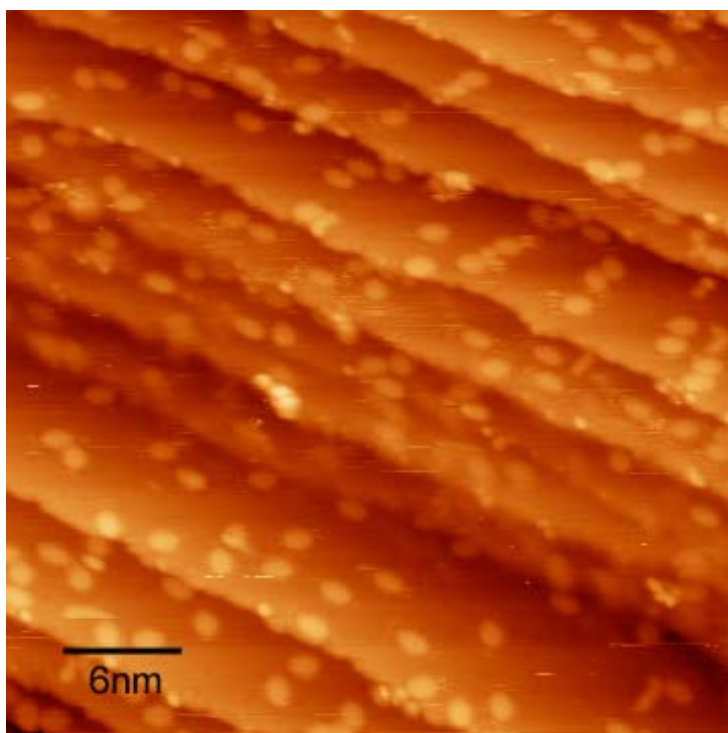


**Figure 3.11** Low coverage (0.1 ML) PTCDI on small terraces after adsorption onto the Ni(111) at 300 K (36.9 nm x 36.9 nm, -1.5 V, 0.4 nA)

At room temperature, on small terraces, PTCDI coverage is low ( $\sim 0.1$  ML). Isolated molecules are observed despite nearest neighbours being only two or three molecular lengths apart. When molecules are in close proximity to each other, they very rarely align as they do on Au(111)<sup>2,20</sup> to allow the formation of two hydrogen bonds between terminal imide groups. In figure 3.11, the molecules are seen mostly as separate from each other, the other notable point to make about the features is the fact that not all of the features which are presumed to be adsorbate molecules are the same shape. Most of the molecules are elliptical in shape, measuring  $\sim 15$  Å long and  $\sim 9$  Å wide, this is consistent with flat-lying PTCDI molecules on Au(111)<sup>2,20</sup> and Ag-Si(111)- $\sqrt{3} \times \sqrt{3} R30^\circ$  surfaces<sup>21</sup>. However, some of the features are similar in length but only  $\sim 5$  Å wide.

Additionally, there are some other smaller features. These observations perhaps confirm the suggestion from the NEXAFS study<sup>18</sup> that the majority of the molecules lie flat and a minority are oriented with respect to the surface.

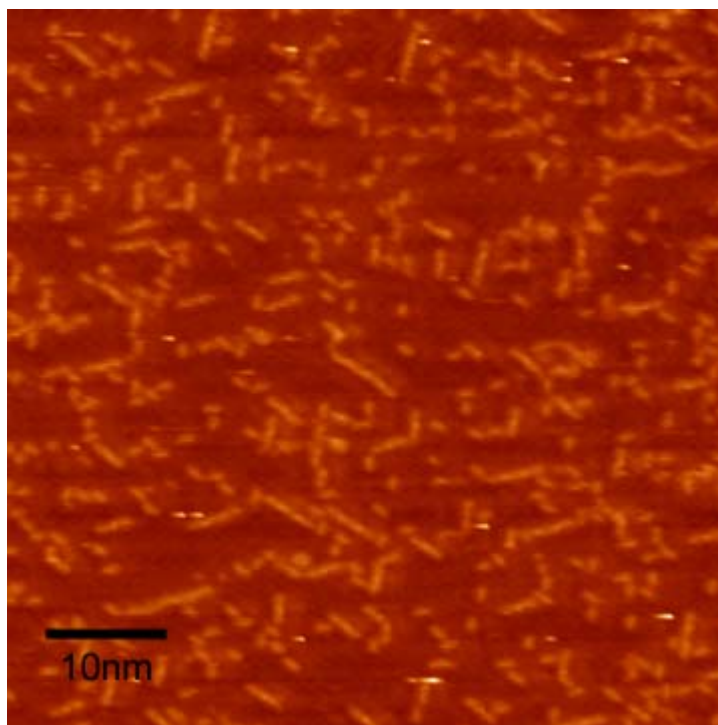


Figure 3.12 Low coverage (0.25 ML) PTCDI on a larger terrace after adsorption onto Ni(111) at 300 K (59.7 nm x 59.7 nm, -1.0 V, 0.2 nA)

On larger terraces where coverage is greater ( $\sim 0.25$  ML), isolated molecules still exist but 1-D chains of 2-4 molecules are formed. Figure 3.12 and 3.13 show areas of the surface of two different localised coverages, both of these images were captured after the surface was annealed to 400 K in attempt to induce ordering. It is clear that the diffusion of PTCDI is limited on the Ni(111) surface, otherwise larger, ordered domains would form from the coalescence of these 1-D chains. Molecules are sometimes slightly off-set with respect to each other along these rows to promote hydrogen bonding but, in some cases, molecules already pinned in position act merely as nucleation points, and as is observed, adjacent molecules are not always optimally aligned.

At higher coverages (0.45 ML), these short rows neither grow, nor coalesce into larger domains of interlocking rows. Instead, the gaps between these short chains are generally filled by molecules whose orientation is apparently not influenced by the presence of previously adsorbed species and as such are disordered. Amongst the poor ordering, several traits can still be identified: firstly, the orientation of the molecules is largely controlled by the 3-fold symmetry of the substrate, this can be deduced by the fact that molecules are related to each other by rotations of  $30^\circ$ , one minority feature that occurs from this is the herringbone-like nucleation of 1-D rows, secondly, parallel pairs of 1-D rows are often separated by 2.45-2.5 nm (centre-to-centre), this behaviour may be a combination of two factors; preference for a specific surface site (2.49 nm equals 10 Ni-Ni spacings) and also that a PTCDI molecule often sits between and nearly perpendicular to the direction of these rows (2.4 nm roughly equates to the length of a PTCDI molecule plus the breadth of a PTCDI molecule, where the length accounts for the gap between the molecules and the breadth accounts for the centre-to-centre type measurement).

The NEXAFS study<sup>18</sup> asserts that PTCDI on Ni(111) is most likely disordered with PTCDI molecules lying at a range of orientations upon the surface. These assertions are confirmed by the STM analysis. Annealing the surface, even for extended periods near to the measured desorption temperature, did not result in ordered arrays visible by STM or improve the consistency of the TPD spectra as occurred for the analogous setup on Au(111).

The STM images, whilst showing that PTCDI can form some short hydrogen bonded rows and linear conglomerates, allude to desorption being controlled in the main by adsorbate-substrate interactions. Such a strong interaction inhibits the diffusion of PTCDI across the surface and the formation of the hydrogen bonded structures observed on Ag-Si(111)- $\sqrt{3}\times\sqrt{3}R30^\circ$  surfaces<sup>21</sup>. Figure 3.14 schematically compares a rarely observed perfect hydrogen bonded 1-D PTCDI chain on Ni(111) with what is more usually observed on Ni(111); molecules do

not align to optimise the strength of the supramolecular interaction between molecules.

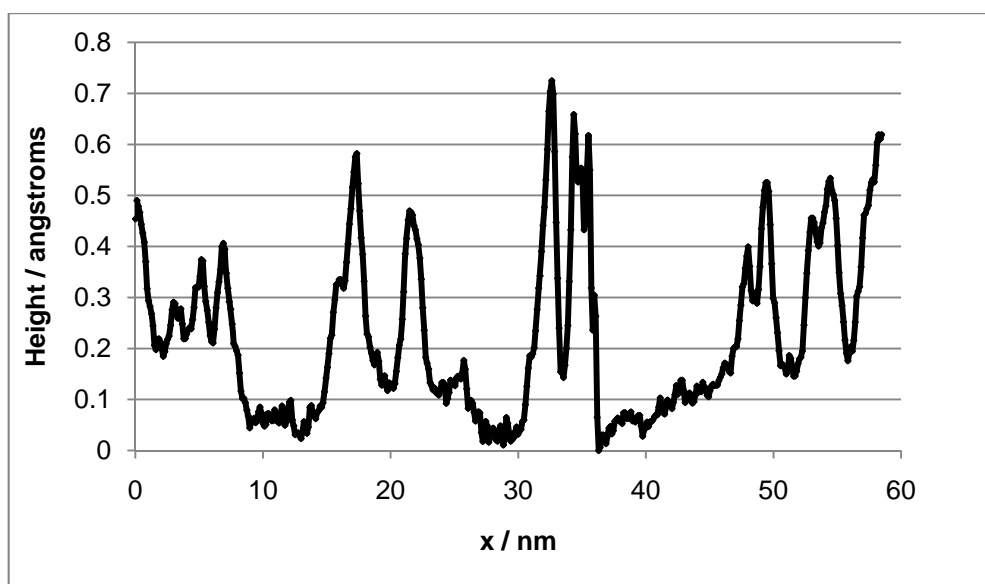
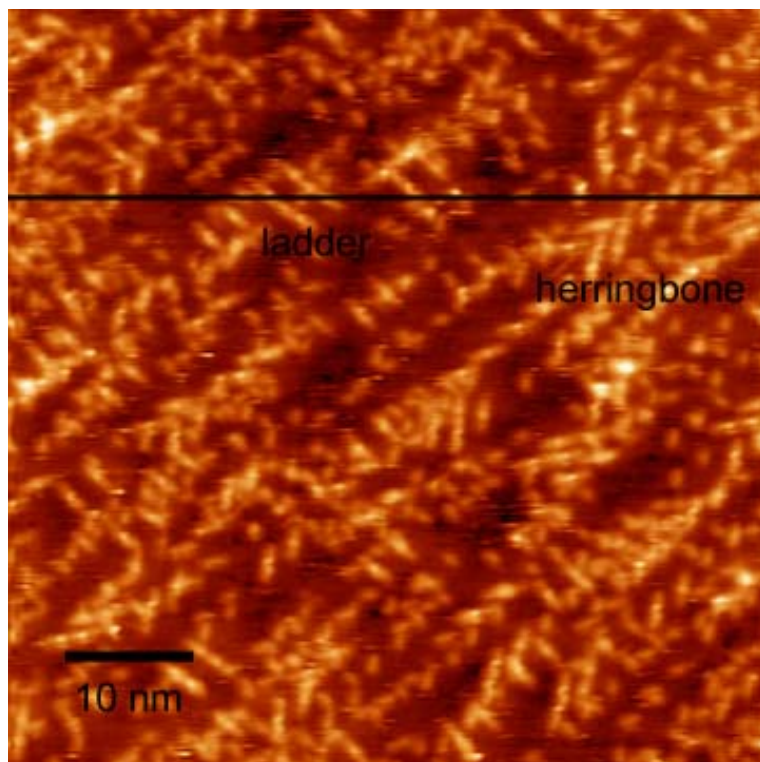


Figure 3.13 Higher coverage (0.45ML) PTCDI on Ni(111) (58.8 nm x 58.8 nm, -2.0 V, 0.3 nA). The apparent height profile across the black line is plotted below. PTCDI molecules appear on 0.3-0.5 Å higher than the Ni surface

As a result of the imperfect 1-D chain formation (with respect to what is observed when PTCDI is deposited on Ag-Si(111)- $\sqrt{3}\times\sqrt{3}R30^\circ$ ) and the strong adsorbate-substrate interaction, dense, organised islands of PTCDI are not formed. As

molecules adjacent to the observed molecular rows become pinned in energetically unfavourable orientations, they have the effect of blocking further 1-D rows from lining up next to each other and forming compact domains. This results in two types of feature that reoccur amongst the disorganised surface landscape; these herringbone and ladder features are schematically shown in figure 3.15.

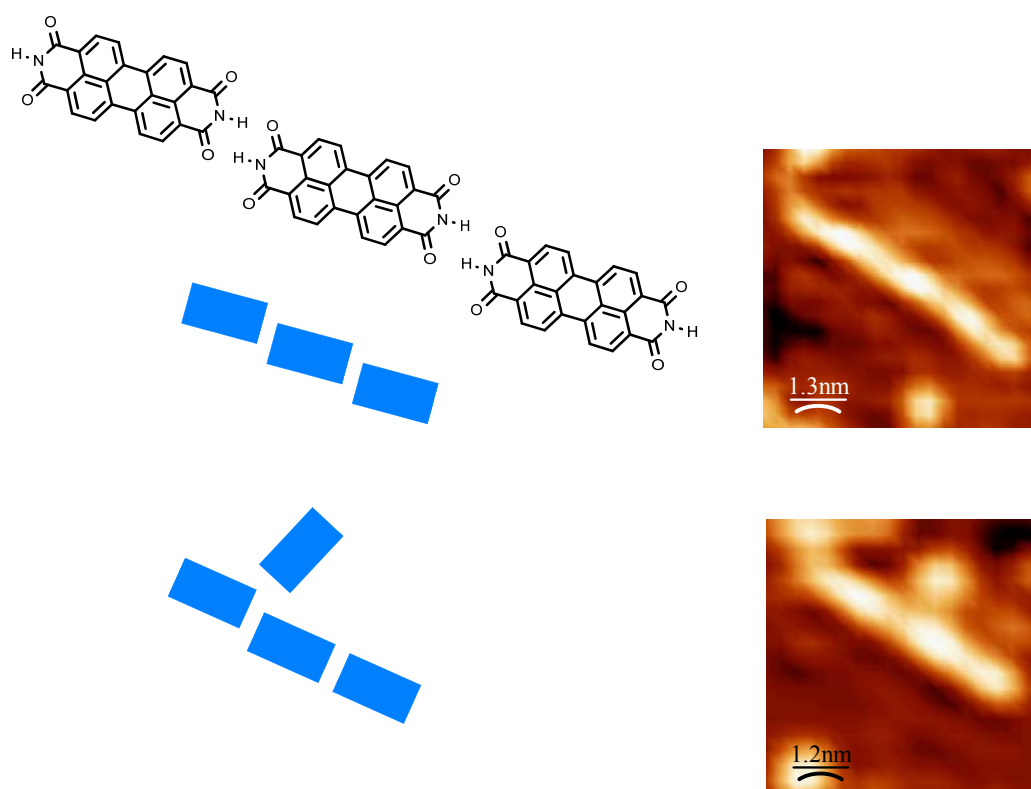


Figure 3.14 Schematic showing two small PTCDI chains on the Ni(111) in the image of figure 3.12 and how molecules rarely align to achieve the two potential N-H...O hydrogen bonds at each two molecule junction. The top example is rarer, the molecules are offset with respect to each other along the chain, therefore the chain likely represents PTCDI molecules in positions close to those optimal for hydrogen bonding<sup>21</sup>. The lower example is typical of the misaligned formations more common on Ni(111).

As is particularly clear in areas of low coverage and near step edges, some of the STM images depict features that are narrower than the majority of the molecular features. These may be PTCDI molecules that do not lie flat upon the surface; as a result, fewer adsorbate-substrate bonds may be formed. If the molecule is tilted, presumably the interaction between the aromatic system and the surface atoms is considerably weaker, and these molecules may be more easily desorbed and perhaps be responsible for the low temperature peak in the TPD spectra, this is

highlighted in figure 3.16. The fact that these features, indicated by the green arrow in figure 3.16 and represented in figure 3.17, are predominantly observed in STM images obtained before annealing samples to 400 K lends weight to this proposal.

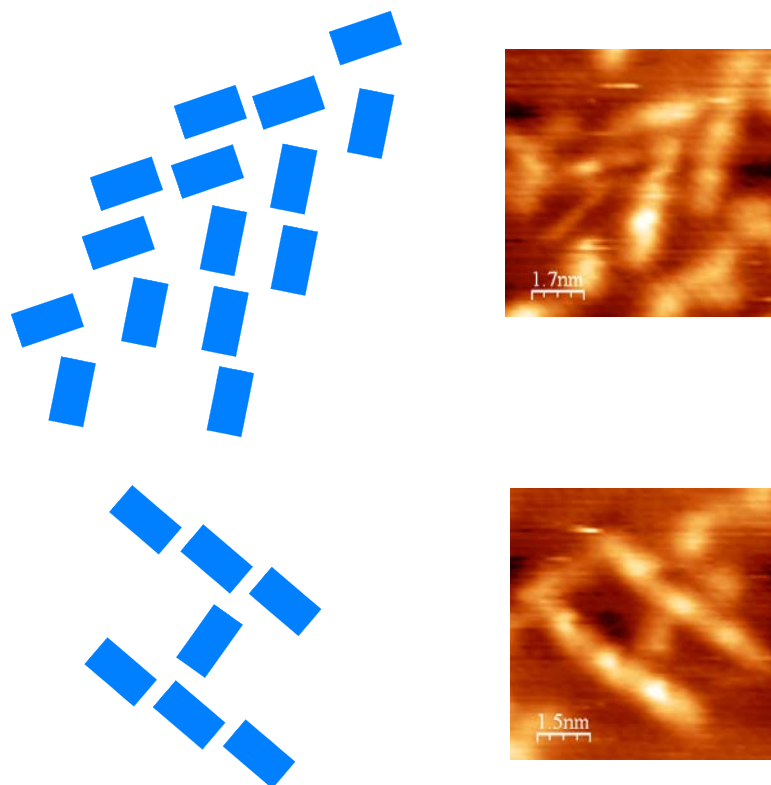


Figure 3.15 Schematic of the herringbone, top, and ladder features indicated in STM image of figure 3.13.

Desorption of flat-lying molecules will most certainly be the cause of the main peak in the TPD spectra; the majority of adsorbed molecules are seen to fall into this category. As aforementioned, states of a few  $E_d$  values in the range  $99 \text{ kJ mol}^{-1}$  to  $120 \text{ kJ mol}^{-1}$  are inputted into the model in attempt to emulate the main desorption peak. The differing conditions of the state each molecule finds itself in may be concerned with different sites upon the surface lattice of the Ni(111) surface or it may be concerned with supramolecular interactions. As discussed, sometimes molecules nucleate adjacent to other molecules that are pinned in place, the supramolecular bonds that form will not be strong. Upon the disorganised surface landscape (figure 3.13), where molecules are isolated or in close proximity to one or two others, these supramolecular interactions may be

significant enough to create the small range of  $E_d$  values required to broaden out the main peak in the TPD model. Since molecules first have to break supramolecular interactions before desorbing from the surface, their  $E_d$  will be increased (equation 2.11)<sup>22</sup>.

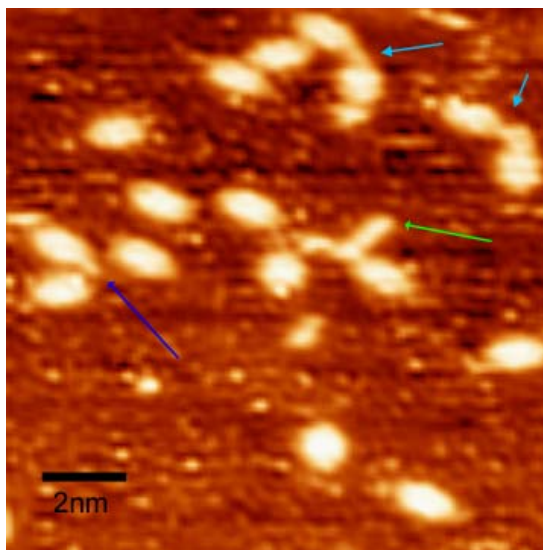


Figure 3.16 STM image, blue arrow indicates a PTCDI molecule with a small round feature affixed at one end, the green arrow indicates a molecule that may not be lying flat (13 nm x 13 nm, 1.5 V, 0.2 nA)

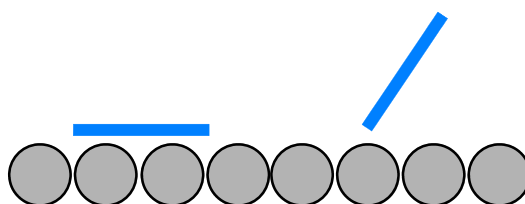


Figure 3.17 Schematic showing possible PTCDI orientation with respect to the surface, the raised molecule may give cause features like that indicated by the green arrow in figure 3.16

Furthermore, small, circular features of up to 5 Å diameter are sometimes seen close to the molecular features, these can possibly be assigned as Ni adatoms partaking in the formation of metal-organic frameworks; such complexes may cause the desorption of PTCDI from the surface to occur at elevated temperatures, as energy must be used to break the metal-organic bond to release the molecular species before it can desorb, this process may possibly explain the long drawn out decay of the TPD spectra acquired from the PTCDI on Ni(111) system. The possibility of nickel coordinating to PTCDI through several schemes (via carbonyl O, imide N or a bridging interaction) also create the possibility of different adsorption states with different  $E_d$  values, from some of the STM images it is

difficult to ascertain the extent to which this occurs. In figure 3.16, for the molecule indicated by the blue arrow, the possible PTCDI-Ni interaction may occur through the imide N (the bright feature is aligned with the central axis of the molecular feature). The features indicated by the turquoise arrows apparently consist of two linked molecular features that are aligned approximately  $90^\circ$  to each other which may be more consistent with coordination involving the carbonyl O atoms (figure 3.18).

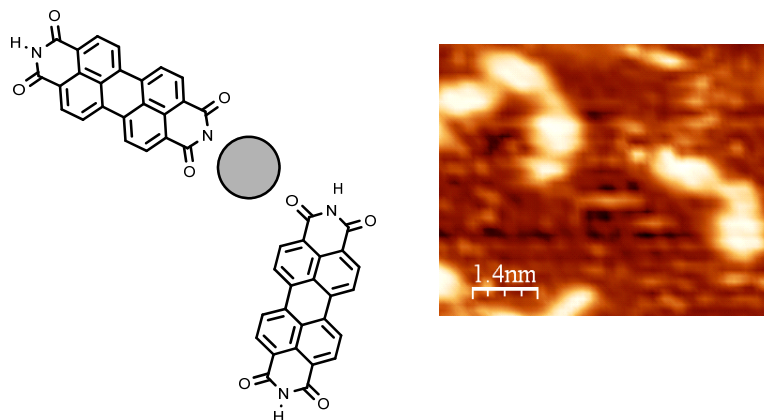


Figure 3.18 Illustration of potential metal-organic arrangements of PTCDI molecules and Ni adatoms

### 3.3.1.3 PTCDI on Ni(111) Summary

TPD analysis based on the empirical spreadsheet model suggests that there are different categories of PTCDI adsorbate on the Ni(111) surface; the main group of molecules on the surface existing in a few adsorption sites of  $E_d$  in the range  $99 \text{ kJ mol}^{-1}$  to  $120 \text{ kJ mol}^{-1}$  which desorb around 450 K and a smaller quantity of molecules of higher  $E_d$  values of up to  $175 \text{ kJ mol}^{-1}$  which remain on the surface above 500 K and are removed only gradually with the increasing temperature. The STM analysis provides substantial evidence to confirm this: the majority of the molecules lie flat across the surface, although their location (near a step edge or on a flat terrace), potential supramolecular interactions with other PTCDI molecules and other orientations may cause them to exist in states of slightly different  $E_d$  which broadens the main desorption peak whilst there is also significant visual evidence of the formation of metal-organic species with surface adatoms.

### 3.3.2 Melamine on Ni(111)

#### 3.3.2.1 TPD of Melamine from Ni (111)

The main feature of the TPD spectra of melamine from Ni(111), in figure 3.19, is an initial sharp burst in desorption after the commencement of heating accompanied by broad desorption peak. The initial spike covers the range 300K to 400 K and is seen to decay in two steps before merging with a much shallower curve that occurs over the range 400 K to almost base level near the end of the heating ramp at 750 K. The 10 L and 20 L doses yield desorption spectra similar in amplitude and shape, these are assumed to give close to 1 ML coverage on the surface. In Chamber 2, doses of up to 25 L were used to acquire STM images of up to 1 ML coverage; differences in chamber set-up and within the packing of the solid doser may account for any differences in the exposure required to give the same coverage.

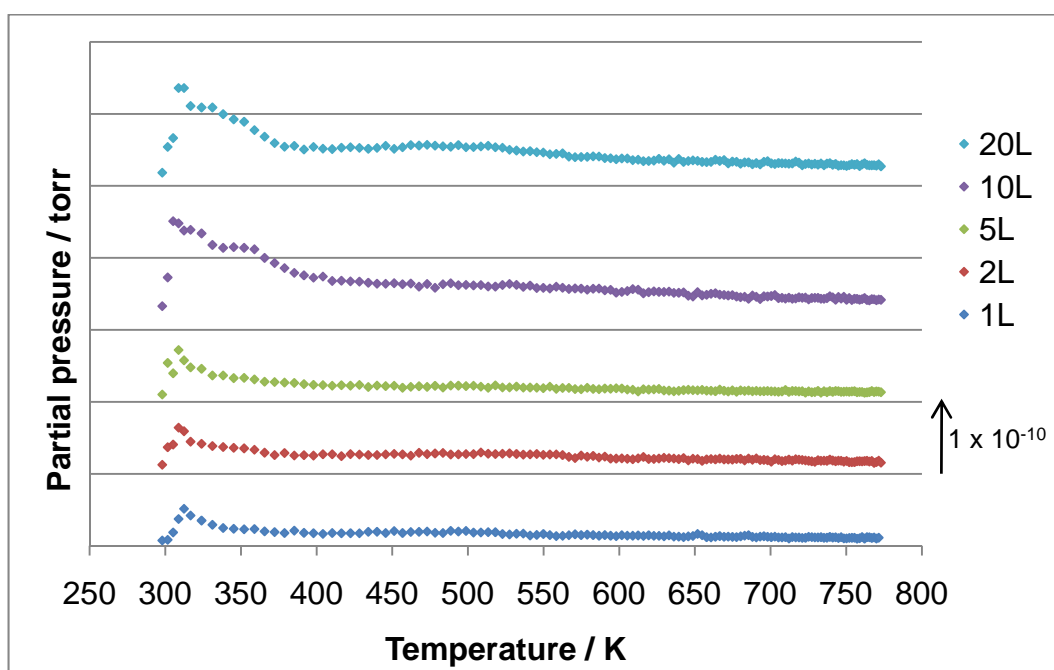


Figure 3.19 TPD of melamine from Ni(111) for a range of initial exposures to the sample at 300 K. Desorption spectra are acquired by monitoring the  $m/z = 43$  mass fragment.

The melamine TPD spectra are generated by monitoring the  $m/z = 43$  fragment ion, other mass fragments and the molecular ion,  $m/z = 126$ , give the same  $T_{max}$

value but a weaker signal from the detector. Analysis by AES after the TPD experiment indicates a clean Ni surface. Finding pre-annealing conditions that still allow for the production of desorption spectra is difficult due to the low temperature of desorption, a procedure of heating to 313 K and then immediately allowing to cool, still affords desorption spectra, however, similar results from normal and pre-annealed samples were experienced.

Melamine is around a third of the mass of PTCDI; melamine has a formula weight of  $126 \text{ g mol}^{-1}$  compared to  $390 \text{ g mol}^{-1}$  for PTCDI. If van der Waals interactions were the dominant force, melamine would be expected to adsorb more weakly to the Ni(111) surface and desorb at lower temperatures. In attempting to simulate the desorption spectra of melamine, the same method as for PTCDI of using equations that are fitted to the pumping speed plot (figure 3.20) and the sample heating rate (figure 3.5) to emulate the environmental factors which could affect the TPD spectra is used. The simulated desorption spectra are compared against the 20 L spectrum from figure 3.19, both the 10 L and the 20 L spectrum were assumed to give a surface coverage of close to 1 ML.

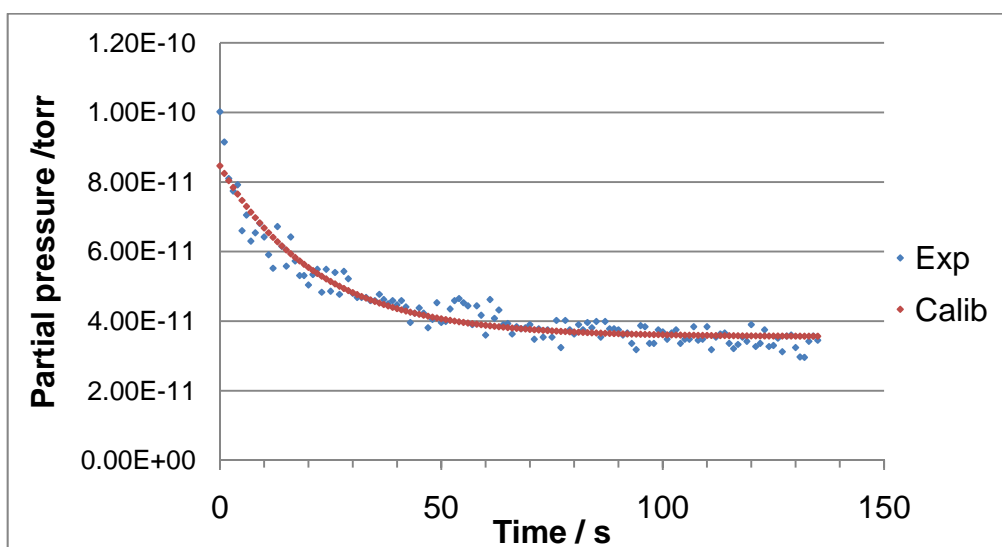


Figure 3.20 Low pressure section of the pumping speed plot for melamine, time  $t=0$  seconds is taken to be when partial pressure,  $p=1.00 \times 10^{-10}$  torr. The relationship  $p=3.553 \times 10^{-11} + 4.911 \exp(-t/22.126)$  was fitted to the pressure decay curve using a spreadsheet programme to produce a pressure calibration graph.

The initial low temperature peaks can be matched fairly closely by inputting starting stocks of molecules into two sites with  $E_d$  values of  $75 \text{ kJ mol}^{-1}$  and  $87 \text{ kJ mol}^{-1}$  (figure 3.21). These seem fairly reasonable estimates; Steinruck et al<sup>24</sup> report the desorption of benzene from Ni(111) at 294 K, this gives an  $E_d$  of  $76 \text{ kJ mol}^{-1}$  estimated via the Redhead equation. The largest stock of molecules is inputted into the lowest  $E_d$  site and this seems to accommodate the stepped decay from the initial desorption around 300 K to 360 K and its decay to 400 K. The rest of the experimental spectrum is rather flat as it slowly decays and this presents a challenge to model as it is too shallow, based on the calibration curve in figure 3.20, to be caused by the removal rate of melamine from the vacuum chamber.

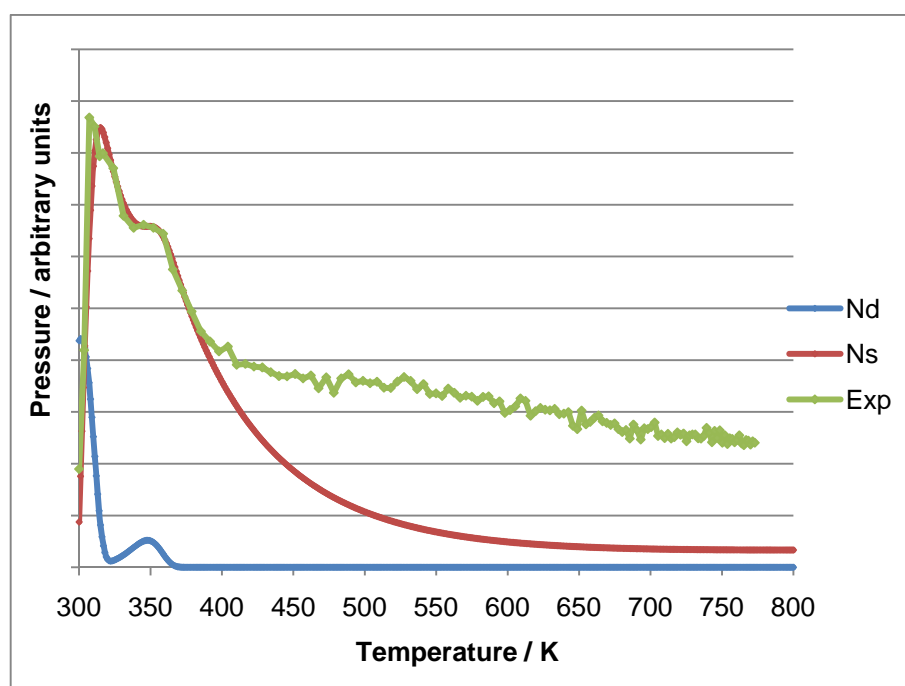


Figure 3.21 Comparison of simulated TPD spectrum which takes into account a number of different adsorption sites and the pumping speed,  $N_s$  (red), with the experimentally obtained TPD spectrum (green) from the 20 L pre-annealed experiment (top spectrum from figure 3.19). The simulated spectrum based on only two desorption states of low  $E_d$  only fits the experimental spectrum in the temperature range 300-400 K.

It seems likely that the high temperature desorption (above 360 K) has a contribution from a number of relatively strongly bound melamine states. These states may incorporate melamine chemisorbed to the surface and melamine molecules that have formed metal-organic complexes with surface adatoms. Using this method of the pumping speed calibration, the only way to simulate the slow pressure decay of the spectrum in the high temperature region of the spectrum is

to input a large number of sites with a range of different  $E_d$  values up to 200 kJ mol<sup>-1</sup>. The simulated TPD spectrum of figure 3.22 shows this may begin to be developed by including a stock of molecules in an extra desorption site with an  $E_d$  of 132 kJ mol<sup>-1</sup>. Melamine could potentially form a large number of different metal-organic complexes as it has six functional groups that could co-ordinate to Ni adatoms, so it may not be unreasonable to incorporate many sites of different  $E_d$  into the simulation. Adding a vast number of sites and optimisation of the stocks inputted into to them would ultimately lead to the simulated spectrum that would match the experimental result very well but there is the possibility that the spectra in the high temperature range is affected by high background pressure of melamine during the experiments.

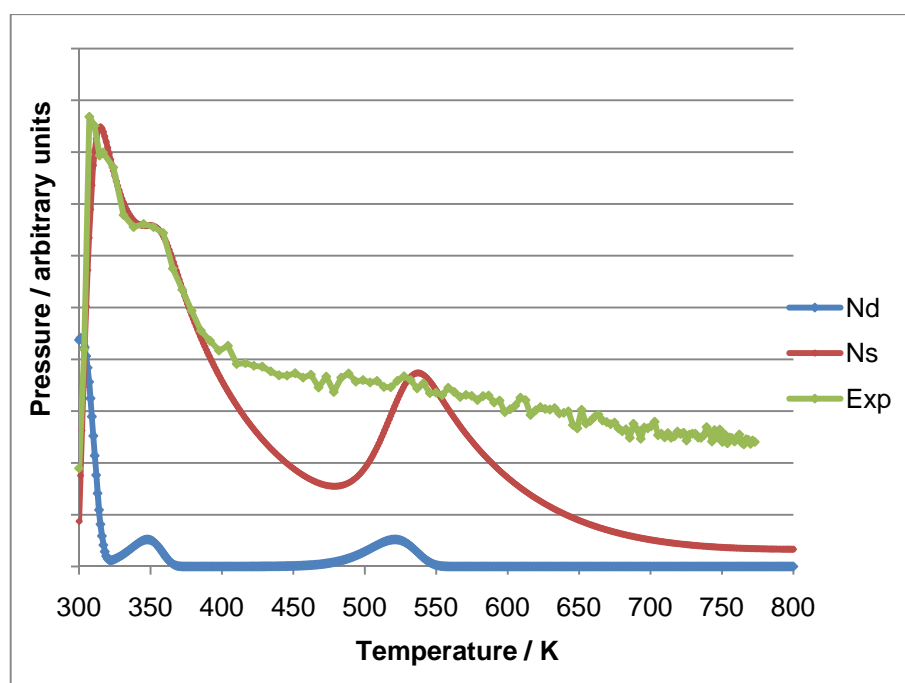


Figure 3.22 The same simulated TPD spectrum of figure 3.21 but with the incorporation of molecules in an extra site of higher  $E_d$ .

Although Chamber 1 was regularly baked to achieve UHV conditions and remove any contaminants, melamine often resides longer than expected in the vacuum chamber. Melamine has the tendency to condense onto the surfaces within the chamber during dosing and TPD experiments. Once deposited onto these surfaces, its vapour pressure is then sufficient to maintain a considerable background pressure. Desorption of melamine from the heating rods upon, upon which the

sample is mounted, during the TPD experiment could also contribute to the high background pressure of melamine. The heating rods will warm up more slowly than the sample during TPD experiments and desorption from their surface may occur after desorption from the sample. A sufficiently high background concentration at high temperatures may obscure any match between the predicted pressure decay trend and the experimentally observed pressure.

The ability of molecules to change desorption sites during the temperature ramp may also play a part but this is difficult to quantify. The high temperature range in the PTCDI TPD simulation could be matched by the incorporation of three higher  $E_d$  sites but this may have masked other processes such as metal coordination with adatoms and transitions between different metal-organic structures.

The mismatch of the melamine TPD may also indicate a problem with the use of a universal pressure decay calibration plot. The plots are derived from pressure decays that were monitored experimentally after initially exposing Chamber 1 to higher pressures than observed during TPD experiments. These plots represent how the pumps respond to higher pressures of melamine and PTCDI in the chamber; obtaining pressure decay curves for much lower initial pressures of melamine and PTCDI would be nearly impossible due to the difficulty in matching the pressure of an initial exposure from a solid doser and the pressure generated from a sample during a TPD experiment.

Relating the number of molecules desorbed,  $N_D$  (and  $N_s$ ), to a pressure on the calibration curve is also a potential weakness in the TPD simulation. The number of molecules is multiplied by a constant such that they can be adjusted to the same order of magnitude as the range of pressures on the calibration plot. Using a constant that is too high or too low will inevitably result in the range of the pressure calibration curve that may produce an unsuitable value of  $\Delta p$  being used for subsequent calculations.

Although these empirical simulations have some limitations, they do allow some insight into the nature of melamine adsorption on the Ni(111) surface. In summary, there seem to be two categories of desorption states: low temperature desorption states and relatively strongly bound states. The low T desorption states can be simulated by input of  $E_d$  values of  $75 \text{ kJ mol}^{-1}$  and  $87 \text{ kJ mol}^{-1}$  into the spreadsheet calculation, these give peaks which are also present in TPD spectra acquired after lower initial exposures (figure 3.19), so these may represent isolated molecules not stabilised on the surface by intermolecular interactions. Desorption at higher temperatures is more difficult to understand due to the high background pressure and the nature of the slope but it may be expected from the STM images of melamine on the surface (section 3.3.2.2) that molecules that have formed some intermolecular hydrogen bonds, metal-organic complexes or stronger adsorbate-substrate bonds may contribute to this.

### 3.3.2.2 STM of Melamine on Ni(111)

The STM evidence at room temperature suggests that the adsorbate falls into two main categories: along step edges or on terraces. The features along the step edges are 6-7 Å in diameter which is in accordance with melamine molecules lying flat in these sites. The normal hydrogen bonding alignment may be present between some pairs of molecule along the step edges but the likelihood is that each molecule merely acts as a nucleation point for its neighbours and compact packing is observed. Away from these, on the terraces, the bright features remain unresolved, often appearing smaller or blurred; this may be due to a different orientation with the surface (figure 3.23).

After annealing to 360 K, disorganised, open networks are observed (figure 3.24). These arrangements are vastly different from the networks melamine typically forms on Ag-Si(111)- $\sqrt{3}\times\sqrt{3}R30^\circ$  surfaces<sup>22</sup>. Chained features are seen to sprawl across terraces and branch randomly to sometimes create misshapen pores, usually around 2 nm wide. Individual molecules cannot always be resolved along the branches, but it seems that branches stretch for 2 to 4 molecules before turning

and centre-to-centre separation between what appear to be molecular features is 8-10 Å. On closer analysis, some of the branches in the chain appear brighter than others (figure 3.25).

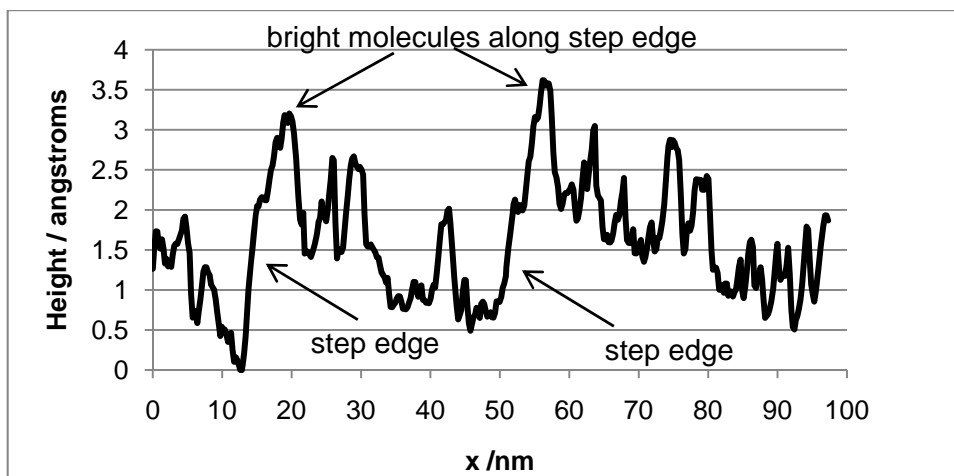
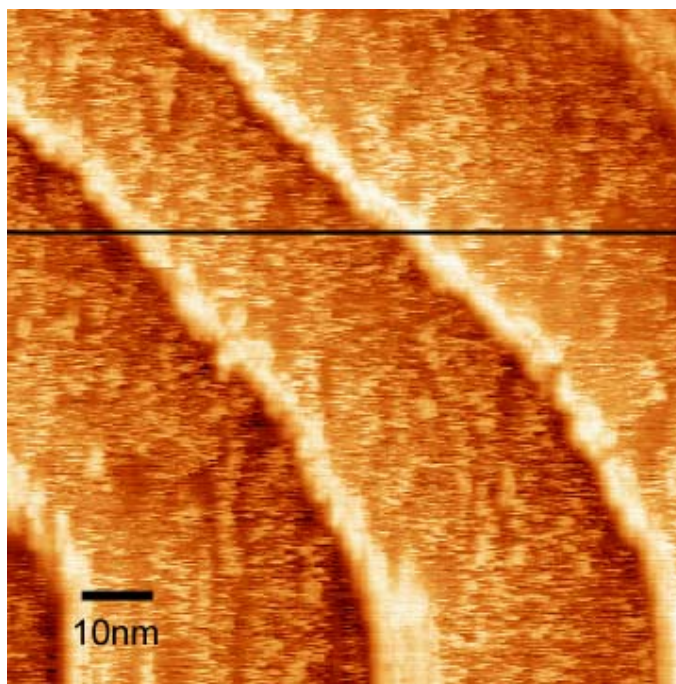


**Figure 3.23** More densely packed melamine along the step edges of after adsorption onto Ni(111) surface at 300 K, disorganised, unresolved arrangements characterise the terraces (95.3 nm x 95.3 nm, -1.5 V, 0.4 nA). The apparent height profile along the black line is shown the plot. Molecules along the step edges appear 1.4 Å higher than the bare surface of the terrace on which they nucleate. Bright features nucleated away from the step edge appear 1.3 Å higher.

Molecules lying out of plane with the surface or molecules in a second layer may contribute to the low temperature peak observed in the TPD. In constructing the TPD model, the lowest  $E_d$  site had to be stocked with the most molecules and

based on STM observation of their population alone, the molecules on the open terraces would be likely candidates to create such a desorption peak, since these molecules do not appear flat. If only part of the molecule is in contact with the surface, the surface-adsorbate interaction may be weaker, hence they may be more easily desorbed.

The molecules along the step edges may be responsible for the highest of the  $E_d$  values that were inputted to simulate the shoulder on first peak of the experimental TPD spectra. This peak may constitute molecules that are only physisorbed to the surface and attracted to each other through weak van der Waals interactions. After annealing to 360-370 K was carried out to investigate whether ordered arrangements could be formed, the aggregates along the step edges are less prominent. This temperature range corresponds with the onset of the pressure decay in the TPD spectra of figures 3.19 and 3.21.

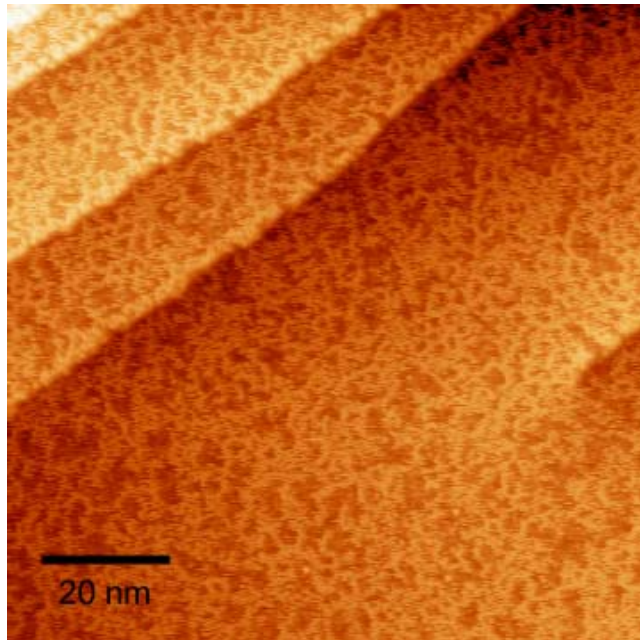


**Figure 3.24 Higher coverage melamine in disorganised networks across Ni(111) after annealing the surface to 360 K (100 nm x 100 nm, 1.5 V, 0.4 nA)**

The open, branched arrangement which is observed after annealing may be rationalised by randomly removing segments of the model of the hexagonal array

observed on Au(111), the result is a disorganised porous network that can be supported without reorganisation, or self-healing, if the substrate-adsorbate interactions are sufficiently strong (figure 3.26).

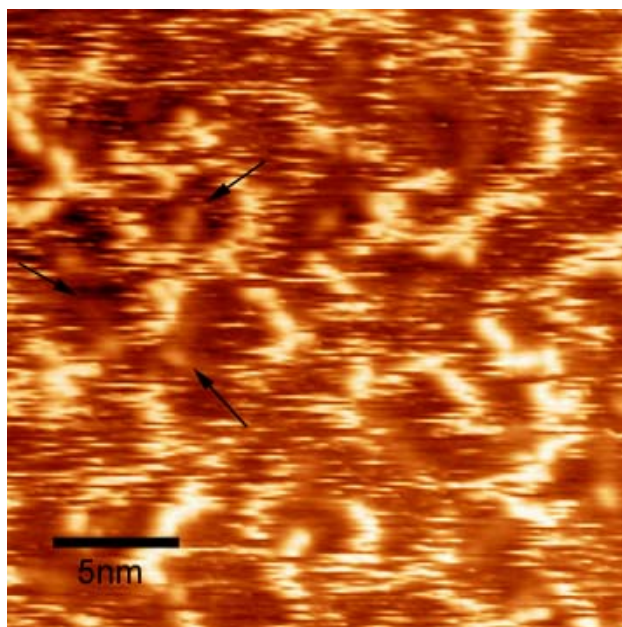


**Figure 3.25** Zoomed STM image of some of the melamine chains on Ni(111), indicated by arrows are some of the branches which are duller than the rest. The bright areas appear  $1.5 \text{ \AA}$  higher than the darkest areas, assumed to be bare surface. The duller branches appear only  $0.8 \text{ \AA}$  higher ( $24.8 \text{ nm} \times 24.8 \text{ nm}$ ).

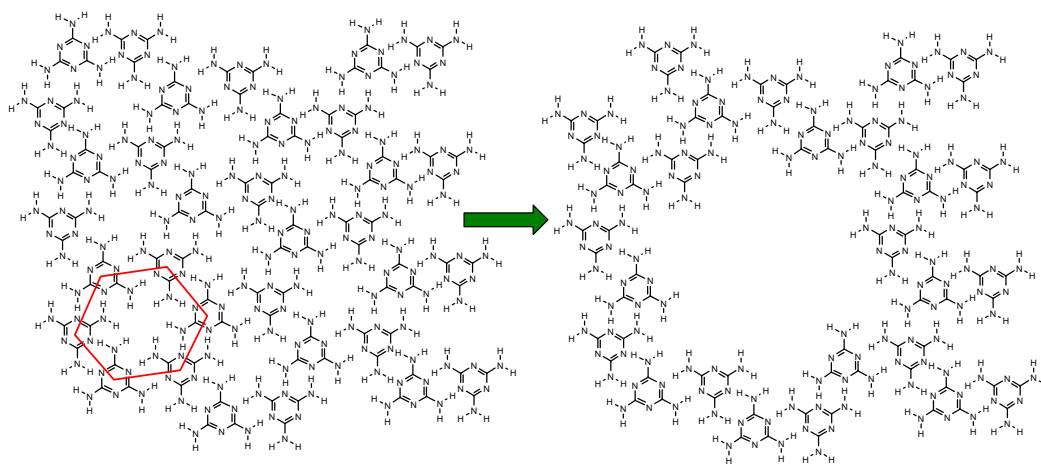


**Figure 3.26** Alteration of 2-D melamine hexagonal array model to explain networks formed on Ni(111)

This more substantial arrangement could potentially be responsible for the desorption of material above 400 K in the TPD experiment. Gradual break-up of

this formation, especially if surface adatoms become integrated, could potentially account for the long, shallow desorption trend that is seen up to high temperatures. Although it is difficult to define the molecular features along these branches, the estimated centre-to-centre separation is greater than that between adjacent melamine molecules in a hydrogen bonding arrangement by 2-4 Å, this may be indicative of metal adatoms placed between melamine molecules; the existence of metal adatoms between the melamine molecules may be the reason why these chains appear as continuous trails rather than adjacent distinct moieties. The differing contrasts of branches may suggest different types of stabilisation; the differences could be between hydrogen bonded branches and metal-stabilised branches or between different types of metal-stabilised branches (more Ni atoms may be incorporated into some limbs than others).

### 3.3.2.3 Melamine on Ni(111) Summary

Based on the changes to the STM images of melamine on the Ni(111) surface after annealing, melamine seems to have more mobility on the surface than PTCDI. As well as desorbing some of the weakly adsorbed molecules, annealing provides enough energy for melamine to diffuse from initial sites along step edges to form new structures. However, these are not the characteristic well-ordered arrangements typical of a hydrogen-bond stabilised melamine monolayer observed on Ag-Si(111)- $\sqrt{3}\times\sqrt{3}R30^{023}$  or Au(111)<sup>25</sup> surfaces and this could possibly be a metal-organic structure formed from Ni adatoms in a similar manner to that observed for PTCDI on the same surface. Desorption for metal-organic complexes may first involve breaking the metal-organic co-ordination bond before desorption; this process may present opportunities for re-capture of melamine by adatoms after initial breakage thus the lability of the Ni-melamine complexes and the diffusion of melamine across the surface may mean that melamine is held on the surface for longer and its TPD spectra become elongated. After accounting for pumping speed, the simulated TPD spectrum matches the experimental spectra at low temperature using  $E_d$  values of 75 kJ mol<sup>-1</sup> and 87 kJ mol<sup>-1</sup>, but the spectra fail to agree throughout the range 400 K to 800 K. High

background pressure may obscure some smaller high T desorption peaks or an insufficient number of adsorption sites were added to the model spectrum. By this method of simulation, it also is difficult to account for diffusion and combination/re-combination events between melamine and Ni surface adatoms in metal-organic structures.

### 3.3.3 Co-deposition of PTCDI and melamine on Ni(111)

#### 3.3.3.1 STM of Co-deposition of PTCDI and melamine on Ni(111)

As single components, neither melamine nor PTCDI display great ability to diffuse across the Ni(111) surface and form ordered supramolecular structures. Nevertheless, co-deposition was carried out in the hope that the limited mobility each exhibits may just be sufficient to result in the formation of, at least, partial, bicomponent networks.

The results of the co-deposition are as expected, despite varying the order of deposition and experimenting with forcing annealing conditions, no consistent interaction scheme was ever witnessed between PTCDI and melamine (figure 3.27). Isolated bright features are seen on the terraces. The majority of the STM image shown in figure 3.27 is less bright and appears orange. A larger dark patch and some small dark spots are seen interspersed amongst these bright features. Based on the height profile shown and previous apparent height profile from the monocomponent melamine deposition (figure 3.23), the brightest features, at 1.0-1.6 Å above the darkest area, may be assigned as melamine molecules. The orange area is around 0.4-0.6 Å higher than the darkest regions; this is similar to the apparent height difference measured between PTCDI and Ni(111) in figure 3.13. This could indicate areas of denser PTCDI around the small, bright melamine chains.

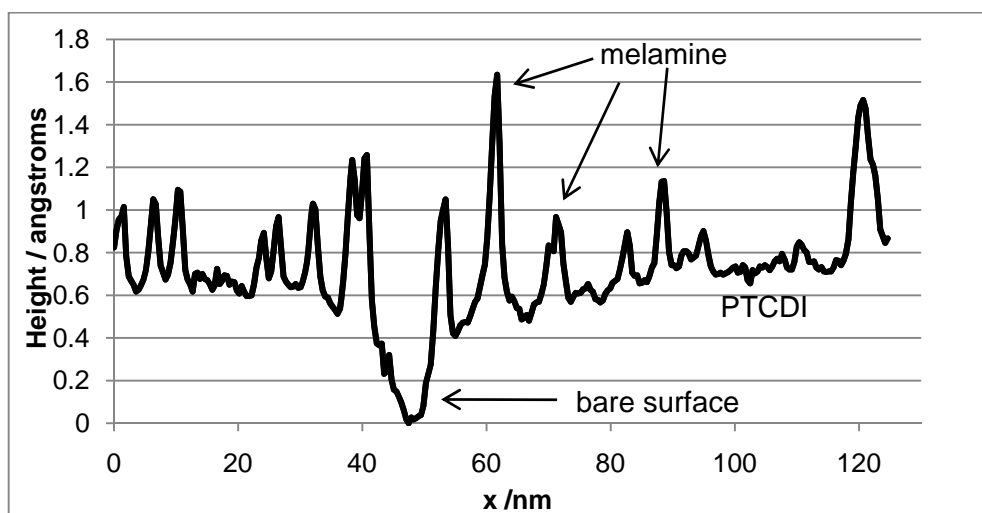
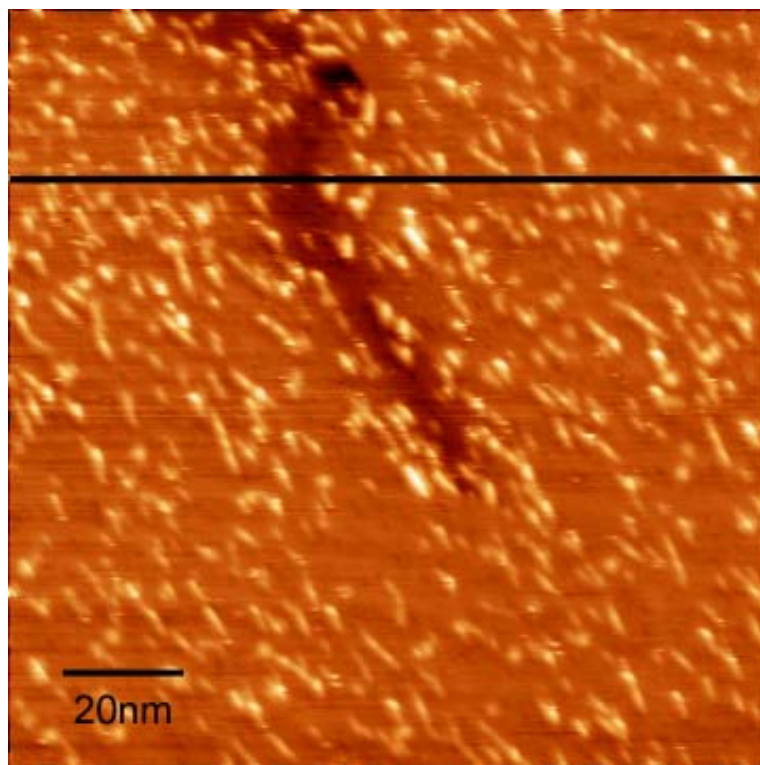


Figure 3.27 STM image of PTCDI and melamine co-deposited on Ni(111) and after annealing to 360 K (125.8 nm x 125.8 nm, -1.5 V, 0.35 nA). The height profile along the line indicated is shown. The bright features may represent melamine molecules, they appear 1.0-1.6 Å higher than the dark area which is assigned as bare surface. The orange areas are 0.4-0.6 Å higher than the lowest point and may consist of PTCDI molecules.

On the evidence of Section 3.3.1.2, it is unlikely that the PTCDI is present in ordered hydrogen bonding-stabilised formations. The observation of small dark spots, measuring 8-16 Å across, randomly interspersed amongst the orange areas perhaps support the idea of disorganised PTCDI formations. It must be noted that

relative to PTCDI, on Ag-Si(111)- $\sqrt{3} \times \sqrt{3}R30^\circ$ <sup>1</sup> and Au(111)<sup>2</sup>, melamine molecules are usually depicted as the dark features, which, based on the analysis of these apparent height profiles, is the opposite of what is thought to occur here. Although the both species appear to be interspersed with each other, it seems unlikely that they are able to diffuse across the surface and interact with each other in the anticipated hydrogen bonding networks. Aside from the small melamine chains that are observed, it seems both species are pinned strongly to their initial nucleation sites and perhaps PTCDI even inhibits the formation of the disorganised melamine networks that are observed after monocomponent deposition (figure 3.24).

### 3.4 Conclusion

The method of combining Ni with the PTCDI-melamine hydrogen-bonded network via self-assembly directly on a nickel surface is unsuccessful and building a network of melamine and functionalised PTCDI derivatives upon this surface would most likely prove a similarly fruitless pursuit. STM observations confirm results of a NEXAFS study of PTCDI on Ni(111)<sup>18</sup> that suggest that PTCDI, except a minority of molecules, lies flat upon surface in disorganised arrangements. Strong interactions with the substrate dominate the behaviour of both PTCDI and melamine on Ni(111) and eliminate the possibility of self-assembly into ordered supramolecular structures. Attempting to overcome these strong interactions by annealing most likely induces the formation of metal-organic structures in both monocomponent systems, the unusually shaped TPD spectra featuring peaks which decay slowly and stretch to high temperatures may be a result of this process.

### 3.5 References

- (1) Theobald, J. A.; Oxtoby, N. S.; Phillips, M. A.; Champness, N. R.; Beton, P. H. *Nature* **2003**, *424*, 1029.
- (2) Perdigao, L. M. A.; Perkins, E. W.; Ma, J.; Staniec, P. A.; Rogers, B. L.; Champness, N. R.; Beton, P. H. *Journal of Physical Chemistry B* **2006**, *110*, 12539.
- (3) Izumi, Y. *Advances in Catalysis* **1983**, *32*, 215.
- (4) Webb, G.; Wells, P. B. *Catalysis Today* **1992**, *12*, 319.
- (5) Baddeley, C. J. *Topics in Catalysis* **2003**, *25*, 17.
- (6) Webb, G.; Wells, P. B. *Catalysis Today* **1992**, *12*, 319.
- (7) Izumi, Y. *Advances in Catalysis* **1983**, *32*, 215.
- (8) Jones, T. E.; Baddeley, C. J. *Surface Science* **2002**, *513*, 453.
- (9) Jones, T. E.; Urquhart, M. E.; Baddeley, C. J. *Surface Science* **2005**, *587*, 69.
- (10) Bonello, J. M.; Williams, F. J.; Lambert, R. M. *Journal of the American Chemical Society* **2003**, *125*, 2723.
- (11) Jones, T. E.; Baddeley, C. J. *Surface Science* **2002**, *519*, 237.
- (12) Jenkins, S. J. *Proceedings of the Royal Society a-Mathematical Physical and Engineering Sciences* **2009**, *465*, 2949.
- (13) Tautz, F. S. *Progress in Surface Science* **2007**, *82*, 479.
- (14) Schaff, O.; Fernandez, V.; Hofmann, P.; Schindler, K. M.; Theobald, A.; Fritzsche, V.; Bradshaw, A. M.; Davis, R.; Woodruff, D. P. *Surface Science* **1996**, *348*, 89.
- (15) Mittendorfer, F.; Hafner, J. *Surface Science* **2001**, *472*, 133.
- (16) Fink, R.; Gador, D.; Stahl, U.; Zou, Y.; Umbach, E. *Physical Review B* **1999**, *60*, 2818.
- (17) Baston, U.; Jung, M.; Umbach, E. *Journal of Electron Spectroscopy and Related Phenomena* **1996**, *77*, 75.
- (18) Taborski, J.; Vaterlein, P.; Dietz, H.; Zimmermann, U.; Umbach, E. *Journal of Electron Spectroscopy and Related Phenomena* **1995**, *75*, 129.
- (19) Horcas, I.; Fernandez, R.; Gomez-Rodriguez, J. M.; Colchero, J.; Gomez-Herrero, J.; Baro, A. M. *Review of Scientific Instruments* **2007**, *78*, 8.

- (20) Canas-Ventura, M. E.; Xiao, W.; Wasserfallen, D.; Mullen, K.; Brune, H.; Barth, J. V.; Fasel, R. *Angewandte Chemie-International Edition* **2007**, *46*, 1814.
- (21) Swarbrick, J. C.; Ma, J.; Theobald, J. A.; Oxtoby, N. S.; O'Shea, J. N.; Champness, N. R.; Beton, P. H. *Journal of Physical Chemistry B* **2005**, *109*, 12167.
- (22) Sales, J. L.; Zgrablich, G. *Physical Review B* **1987**, *35*, 9520.
- (23) Perdigao, L. M. A.; Champness, N. R.; Beton, P. H. *Chemical Communications* **2006**, 538.
- (24) Steinruck, H. P.; Huber, W.; Pache, T.; Menzel, D. *Surface Science* **1989**, *218*, 293.
- (25) Silly, F.; Shaw, A. Q.; Castell, M. R.; Briggs, G. A. D.; Mura, M.; Martsinovich, N.; Kantorovich, L. *Journal of Physical Chemistry C* **2008**, *112*, 11476.

## **4 PTCDI- and Melamine-based Metal-Organic Structures on Au(111)**

The Ag-Si(111)- $\sqrt{3}\times\sqrt{3}R30^\circ$  surface was specifically identified as a substrate for the self-assembly of the PTCDI-melamine network because it afforded a high rate of diffusion to network components thus promoting the intermixing of components and optimisation of intermolecular hydrogen bonding forces that are key to its stabilisation<sup>1-10</sup>. The Au(111) surface then became the focus of research as it afforded similar mobility of adsorbates<sup>11</sup> but crucially, its inertness and stability offered the potential to study and utilise the PTCDI-melamine network in real applications at atmospheric pressures<sup>12,13</sup>.

In Chapter 3, it was shown that the distribution of PTCDI and melamine on the Ni(111) surface was governed by a strong substrate-adsorbate bond which meant that molecules were pinned in place after initial adsorption. The formation of metal-organic coordination structures was also strongly suspected via capture of adatoms upon the Ni(111) surface. The co-deposition of each of the network components on Au(111) with nickel will allow the lateral interaction of each component with Ni to be examined in isolation from controlling adsorbate-substrate interactions with a view to possible Ni deposition and cluster growth in a PTCDI-melamine network grown on Au(111).

### **4.1 Au(111) Surface Reconstruction**

Gold is the only fcc metal that exhibits a reconstruction of the close-packed (111) surface at room temperature; this occurs in UHV<sup>14</sup>, air<sup>15</sup> and electrochemical<sup>16</sup> environments. The ‘elbows’ of the ‘herringbone’ reconstruction have been shown to act as nucleation sites for a number of transition metals including Pd<sup>17</sup>, Ni<sup>18</sup>, Fe<sup>19</sup>, Co<sup>20</sup>, Rh<sup>21</sup> and Mn<sup>22</sup>.

Au exhibits fcc packing in its bulk crystal lattice, however, reconstruction of the surface layers of Au(111) occurs to reduce the significant strain created by the distribution of 23 atoms among 22 bulk sites within the surface unit cell. Within the surface reconstruction, the registry of the surface gold atoms varies between regions of fcc and hcp stacking, buckling occurs as the two structures meet; the resulting reconstruction is commonly described as the ‘herringbone reconstruction’. The surface was studied explicitly by Barth et al<sup>14</sup>. Within large, atomically flat terraces, a periodic pattern of pairwise-arranged parallel lines and the formation of a 120° zig-zag pattern of ridges are visible to STM. Co-existing equivalent domains, rotated by 120°, of this pattern are observed, often on the same terrace. The lines mark the transition between fcc and hcp regions in the surface layers; within the pairs of lines are regions of hcp stacking, between the pairs, the pairs are separated by regions of fcc stacking. The term, hexagonal close-packed (hcp) describes ABABAB packing; where the third layer lies directly above the first. Face-centred cubic (fcc) packing describes ABCABC packing; where the third layer is offset from both the first and second layers and it is only in the fourth layer that the packing the sequence begins again.

In most cases of molecular adsorption, the herringbone reconstruction is insignificant and the Au(111) surface acts as a nearly perfect hexagonal, close-packed substrate. However, it can influence the growth of some molecular overlayers; for some compounds, like 1-nitronaphthalene<sup>23,24</sup> or cyano-substituted porphyrins<sup>25</sup>, nucleation, similar to the afore-mentioned metals, is preferred in the elbow sites; and, significantly, domain orientation<sup>26</sup>, growth and defect formation<sup>27</sup> can be induced.

## **4.2 Metal-organic networks on Au(111)**

Construction of metal-organic frameworks has not only been realised upon single crystal surfaces, by co-deposition of organic and metal species, but on surfaces patterned by the growth of 2-D nanoclusters. It has been shown that metal-organic

frameworks can be formed after clusters of Fe<sup>28</sup> and Co<sup>29</sup> are corrosively oxidised by coadsorption of terephthalic acid, Ni clusters are corrosively oxidised by glutamic acid<sup>30</sup> and Mn clusters are leached by stilbenedicarboxylic acid<sup>31</sup>. Dicarboxylic acids are not the only group of compounds that have been observed to act as linker molecules in the creation of metal-organic frameworks by this route; Mendez et al<sup>32</sup> reported the formation of chain and ladder structures from Fe clusters after the coadsorption of perylene tetracarboxylic dianhydride (PTCDA).

### **4.3 Experimental**

The STM experiments were carried out in an Omicron UHV system, described in Section 2.1, with a base pressure of  $1 \times 10^{-10}$  mbar. The Au(111) sample was prepared by cycles of argon ion bombardment (1 kV) and annealing to 873 K until low energy electron diffraction (LEED) and STM indicated the presence of a clean Au(111) surface exhibiting the herringbone reconstruction<sup>14</sup>. Ni was evaporated onto the sample (held at 300 K) by means of a resistively heated W filament around which Ni wire (Advent Research Materials) had been wound. The Ni deposition rate was calibrated via STM by monitoring the size of the 2-D Ni clusters which nucleate into the elbows of the Au(111) herringbone reconstruction. PTCDI (Alfa Aesar) and melamine (Sigma-Aldrich) were sublimed into the chamber from dosers, also described in Section 2.1, after heating to 638 K and 363 K, respectively, with the substrate held at 300 K. Images of the surfaces are acquired by transferring under UHV conditions to the STM chamber where data were taken in constant current mode using an electrochemically etched W tip. All STM images were acquired at room temperature.

## 4.4 Results and Discussion

### 4.4.1 PTCDI on Au(111)

PTCDI readily assembles into large ordered islands on the Au(111) surface. Island formation may occur in the middle of open terraces or by growth outwards from initial nucleation sites along step edges. This is seen in an STM image acquired at low PTCDI coverage in figure 4.1.

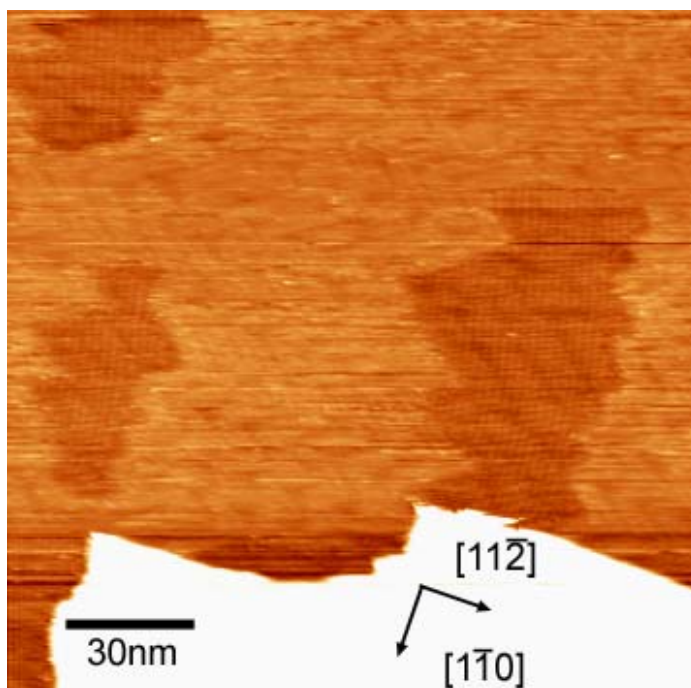


Figure 4.1 STM image of low coverage PTCDI on the Au(111) surface at 300K. Domains can be seen growing out from and also isolated from the step edge (156.7 nm x 156.7 nm, 1.9 V, 0.2 nA)

A single phase is observed up to monolayer coverage, with the exception that at extremely low coverage, only 1-D rows of molecule may be present. PTCDI assembles into these rows in a head-to-tail fashion, the rows are stabilised by hydrogen bonding between the terminal imide groups of each junction (figure 4.2). Molecules are staggered along these rows to optimise the strength of two N-H...O hydrogen bonds at each junction and negate repulsive electrostatic interactions<sup>7,11</sup>.

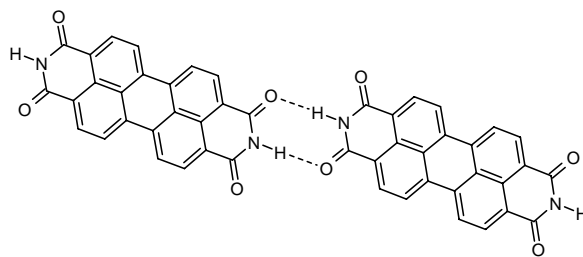


Figure 4.2 Formation of the double hydrogen bond at each PTCDI-PTCDI junction which stabilises 1-D rows and subsequently, 2-D islands<sup>7,11</sup>

These rows are kinetically unstable and PTCDI molecules will preferentially form larger 2-D islands of interlocked rows which may be stabilised by relatively weak interactions between the imide carbonyls and hydrogens of the perylene cores of molecules in adjacent rows. A model of the 2-D arrangement of PTCDI is shown in figures 4.3 and 4.4.

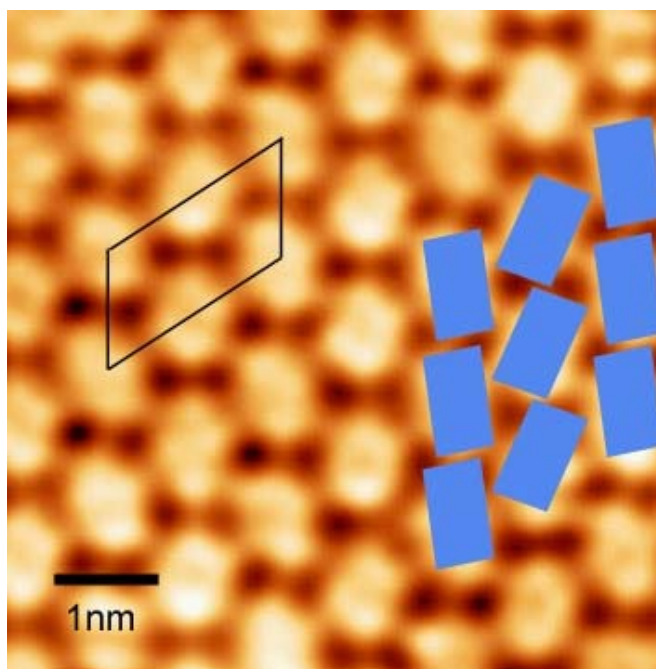
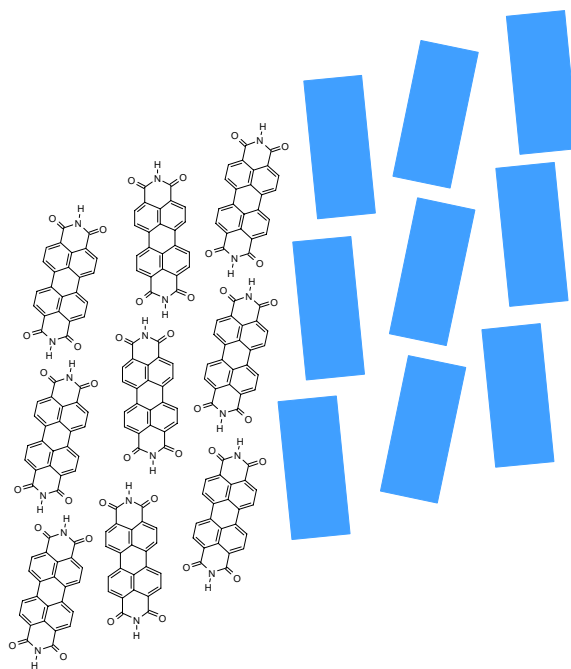


Figure 4.3 Zoomed STM image of PTCDI on Au(111) (1.5 V, 0,2 nA, 6.3 nm x 6.3 nm)



**Figure 4.4** Model of PTCDI hydrogen bonding phase, blue rectangles are schematically used to represent the orientation in the corresponding STM image of figure 4.3.

The unit cell is shown with lattice constants  $\sim 1.45$  nm and  $\sim 2.01$  nm and an angle of  $\sim 60^\circ$  between the axes. No particular preference is observed for a specific orientation with respect to the close-packed directions of the Au(111) surface. These dimensions are consistent with the close packed PTCDI phase previously reported on Au(111)<sup>11</sup> and Ag-Si(111)- $\sqrt{3}\times\sqrt{3}R30^\circ$ <sup>7</sup>. Despite the presence of nickel in the surfaces described in the following sections, the hydrogen bonding phase of PTCDI is most abundant and largely stable until PTCDI begins to desorb from Au(111) above 450 K.

#### 4.4.2 PTCDI Deposition onto Au(111) Surfaces Modified by 2-D Ni Clusters

A series of experiments were carried out where submonolayer coverages of nickel were deposited onto the Au(111) surface at 300 K. As well as the nickel coverage, the PTCDI coverage was varied. It must be noted that throughout the series, the hydrogen bonding phase, as described in the previous section, was most abundant

and largely stable, particularly at lower Ni coverage (<0.3 ML), until molecules began to desorb from above 450 K.

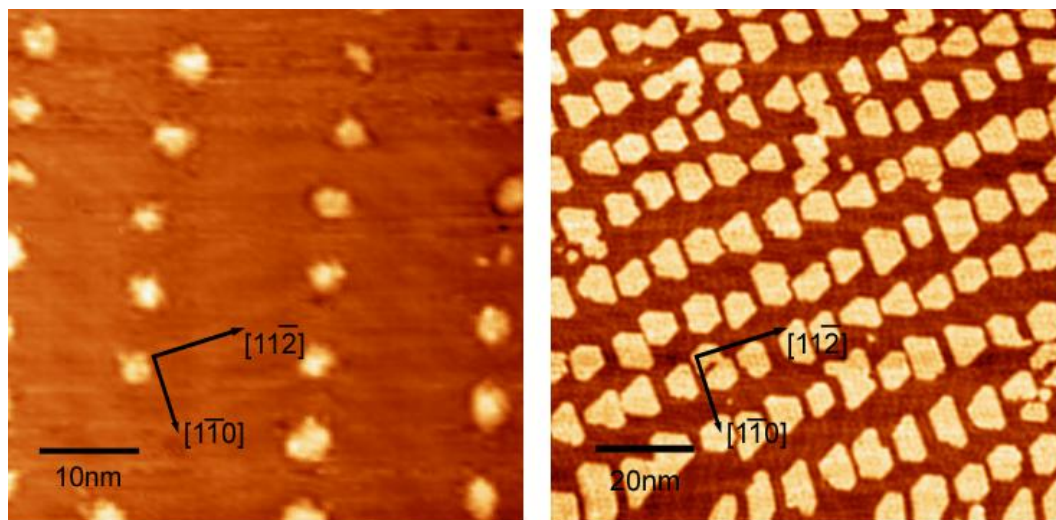


Figure 4.5 STM images showing examples of Ni cluster formation on the Au(111) surface at 0.1 ML, left, and 0.5 ML, right.

#### 0.05 ML Ni on Au(111)

Following the deposition of 0.05 ML Ni on Au(111), the typical Ni cluster diameter is ~2 nm (i.e. ~60 atoms). Figure 4.6 shows a domain of a close-packed hydrogen-bonded PTCDI phase on this surface after deposition leading to almost 0.5 ML PTCDI coverage, the unit cell size is consistent with that previously observed. Domain growth is seen to extend right up to, and often through, the rows of small Ni clusters.

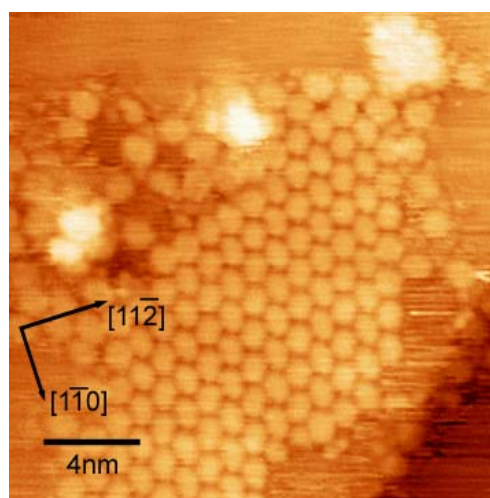


Figure 4.6 STM image of PTCDI on Au(111)/0.05 ML Ni at 300 K (1.5 V, 0.2 nA, 20 nm x 20 nm)

At sufficiently large PTCDI coverage, interaction between PTCDI and Ni may occur at room temperature, figure 4.7 highlights the changes to PTCDI structures that occur initially only around Ni clusters, the image shows a Ni cluster nearby the edge of a domain of the hydrogen bonding phase. Feature **A** is a small intrusion of an arrangement that will be referred to as the gridiron phase. Molecules are seen aligned in a close-packed, rectangular arrangement where it is noticeable that PTCDI molecules no longer exist in their optimal hydrogen bonding arrangements. The stabilisation of this phase, which possibly incorporates metal atoms from the nearby Ni cluster, **B**, will be discussed below. A disorganised, porous phase exists with circular features of atomic dimensions separating the PTCDI features, feature **D**. This is shown in isolation in the zoom capture of figure 4.8. It is thought that these circular features may represent Ni particles. Using their relative locations, which are easily viewed in this image of good resolution, the nature of similar porous structures, discussed below, can be better understood.

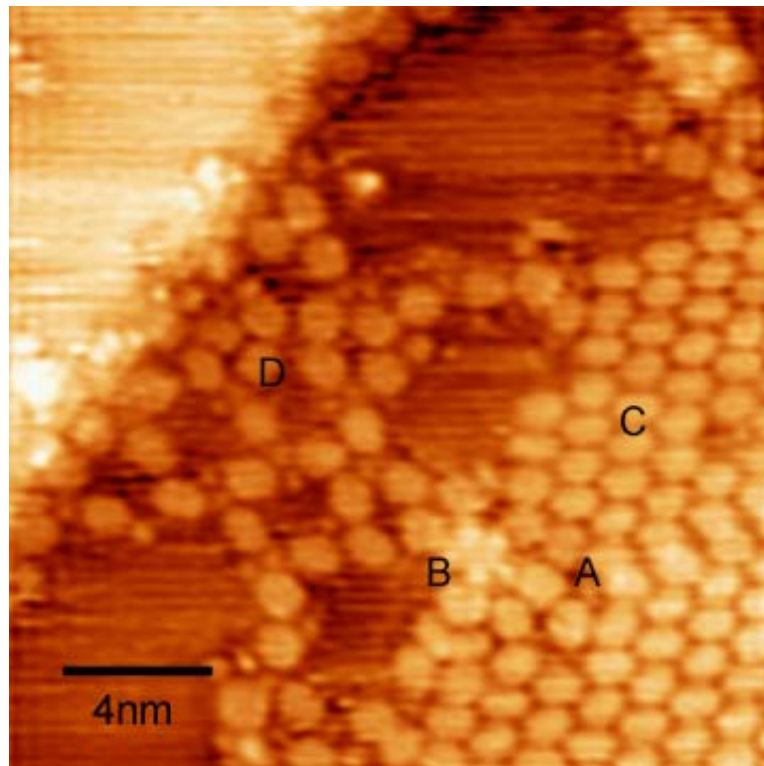


Figure 4.7 STM image of PTCDI on a Au(111)/0.05 ML Ni surface at 300 K (19.3 nm x 19.7 nm, 0.15 V, 0.19 nA). Intrusions of the gridiron phase, A, can be seen emanating from a nearby nickel island, B, into the domain of molecules in the hydrogen bonding phase, C. A network of molecules stabilised by small clusters, D, lies between the major domain and the step edge.

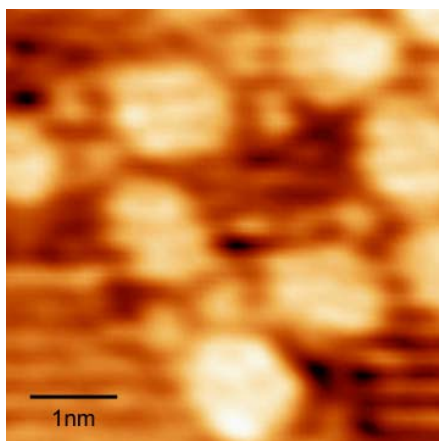


Figure 4.8 A zoomed image showing atomic scale features (Ni atoms/clusters) between PTCDI molecules

After annealing the surface above 350 K, the intrusions of the gridiron phase from Ni clusters grow such that larger areas of PTCDI islands are converted from the hydrogen bonded phase. These areas of gridiron phase appear brighter than the herringbone phase and these can be seen in figure 4.9, a Ni cluster can usually be related to the end of these brighter strips.

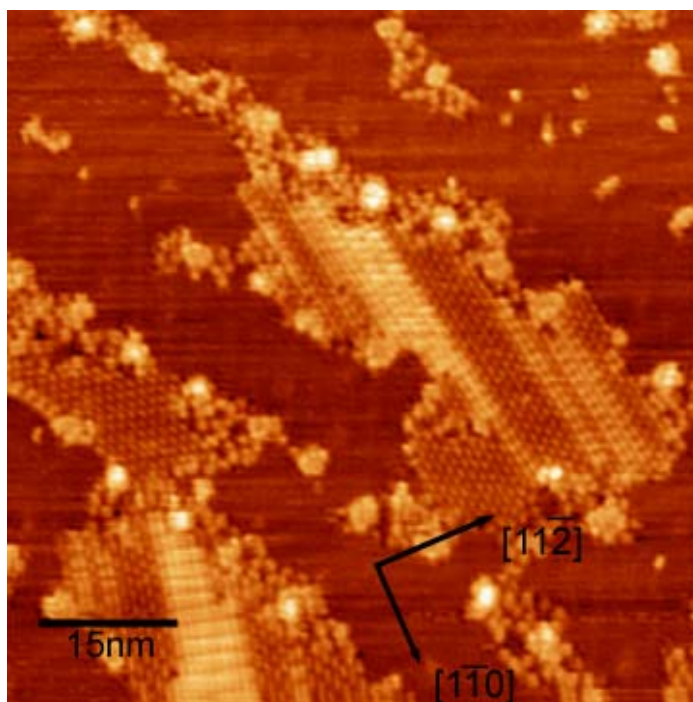


Figure 4.9 STM image of PTCDI on 0.05 ML Ni/Au(111) (75.2 nm x 75.2 nm, 1.5 V, 0.5 nA)

Disorganised arrangements of molecules can also be seen around each of the Ni clusters, it is highly likely that nickel atoms displaced from the clusters are present amongst these small, amorphous aggregates.

#### 0.10 ML Ni on Au(111)

At a Ni coverage of 0.1 ML, the 2-D Ni clusters have average diameters of  $\sim 3$  nm. Figure 4.10 shows an STM image of the Au(111)/0.1 ML Ni surface shortly after the deposition of PTCDI. Ordered domains of the hydrogen bonded phase are initially seen to form away from the rows of Ni clusters along the  $\langle 11\bar{2} \rangle$  direction of the surface giving a striped appearance to the surface. The areas in the immediate vicinity of the Ni clusters appear to be characterized by diffusing molecules or atoms which cannot be resolved. After several hours, PTCDI island growth adjacent to the Ni clusters can be imaged. This suggests that PTCDI diffusion is more facile along the gaps between rows of Ni clusters than across the regions occupied by the clusters.

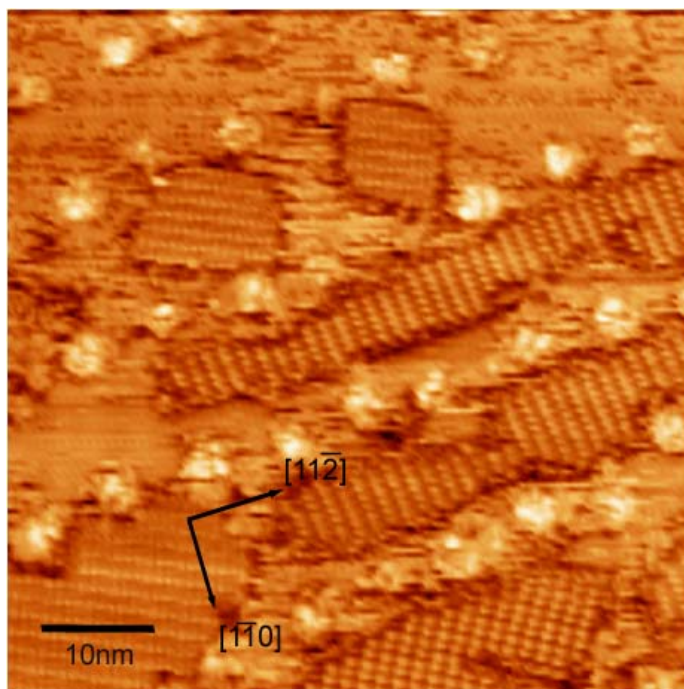


Figure 4.10 STM image showing the Au(111)/0.1 ML Ni surface after deposition of PTCDI at 300 K. Ordered structures are only observed in strips that run between the rows of Ni 2-D islands (65 nm x 65 nm, 1.5 V, 0.2 nA)

Heating the surface displayed in figure 4.10 to above 350 K induces the formation of ordered porous frameworks. Since these structures exhibit square or rectangular pores, they could prove useful as hosts of guest molecules, as in the examples of networks of aromatic carboxylic acids and Fe on a Cu substrate<sup>33</sup> or PTCDI and melamine networks on Au(111)<sup>11</sup> and on Ag-Si(111)-( $\sqrt{3}\times\sqrt{3}$ )R30<sup>34</sup>. However, their size and shape may rely upon the number of nickel atoms/ions incorporated in the structures.

Figure 4.11 shows the “double row stile” framework structure that formed when a low coverage of PTCDI was deposited onto a Au(111)/0.1 ML Ni surface following annealing to 350 K. The structure consists of pairs of straight rows of PTCDI molecules, within which the centre-to-centre separation is 2.4 nm, oriented at around 70° to the  $\langle 11\bar{2} \rangle$  direction. Parallel pairs of rows are separated by approximately 1.5 nm. This space is partially occupied by PTCDI molecules that are perpendicular to those in the rows. They are spaced equally along the channels between the “double stiles” and meet them at the junctions within the parallel rows such that the imide groups of three PTCDI molecules converge at the same point. There is no evidence of these structures after increasing the surface temperature to 420 K. Instead, “single row stile” frameworks are present.

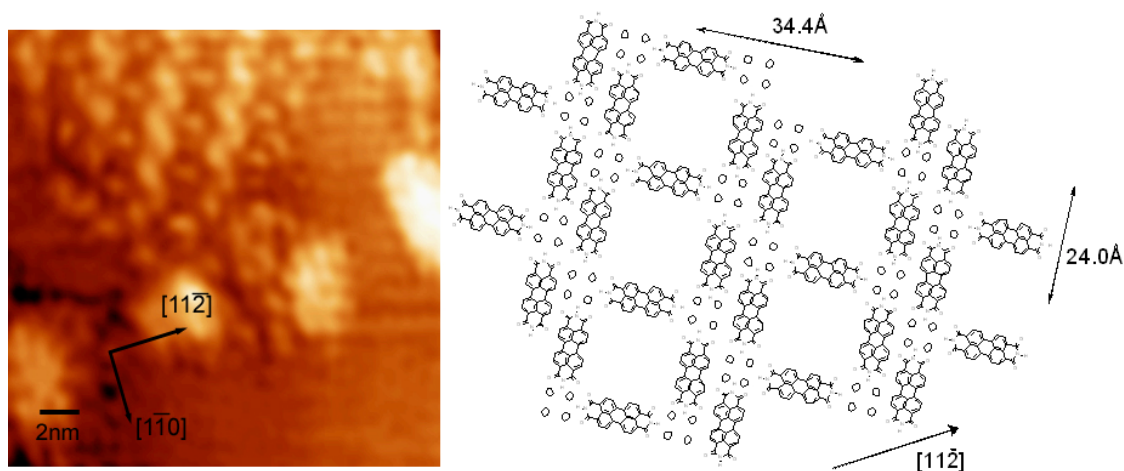
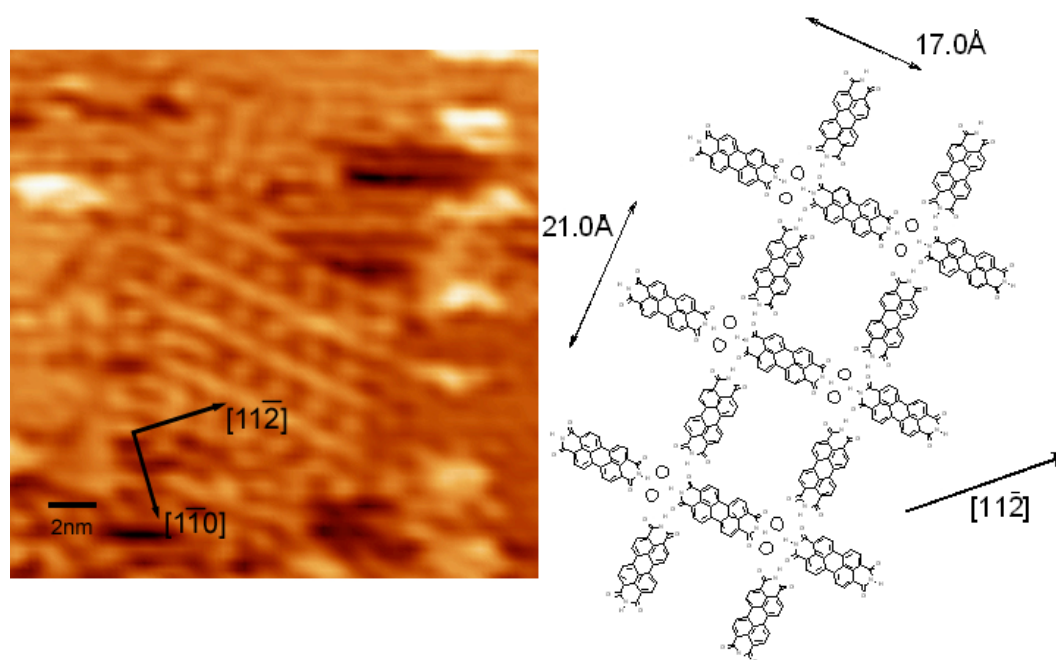


Figure 4.11 STM image of the “double stile framework” formed on a low coverage of PTCDI on a Au(111)/0.1 ML Ni surface after annealing to 350 K (22 nm x 22 nm, 0.46 V, 0.46 nA).

These structures, shown in figure 4.12, are very similar but consist of parallel single rows of PTCDI molecules. The centre-to-centre separation within the single rows is around 1.7 nm, these are also oriented at  $70^\circ$  to the  $\langle 11\bar{2} \rangle$  direction of the surface. PTCDI molecules, lying perpendicular to the rows, are spaced equally along the channels. They intercept the rows at the junctions between molecules within them such that imide groups of 4 molecules come together at the same point. These structures also formed on the Au(111)/0.3 ML Ni surface after heating to 350 K (vide infra).



**Figure 4.12** STM image of the “single stile framework” formed on the Au(111)/0.1ML Ni surface with low coverage of PTCDI after annealing to 430 K (19 nm x 19 nm, 0.46 V, 0.46 nA) A model of this single row stile framework, the stabilisation of the structure by the insertion of 2 metal atoms at each junctions has been denoted.

Models for the “double-“ and “single-stile” structures are presented alongside the STM images in figures 4.11 and 4.12. Within the “stiles” of the frameworks, adjacent PTCDI molecules appear to align with the long dimension of the molecules in a straight line. This contrasts with the staggered 1-D rows that PTCDI forms on the bare Au(111) substrate<sup>11</sup>. The Ni atoms incorporated in the structures would supply the additional stabilization required to counteract the repulsive dipole-dipole interaction that would exist when the imide groups face each other straight on. Furthermore, no attractive hydrogen bonding interaction

exists between the molecules in the stiles and those that sit perpendicular to them in the “rungs” of the frameworks. In this arrangement, oxygen atoms of the imide carbonyl functionality would be the closest points of each rung molecule to the junctions at which they meet two stile molecules and their imide carbonyl oxygen atoms.

The double-stile structure consists of two straight, parallel rows of molecules. The rows are offset with respect to each other such that the molecules within these double stiles appear as a series of diagonal pairs and that the frameworks do not represent a regular square lattice. The molecules within the rows, as well as being aligned parallel to the long dimension of PTCDI, are too far apart to allow significant hydrogen bonding. Hence the structure is likely to be stabilised by the incorporation of metal atoms at junctions between the molecules.

The proposed model for the single-stile structure (figure 4.11) incorporates two nickel atoms into the junctions of the stiles as in the model proposed by Mendez et al<sup>35</sup>. Further evidence for this type of stabilisation between molecules is seen in Figure 4.8, albeit in an image of an imperfect framework. This relatively clear image shows two circular features, which are interpreted as nickel atoms/ions, between molecules in the stiles of these frameworks. Line profiles reveal that the features assigned to “metallic” features are 140 pm above the substrate compared with the molecular features whose “height” above the surface is typically 90 pm.

Stabilisation of the 2-D frameworks may take place by insertion of one or two Ni atoms between terminal imide groups of adjacent molecules as is proposed for the stabilisation of Fe-PTCDA chains and ladders<sup>35</sup>. However, it may be the case that small clusters of Ni atoms (more than 2 atoms) sometimes exist at the junctions between molecules in these structures and this is then reflected in a variability of pore shapes and sizes. This is one of the major differences between the double stile and the single stile frameworks observed. The centre-to-centre separation between molecules in the rows that form the single stiles is shorter than that those

in the double stile structure (~1.7 nm versus ~2.4 nm). The greater inclusion of metal into the double stile framework could provide the driving force for its formation; the relative orientations of PTCDI species in adjacent rows in the stiles and the quantity of metal atoms between each molecule within the rows may also be sufficient to bond the pairs of rows that make up the double stiles.

The pores in the single stile frameworks are rectangular in shape. The proposed model is similar to that presented for the rectangular pore network reported by Zhang et al for stilbenedicarboxylic acid adsorption on an Au(111)/Mn surface<sup>31</sup>. They observed two metal-organic frameworks that incorporated Mn atoms from 2-D islands in the herringbone elbows. They suggested that pairs of Mn atoms that alternate perpendicularly in their orientation along rows in the framework create a square-pored structure whilst if all the pairs are aligned parallel, a rectangular-pored network results. The same study suggests that the nature of the network observed depends on whether network formation occurs on fcc or hcp regions of the reconstructed Au(111) surface. In the present case, determination of whether the reconstruction influenced the growth of these porous metal organic networks could not be achieved.

The exact coordination scheme of PTCDI molecules to nickel within the frameworks is unclear. Along the stiles or 1-D chains in the model proposed by Mendez<sup>35</sup>, the nature of the interactions with the two metal atoms is uncertain, coordination may be through the imide or anhydride carbonyls only, coordination may also be through the central atom, N or O respectively, and coordination of these atoms may only be with one of the metal centres or it may bridge them. The oxidation state of the incorporated metal atoms is unknown. Identification by spectroscopic methods may offer additional insight into the understanding of these structures. The stabilization and co-ordination of the perpendicular “rung” molecules also needs to be considered. The rung molecules may only be held by a monodentate interaction through one of their carbonyls at each vertex, this can be deduced from the apparent offset of the rung molecules to the pair of nickel atoms such that they are aligned with one of their carbonyl oxygen atoms rather than

their central axes, this may also grant further stabilisation through hydrogen bonding of the imide N-H in the rung molecules to the carbonyls of the perpendicular stile molecules.

#### 0.30 ML Ni on Au(111)

At a Ni coverage of 0.3 ML, the 2-D Ni clusters have average diameters of  $\sim 5$  nm. Figure 4.13 shows the behaviour of a low coverage of PTCDI on the Au(111)/0.3 ML Ni surface. Initially, the molecules could not be resolved as they adsorb in a random arrangement around and atop the 2-D islands.

The sample was annealed to 350 K to facilitate the formation of ordered structures (figure 4.14). As well as the hydrogen bonding phase, some ladder structures were observed emanating from the islands of molecules. Metal atoms or very small metal clusters are just visible around the edges of these structures.

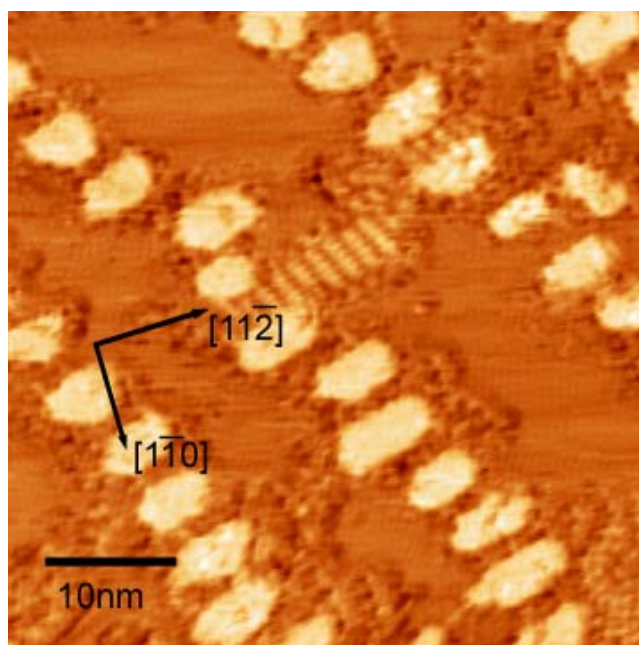


Figure 4.13 STM image of PTCDI on the Au(111)/0.3 ML Ni surface at 300 K (1.5 V, 0.2 nA, 48.7 nm x 47.8 nm)

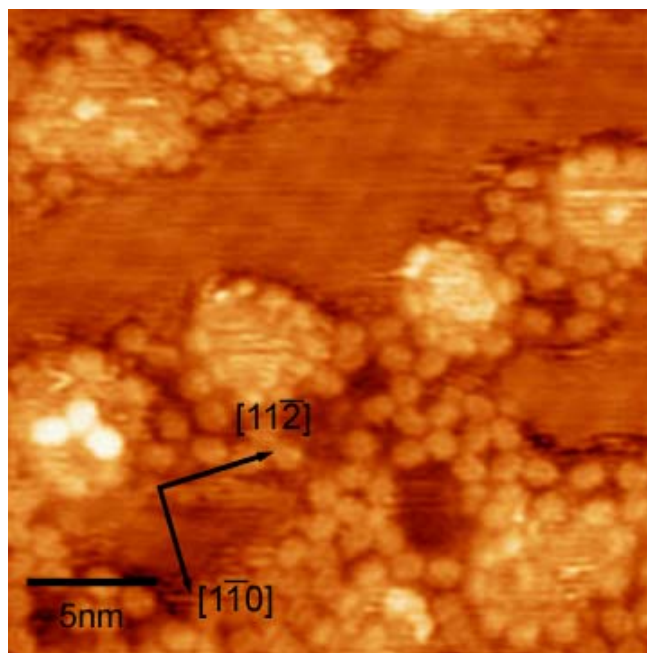


Figure 4.14 STM image of PTCDI on the Au(111)/0.3 ML Ni surface after annealing to 350 K (1.5 V, 0.2 nA, 25 nm x 25 nm)

Figure 4.15 shows that annealing the sample above 420 K increases the number of chains that grow outwards from the groups of molecules nucleated around the 2-D nickel islands.

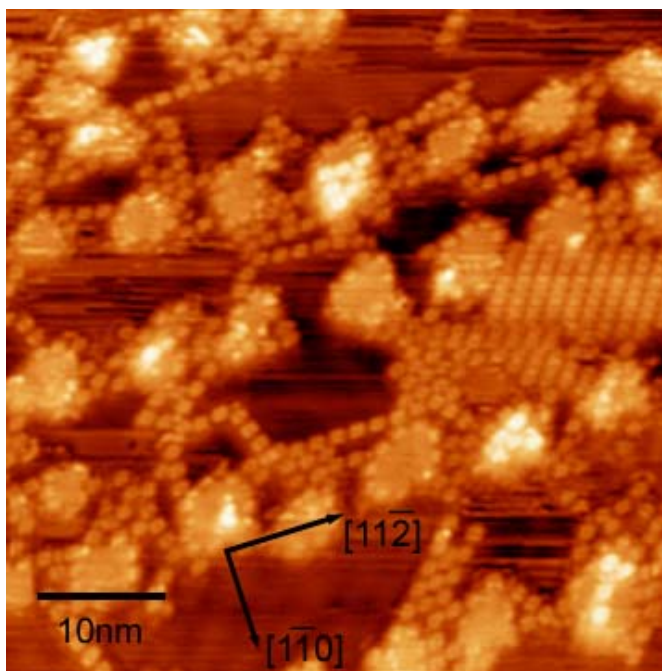


Figure 4.15 STM image of PTCDI on the Au(111)/0.3 ML Ni surface after annealing to 420 K (1.5 V, 0.2 nA, 51.9 nm x 51.9 nm)

When the PTCDI exposure was close to monolayer coverage at room temperature, extended areas of porous networks were produced (figure 4.16). The orientation of the ladder frameworks varies greatly across the surface when the PTCDI coverage is high. The pores in these structures are rectangular with one of the dimensions being close to the length of a PTCDI molecule and it is thought that these structures are equivalent to the single-stile frameworks. Domains of the hydrogen bonding phase, equivalent to those discussed in Section 4.4.1, are also present on the surface.

Figure 4.17 shows the same surface after annealing to 420 K. Heating destroys the porous networks and leaves a largely disordered surface on which the molecules are arranged randomly around small clusters of a few Ni atoms that have diffused from the initial growths at the herringbone elbows.

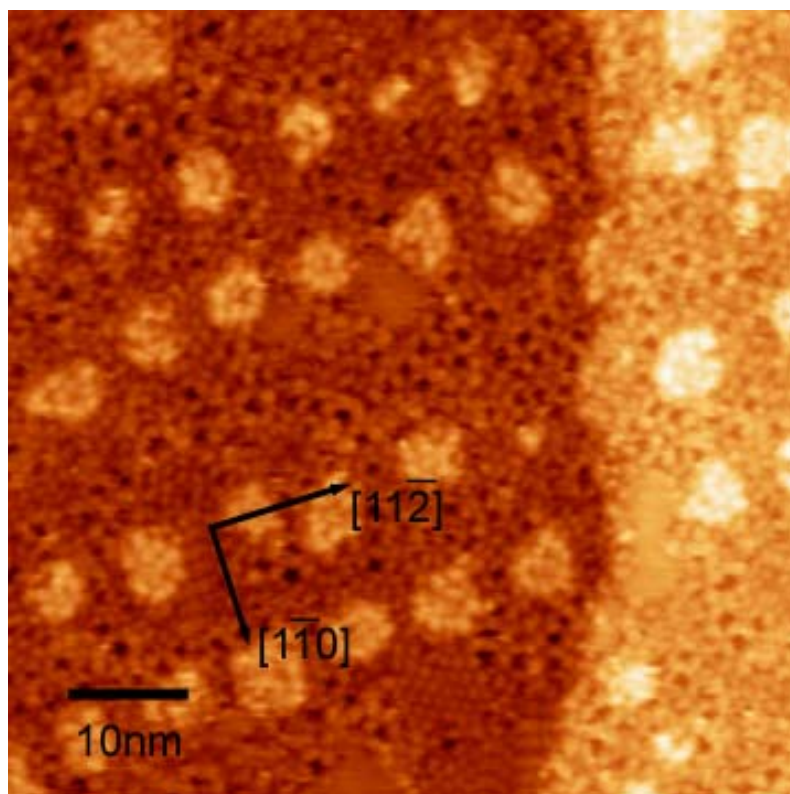


Figure 4.16 STM image showing several porous domains upon Au(111)/0.3 ML Ni substrate at 300 K where PTCDI coverage is close to monolayer coverage (63.4 nm x 63.4 nm, 1.40 V, 0.16 nA)

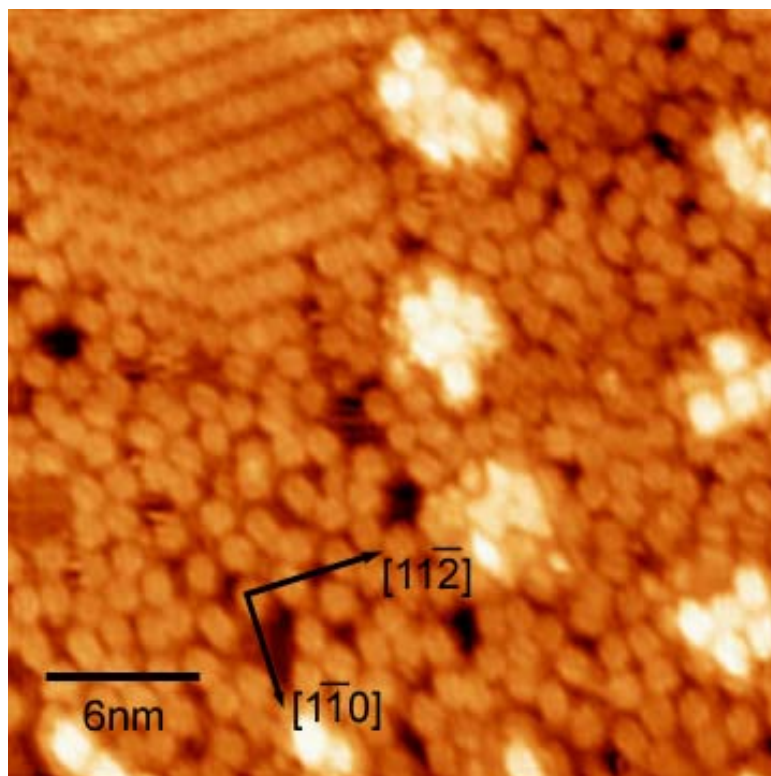


Figure 4.17 STM image of an island of gridiron and brickwork domains amidst an amorphous phase after the surface was heated to 400 K (30.1 nm x 30.1 nm, 1.82 V, 0.14 nA)

Ordered close-packed domains are present on this surface; they consist of straight 1-D rows of molecules. The centre-to-centre molecular spacing within rows is similar to that between the rows of the single stiele frameworks at 1.73 nm, the centre-to-centre molecular spacing between rows are 0.91 nm. Two different structures can exist: adjacent rows can either be aligned with each other in two dimensions so as to form a gridiron-like array or staggered with respect to each other to give a brickwork-like arrangement. The most common orientations of the rows in these structures is either within  $0\text{-}15^\circ$  or at around  $70^\circ$  to the  $\langle 1\bar{2}1 \rangle$  direction of Au(111).

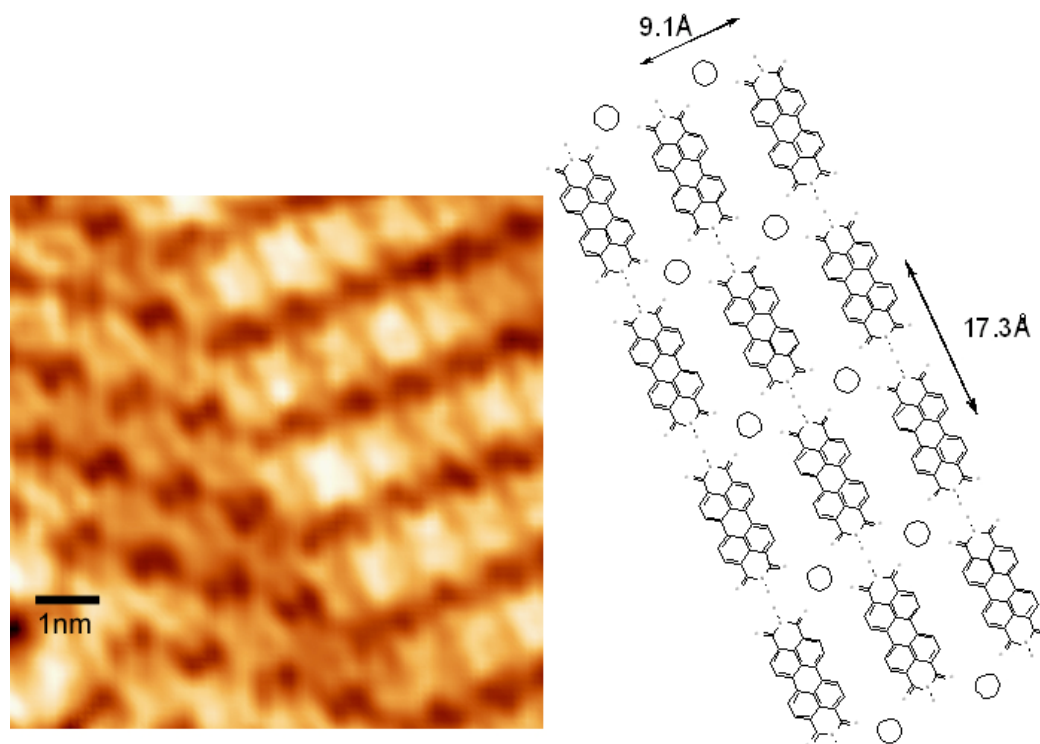


Figure 4.18 Zoomed section of STM image of figure 4.17 alongside the proposed model of the gridiron-like phase

In the crystal structures of nickel complexes where 4 carbonyl ligands are coordinated in the same plane to a Ni atom<sup>36,37</sup>, the O...O separation in both dimensions are typically in the range 0.28 – 0.30 nm. This additional distance upon the length of the PTCDI molecule (1.44 nm) could plausibly fit the measured centre-to-centre separation within rows of ~1.7 nm and whilst the breadth of the perylene core is around 0.65 nm, the additional O...O distance may reasonably fit the measured centre-to-centre separation between rows of 0.91 nm (figure 4.18). As in the porous frameworks, spectroscopic evidence would be required to identify the oxidation state of nickel in these arrangements.

In the amorphous form (figure 4.17) created after the rearrangement of the structures of figure 4.16, PTCDI molecules are scattered across the surface, but their distribution still appears to be controlled by coordination to metal atoms. There is no evidence of the structures the molecules would take if hydrogen

bonding was the major force controlling distribution – i.e. 1-D rows or the close-packed PTCDI phase (Section 4.4.1). The surface is covered with circular features, which are thought to be small metal clusters, where up to five PTCDI molecules meet and to which their imide functionalities face.

It is less straightforward to propose a model for the brickwork phase observed on the left of the close-packed island in figure 4.18. The centre-to-centre separation along the rows matches the gridiron phase suggesting a similar stabilisation mechanism. However, this does not explain the offsetting of rows giving rise to the brickwork appearance. This may be some form of metastable state in the transformation of a hydrogen bonded domain to a gridiron domain. If the model of 4 imide carbonyls coordinated to Ni representative of the gridiron phase was applied to the brickwork phase, only half of the rows would be coordinated to Ni atoms that lie adjacent to the perylene bay regions of the other half of the rows. Of course, it is impossible to know the exact quantity, position and role of the Ni atoms in these structures and although stabilisation of the brickwork phase is, from these tentative models, apparently weaker than in the gridiron phase. The limited stabilisation from Ni is sufficient to overcome the anticipated electrostatic repulsion between imide carbonyl groups.

Close-packed Ni-PTCDI structures can also form from the hydrogen bonding phase. Through time, and enhanced by increasing temperature, nickel atoms diffuse from the initial growths at the elbows of the herringbone reconstruction into domains of the hydrogen bonding phase. The shape of the nickel islands is also seen to change; they become more ragged and eventually rounded as particles diffuse from them. However, they are never completely corroded to the extent as observed by Trant et al in the case of glutamic acid adsorption on Au(111)/Ni<sup>30</sup>. The PTCDI phases that incorporate metal atoms eventually dominate as initial intrusions of the gridiron-like phase, seen stretching from nickel islands in figure 4.7, or increases in the centre-to-centre separation of molecules in the hydrogen bonding phase eventually lead to complete domains of metal-containing structures as is nearly achieved in figure 4.9. The hydrogen bonding phase shows limited

registry with the substrate and can be observed growing at a variety of orientations. It may be the case that if the rows in hydrogen bonding domains are at orientations close to the favoured growth directions of the gridiron Ni-PTCDI rows, then these domains are more susceptible to transformation.

*0.50 ML Ni on Au(111)*

At a Ni coverage of 0.5 ML, the 2-D Ni clusters have average diameters of  $\sim 7$  nm and there is some coalescence of adjacent clusters since this dimension is similar to the separation of adjacent herringbone elbows.

Figure 4.19 shows the behaviour of PTCDI on a 0.5 ML Ni/Au(111) surface. Initially (figure 4.19a), molecules lie atop and border the large 2-D islands. Linkages between the groups of molecules that form around the islands take the form of chains, in which the stabilisation is thought to be due to the incorporation of nickel. Figure 4.19b demonstrates that most of the molecules are removed from the islands after the surface is annealed to 400 K, the remaining molecules are close-packed in narrower channels between the nickel islands.

The nickel islands are significantly more rounded in shape after annealing to 500 K (figure 4.19c). Despite their change in appearance, every island is still completely bordered by PTCDI molecules. Chains of PTCDI molecules still link between the rows of islands, the centre-to-centre separation between molecules is around 1.59 nm. Some PTCDI is still detectable on the surface after annealing to 600 K (figure 4.19d). Thermally induced restructuring of the surface progresses further and the islands are seen to disappear or coalesce. 1-D chains decorate a number of the expanded islands after the annealing step. The chains that litter the surface often converge, and usually they form “Y-shapes”. The chains are often terminated by small metal clusters that may be groups of atoms that have diffused

from nickel islands or are the remains of islands that have been consumed by the underlying crystal lattice upon heating the sample.

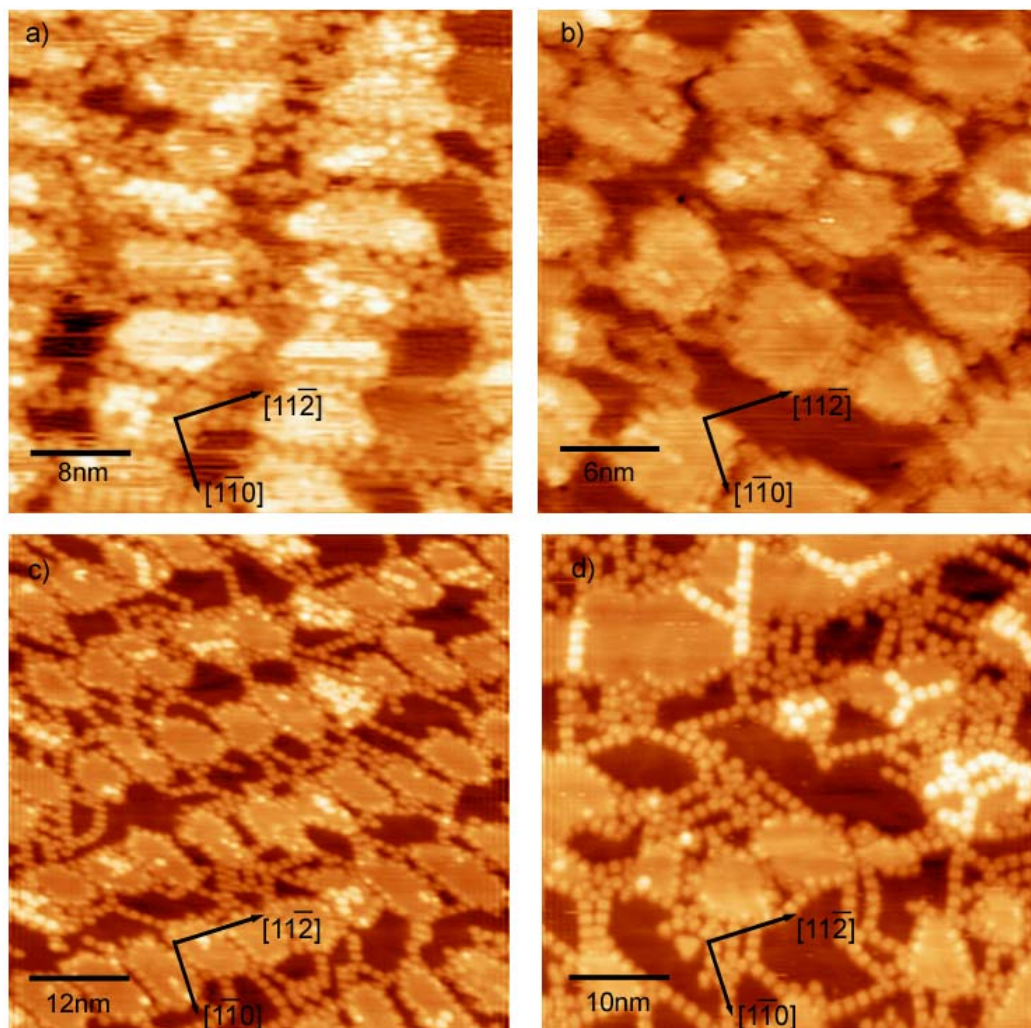


Figure 4.19 STM images of PTCDI after deposition on a Au(111)/0.5 ML Ni surface (1.51V, 0.15nA); (a) at 300 K (40.2 nm x 40.2 nm), (b) then 400 K, where most of the molecules have desorbed from the surface of the Ni islands (30.5 nm x 30.5 nm), (c) 500 K (60.2 nm x 60.2 nm) and (d) 600 K (50.2 nm x 50.2 nm).

Under conditions of very low coverage, 1-D molecular chains are the main feature of the surface (see figures 4.15 and 4.19). In this series of experiments, these conditions were arrived at by raising the surface temperature, PTCDI begins to desorb from the surface at around 450 K but there is still evidence of PTCDI on the surface beyond 600 K. These molecules are to be found bordering the nickel islands and in chains that cross between the rows of islands. The imide groups of the molecules face each other in the chains of molecules around the islands, thus it can be reiterated that the stabilisation offered by adhesion to nickel must be greater than any electrostatic repulsion between molecules. The structure of the

chains, as argued above with respect to their linearity, most likely accommodates nickel. As with the frameworks and the gridiron phase, the stabilisation of the structures is unclear. The centre-to-centre separation in the chains is less than in the gridiron and framework structures; at  $\sim 1.59$  nm. Since PTCDI measures 1.44 nm in length between its two extremities, it seems most likely that a N-Ni-N interaction is present via thermally induced dehydrogenation of the NH functionality (figure 4.20).

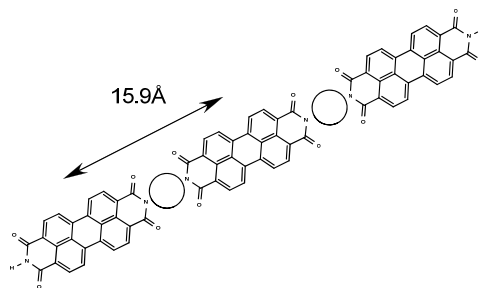


Figure 4.20 Model of 1-D chains formed by dehydrogenation and coordination to Ni

The mechanism for this transformation is unknown, though analogous chemistry has been observed in the formation of copper phthalimide complexes<sup>38</sup>. The N to N separation in nickel diimide complexes<sup>39,40</sup>, across the N-Ni-N coordination, is around 0.4 nm, which would result in a centre-to-centre separation in continuous PTCDI-Ni-PTCDI chain of around 1.64 nm – i.e. consistent within experimental error with the STM periodicity. Sometimes larger clusters are visible between molecules in chains and frequently the chains change direction of growth, meet or terminate around these clusters.

Following annealing treatments to temperatures greater than 450 K the surface undergoes reconstruction and the 2-D islands begin to coalesce or disappear as Ni atoms diffuse into the underlying Au lattice. Most of the molecules desorb from or diffuse away from the nickel islands after annealing to 400 K, however, the molecules tightly bordering their edges remain throughout the stages of annealing and the growth of 1-D molecular chains, like those discussed above, is observed upon the islands that have expanded during the thermally induced restructuring and alloying processes. As Cullen and First discussed, after annealing to high

temperatures, these larger islands likely consists mostly of gold atoms<sup>41</sup>. The temperature dependent behaviour suggests that PTCDI adsorption at steps and the formation of molecular chains incorporating metal atoms (ions) are thermodynamically favoured.

#### **4.4.3 Nickel Deposition onto Au(111) Surfaces Bearing PTCDI Islands**

Where the local concentration of Ni is sufficiently low and the resolution of the STM images is sufficiently good, the initial nucleation process around molecular domains can be probed. It is thought that such conditions exist in figure 4.21, where an overall surface coverage is  $<0.08$  ML, an arrangement of small features around the molecular domain can be seen.

At low concentration of Ni around the vicinity of PTCDI domains, individual atoms may associate with carbonyl atoms of the imide functional groups of PTCDI molecules, this is what is thought to be represented by the small round features which flank the two PTCDI domains of figures 4.21 and 4.22. In these examples, there are two sizes of these bright features, one is more circular of diameter 2-3 Å, whilst the other, associated with the lower domain of the image, is more oval, with a width of 2-3 Å, and a length of 6-7 Å, these two types may represent one Ni atom and two nearby Ni atoms, respectively.

The proposed relationships at the edge of a hydrogen bonded domain are shown beside the respective STM images, it is thought that Ni atoms may be attracted by the electronegative charge of carbonyl oxygen atoms that protrude from the domain. There may, of course, be no interaction with specific parts of the PTCDI molecules and the stepped edge of the hydrogen bonding PTCDI domain may simply provide a barrier to the diffusing Ni atoms before they find more preferable nucleation sites or are consumed by the interior of the domain or new coordination regimes.

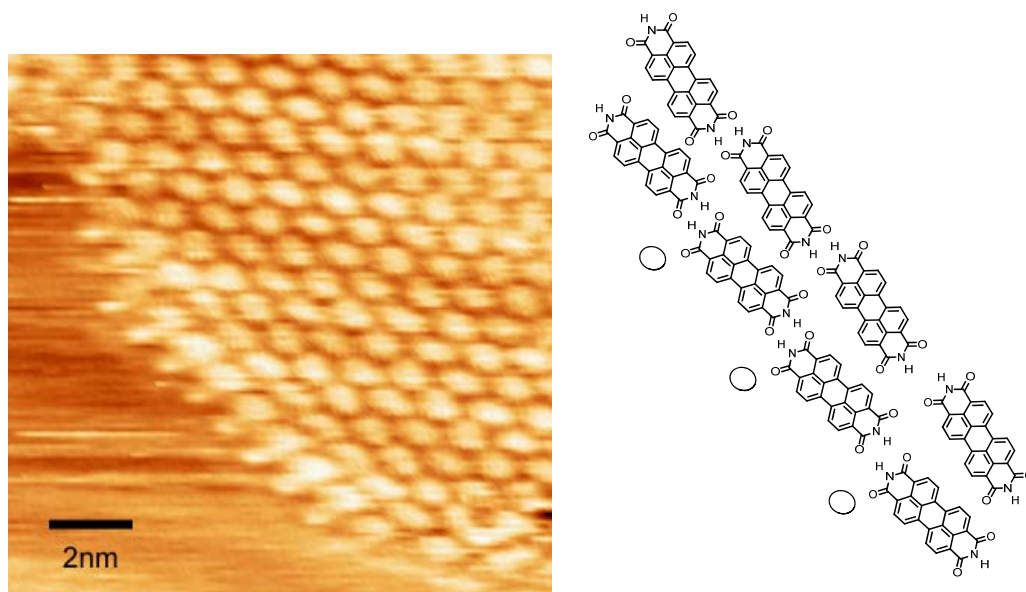


Figure 4.21 STM image showing a domain of PTCDI which shows an edge characterised by features thought to organised deposits of Ni atoms (13.5 nm x 13.5 nm, -1.5 V, 0.2 nA)

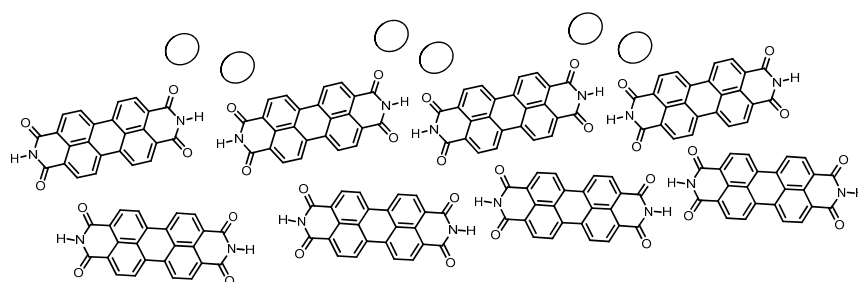
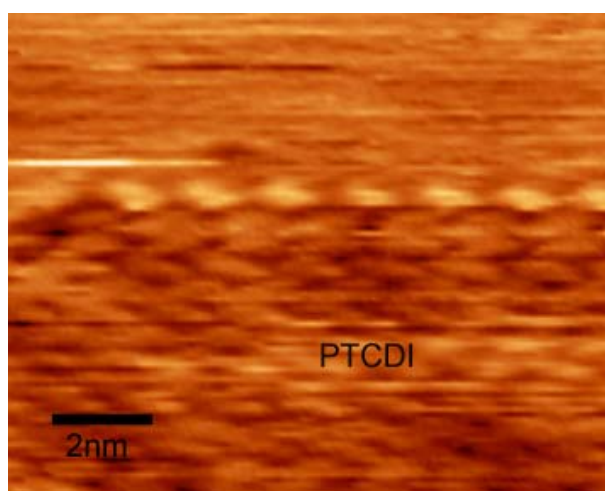


Figure 4.22 STM image showing a domain of PTCDI which shows an edge characterised by features thought to organised deposits of Ni atoms (12.0 nm x 12.0 nm, -1.5 V, 0.2 nA)

After greater exposures to Ni vapour (equivalent to  $>0.1$  ML), a ‘skimming effect’ on PTCDI domains is observed in initial STM images (figure 4.23). This effect is

not limited to PTCDI domains but it is most evident atop them due to their close-packed nature creating the least variable contrast from edge-to-edge across of all the molecular structures observed. This ‘skimming effect’ sees the interiors of domains appear significantly brighter than their edges; this may be the result of the STM tip brushing Ni atoms that lie atop PTCDI molecules across expansive domains. After several hours, STM images can be acquired that are free from the ‘skimming’ phenomenon and it can be seen that the evaporation of nickel can cause a range of changes to the large islands of PTCDI in its hydrogen bonded phase (figure 4.24).

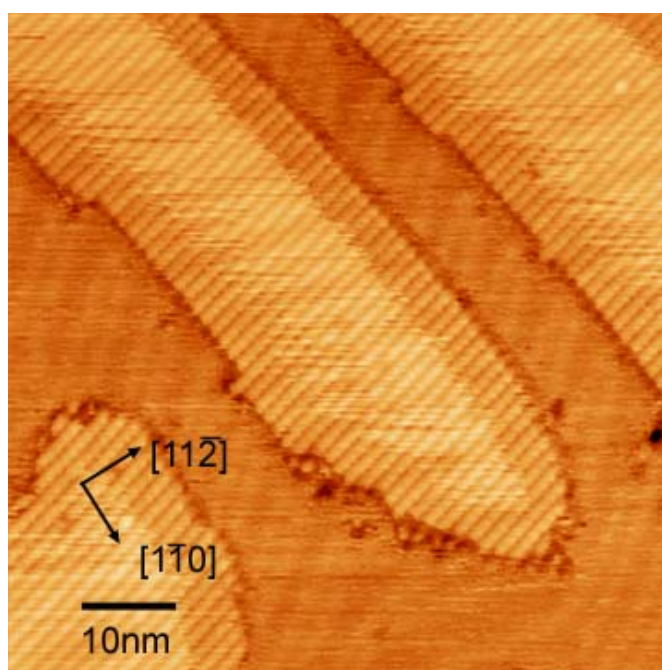


Figure 4.23 STM image of PTCDI domains after a very recent deposition of Ni, the 'skimming effect' can be seen across their surface (74.3 x 74.3 nm, 1.5 V, 0.5 nA)

The preliminary changes to PTCDI domains see single molecules distributed randomly throughout the domain appear depressed or occupy less space than standard molecules of the domain, the molecules in question have apparent widths  $\sim 1 \text{ \AA}$  less than the standard PTCDI molecule (Scenario **A**, figure 4.26) in the phase.

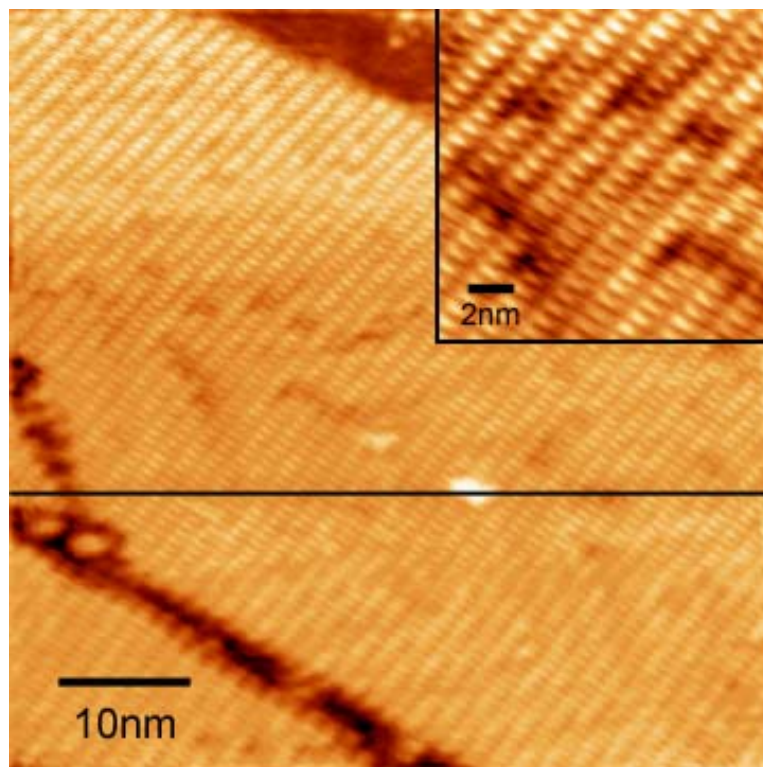


Figure 4.24 STM image of a PTCDI domain on Au(111), nickel, equivalent to 0.01 ML coverage, has been evaporated onto the sample. Amongst the domain, some molecules appear darker, smaller or appear to be sitting in a depression, a Ni island can also be seen to have grown into the elbow of the surface reconstruction below the domain (57.8 nm x 57.8 nm, 1.8 V, 0.4 nA).

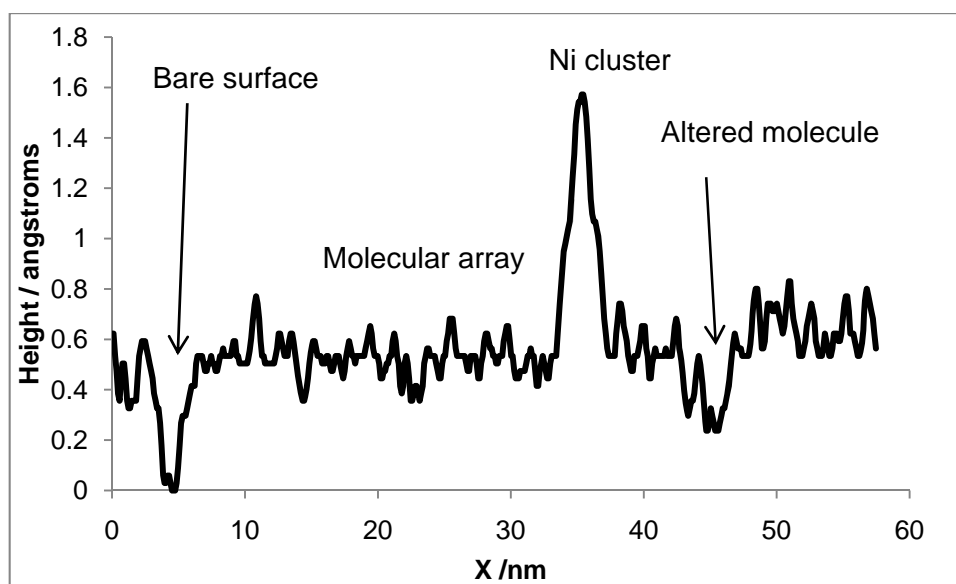


Figure 4.25 Height profile across the line indicated in the STM image of figure 4.24

These instances may be caused by slight perturbations of the hydrogen bonded domain to accommodate a single nickel atom; for example, tilting of a flat PTCDI

molecule due to a Ni atom lying underneath it will change its elevation in the vertical axis and reduce its area in the plane of scanning and gives rise to darker features in the domain (Scenario **B** in figure 4.26), although the fact that the domain remains largely unperturbed and that adjacent molecules are often unaffected by this effect may suggest that this is an electronic effect and that the PTCDI molecules do remain flat in order to ensure the retention of the hydrogen bonding stabilisation (Scenario **C**), in this scenario, tunnelling through molecules in this situation may be diminished, below the PTCDI molecule and either side of the Ni adatom a gap is created which may limit the current flow.

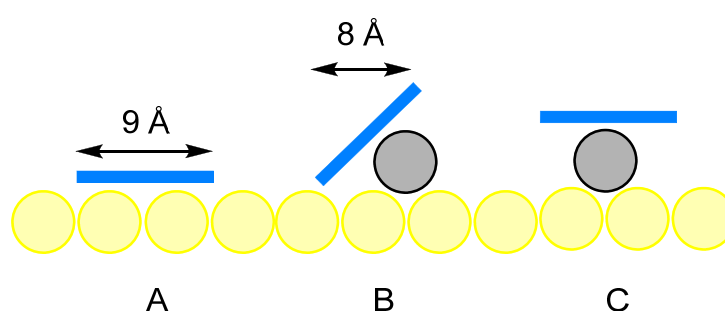


Figure 4.26 Possible scenarios causing the change in appearance from a standard molecule, A, which appears as 9 Å in width, to a narrower, dimmer feature. Scenario B shows the observed width may be decreased by the tilting of a molecule, however, Scenario C where molecules may still remain flat despite the presence of a Ni atom underneath them cannot be ruled out

Profiles of apparent height, shown in figure 4.25, do not support an elevation associated with a tilt of the PTCDI molecules with respect to the flat surface, the molecules in question usually appear as 0.3 Å lower than normal molecules. Such a tilt may mean that the accessibility of the tip to the orbitals of PTCDI is restricted and that is why they appear darker within the domain.

Presence of PTCDI islands does not prevent Ni atoms from nucleating in the elbows of the reconstruction; cluster growth in these sites can have two results for the PTCDI domain: nickel atoms can nucleate in elbows and exist below the molecular domain or nickel can nucleate in the elbows and induce a split in the domain. This is seen in the STM image of figure 4.27 where the Ni coverage is approximately 0.2 ML.

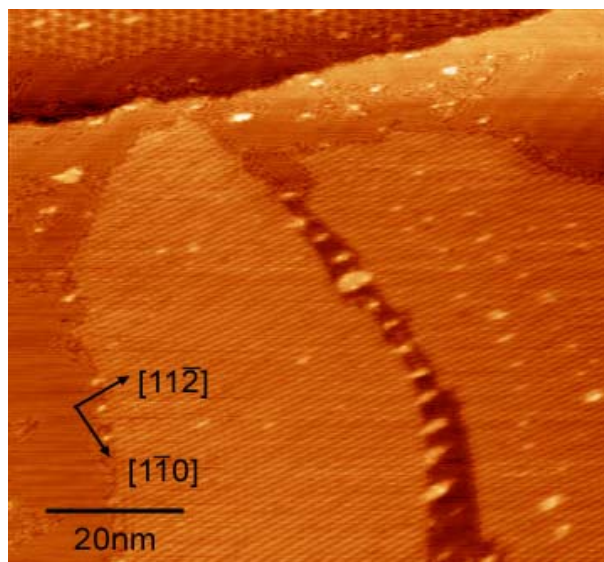


Figure 4.27 STM image that shows that PTCDI domains can either continue to exist above Ni islands or be split by the rows of them (87.7 nm x 87.7 nm, -1.5 V, 0.2 nA).

The extent to which splitting of molecular domains down the  $\langle 11\bar{2} \rangle$  and equivalent directions occurs can probably be attributed to cluster size. The orientation of PTCDI with respect to the  $\langle 11\bar{2} \rangle$  direction may bear a small influence on the outcome. In the figure shown, the Ni islands along the split in the molecular domain are sized in the range 3-6 nm in diameter, whilst those that exist below the molecular domain are all smaller than 3 nm in diameter.

When domains are split, the formation of 1-D chains stretching between Ni islands along the  $\langle 11\bar{2} \rangle$  direction or its equivalents occurs frequently, an example is seen in figure 4.28. These 1-D chains have a centre-to-centre separation of  $\sim 18 \text{ \AA}$  between molecular features – this may suggest that insertion of Ni between molecules takes place rather than formation of N-Ni-N bonds, the fact that this occurs at room temperature and not after annealing, which might require the breaking of the N-H bond of the imide, may support this idea.

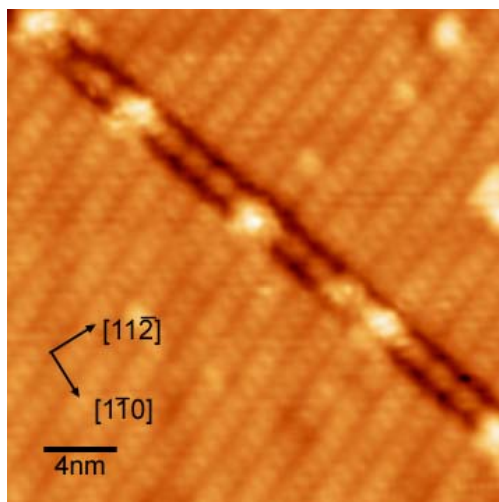


Figure 4.28 1-D Ni-PTCDI chains stretching between Ni clusters along a split PTCDI island (26.4 nm x 26.4 nm, 1.5 V, 0.4 nA)

Through time, changes to the positions and orientation of molecules within the PTCDI islands are observed with the arrangements either taking on gridiron or brickwork patterns as observed in the previous study of PTCDI deposition onto Ni/Au(111) surfaces.

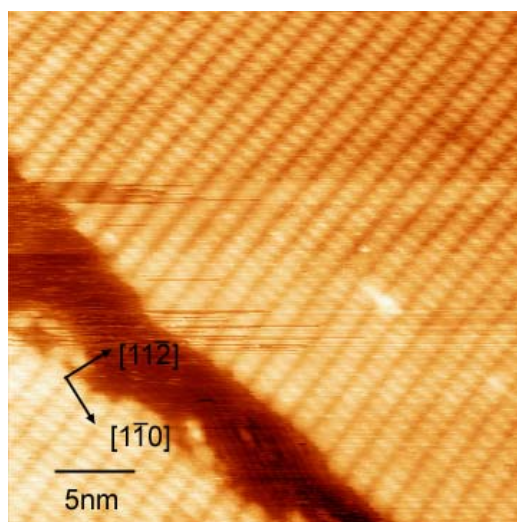


Figure 4.29 STM image of two domains of PTCDI in its gridiron phase, this image was captured a day after the deposition of 0.1 ML Ni to an Au(111) surface bearing PTCDI (32.3 nm x 32.3 nm, 1.8 V, 0.4 nA)

Limited annealing of samples after Ni deposition was undertaken in this series of experiments thus the occurrence of gridiron-like formations, where rows in close-packed domains straighten to accommodate metal atoms between molecules, is

mostly restricted to smaller areas of PTCDI. Furthermore, these are usually situated towards the edges of domains and the change occurs on a timescale of days (figure 4.30).

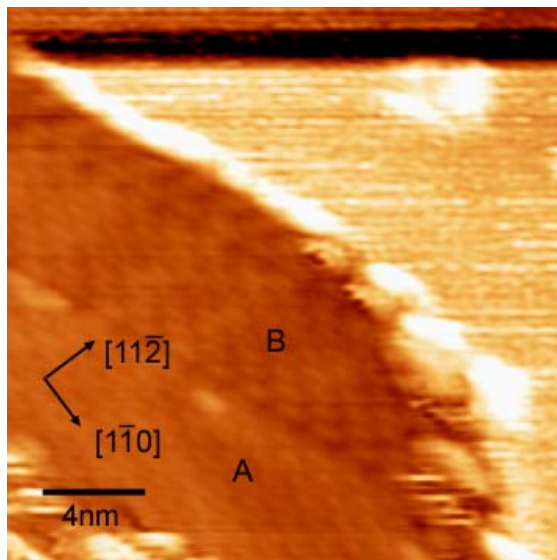


Figure 4.30 STM image of a PTCDI domain that has undergone change after the deposition of 0.3 ML Ni; A (toward the interior) shows close-packed molecules in hydrogen bonding formation, B (towards the edges of the domain where Ni has collected) shows molecules in rows with greater centre-to-centre spacing in gridiron and brickwork formations (21.9 nm x 21.9 nm, -1.5 V, 0.2 nA).

Figure 4.30 shows a PTCDI island that has undergone change from the PTCDI phase, **A**, to gridiron/brickwork phase, **B**, approximately 2 days after first being exposed to a higher dose of nickel (~0.3 ML), it is presumed that the layer of brightness (approximately 1 nm in lateral thickness) around the domain is caused by nickel atoms banked up against the domain edges by extension of the initial nucleation traits discussed at the beginning of this section.

#### 4.4.4 Melamine Deposition onto Au(111)

On Au(111), melamine will assemble into a hexagonal arrangement that is stabilised by each molecule forming two N-H...N hydrogen bonds with its three adjacent molecules. The structure has a unit cell consisting of vectors, measured between the centres of adjacent hexagons, of equal length 10.8 Å separated by an angle of ~60°. The unit cell is usually closely aligned with the  $\langle 10\bar{1} \rangle$  direction of the surface. A number of studies of melamine on Au(111) have reported similar if

slightly discordant experimental and theoretical measurements, the parameters listed above are largely similar to those measured by Perdigão et al<sup>42</sup>, whilst alignment of the hexagon centres along the  $\langle \bar{3} \bar{2} 1 \rangle$ ,  $\langle 11 \bar{2} \rangle$  and  $\langle \bar{4} 13 \rangle$  directions have also been reported<sup>43-45</sup>. Although melamine is an achiral molecule, the hydrogen bonding regime adopted is chiral<sup>11</sup>. Resolution of the two separate enantiomeric arrangements was not attained in these STM experiments. Improved image quality might be achieved by imaging samples at low temperature.

Figure 4.31 shows a close-up view of a melamine domain. The raised ridges of the herringbone surface reconstruction can be seen through the molecular array and in this image of a small area, run diagonally from bottom left to top right. The arrow indicates one pore which does not appear dark like the others. A previous study has proposed similar effects to be caused by molecules, lying perpendicular to the surface, being trapped inside the pores<sup>45</sup>. However, this may be caused by trapped surface adatoms or other electronic effects. A schematic showing the arrangement of melamine molecules on the surface is shown in figure 4.32.

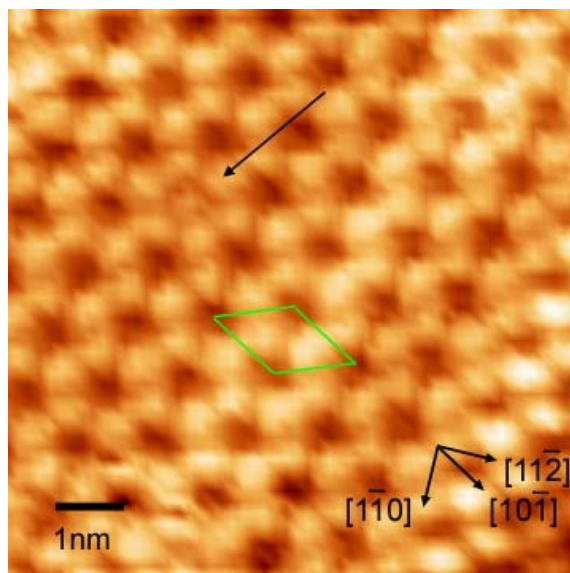


Figure 4.31 Close-up STM image of a melamine island, the arrow indicates a molecule that is trapped in one of the pores (8.4 nm x 8.4 nm, 1.5 V, 0.35 nA)

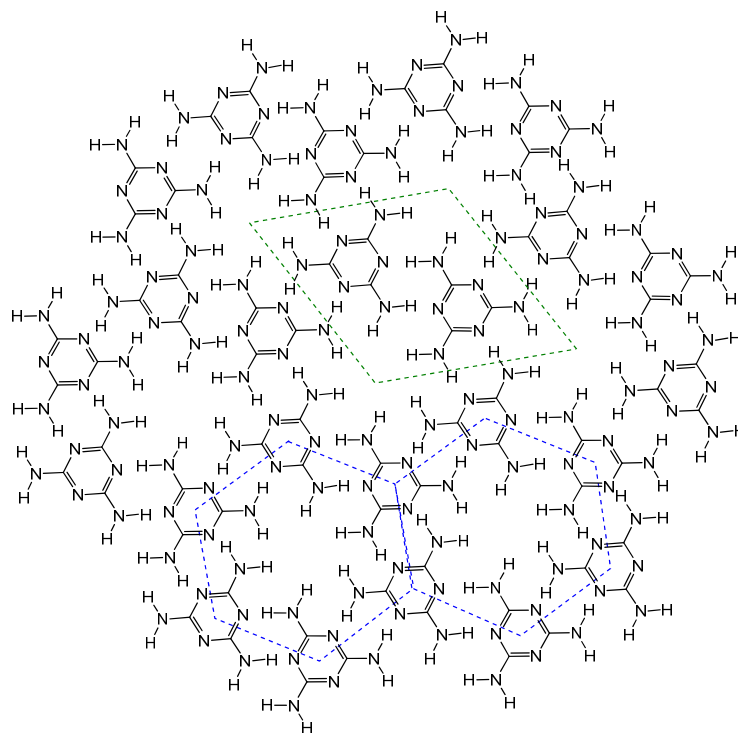


Figure 4.32 Model of the hexagonal arrangement melamine adopts on the Au(111) surface<sup>11,43,46</sup>

#### 4.4.5 Melamine Deposition onto Au(111) Surfaces Modified by 2-D Ni Clusters

With nickel loadings equivalent to 0.2 ML coverage, clusters sized 2-5 nm were observed in the elbows of the herringbone surface reconstruction. The results after the deposition of high and low coverages of melamine on the surface suggest a high reactivity between melamine and nickel.

The STM image of figure 4.33 shows an area of the sample where definite Ni islands appear as bright features in elbow sites but black features, which sometimes lie upon elbow sites, which are thought to represent Ni also exist. Between the rows of elbow sites, melamine forms close-packed domains which, based on their periodicities, cited in Section 4.4.4, are consistent with the normal hydrogen bonding protocol of melamine. However, unusual stripes and chains of bright features occur frequently within the domain.

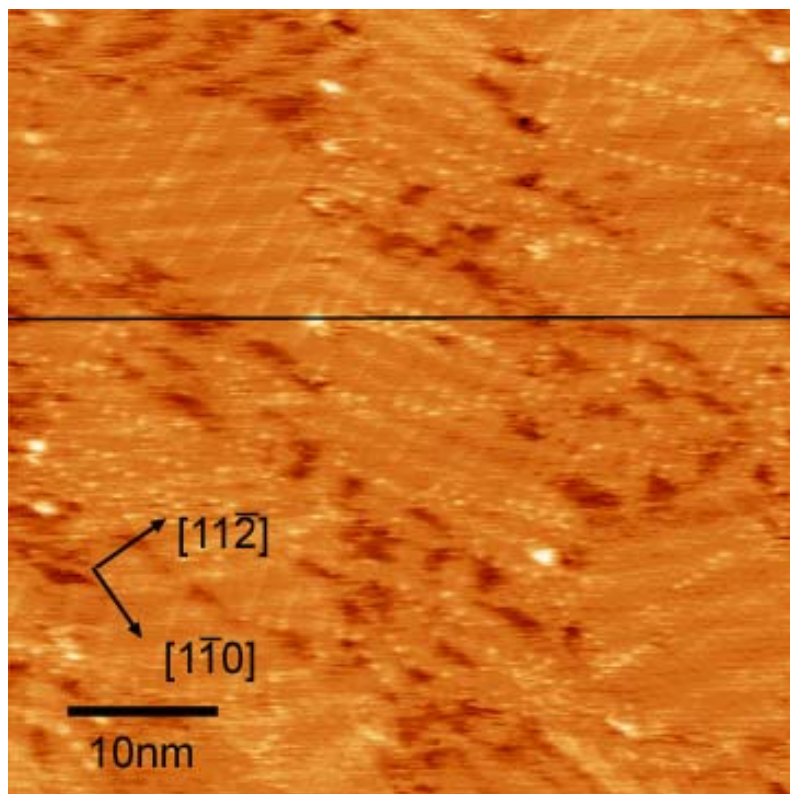


Figure 4.33 STM image of unusual formations after melamine is deposited on 0.1 ML Ni/Au(111) surface at 300 K (52.5 x 52.5 nm, -1.0 V, 1.0 nA)

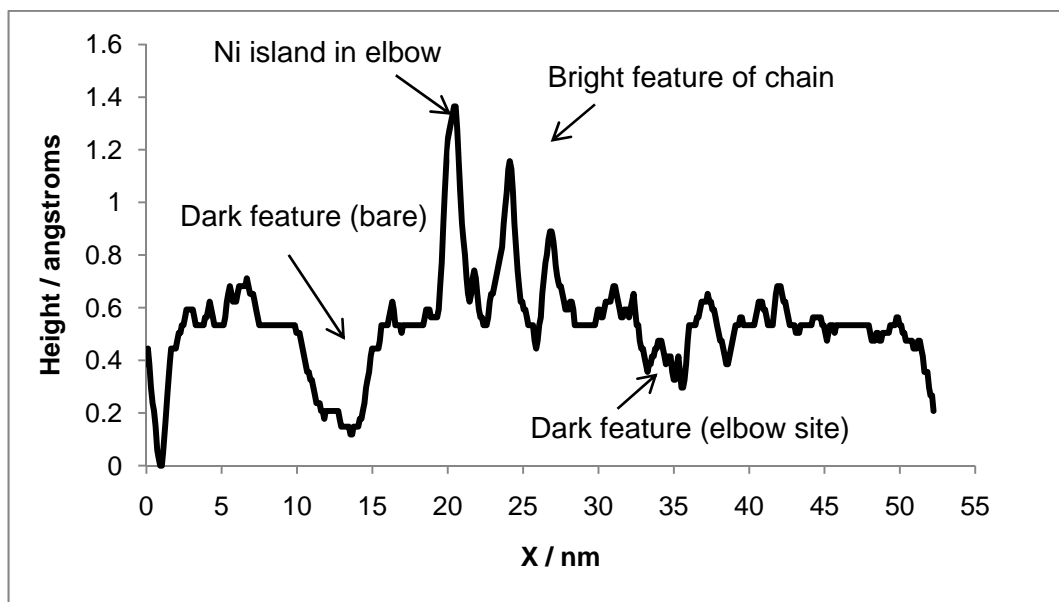


Figure 4.34 Apparent height profile across the line segment indicated in figure 4.33

Figure 4.34 shows the line profile taken across a variety of features in figure 4.33. The intact nickel clusters have the greatest apparent heights and these are almost

matched by the bright features that form part of the chains indicated more clearly by the blue arrows in the zoomed STM image of the area shown in figure 4.35. The dark features above certain elbow sites do not show the same apparent height as areas thought to indicate clean Au surface. Ergo it might be suggested that the dark areas above elbow represent areas of mobile Ni atoms, perhaps after the Ni clusters are broken up by the leaching actions of melamine, only a few mobile atoms remain in these areas; in the STM images of a study of Cu deposition into oligopyridine networks on HOPG carried by Breitruck et al<sup>47</sup>, dark areas were assigned as containing mobile Cu adatoms, an analogous effect might be observed above.

The zoomed STM image is featured in figure 4.35. The stripes (indicated by the green direction, running parallel to the  $[0\bar{1}1]$  direction in this instance), relative to the bulk of the domain, appear as brighter rows accompanied closely by darker ones, and these are usually spaced around 22 Å apart (around 4 molecules), but the spacing is not uniform and the stripes may only result from sources of Ni on the surface – the locations to which Ni has been leached.

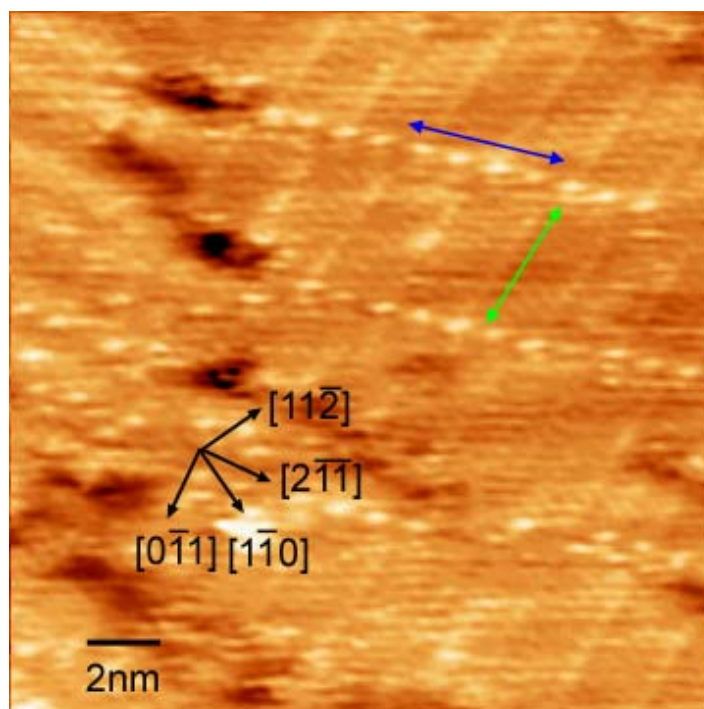


Figure 4.35 Zoomed section of figure 4.33, the features discussed as ‘stripes’ run parallel to the green direction, the bright features referred to as ‘chains’ run parallel to the blue direction (21 nm x 21 nm, -1.0 V, 1.0 nA)

Chains of bright features exist throughout the domain too, indicated by the blue direction running parallel to the  $[2\bar{1}1]$  direction in the figure 4.35. The features in the chains are around 11 Å apart – a distance that corresponds closely with the separation between pores in the normal hydrogen bonding array of melamine. However, they are around 6 Å across – a distance that corresponds closely with the diameter of a melamine molecule. This creates dispute over their identity; they could be deposits of Ni within the pores of the melamine hexagonal array. These bright features may represent melamine molecules that are standing upright<sup>45</sup> in pores due to compression of the melamine domains induced by the presence of nickel. However, reaction with melamine may be more likely given the results shown in figure 4.36. These bright features might also be melamine molecules that interact differently to those around them (potential metal coordination). If these bright features are growths of Ni, and, as discussed, they are comparable in height with Ni deposits in the elbows, then the stripes (green direction) may also be Ni induced features as they seem to always originate from these features. Perhaps the stripes are rows of Ni-coordinated melamine units amongst the normal hydrogen bonding array.

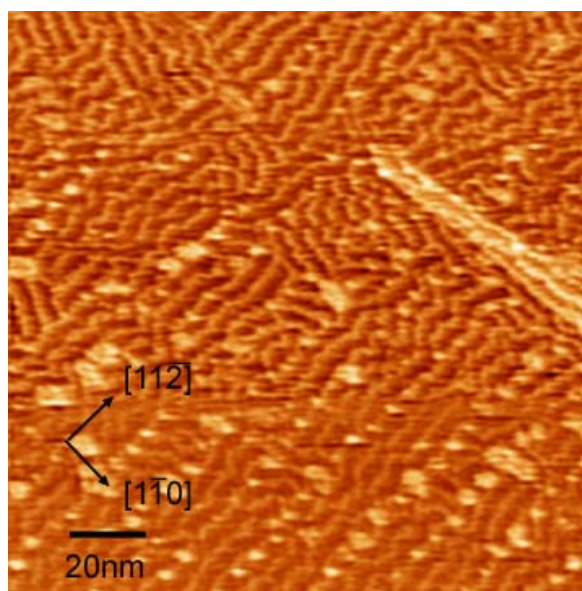
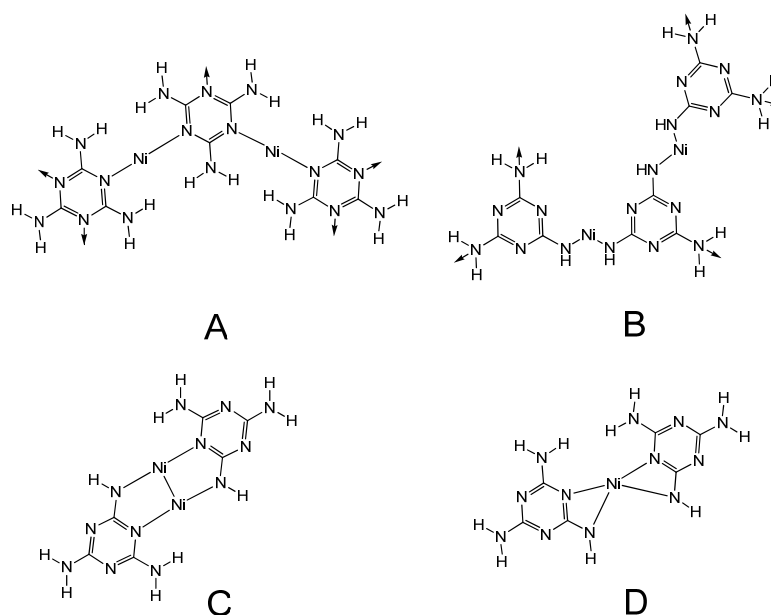


Figure 4.36 STM image of possible Ni-melamine chains on the 0.1 ML Ni/Au(111) surface (153.2 x 153.2 nm, -1.1 V, 0.8 nA)

Evidence of chain formation, at room temperature, can be seen in figure 4.36 where a low coverage of melamine has been deposited on a 0.2 ML Ni/Au(111)

surface. Resolution is not especially good in this STM image. However, it does appear that bright chains of molecules run amongst the typical hydrogen bonding array of melamine. The chains are not straight but the majority run along the  $\langle 11\bar{2} \rangle$  equivalent directions, sometimes they link the nickel islands of the elbow sites.



**Figure 4.37** Potential bonding interactions of melamine with a metal centre: coordination via triazine N, A, via amino N, B, melamine bridging two metal centres, C, and coordination to the same Ni centre via both amino and triazine N of the same molecule

The three-fold symmetry axis of melamine generally means that it does not form straight chains regardless of the bonding interactions between molecules, and given the richness of possibilities for metal coordination, non-linear chains are an unsurprising result (figure 4.37). Although there are countless examples of metal complexes with amino ligands, melamine ligands typically coordinate to metals via the triazine N atom. In the crystal structures of complexes that contain two melamine-based ligands coordinated to the same metal centre via triazine N atoms, these particular ligands are not usually aligned with their aromatic groups in the same plane<sup>48</sup>. Lengthening and subsequent weakening of the M-N bond may be required to maintain the existence of both melamine ligands in the same plane and their interactions with the surface.

Melamine-based ligands have been shown to bridge two metal centres, both the triazine N atom and the adjacent amino N can coordinate to different metal atoms within metal complexes<sup>49</sup>. Similar behaviour cannot be ruled out within the structures observed. This outcome may be more likely in areas of the sample where local Ni concentration is higher.

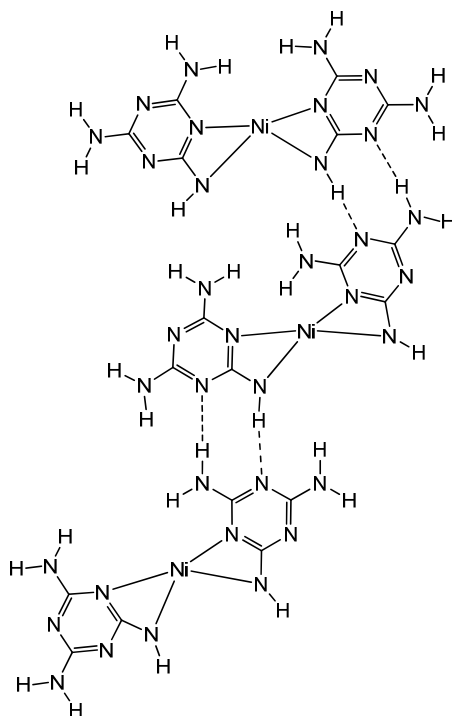


Figure 4.38 Potential case of discrete bis-melamine Ni complexes hydrogen bonding to form a non-linear chain

Melamine-based ligands may also coordinate via their triazine N and amino N to the same metal centre. In the crystal structure of a Cu-melamine analogue<sup>50</sup>, two melamine-type ligands co-ordinate to the metal centre and their aromatic groups lie within the same plane, this may be a result of the other steric bulk of the triazine ring substituents and the other ligands, but the possibility of this bonding may be crucial to the formation of 2-D metal-melamine complexes. The metal-triazine N bond is  $\sim 1.95 \text{ \AA}$  long and the metal-amino N bond is  $\sim 2.4 \text{ \AA}$ , this means that melamine groups should be separated by over  $4 \text{ \AA}$  (hydrogen bonds measure only  $\sim 2 \text{ \AA}$ ). With respect to figure 4.35, the greater distance may be sufficient to create the dark stripes that run next to the bright stripes throughout the domains as it may represent a small misfit channel between melamine molecules whose

orientation and position has been skewed by insertion of metal atoms into the nearby row of molecules.

Discrete molecules are not resolvable in figure 4.36. Brightness from each feature tends to run into the next but it appears as if the widths of the chains, measuring 15-20 Å, are significantly greater than that of a melamine molecule. Thus the situation where a series of discrete metal complexes stabilised into a chain by intermolecular hydrogen bonds, similar to those formed by glutamic acid on Ni/Au(111)<sup>51</sup>, cannot be ruled out (figure 4.38).

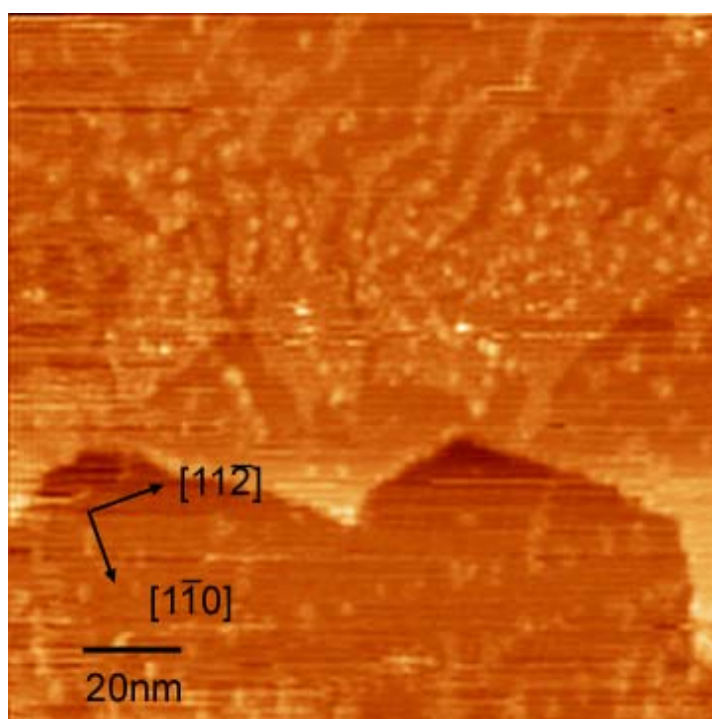


Figure 4.39 STM image of melamine on the 0.1ML Ni/Au(111) surface after annealing to 350K (145.0 x 145.0 nm, 1.5 V, 0.2 nA).

Annealing these surfaces to 350K seems to result in the removal of any melamine that was subject to only hydrogen bonding, these molecules may have been desorbed or have undergone reaction with nickel and become incorporated in the seemingly amorphous mass aggregates that result, this is shown in figure 4.39. Some of the smaller fingers of these growths can be seen to follow the ‘herringbone’ surface reconstruction.

## **4.4.6 Conclusions**

### **4.4.6.1 Interaction of PTCDI and Ni on Au(111)**

On Ni/Au(111) surfaces, the formation of H-bonded PTCDI structures is favoured at low Ni loadings. Larger Ni islands disrupt the ability of PTCDI to diffuse into ordered domains. There is evidence that Ni is able to diffuse from clusters at the elbows of the herringbone reconstruction to produce metal-organic structures even at room temperature. The rate at which this occurs is dependent on the surface coverage of both PTCDI and nickel, both relate to the chance of the two species coming into contact. If the nickel loading is low but the PTCDI coverage is high then metal-organic structures will still result at room temperature, this was observed on the 0.05 ML Ni/Au(111) surface. If the nickel and PTCDI loadings are low, the H-bonding phase will prevail unless the surface is sufficiently annealed.

Several porous structures are identified, though these might only be ordered over relatively small domains. Close-packed domains of PTCDI which, due to the relative orientation of neighbouring molecular species, contain metal atoms or ions are also produced as a result of leaching from the Ni clusters.

At higher annealing temperatures, 1-D molecular chains are formed whose dimensions are such that it is likely that N-Ni-N interactions have been produced via the thermally induced dehydrogenation of the imide functionality.

In the reverse system, where Ni is deposited onto the Au(111) surface bearing PTCDI islands, the nickel adatoms initially ignore the PTCDI islands and tend towards their typical nucleation sites in the herringbone elbows. This may have the effect of splitting the PTCDI domains if the clusters grow large enough. In general, the hydrogen-bonded PTCDI arrangements are more stable in this

system, most likely because vast islands can assemble on the clean Au(111) surface prior to nickel deposition whereas on Ni/Au(111) surfaces, the PTCDI is mixing with the nickel islands as it diffuses around the surface after deposition. No annealing was carried out but after a few days, some of the hydrogen-bonded islands were converted into what are thought to be close-packed Ni-PTCDI assemblies. If annealing was carried out, more disruption of the PTCDI islands might be expected and result in some of the porous or chain formations observed in the reverse system.

#### **4.4.6.2 Interaction of Melamine and Ni on Au(111)**

STM analysis of the interaction of melamine with nickel clusters on the Au(111) surface suggests a high reactivity between melamine and nickel even at room temperature.

The clusters grown in the elbows of the surface reconstruction become heavily corroded by melamine to the extent that some are no longer visible by STM. When a high coverage of melamine is present, nickel is consumed by the interior of the melamine array and changes in the contrast across domains seem to indicate this. Where a low coverage of melamine is present, the surface becomes characterised by metal-organic chains. Annealing, in both situations, results in dense, amorphous islands consisting of melamine coordinated to nickel.

In conclusion, the hydrogen bonding regime of melamine shows low resistance to the presence of nickel and metal-coordination readily becomes the dominant supramolecular interaction controlling the surface assembly of melamine.

#### 4.4.7 References

- (1) Keeling, D. L.; Oxtoby, N. S.; Wilson, C.; Humphry, M. J.; Champness, N. R.; Beton, P. H. *Nano Letters* **2003**, *3*, 9.
- (2) Ma, J.; Rogers, B. L.; Humphry, M. J.; Ring, D. J.; Goretzki, G.; Champness, N. R.; Beton, P. H. *Journal of Physical Chemistry B* **2006**, *110*, 12207.
- (3) Perdigao, L. M. A.; Champness, N. R.; Beton, P. H. *Chemical Communications* **2006**, 538.
- (4) Perdigao, L. M. A.; Fontes, G. N.; Rogers, B. L.; Oxtoby, N. S.; Goretzki, G.; Champness, N. R.; Beton, P. H. *Physical Review B* **2007**, *76*, 6.
- (5) Perdigao, L. M. A.; Saywell, A.; Fontes, G. N.; Staniec, P. A.; Goretzki, G.; Phillips, A. G.; Champness, N. R.; Beton, P. H. *Chemistry-a European Journal* **2008**, *14*, 7600.
- (6) Perdigao, L. M. A.; Staniec, P. A.; Champness, N. R.; Kelly, R. E. A.; Kantorovich, L. N.; Beton, P. H. *Physical Review B* **2006**, *73*, 195423.
- (7) Swarbrick, J. C.; Ma, J.; Theobald, J. A.; Oxtoby, N. S.; O'Shea, J. N.; Champness, N. R.; Beton, P. H. *Journal of Physical Chemistry B* **2005**, *109*, 12167.
- (8) Swarbrick, J. C.; Rogers, B. L.; Champness, N. R.; Beton, P. H. *Journal of Physical Chemistry B* **2006**, *110*, 6110.
- (9) Theobald, J. A.; Oxtoby, N. S.; Champness, N. R.; Beton, P. H.; Dennis, T. J. S. *Langmuir* **2005**, *21*, 2038.
- (10) Theobald, J. A.; Oxtoby, N. S.; Phillips, M. A.; Champness, N. R.; Beton, P. H. *Nature* **2003**, *424*, 1029.
- (11) Perdigao, L. M. A.; Perkins, E. W.; Ma, J.; Staniec, P. A.; Rogers, B. L.; Champness, N. R.; Beton, P. H. *Journal of Physical Chemistry B* **2006**, *110*, 12539.
- (12) Madueno, R.; Raisanen, M. T.; Silien, C.; Buck, M. *Nature* **2008**, *454*, 618.
- (13) Silien, C.; Raisanen, M. T.; Buck, M. *Angewandte Chemie-International Edition* **2009**, *48*, 3349.

- (14) Barth, J. V.; Brune, H.; Ertl, G.; Behm, R. J. *Physical Review B* **1990**, *42*, 9307.
- (15) Zhang, H.-L.; Li, H.-L.; Liu, Z.-F. *Microelectronic Engineering* **2002**, *63*, 381.
- (16) Gao, X. P.; Hamelin, A.; Weaver, M. J. *Journal of Chemical Physics* **1991**, *95*, 6993.
- (17) Stephenson, A. W.; Baddeley, C. J.; Tikhov, M. S.; Lambert, R. M. *Surface Science* **1998**, *398*, 172.
- (18) Chambliss, D. D.; Wilson, R. J.; Chiang, S. *Physical Review Letters* **1991**, *66*, 1721.
- (19) Voigtlander, B.; Meyer, G.; Amer, N. M. *Surface Science* **1991**, *255*, L529.
- (20) Voigtlander, B.; Meyer, G.; Amer, N. M. *Physical Review B* **1991**, *44*, 10354.
- (21) Altman, E. I.; Colton, R. J. *Surface Science* **1994**, *304*, L400.
- (22) Fonin, M.; Dedkov, Y. S.; Rudiger, U.; Guntherodt, G. *Surface Science* **2003**, *529*, L275.
- (23) Bohringer, M.; Morgenstern, K.; Schneider, W. D.; Berndt, R. *Journal of Physics - Condensed Matter* **1999**, *11*, 9871.
- (24) Bohringer, M.; Morgenstern, K.; Schneider, W. D.; Wuhn, M.; Woll, C.; Berndt, R. *Surface Science* **2000**, *444*, 199.
- (25) Yokoyama, T.; Yokoyama, S.; Kamikado, T.; Okuno, Y.; Mashiko, S. *Nature* **2001**, *413*, 619.
- (26) Maksymovych, P.; Dougherty, D. B. *Surface Science* **2008**, *602*, 2017.
- (27) Silly, F.; Shaw, A. Q.; Briggs, G. A. D.; Castell, M. R. *Applied Physics Letters* **2008**, *92*, 023102.
- (28) Clair, S.; Pons, W.; Brune, H.; Kern, K.; Barth, J. V. *Angewandte Chemie-International Edition* **2005**, *44*, 7294.
- (29) Clair, S.; Pons, S.; Fabris, S.; Baroni, S.; Brune, H.; Kern, K.; Barth, J. V. *Journal of Physical Chemistry B* **2006**, *110*, 5627.
- (30) Trant, A. G.; Jones, T. E.; Baddeley, C. J. *Journal of Physical Chemistry C* **2007**, *111*, 10534.
- (31) Zhang, Y. F.; Zhu, N.; Komeda, T. *Journal of Physical Chemistry C* **2007**, *111*, 16946.

- (32) Mendez, J.; Caillard, R.; Otero, G.; Nicoara, N.; Martin-Gago, J. A. *Advanced Materials* **2006**, *18*, 2048.
- (33) Stepanow, S.; Lingenfelder, M.; Dmitriev, A.; Spillmann, H.; Delvigne, E.; Lin, N.; Deng, X. B.; Cai, C. Z.; Barth, J. V.; Kern, K. *Nature Materials* **2004**, *3*, 229.
- (34) Theobald, J. A.; Oxtoby, N. S.; Phillips, M. A.; Champness, N. R.; Beton, P. H. *Nature* **2003**, *424*, 1029.
- (35) Mendez, J.; Caillard, R.; Otero, G.; Nicoara, N.; Martin-Gago, J. A. *Advanced Materials* **2006**, *18*, 2048.
- (36) Stone, M. E.; Robertson, B. E.; Stanley, E. *Journal of the Chemical Society a -Inorganic Physical Theoretical* **1971**, 3632.
- (37) Hay, R. W.; Albedyhl, S.; Lightfoot, P. *Transition Metal Chemistry* **1998**, *23*, 257.
- (38) Tye, J. W.; Weng, Z.; Johns, A. M.; Incarvito, C. D.; Hartwig, J. F. *J Am Chem Soc* **2008**, *130*, 9971.
- (39) Shimizu, N.; Uno, T. *Crystal Structure Communications* **1980**, *9*, 223.
- (40) Cumming, H. J.; Hall, D. *Acta Crystallographica Section B-Structural Science* **1976**, *32*, 1281.
- (41) Cullen, W. G.; First, P. N. *Surface Science* **1999**, *420*, 53.
- (42) Perdigao, L. M. A.; Fontes, G. N.; Rogers, B. L.; Oxtoby, N. S.; Goretzki, G.; Champness, N. R.; Beton, P. H. **2008**.
- (43) Silly, F.; Shaw, A. Q.; Castell, M. R.; Briggs, G. A. D.; Mura, M.; Martinsovich, N.; Kantorovich, L. *Journal of Physical Chemistry C* **2008**, *112*, 11476.
- (44) Xu, W.; Dong, M. D.; Gersen, H.; Rauls, E.; Vazquez-Campos, S.; Crego-Calama, M.; Reinhoudt, D. N.; Stensgaard, I.; Laegsgaard, E.; Linderoth, T. R.; Besenbacher, F. *Small* **2007**, *3*, 854.
- (45) Zhang, H. M.; Xie, Z. X.; Long, L. S.; Zhong, H. P.; Zhao, W.; Mao, B. W.; Xu, X.; Zheng, L. S. *Journal of Physical Chemistry C* **2008**, *112*, 4209.
- (46) Staniec, P. A.; Perdigao, L. M. A.; Rogers, B. L.; Champness, N. R.; Beton, P. H. *Journal of Physical Chemistry C* **2007**, *111*, 886.
- (47) Breitruck, A.; Hoster, H. E.; Meier, C.; Ziener, U.; Behm, R. J. *Surface Science* **2007**, *601*, 4200.

- (48) Zhu, H. G.; Yu, Z.; You, X. Z.; Hu, H. M.; Huang, X. Y. *Journal of Chemical Crystallography* **1999**, 29, 239.
- (49) Dorta, R.; Stoeckli-Evans, H.; Bodensieck, U.; Suss-Fink, G. *Journal of Organometallic Chemistry* **1998**, 553, 307.
- (50) Macias, B.; Villa, M. V.; Sanz, F.; Borrás, J.; Gonzalez-Alvarez, M.; Alzuet, G. *Journal of Inorganic Biochemistry* **2005**, 99, 1441.
- (51) Trant, A. G.; Jones, T. E.; Baddeley, C. J. *Journal of Physical Chemistry C* **2007**, 111, 10534.

## 5 PTCDI and Melamine Bicomponent Network on Au(111)

The PTCDI-melamine hydrogen bonding hexagonal network has been shown, in UHV, to control the spatial distribution of fullerenes<sup>1,2</sup> and decanethiol<sup>3</sup>, whilst in ambient solution-based experiments, the networks have been used to direct the underpotential deposition (UPD) of copper after the capture a range of different thiols and use of electrodeposition techniques<sup>4-6</sup>. The ability of 2-D nanostructures to capture and control growth of metal species may add further desirable properties to the surface architecture, for example, by changing its magnetic properties, by adding catalytic sites or by adding ordered anchor points to which further guest species can be coordinated.

STM and TPD will be used to examine the thermal stability of the components of the hydrogen bonding network on Au(111). Although PTCDI and melamine have been shown to be susceptible to metal-organic interactions, their combined robustness towards nickel requires examination in order to assess the usefulness of this system for further applications. Of course, in attempting to control the distribution of nickel, networks are in competition against the well-established growth pattern for nickel, which, as discussed, initiates from nucleation sites in the elbows of the herringbone surface reconstruction<sup>7</sup>.

Figure 5.1 illustrates two potentially attractive outcomes from nickel deposition onto PTCDI-melamine networks on the Au(111) surface. The first route parallels the observed behaviour of C<sub>60</sub> fullerenes upon the Au(111) surface bearing porous networks<sup>1</sup> where the network acts as a diffusion barrier and clusters of the new adsorbate build up in each network pore. Such an outcome might offer opportunities for the manufacture of new heterogeneous catalysts. Catalysis of reactions is known to take place on an atomic scale and the production of ordered arrays of nickel nanoparticles might prove useful. The ability to further customise these nanoparticles through the coordination of guest species or shape them via the use of PTCDI derivatives in the network is also an attractive downstream step.

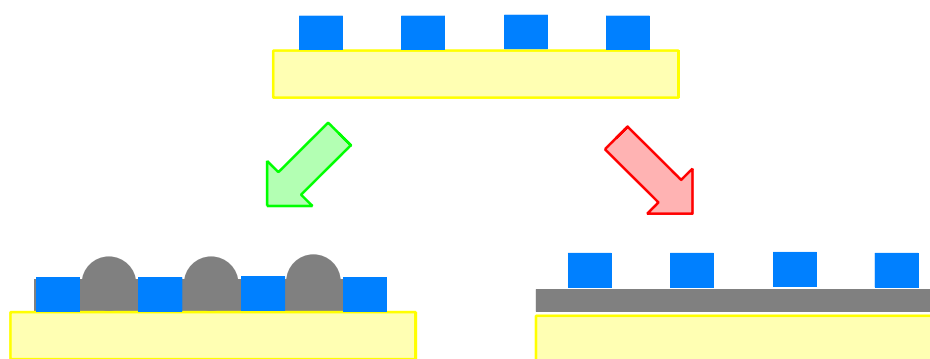


Figure 5.1 Schematic showing potential nickel growth scenarios on the Au(111) surface bearing the PTCDI-melamine network (pore walls are shown as blue): the network may control the distribution of nickel atoms (grey) allowing for the growth of an ordered array of clusters (green route) or nickel may pass through the molecular layer and form a new metal surface overlayer (grey) which allows the network to exist (red route).

There is already evidence to suggest that the second outcome is a strong possibility. It has already been shown that, after the deposition of nickel onto Au(111) bearing PTCDI (Section 4.4.3), nickel can eventually lie underneath the molecular layer. Such an outcome may circumvent the problem of the inability to create PTCDI-melamine networks on Ni(111), the difference being that the nickel surface layer is applied after the molecular modifier.

### 5.1 Self-assembled Organic Monolayers Hosting Metal Adatoms

There are relatively few reports of molecular species being used as templates for metal nucleation and it is apparent that the motivation for most studies where metal is deposited after the deposition of organic species is the formation of metal organic frameworks rather than creating host-guest relationships. For example, iron was evaporated onto the surface after deposition of phenyl dicarboxylate compounds by the group of Barth and Kern in the construction of rectangular frameworks on Cu(100)<sup>8</sup>, whilst manganese could be deposited before, after or co-deposited with biphenyl dicarboxylate compounds to form square and rectangular frameworks on Au(111)<sup>9</sup>.

Arrays of porphyrin and phthalocyanine species upon surfaces have been directly metallated via vapour deposition of a range of metals including Fe<sup>10</sup>, Zn<sup>11</sup> and Co<sup>12</sup>. In the STM images attained, metal deposition into ordered porphyrin monolayers is often characterised by the appearance of bright features in the central pore of the molecules. The mechanism of formation of metalloporphyrins is thought to involve the initial capture of neutral metal adatoms by nitrogen atoms of the porphyrin pore walls, before oxidation of the metal and evolution of hydrogen from the molecular moiety.

Breitruck et al<sup>13</sup> studied the deposition of Cu into a porous 2-D oligopyridine network that had been prepared upon HOPG. They found that, after annealing to 200°C, the 2-D network was transformed into a new structure which they proposed must be a metal-organic framework that incorporates Cu atoms. This result is perhaps unsurprising given the annealing temperature and that the original structure was only based upon weak C-H...N interactions at junctions between molecules.

Schiffirin et al<sup>14</sup> showed organic molecules can be used to influence order in metal adatoms. They observed 1-D atomic strings when Co was deposited on Ag(111) where 1-D ‘nanogratings’ had previously formed via self-assembly of either enantiomer of methionine. The order achieved is remarkable but the experiment was carried out at 18 K using molecular species that show greater interaction with the substrate than PTCDI and melamine exhibit upon Au(111). The presence of zwitterionic molecules is another of the significant differences between the methionine nanogratings and the PTCDI-melamine supramolecular network.

## **5.2 PTCDI-Melamine Hydrogen Bonding Network on Au(111)**

Construction of the hexagonal PTCDI-melamine network on Au(111) was reported in UHV after annealing the surface bearing co-deposited PTCDI and melamine in the 323-353 K range<sup>1</sup>. As on the Ag-Si(111)- $\sqrt{3}\times\sqrt{3}R30^\circ$  surface<sup>15</sup>,

the networks are capable of hosting seven C<sub>60</sub> fullerenes. Further study showed that the herringbone surface reconstruction could have an influence on the integrity of the hexagonal network. In networks created after annealing the surface bearing PTCDI and melamine at 353 K for 15 hours<sup>16</sup>, rows of defect parallelogram pores are seen to follow the ridges of the herringbone surface reconstruction. These defect pores are formed at the intersection of two regions of perfect hexagonal network. They were discussed in the earlier publication<sup>1</sup>, where they were shown to contain only two C<sub>60</sub> fullerenes, although no correlation with the surface was remarked upon.

A porous parallelogram network of PTCDI and melamine has also been reported<sup>17</sup>, the network possesses the same 3:2 PTCDI:melamine stoichiometry as the hexagonal network and it is formed by rearrangement of its network components above 363 K. The parallelogram network pores are shown to be capable of holding two C<sub>60</sub> fullerenes each.

Two separate mixed phases that are precursors in porous network formation are also discussed. The mixed phase reported by Perdigão et al<sup>1</sup> occurs after annealing at 323 K, it consists of small melamine islands with PTCDI adsorbed around their edges such that they bridge neighbouring islands. The PTCDI-melamine interactions are again stabilised by three hydrogen bonds. The other mixed phase reported by Saywell et al<sup>18</sup> is more ordered, it features PTCDI:melamine in, typically, 2:1 stoichiometry and consists of barrier columns of PTCDI interspersed between regions of melamine. There are two most common versions: one where each melamine molecule interacts with two other melamine molecules and a PTCDI barrier molecule via hydrogen bonding and a second version that stores twice the quantity of melamine between PTCDI barriers, this allows the formation of complete melamine hexagons. It has been observed that these structures can extend to barriers between regions of melamine that can be of more than 20 PTCDI molecules side-by-side<sup>18</sup>.

Silly et al<sup>19</sup> report a ‘chiral pinwheel’ mixed phase, although it is not clear if this is a precursor to network formation. This phase has a 3:4 PTCDI:melamine ratio, hexagonal arrangements of six melamine molecules are separated by side-by-side PTCDI pairs. Further isolated melamine molecules link PTCDI pairs that bound adjacent melamine hexagons.

### 5.3 Experimental

TPD experiments were carried out in Chamber 1, a PSP Vacuum Technologies UHV system with a base pressure of  $1 \times 10^{-10}$  mbar; the system is described in Section 2.1. The Au(111) sample was prepared by cycles of argon ion bombardment (1 kV) and annealing to 873 K until a sharp (1x1) LEED pattern and no surface impurities were detected by Auger electron spectroscopy (AES). Clean samples were allowed to cool to room temperature before exposure to the species being examined. PTCDI and melamine were sublimed into Chamber 1 from dosers, also described in Section 2.1, after heating to 638 K and 363 K. After exposure, the pressure is allowed to return to base level before carrying out the temperature-programmed desorption experiment. In some cases, the sample is annealed prior to performing the experiment, this allows for the adsorbate layer to become more ordered. When this step is taken, the sample is allowed to cool to room temperature before proceeding. The temperature-programmed desorption experiment is carried out by positioning the sample in close proximity to the quadrupole mass spectrometer. The sample is heated at  $4 \text{ K s}^{-1}$  through heating wires that are used to mount the sample onto the manipulator. The mass spectrometer is used to measure desorbed species throughout the duration of the temperature ramp. The characteristic mass fragment  $m/z = 69$  is used to monitor PTCDI, whilst fragments  $m/z = 43, 68, 83, 85$  and the molecular ion  $m/z = 126$  can be used to monitor melamine. The choice of which of these fragments to use in this study is limited by the  $m/z$  range of the mass spectrometer and its sensitivity; the molecular ion for PTCDI ( $m/z = 390$ ) lies outside the range of detectable  $m/z$  hence  $m/z = 69$  is used, whereas  $m/z = 43$  lies within the most sensitive  $m/z$  range for this instrument and is used, the other characteristic

melamine fragments are used to establish whether molecular desorption occurs or if the molecule dissociates before desorption.

STM experiments were carried out in an Omicron UHV system with a base pressure of  $1 \times 10^{-10}$  mbar. The system consists of three linked chambers: a preparation chamber with facilities for argon ion sputtering, AES and LEED and dosing and two analysis chambers for reflection absorption infrared spectroscopy (RAIRS) and STM. Sample cleaning and dosing of PTCDI and melamine is carried out as in the TPD experiments in the preparation chamber before images of the surface were acquired by transferring under UHV conditions to the STM chamber where data were taken in constant current mode using an electrochemically etched W tip. All STM images were acquired at room temperature. STM images were processed using WSxM software<sup>20</sup>.

## 5.4 Results and Discussion

### 5.4.1 TPD of PTCDI from Au(111)

The initial spectra obtained from temperature-programmed desorption experiments of PTCDI on Au(111) consist of broad peaks over large temperature ranges (figure 5.2). Spectra are acquired by monitoring the occurrence of the  $m/z = 69$  fragment ion throughout the temperature ramp. After the TPD experiments, Auger spectroscopy analysis indicates a clean Au surface.

The amplitude and position of  $T_{max}$  appears unrelated to the PTCDI exposures. The desorption spectra acquired after the 100 L dose is the largest in amplitude, but the spectra acquired after lower exposures do not reliably fit into this trend. The lack of consistency in dosing levels from solid dosers has been discussed earlier in Section 3.3.1.1. Repeated experiments incorporating a pre-annealing treatment before conducting the TPD experiment were used to obtain more uniform spectra. The results are shown in figure 5.3. In the pre-annealing

treatment, the surface is annealed to a temperature much lower than  $T_{max}$  before being allowed to cool to room temperature prior to carrying out the standard TPD experiment.

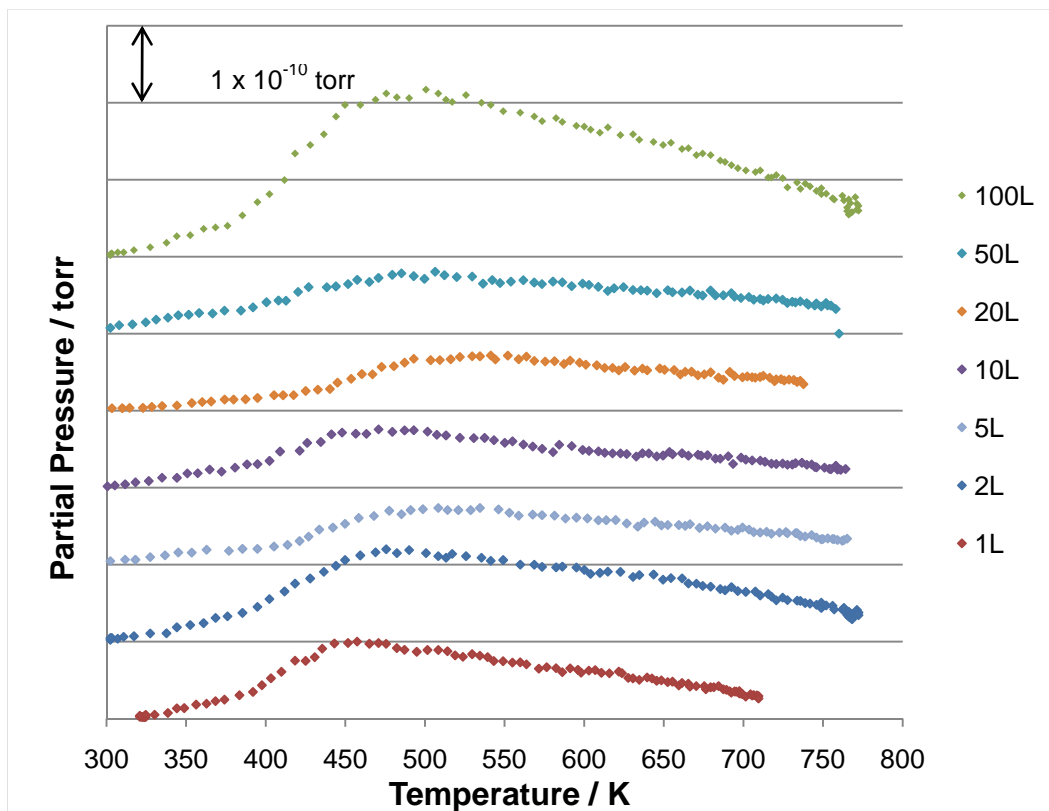
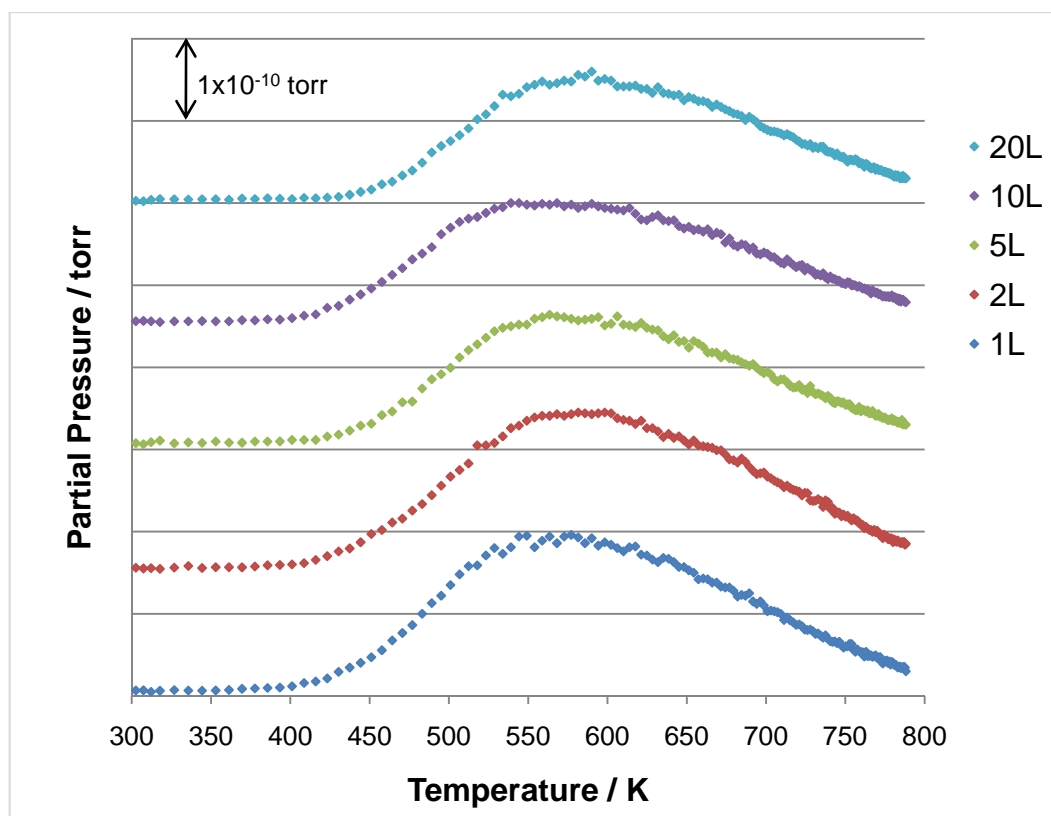


Figure 5.2 TPD of PTCDI from Au(111) for a range of PTCDI initial exposures to the Au(111) surface held at room temperature. Desorption spectra are acquired by monitoring the  $m/z=69$  fragment ion.

As the pre-annealing treatment of annealing the PTCDI-bearing Au(111) sample to  $\sim 373$  K and holding at temperature for 5 minutes, results in spectra of peaks that are similar in width, amplitude and position, it must be producing ordered, monolayer arrangements on the surface prior to the TPD experiments.

TPD experiments usually result in sharp peaks over short temperature ranges, however, the peaks in the PTCDI TPD experiments sprawl over the range 400 K to 800 K. The  $T_{max}$  occurs as a plateau ranging from 550 K to 600 K and the decay of these peaks is almost linear. Similar to the TPD experiments of PTCDI on Ni(111), the  $T_{max}$  range is below the temperature required to sublime PTCDI onto the surface. By STM, doses typically around 10 L in Chamber 2 were used to

achieve 1 ML coverage. Multilayer formation was rarely observed. Complete formation of a monolayer must take place before multilayers occur. The upper limit of the  $T_{max}$  incorporates the desorption temperature of 600 K reported by Mura et al<sup>21</sup>. Factors such as extensive supramolecular interactions, pumping speed (the removal of PTCDI from the vacuum chamber) or rate of detection of PTCDI may be significant in the shape of the desorption spectra obtained (as discussed on as Chapter 3).



**Figure 5.3** TPD of PTCDI from Au(111) after pre-annealing treatments. Initial PTCDI exposure occurs at room temperature. Samples are heated to 373 K and allowed to cool to room temperature before performing the TPD experiment. Desorption spectra acquiring after monitoring  $m/z=69$  ion.

The TPD of perylene, which can be considered a non-hydrogen bonding analogue of PTCDI, yields sharp peaks, for the standard and pre-annealed experiments, in the range 345 K to 355 K. An estimated  $E_d$  of  $84.3 \text{ kJ mol}^{-1}$  is obtained by using the value of 352.2 K as  $T_{max}$  in the Redhead equation where  $1 \times 10^{12} \text{ s}^{-1}$  is used as the pre-exponential factor.

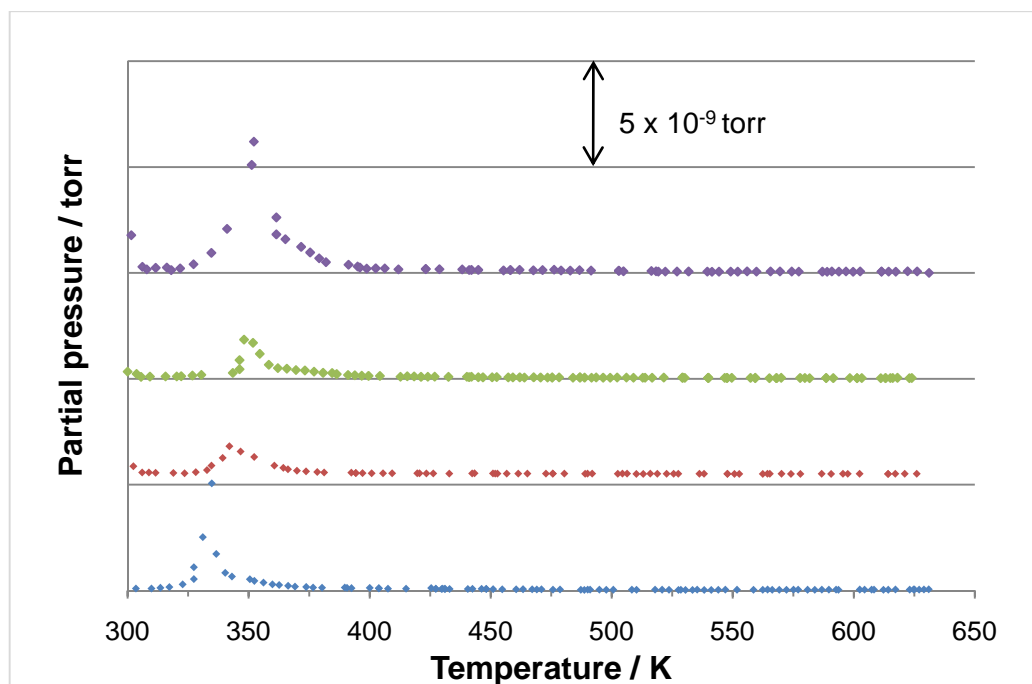


Figure 5.4 TPD of perylene from Au(111) using two exposure levels. Initial perylene exposures are performed at room temperature. The top, purple, spectrum was acquired after a 20 L exposure. The green spectrum was acquired after administering a 20 L exposure then carrying out a pre-annealing treatment of flashing the sample to 313 K. The red spectrum was acquired after a 10 L exposure. The blue spectrum was acquired after a 10 L exposure and the pre-annealing treatment. The sample is allowed to return to room temperature before beginning TPD experiments. The molecular ion  $m/z=253$  is monitored to acquire desorption spectra.

The heating applied to the sample is shown in figure 5.5; the temperature gradient is close to linear until higher temperatures are achieved. Above 600 K, the rate of sample temperature increase gradually decreases.

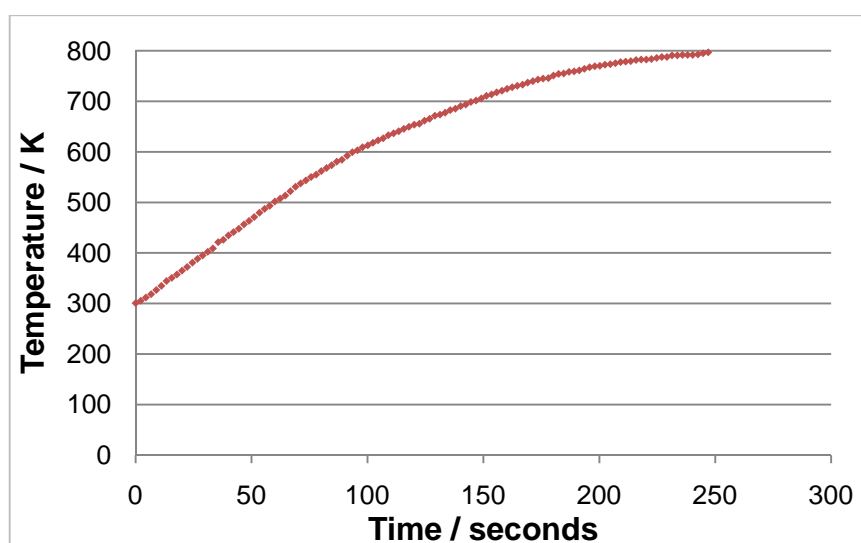


Figure 5.5 Au(111) sample heating curve, the equation  $T = 278.4 + 3.74t - 0.00609t^2$  was found to be the best fit for this curve using a spreadsheet programme

A spreadsheet can be used in an attempt to simulate the desorption spectrum of PTCDI from Au(111) in much the same way as discussed in Section 3.3.1.1 using equations 3.2 and 3.3 for TPD experiments from Ni(111). A number of molecules on the surface at a given temperature,  $N_T$ , and the number of molecules desorbed at a given temperature,  $N_d$ , can be represented as:

$$N_d = \gamma N_T \exp\left(-\frac{E_d}{RT}\right) \quad \text{Equation (3.2)}$$

Simple subtraction takes into account the number of molecules lost over a temperature increment:

$$N_T = N_{T-1} - N_d \quad \text{Equation (3.3)}$$

A desorption spectrum can be generated by plotting the number of molecules desorbed with temperature,  $N_d$ , versus  $T$ , if values are inputted for  $\gamma$  and  $E_d$  and a large stock of molecules are inputted as being present at the beginning of the heating ramp,  $N_T$  at  $T = 300$  K (room temperature, when heating ramp is started).

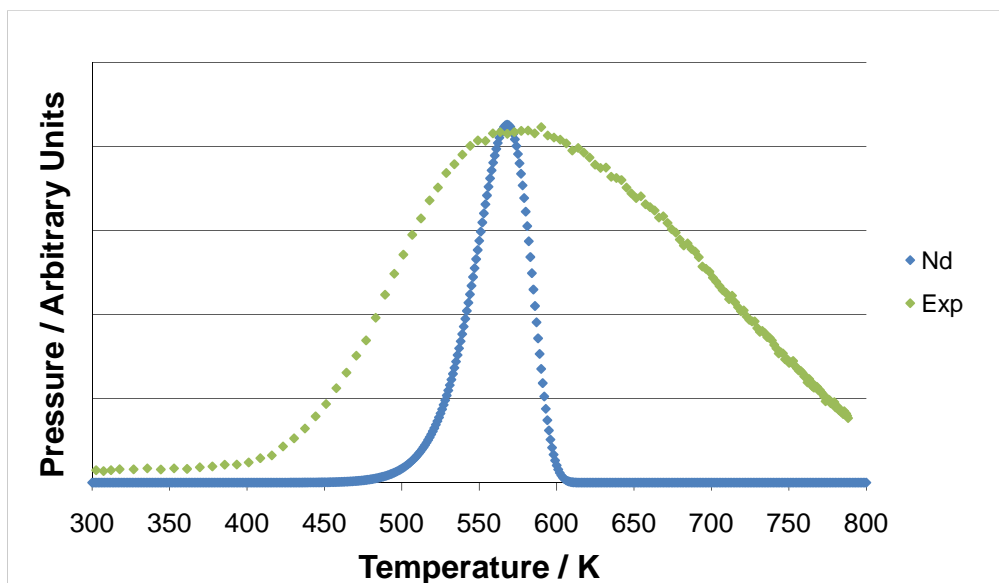


Figure 5.6 Comparison of the experimentally obtained TPD spectrum (green) with a simulated spectrum where  $N_d$  is plotted versus temperature (blue). A value of  $144.3 \text{ kJ mol}^{-1}$  is used to match align the peaks of the experimental and the simulated TPD spectra. The experimental desorption spectrum is the sum of all five spectra shown in figure 5.3.

The position of the peak in desorption intensity can be altered and optimised to match the position in the experimental spectrum by varying the value of  $E_d$  in

equation 3.2. A value of  $144.3 \text{ kJ mol}^{-1}$  is used in figure 5.6 to align the maximum in the simulated desorption spectrum with that of the experimental result. Although the peak positions can be matched using this simple method, the peak shapes are vastly different and, as alluded to in the Chapter 3, the removal of PTCDI from the chamber by pumping, a lag in detection by the sensor or supramolecular interactions may be responsible for the broad peak shapes observed.

As before, the PTCDI pumping speed plot (Section 3, figure 3.3) and the Au(111) sample heating rate plot (figure 5.5) are used to incorporate environmental factors (processes related to the experimental apparatus such as sample heating, chamber pumping) into the simulation of the TPD results obtained and as figure 5.7 shows, the nature of decay from  $T_{max}$  in the spectrum can be replicated quite well. However, a mismatch in the overall spectra suggests that other processes, most likely related to the behaviour of the molecules on the sample itself during the TPD experiment need to be considered.

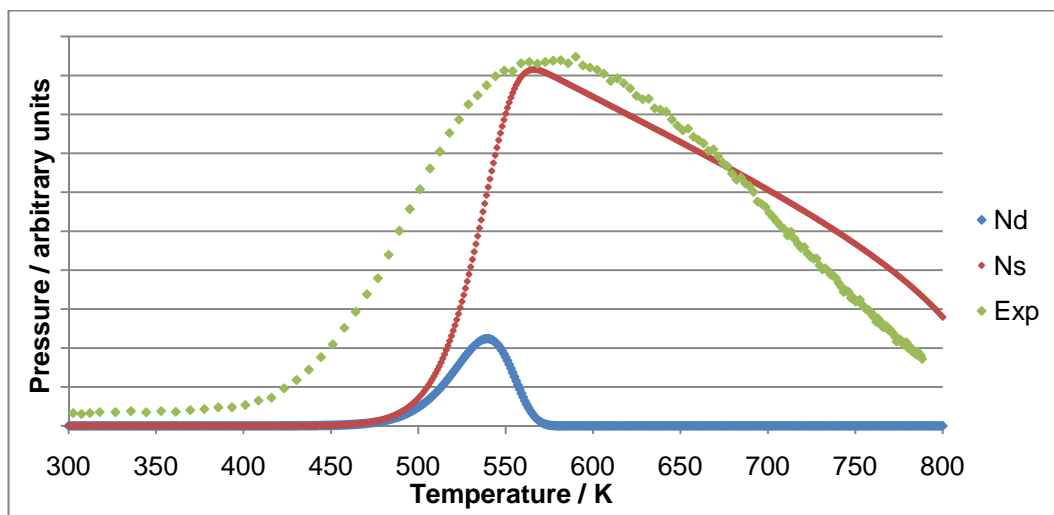


Figure 5.7 The red curve incorporates the lag generated in PTCDI detection/removal from chamber into a simulated TPD spectrum (red), this is compared with the simulated TPD based only on  $N_d$  (blue) and the experimental result (green). The experimentally obtained spectrum is the sum of all five spectra shown in figure 5.3.

The observed desorption spectrum peak has a very broad maximum plateau which suggests that more than one desorption site and the generation of overlapping

peaks; as before, equation 3.4 which describes the total number of molecules desorbing from the surface,  $N_D$ , during each temperature increment as a sum of the number of molecules desorbing,  $N_d$ , from each site is used.

$$N_D = \sum_{site\ 1}^{site\ n} N_d \quad \text{Equation (3.4)}$$

The situation involving PTCDI on Au(111) is more complex, not only because the map of PTCDI configuration (figure 5.9) has many sites, but because the molecules rapidly change between those states, thus the task of modelling the desorption can be seen as merging the peaks of multiple desorption states.

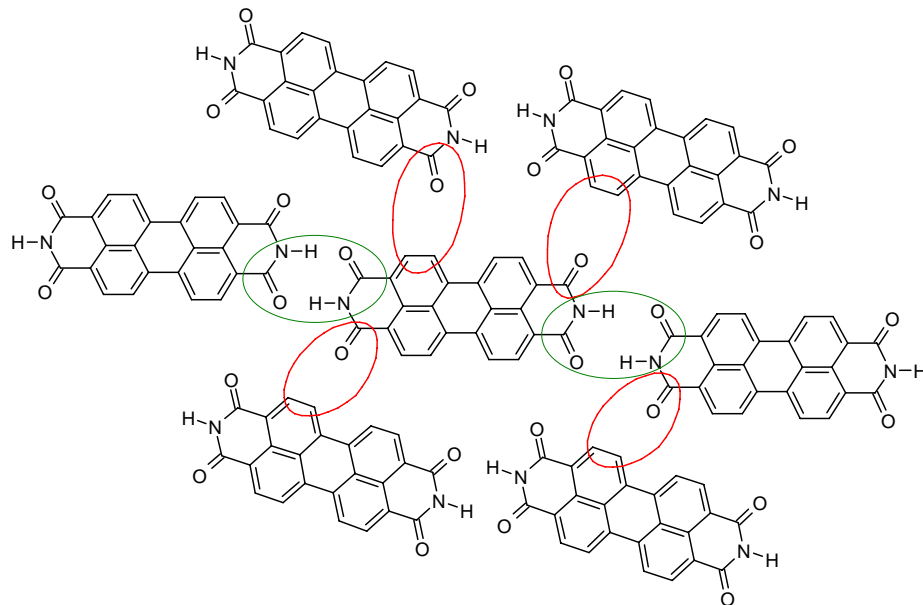


Figure 5.8 PTCDI configuration on the surface showing the two different types of supramolecular interaction,  $S_1$  is shown as green,  $S_2$  as red

Using a method suggested by Sales and Zgrablich<sup>22</sup>, the supramolecular interactions between PTCDI molecules can be defined and used to assign a value for  $E_d$ . Sales and Zgrablich<sup>22</sup> define  $E_d$  of a particular molecule by taking into account the interaction energy with its nearest neighbour and its next nearest neighbour within an island. In equation 5.1, the interactions with neighbouring molecules have been replaced with two different supramolecular interactions:

$$E_d = E_{Au-PTCDI} + xS_1 + yS_2 \quad \text{Equation (5.1)}$$

$E_{Au-PTCDI}$  is the interaction between an isolated PTCDI molecule and the surface,  $S_1$  and  $S_2$  represent the two supramolecular interactions (as shown in figure 5.8),  $x$  and  $y$  are the number of each interaction experienced by a particular molecule.

The monolayer hydrogen bonding array for PTCDI has been observed via STM analysis and as such a molecule within a typical island on the surface can be assigned activation energies of desorption,  $E_d$ , which are a sum of three terms,  $E_{Au-PTCDI}$ ,  $S_1$  and  $S_2$ , where the  $E_{Au-PTCDI}$  accounts for the interaction of an isolated PTCDI molecule with the Au(111) surface. The following two terms refer to supramolecular interactions with neighbouring molecules;  $S_1$  represents the head-to-tail imide-imide hydrogen bonding junction,  $S_2$  represents the side-by-side interactions; these are indicated in figure 5.8. The initial ordered monolayer may exist as one vast island. The map in figure 5.9 shows three states of PTCDI: isolated molecules, 1-D chains and larger islands.

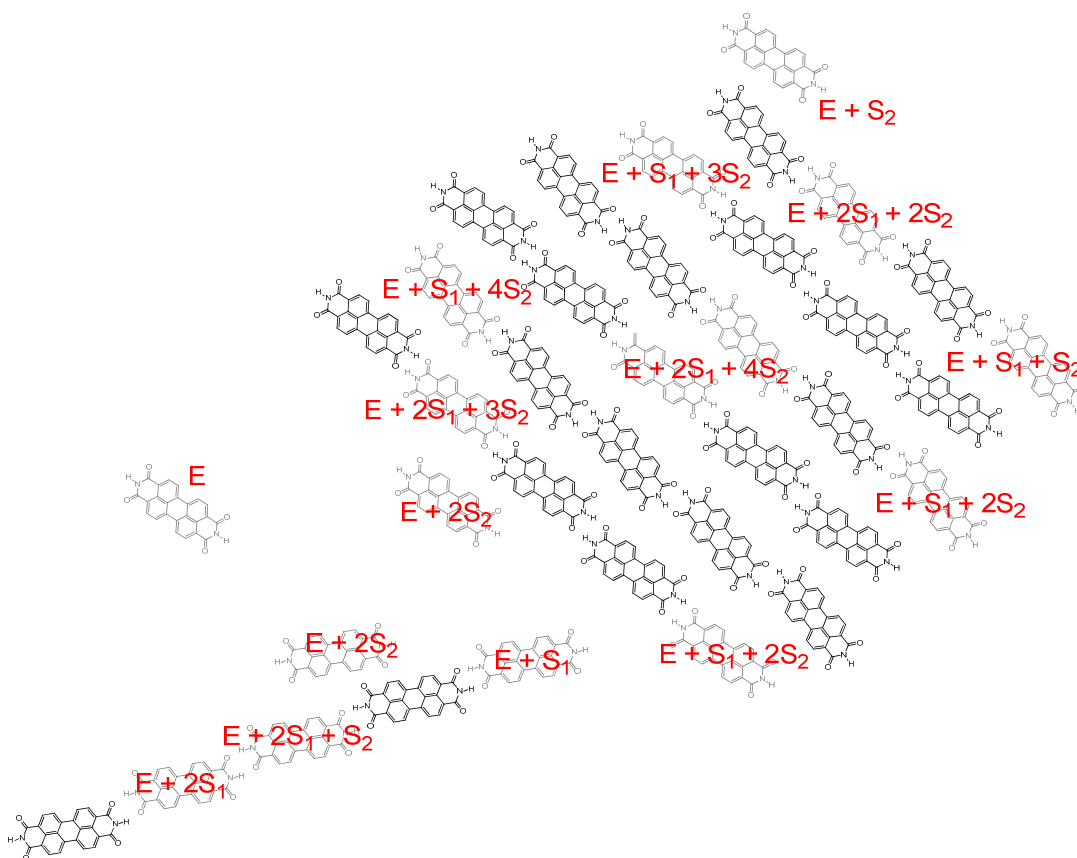


**Figure 5.9** Map of PTCDI upon the surface, examples of each site within large domains, 1-D chains or isolated molecules are labelled,  $E_{Au-PTCDI}$  is shown as E in this diagram

Molecules around the edge of a large island will have a lower value of  $E_d$  than the molecules at the centre of the domain because they are subject to fewer intermolecular interactions. As aforementioned, if two desorption states are considered; notionally, centre molecules and edge molecules, with no transformation between the two, then a peak for each will be generated in simulated spectra. If all the desorption states are introduced, each having their own peak, then some of these will overlap and merge but spectra may still have more than one peak, and fail to match the experimentally observed spectra.

In order to better simulate the real spectra, realistically proportional stocks of molecules are fed into each state; for example, the number of centre molecules is much greater ( $> 2 \times 10^{13}$ ) than the number in each of the edge states ( $< 4 \times 10^{12}$ ). As the temperature is increased, molecules from the edges of domains have a higher probability of desorbing at a given temperature as they have lower  $E_d$ . Equation 3.2 is applied to all sites to calculate the number of molecules that would desorb from each site during each temperature interval,  $N_d$ . These  $N_d$  values are noted and added towards  $N_D$  but the number of edge molecules is held constant and inputted into the calculation for the next  $\Delta T$  increment (i.e. for states other than the centre state,  $N_T = N_{T-1}$ ) because it is assumed that as edge molecules are removed, they are replaced in edge states by molecules that were previously considered centre molecules. Centre molecules are molecules that are subject to a full set of six intermolecular interactions. Those molecules just one layer from the island edges fulfil this specification and are assigned the same label as molecules further inside the domain. In this layer-by-layer desorption of the domain, only the number of centre molecules are allowed to decrease after each  $\Delta T$  increment and this is accounted for by an equation that only applies to the number of centre molecules, which is say, site 1:

$$N_T = N_{T-1} - \sum_{\text{site } 1}^{\text{site } n} N_d \quad \text{Equation (5.2)}$$

Keeping the number of molecules in the edge states (of low  $E_d$ ) constant, a major mathematical hurdle is encountered. As  $T \rightarrow \infty$ ,  $e^{-\frac{E_d}{RT}} \rightarrow 1$ . By equation 3.2, at high T, the number of molecules desorbing,  $N_d$ , may exceed the actual number of molecules present,  $N_T$ , in that site. Unfortunately, this undermines the logic of the layer-by-layer desorption model. To partially negotiate this, the number of molecules in the edge sites is only held constant until 500 K before being allowed to decay normally by equations 3.2 and 3.3. This results in a large spike in the plot based on  $N_d$  in figure 5.10. Ideally, rules governing the transfer of molecules between sites would be incorporated into a more accurate model, and the  $N_d$  would be much smoother representing the more gradual desorption of molecules from large hydrogen bonding arrays which is believed to occur. Rationally, the stocks of molecules in centre sites, should expire before those in the edge sites, thus the number of molecules that each site is initially stocked with and the values of  $E_d$  given to these sites are very important in creating a logical, if simple, spreadsheet model of the TPD results, the resultant spectrum is compared to the experimental result in figure 5.10.

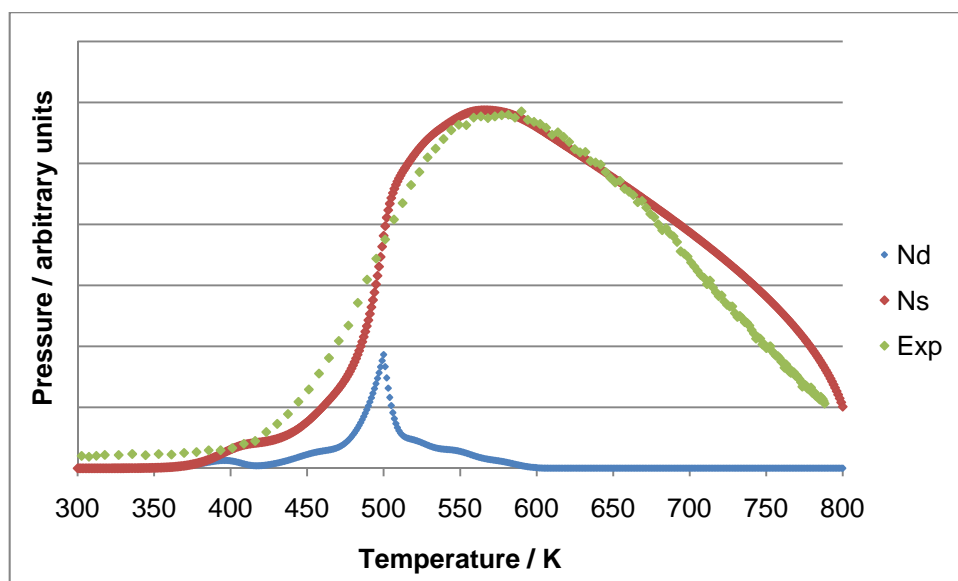


Figure 5.10 Comparison of simulated TPD spectrum that takes into account multiple desorption sites and pumping speed, red, with the experimentally obtained spectrum, green. The experimental spectrum is a sum of the five spectra obtained in figure 5.3

Obviously, the values of the interaction strengths,  $E_{Au-PTCDB}$ ,  $S_1$ , and  $S_2$  that are entered into the spreadsheet simulation are very important. The values used for

the simulation shown in figure 5.10 are  $84.3 \text{ kJ mol}^{-1}$ ,  $30 \text{ kJ mol}^{-1}$  and  $7.5 \text{ kJ mol}^{-1}$  respectively. The estimated  $E_d$  for perylene is used as  $E_{Au-PTCDI}$  as perylene is thought of as an analogue to PTCDI that does not form hydrogen bonds. Calculations<sup>23</sup> have shown that the interaction at an imide-imide junction in the PTCDI domain has strength of  $48.2 \text{ kJ mol}^{-1}$ . This value will consist of the anisotropic attraction, the directional hydrogen bonding at the junction, and the isotropic van der Waals force. A lower value of  $S_I$  has been used in this simulation than the literature value in order to isolate the hydrogen bonding forces; perylene is of a similar size to PTCDI thus will experience comparable van der Waals interactions to PTCDI so this force is built into the value of  $E_d$  for perylene, and subsequently,  $E_{Au-PTCDI}$ .

One of the other problems of simulating TPD spectra in such a way is that the changing shapes of the PTCDI islands is never really accounted for. As aforementioned, the number of edge molecules is held constant, but obviously, as desorption progresses, the islands will decrease in size and their edges may vary in shape. The number of the edge molecules may well remain fairly constant as larger islands break up into several smaller islands. The break-up of larger islands may result in isolated molecules or 1-D chains; 1-D chains are probably fairly well represented at high temperatures by this simulation as they are given a relatively high value of  $E_d$  in the map of PTCDI configurations (figure 5.9) of  $E_{Au-PTCDI} + 2S_I$ . Due to the aforementioned problem of  $e^{-\frac{E_d}{RT}}$  quickly growing towards 1 where  $T$  is high and  $E_d$  low, it is impossible to replicate the existence of loose isolated molecules in this spreadsheet at high  $T$  by feeding in a stock of molecules into sites with suitably low  $E_d$  values.

The initial stocks of molecules in each state can be altered to try to obtain a better fit to the experimental result. PTCDI islands will, in general, be greater in length than width because the head to tail imide-imide hydrogen bonding interaction is stronger than the side-by-side interaction. In figure 5.11, it is schematically shown that molecules along the long edges are of higher  $E_d$  ( $E_d = E_{Au-PTCDI} + 2S_I + 3S_2$ ).

These edge molecules shown in green would first adopt a lower  $E_d$  value because islands would contract in length before width if  $E_d$  is the determining factor. Many more complex rules governing the transfer of molecules between sites should be included in a complete Monte Carlo simulation. Here, only the transfer between centre and edge sites is considered but in the actual desorption process, transfer between edge sites would occur. Conversely, removing an edge molecule may not necessarily result in a centre molecule adopting an edge position.

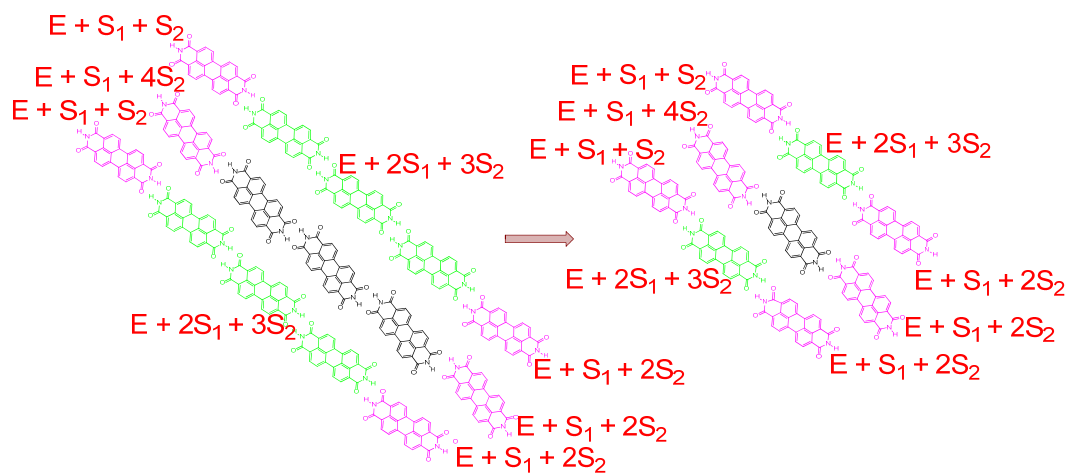


**Figure 5.11** Schematic illustrating how molecules in high  $E_d$  edge sites (green) adopt lower  $E_d$  values. The pink molecules will be removed first, Green edge molecules and black centre molecules replace the desorbed pink molecules. The number of pink edge molecules is held constant.

In this simulation, the number of centre molecules is at least 10 times the number in any of the other sites. This results in the simulation peak being centred over the range 540 K to 590 K. As shown in figure 5.7, the desorption of molecules from a single site with  $E_d$  of  $144.3 \text{ kJ mol}^{-1}$  gives a  $T_{max}$  of 575 K. Similarly, in trying to align the simulated spectrum with the experimental spectrum, values of  $E_d$  ranging  $121.8 \text{ kJ mol}^{-1}$  to  $144.3 \text{ kJ mol}^{-1}$  which correspond to the edge sites,  $E_{Au-PTCDI} + S_1 + 4S_2$ ,  $E_{Au-PTCDI} + S_1 + 3S_2$ ,  $E_{Au-PTCDI} + S_1 + 2S_2$  and  $E_{Au-PTCDI} + S_1 + S_2$ , proved most important for the position of the peak in the TPD spectra. Having a range of sites of similar  $E_d$  is probably one of the main causes of the broad plateau. The rules governing the simulation have been focused upon a layer-by-layer conversion of centre molecules to edge molecules and this has been carried out empirically by holding the number of molecules in each edge site constant and subtracting from the number of centre molecules as desorption progresses, to further improve the simulated spectrum, more complex rules modelling the

conversion of molecules between edge sites may be needed as with the removal of every molecule the  $E_d$  of those in its vicinity changes.

By inputting a large number of adsorption sites of varying desorption activation energies (assigned on the basis of anticipated adsorbate-substrate and intermolecular interactions) and by implementing a few simple rules, these spreadsheet models can be used to obtain a qualitative understanding of the desorption behaviour of PTCDI. From these simulations, and by comparison to the perylene TPD results, it is quite clear that intermolecular hydrogen bonding interactions suggested by STM studies<sup>24,25</sup> are significant to the desorption process. Although it is clear that more sophisticated theoretical calculations would need to be carried out to model the desorption process comprehensively, the semi-empirical approach utilised here, which incorporates simple rules to simulate a layer-by-layer desorption process from molecular islands and calculated hydrogen bonding energies, gives a reasonable fit to the experimental data.

#### 5.4.2 TPD of Melamine from Au(111)

The TPD spectra of melamine from Au(111), measured after the initial deposition, as shown in figure 5.11, are a little disorganised. The spectra shown are based on the  $m/z = 43$  ion, although other characteristic melamine mass fragments generate spectra of matching shape and  $T_{max}$ . Each plot shows a small peak at low temperature, for most exposure levels this occurs below 310 K. The temperatures of maximum desorption,  $T_{max}$ , for all the plots lies within the range 383 K to 422 K, somewhere along the broad main desorption band, and for the majority of the exposure levels,  $T_{max}$  is below 400 K.

Pre-annealing treatments were carried out before standard TPD experiments; the practice of annealing the sample to 313 K then allowing to cool removes the low temperature peak and sharpens the main desorption peak. The  $T_{max}$  position for the 10 L and 20 L exposure levels is at 377 K, whilst slightly lower values are

observed for shorter exposures. Analysis of the surface after TPD experiments by Auger spectroscopy indicated a clean surface. The fragment ion  $m/z = 43$  is used to generate TPD because it gives the strongest response from the mass spectrometer but other the other characteristic melamine fragments and the molecular ion  $m/z = 126$  also generate spectra with matching  $T_{max}$ .

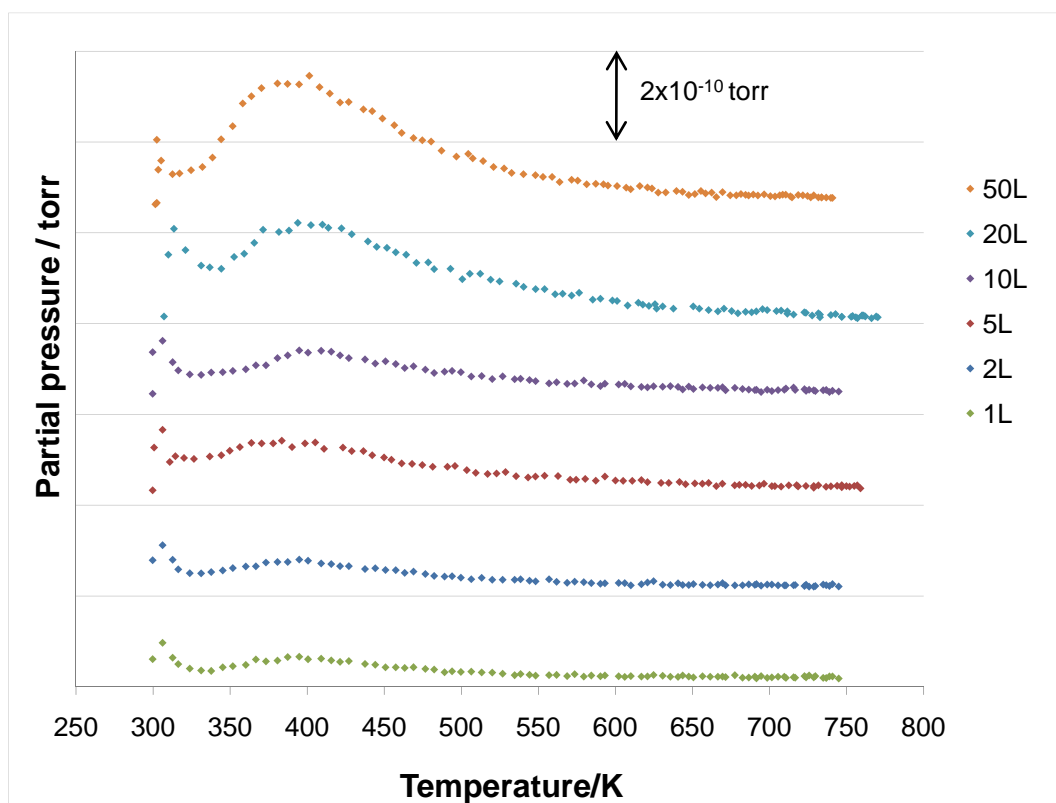


Figure 5.12 TPD spectra of melamine from Au(111) for a range of melamine exposures. Initial melamine exposures were at room temperature. Desorption spectra were acquired after monitoring the  $m/z=43$  fragment

The pre-annealing treatment of flash-annealing melamine-bearing samples to 313 K before TPD experiments has been used before in STM experiment to obtain ordered monolayer structures quicker and demonstrated here it helps to define the TPD spectra. The two spectra obtained after pre-annealing samples exposed to 10 L and 20 L are identical and most likely represent the desorption of ordered monolayer formations close to 1 ML in coverage,  $T_{max}$  of these spectra is 378 K.

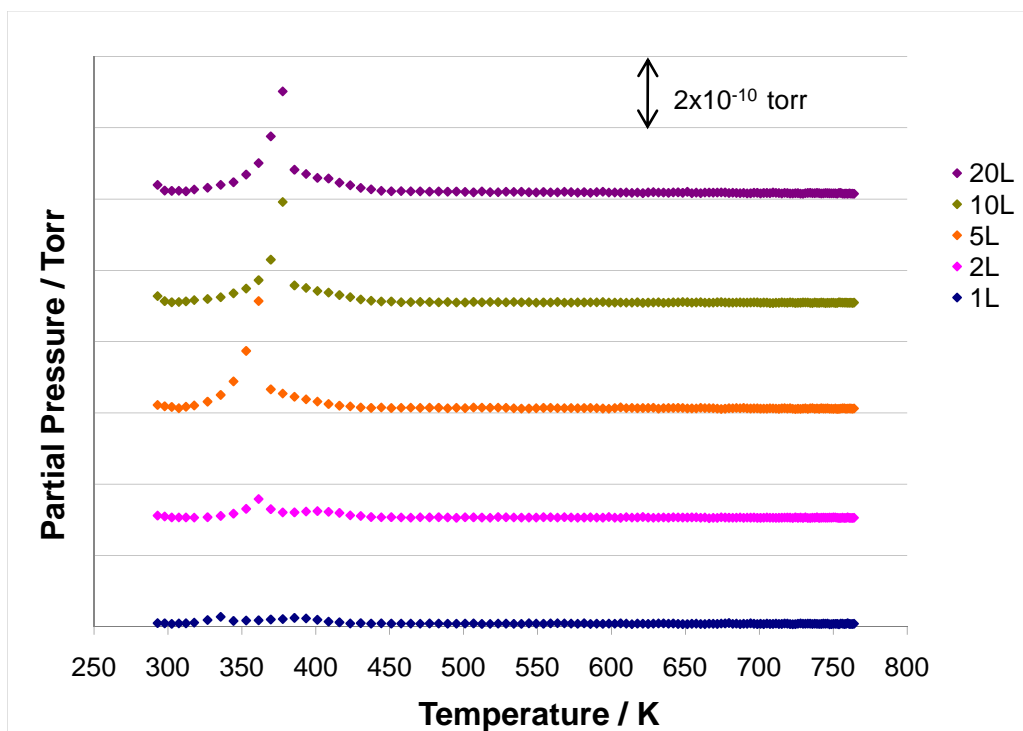
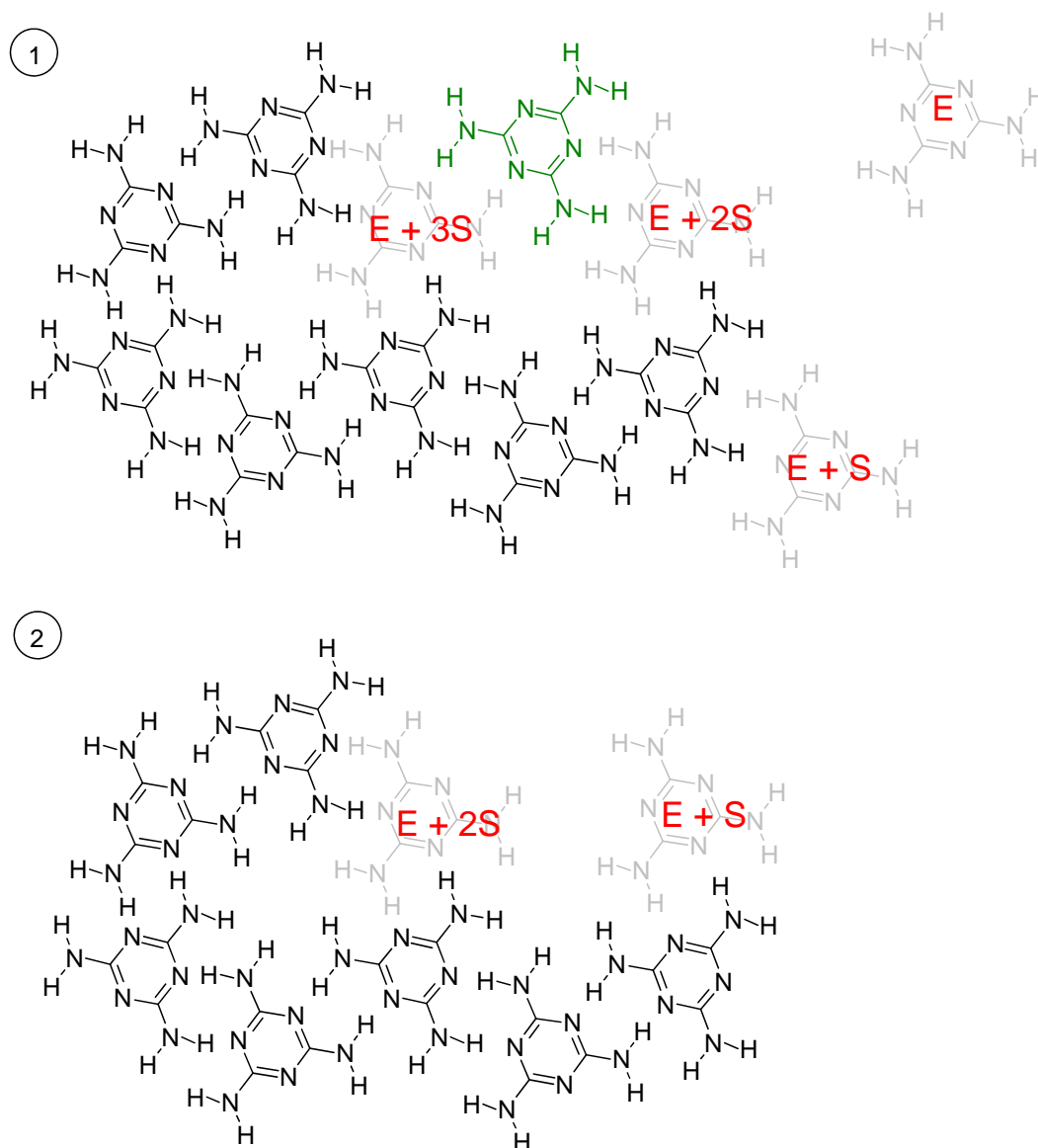


Figure 5.13 TPD spectra of melamine from Au(111) where pre-annealing has been carried out. Initial melamine exposures were at room temperature. Samples were flash annealed to 313 K and allowed to cool before commencing TPD experiments.

Using a similar method as the analysis of PTCDI on Au(111), the surface configuration of melamine is mapped out (figure 5.14). As the anticipated array is porous, only one type of supramolecular interaction need be considered and this melamine-melamine interaction has been calculated<sup>23</sup> as  $43.8 \text{ kJ mol}^{-1}$  ( $0.45 \text{ eV}$ ), thus the molecules in the melamine islands can be described by two terms,  $E_{Au-mel}$ , the  $E_d$  energy of an isolated melamine molecule on the Au(111) surface, and  $S_{mel-mel}$ , the interaction strength between two melamine molecules.

Crudely, the  $E_d$  of an isolated molecule has been assigned as  $3.4 \text{ kJ mol}^{-1}$  by using the terms described in figure 5.14 and estimates obtained by trial values of  $E_d$  in simulated TPD spectra after moving it to align with the experimental result. This estimated value is too low in comparison to the calculated adsorption energy<sup>26</sup> between an isolated melamine molecule and the Au(111) surface of  $17.4 \text{ kJ mol}^{-1}$ .



**Figure 5.14** Map illustrating the adsorption states of melamine within an island. The change in  $E_d$  assignments to adjacent molecules by the removal of the green molecule is illustrated by situation (1), before, and situation (2), after.

This discrepancy perhaps points to a weakness in the approach of dividing the  $E_d$  up into constituent substrate-adsorbate interaction ( $E_{Au-mel}$ ) and intermolecular interactions ( $S_{mel-mel}$ ). Alternatively, the calculated hydrogen bonding interaction energy<sup>23</sup> between melamine molecules may be slightly over-estimated. Using both the calculated hydrogen bonding interaction energy<sup>23</sup> as  $S_{mel-mel}$  and the calculated adsorption energy<sup>26</sup> as  $E_{Au-mel}$  leads to values of estimated  $E_d$  values for melamine that are too high. A centre molecule of  $E_{Au-mel} + 3S_{mel-mel}$  would have an  $E_d$  of  $148.8 \text{ kJ mol}^{-1}$  by the method of Sales and Zgrablich<sup>22</sup> for assigning desorption

energies; this is greater in magnitude than values assigned to many of the PTCDI sites and much larger than  $E_d$  values,  $61.5 \text{ kJ mol}^{-1}$  and  $57.9 \text{ kJ mol}^{-1}$ , estimated by Syomin et al<sup>28</sup> and Wetterer et al<sup>29</sup>, respectively, for benzene from Au(111). Of course, an interplay between the adsorption energy of the melamine to Au(111) and intermolecular hydrogen bonding stabilisation energy may exist; as melamine forms more intermolecular hydrogen bonds, perhaps its interaction with the surface decreases.

Using the above values for  $E_{Au-mel}$  and  $S_{mel-mel}$ , it is predicted that the molecules in states of  $E_{Au-mel}$  and  $E_{Au-mel} + S_{mel-mel}$  would desorb below 300 K using equation 3.2 discussed earlier. Clearly, these are still important and viable states above 300 K, since it is known that melamine molecules can diffuse across the Au(111) surface and join onto the edges of molecular islands. With reference to the melamine map (figure 5.14), should a molecule of  $E_{Au-mel} + 2S_{mel-mel}$  be removed (the green molecule), a molecule of  $E_{Au-mel} + S_{mel-mel}$  would be created. The schematic shows that removing a molecule on the edge of a hexagonal array, a centre molecule of  $E_{Au-mel} + 3S_{mel-mel}$  has lost a neighbour and now takes on the  $E_d$  of the departed molecule, whilst the other neighbour of the removed molecule, on the edge of the array becomes a molecule of  $E_{Au-mel} + S_{mel-mel}$  which should desorb fairly quickly after being created. Certain simple rules can be implemented into a spreadsheet to simulate these changes.

As for PTCDI, the equation 5.2 can be applied to centre molecules (site 1, those of  $E_d = E_{Au-mel} + 3S_{mel-mel}$ ) and the stock of molecules,  $N_T$ , in this state should expire before that of the other states:

$$N_T = N_{T-1} - \sum_{\text{site } 1}^{\text{site } n} N_d \quad \text{Equation (5.2)}$$

As centre molecules replace edge molecules of  $E_{Au-mel} + 2S_{mel-mel}$ , the stock of molecules in these sites,  $N_T$ , can be held constant up until a set temperature, say 380 K, before being allowed to decay as the exponential term of equation 3.2

becomes too large (tends towards 1) to keep the number of molecules desorbing,  $N_d$ , less than  $N_T$ .

The  $E_d$  of  $E_{Au-mel} + S_{mel-mel}$  molecules gives desorption peaks outside the temperature range of the simulated spectra, yet molecules of this type would be created via the removal of  $E_{Au-mel} + 2S_{mel-mel}$  molecules from domains and it is assumed that they will desorb quickly after being created so when calculating  $N_D$  (the number of molecules desorbing from all sites),  $N_d$  from the  $E_{Au-mel} + 2S_{mel-mel}$  state is multiplied by two to accommodate desorption from  $E_{Au-mel} + S_{mel-mel}$  states at higher temperatures such that for each  $\Delta T$  increment:

$$N_D = N_{d(E+3S)} + 2N_{d(E+2S)} \quad \text{Equation (5.3)}$$

The simulated spectrum based only on  $N_D$  versus  $T$  seems to match the experimental result very well (figure 5.15). In the experimental spectra, there is a slight delay observed in the return to base pressure after the main desorption peak, such a small lag can be related to the removal rate of melamine from the chamber.

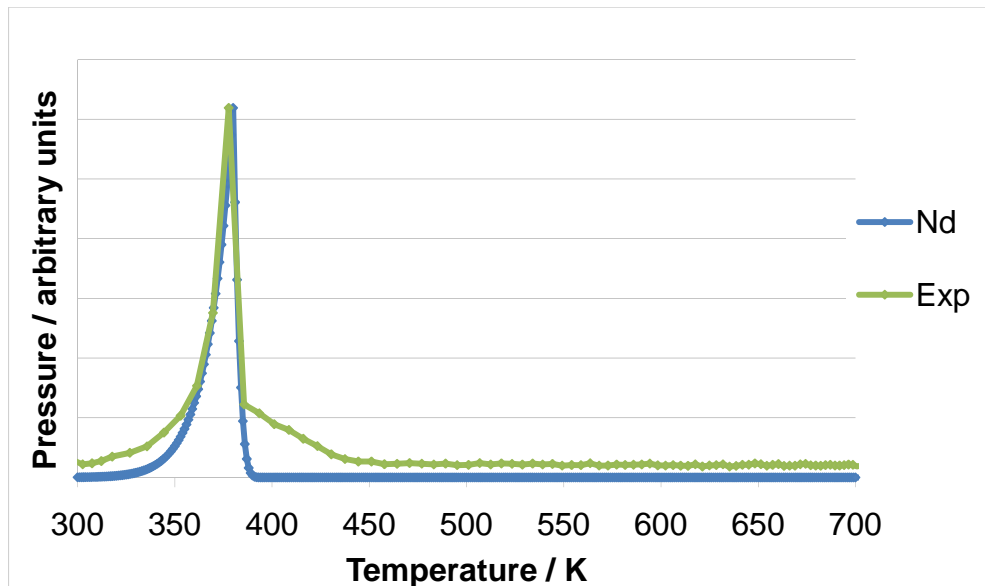


Figure 5.15 Comparison of the simulated TPD spectrum based on  $N_D$ , the number of molecules desorbing (blue), with the experimentally obtained spectrum (green). The desorption spectrum based on the 20 L pre-annealed experiment, the top spectrum in figure 5.13, is used in this comparison.

Melamine is known to condense on surfaces inside the vacuum chamber and give background contamination via its vapour pressure thus when carrying out

experiments with melamine, vacuum chambers need to be baked frequently and thoroughly. The discussed method for incorporating the effect of the sample heating rate and pumping speed into the simulated spectrum, based on  $N_S$ , the number of molecules detected by the sensor, can be implemented, but in this case, this seems to over-estimate the lag in the return to the baseline after the main desorption peak (figure 5.16).

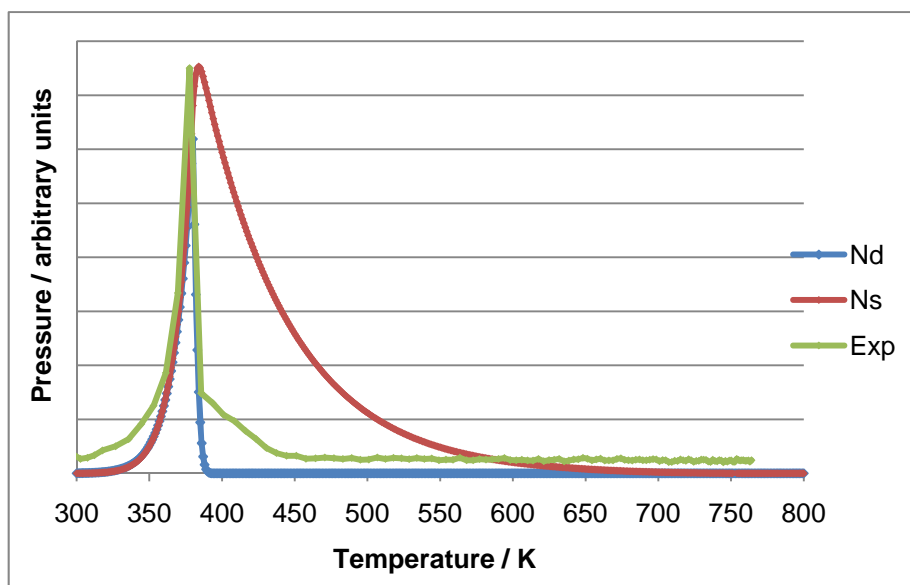


Figure 5.16 Comparison of the simulated TPD spectrum based on the number of molecules at the sensor (red),  $N_S$ , which incorporates the effect of the pumping speed, and the experimentally obtained spectrum (green). The desorption spectrum based on the 20 L pre-annealed experiment, the top spectrum in figure 5.13, is used in this comparison.

The pumping speed experiment and the TPD experiments may both be affected by the background pressure from melamine contamination and give distorted results thus, in this case,  $N_D$  versus temperature does not give a sufficient insight into the process of desorption then detection. As discussed, estimated values of  $3.4 \text{ kJ mol}^{-1}$  and  $43.8 \text{ kJ mol}^{-1}$  are assigned to  $E_{Au-mel}$  and  $S_{mel-mel}$  respectively (despite the likelihood of the estimate for  $E_{Au-mel}$  actually being closer to the calculated value<sup>26</sup> of  $17.4 \text{ kJ mol}^{-1}$ ). The most important sites are undoubtedly the edge sites of  $E_d = E_{Au-mel} + 2S_{mel-mel} = 91.0 \text{ kJ mol}^{-1}$  as they yield the peak position obtained experimentally. When compared to the calculated activation energies of desorption for the benzene (which will not form hydrogen bonded assemblies) of  $57.9 \text{ kJ mol}^{-1}$  and  $61.5 \text{ kJ mol}^{-1}$ , this value seems a reasonable estimate for  $E_d$ , but again, more complex calculations would need to be carried out to quantify the

potential interplay between substrate-adsorbate interactions and intermolecular interactions. Where lower coverages of melamine are involved, with reference to figure 5.13, the lower initial doses of melamine are seen to give desorption spectra featuring slightly lower  $T_{max}$  values, smaller islands would most likely form. In this situation, a greater proportion of molecules will be in edge sites of lower  $E_d$ , therefore  $T_{max}$  may be decreased for lower surface coverages.

In comparison with PTCDI, the three-fold symmetry of melamine and the directionality of its hydrogen bonding functionalities means that it forms porous, hexagonal arrangements where the supramolecular interactions are less complex compared to the two-fold symmetry of PTCDI where it can form rows based on primary supramolecular interactions that interlock with each other via secondary supramolecular interactions. The smaller size of melamine relative to PTCDI, as well as its simpler monolayer structure, means that it desorbs at a lower temperatures and over a much smaller range.

As with PTCDI, the simple spreadsheet model does not take into account some of the more dynamic processes occurring on the surface; diffusion of loose molecules, re-attachment to domains and the changing domain shape all have a significant effect on the shape of the TPD spectra. More complex relationships and more powerful computational methodology may be required to fully incorporate these into model spectra whilst optimal conditions inside the UHV chamber (fast pumping speed, low background pressure and no contamination) may help to match experimental to theoretical results.

### 5.4.3 TPD of co-deposited PTCDI and Melamine from Au(111)

A series of TPD experiments were carried out after depositing both network components onto the Au(111) sample. PTCDI was deposited before melamine in order that the conditions in the TPD experiments replicated those reported for successful network construction<sup>1</sup>.

The spectrum shown in figure 5.17 is typical of data acquired for desorption of PTCDI, represented by  $m/z = 69$ , in this series. In contrast to data for PTCDI in the monocomponent experiments, the desorption of PTCDI from Au(111) after melamine has been co-deposited occurs in two stages, there are two peaks in the desorption profile ( $T = 410$  K and  $T = 755$  K). There is a trough in the bicomponent spectrum that is almost coincident with  $T_{max}$  in the monocomponent TPD spectrum. It is perhaps fair to assume, based on its shape and the effect of the pumping speed and detector, that the spectrum can be extrapolated further to higher temperatures above the limit of the heating range measured.

The desorption plot acquired seems to suggest that PTCDI still exists upon the surface above 750 K. Although PTCDI was observed on the Ni/Au(111) surface above 600 K, it is unlikely that PTCDI would still be present on the Au(111) surface at a similar temperature. The extension of the curve to higher temperatures suggests some additional stability of PTCDI upon Au(111) is induced by co-adsorption of melamine. This ensures that not all PTCDI is desorbed by the end of the heating ramp. If there was enough melamine left on the surface at these higher temperatures, it may be reasonable to suggest that its apparent stabilisation is caused by the formation of a hydrogen bonding network and that the PTCDI-melamine hydrogen bonding interactions hold molecules down more strongly than PTCDI-PTCDI interactions. If this was the case, then the broad desorption profile could arguably be caused by slow, gradual break-up of the network. Given the low desorption temperature of melamine, it is unlikely that this stabilisation is caused by the continued existence of hydrogen bonding PTCDI-melamine networks at high temperatures. This result may be an artefact of the experimental apparatus, PTCDI may gain some stabilisation from the presence of melamine on the surface, but a lag in the removal of molecules from the main PTCDI desorption peak may result as the pump copes with molecules generated from two previous desorption events: the melamine desorption and the low temperature PTCDI desorption.

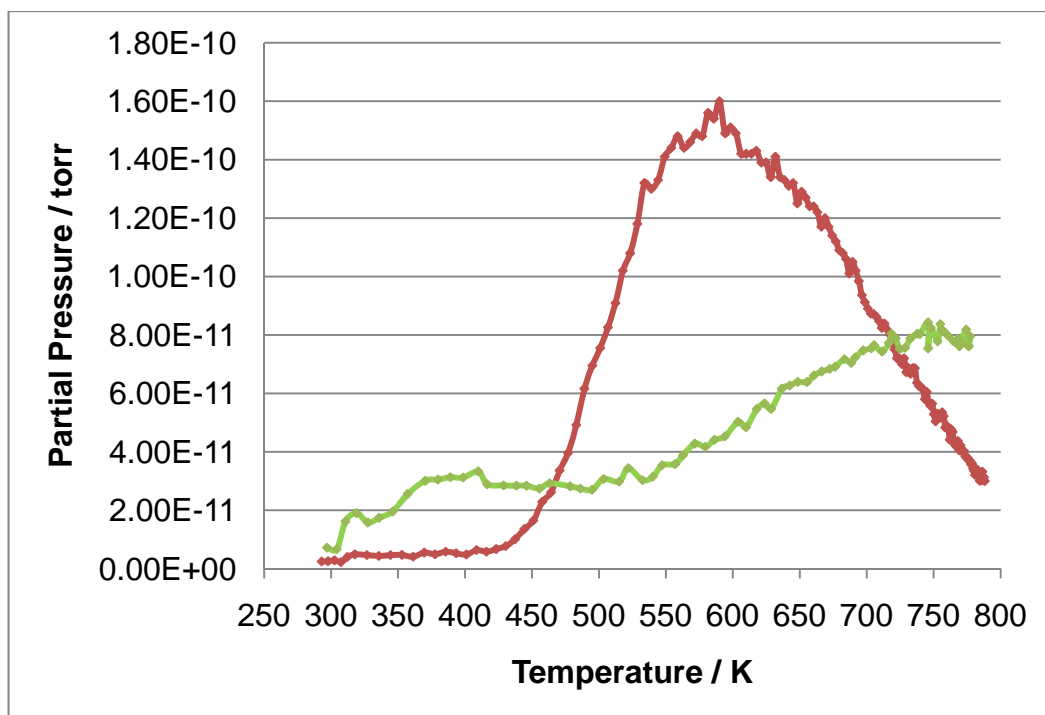


Figure 5.17 TPD data for PTCDI desorption from Au(111) based on the fragment ion  $m/z = 69$  after the Au(111) surface is exposed to PTCDI and melamine at room temperature. The red plot represents the desorption of PTCDI when deposited alone, the green plot represents the desorption of PTCDI after melamine has been co-deposited.

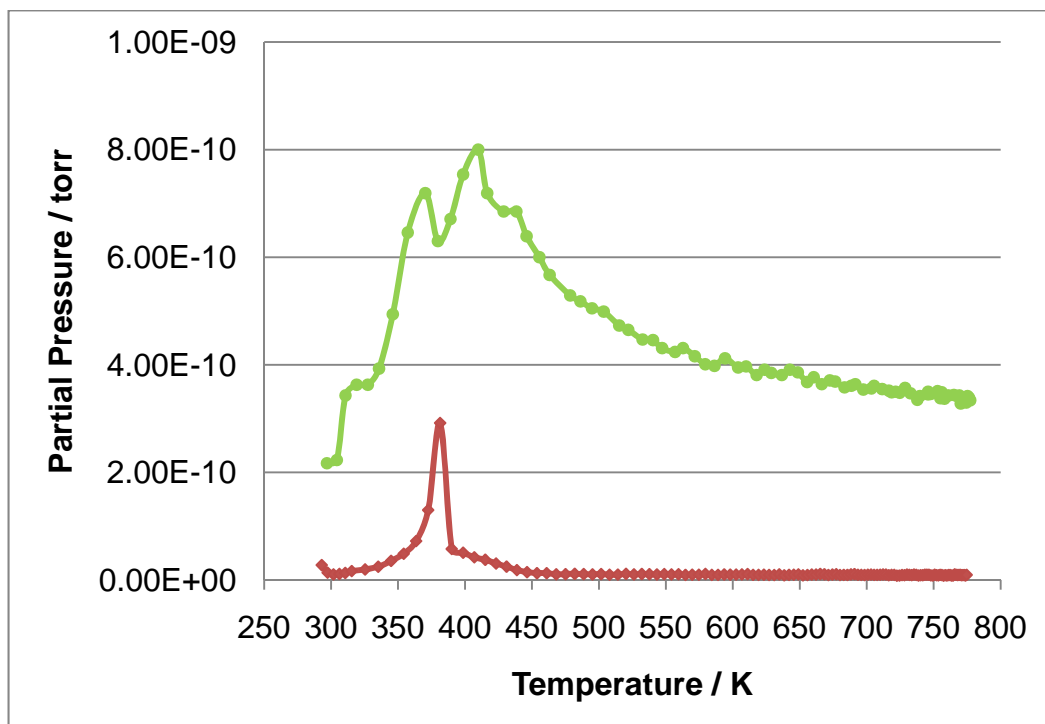


Figure 5.18 TPD data for melamine desorption from Au(111) based on the fragment ion  $m/z = 43$  after the Au(111) surface is exposed to PTCDI and melamine at room temperature. The red plot represents the desorption of melamine when deposited alone, the green plot represents the desorption of melamine after being deposited on a surface where PTCDI is already present

The melamine desorption spectrum from the same experiment, figure 5.18, is vastly greater in amplitude relative to the monocomponent experiment (also shown in figure 5.18). The melamine desorption peak in the bicomponent experiment has two peaks at 370 K and 409 K and it is centred over the desorption peak in the monocomponent spectrum. The melamine desorption also coincides with the low temperature PTCDI desorption which peaks at 400 K. From monocomponent TPD experiments and previous STM studies<sup>1, 16-19</sup>, it is known that as temperature increases, the stability of melamine on the Au(111) surface is the limiting factor in the survival of the network. The formation of a network would probably have a significant effect on the desorption behaviour of each species and this may be responsible for the low temperature PTCDI desorption peak observed in figure 5.17. The possibility of multilayer desorption cannot be ruled out, with PTCDI already present on the surface, the multilayers may result upon the addition of melamine to the surface and it may not be unreasonable to suggest that this has some influence on the shape of the green spectrum (bicomponent) observed in figure 5.18.

If a network or a mixed phase is formed, and the temperature is increased sufficiently high to desorb the melamine units from the structure, then momentarily, PTCDI molecules will exist as isolated molecules on the Au(111) surface (figure 5.19). By previous reasoning, isolated molecules will have a lower  $E_d$  than molecules that are part of an island. If these molecules desorb before diffusing across the surface and assembling into a new compact island, they will contribute to a low temperature peak which matches that of the melamine desorption.

The possibility of poor resolution in the mass spectrometer must also be considered. As melamine has a fragment ion of  $m/z = 68$ , the desorption of melamine may contribute to the  $m/z = 69$  signal being monitored as the PTCDI desorption. In figure 5.18, the  $m/z = 43$  partial pressure desorption intensity at  $T_{max}$  has a value of approximately  $8 \times 10^{-10}$  torr in comparison to the value of approximately  $3 \times 10^{-11}$  torr recorded for  $m/z = 69$ ; melamine also has a fragment

ion of  $m/z = 68$  and at these desorption intensities, poorly resolved signals for  $m/z = 68$  could obscure the real  $m/z = 69$  intensity caused by PTCDI.

The bicomponent melamine spectrum (figure 5.18) has two clear peaks at 370 K and 410 K and a shoulder that reaches to 440 K in comparison to the single peak of the monocomponent spectrum at 381 K. Without STM evidence, it is difficult to determine the phases present on the surface and try to interpret the spectrum in terms of what phases or types of molecular domains are being desorbed. In the bicomponent spectrum, the first peak at 370 K may represent desorption of melamine molecules from monocomponent phases or mixed phases where melamine-melamine hydrogen bonding still prevails, such as the mixed phase reported by Saywell et al<sup>18</sup> or those observed in Section 5.4.2.1. In these mixed phases, some hexagonal arrangements are still present. The second peak at 410 K may be caused by stabilisation of melamine on the surface through interaction with PTCDI. The hydrogen bonding interaction between a pair of melamine molecules has been calculated<sup>23</sup> as 0.43 eV (41.5 kJ mol<sup>-1</sup>) whereas the hydrogen bonding energy between melamine and PTCDI is calculated<sup>23</sup> as 0.74 eV (71.4 kJ mol<sup>-1</sup>). The additional stabilisation most likely explains why the melamine peak stretches to above 440 K in the bicomponent experiments.

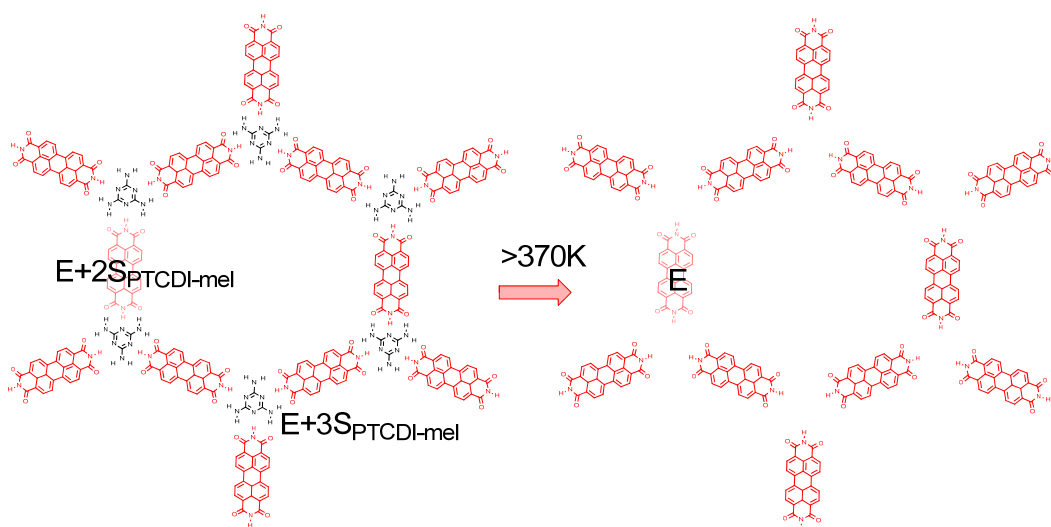


**Figure 5.19** Schematic showing the generation of isolated PTCDI molecules after removal of melamine from a bicomponent network

If the rules which were adapted from those of Sales and Zgrablich<sup>22</sup> for assigning desorption energies for molecules are applied to the porous hexagonal arrangement, then  $E_d$  for a melamine molecules would be  $E_{Au-mel} + 3S_{PTCDI-mel}$ , where  $S_{PTCDI-mel}$  is the hydrogen bonding energy between PTCDI and melamine which has been calculated<sup>23</sup> as  $71.4 \text{ kJ mol}^{-1}$ . Each melamine molecule would be assigned an  $E_d$  value of  $231.6 \text{ kJ mol}^{-1}$ ; this appears to be a huge over-estimation in relation to the observed spectrum. This indicates that this set of rules may only really be applicable to compact islands or that the  $E_d$  of individual molecules falls rapidly as soon as some of the hydrogen bonding interactions are broken. It may be more relevant to consider the individual stabilisation energy of the intermolecular hydrogen bonding junctions rather than the gradual desorption of molecular islands especially when there is no evidence of which PTCDI-melamine phases are actually present when the TPD experiments are carried out.

#### 5.4.4 STM of Nickel Deposition into PTCDI and Melamine Phases on Au(111)

In optimising the conditions for construction of the PTCDI-melamine hexagonal network, other mixed phases of PTCDI and melamine were also observed. After the assembly of porous hexagonal and parallelogram networks, nickel was deposited onto the sample to determine if the networks are capable of controlling its distribution and templating its growth. As the nickel exposure is uniform across the sample, the interaction of nickel with some of the other PTCDI-melamine phases present was also examined.

After deposition of PTCDI and melamine on Au(111), melamine tends to nucleate at step edges, whilst PTCDI prefers to form extensive domains on the wide, flat terraces. Mixing can occur at room temperature. However, this can be accelerated via annealing the sample; a temperature of 320 K is usually adequate. If coverages of the two components are appropriate, suitable space is available for networks to

grow into and freedom from heteromolecular domains is attained, the target hexagonal structure may arise.

The literature suggests that hexagonal networks form via a two step process once both species are present on the surface<sup>1</sup>: annealing of the sample to allow intermixing, then further annealing to remove excess melamine and leave only the hexagonal network behind. In this study, it was found that mixing of the two species occurred quite easily, but conversion of mixed phases into the hexagonal network requires optimal conditions.

#### 5.4.2.1 Mixed Phase

The precursor mixed phase observed by Saywell et al<sup>18</sup> (figure 5.20) was observed in this series of experiments, it is shown in figures 5.20 and 5.21, but annealing generally did not result in its conversion to the target hexagonal phase but the rearrangement into a new variation which was the most abundant throughout this series of experiments across all the annealing temperatures tested.

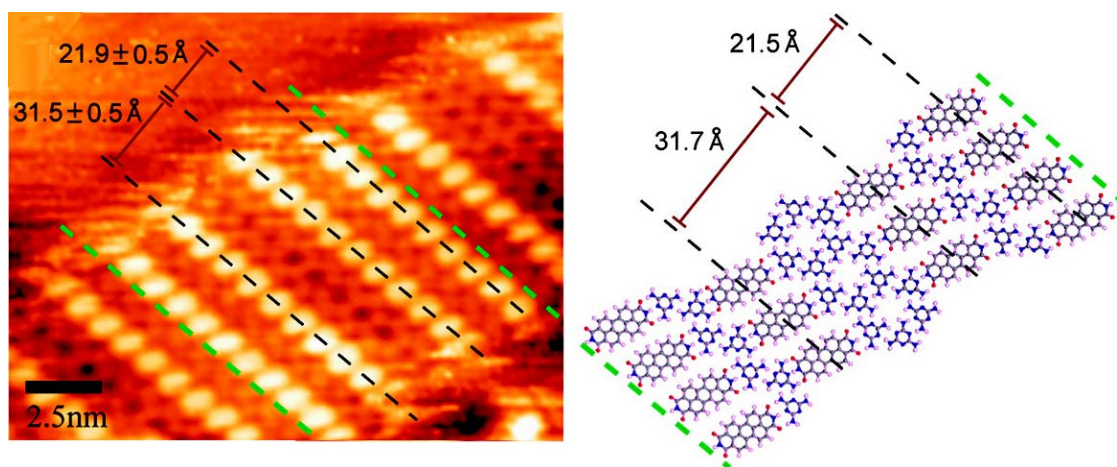


Figure 5.20 STM image and model of mixed phase taken from previous report<sup>17</sup>

The new unreported mixed phase combines elements of two phases that have been reported previously; the aforementioned mixed phase<sup>18</sup> and the parallelogram phase<sup>17</sup>. If the ‘stile’ junctions of the parallelogram phase are inserted to the mixed phase, the structure of figure 5.22 results, this is modelled in figure 5.23.

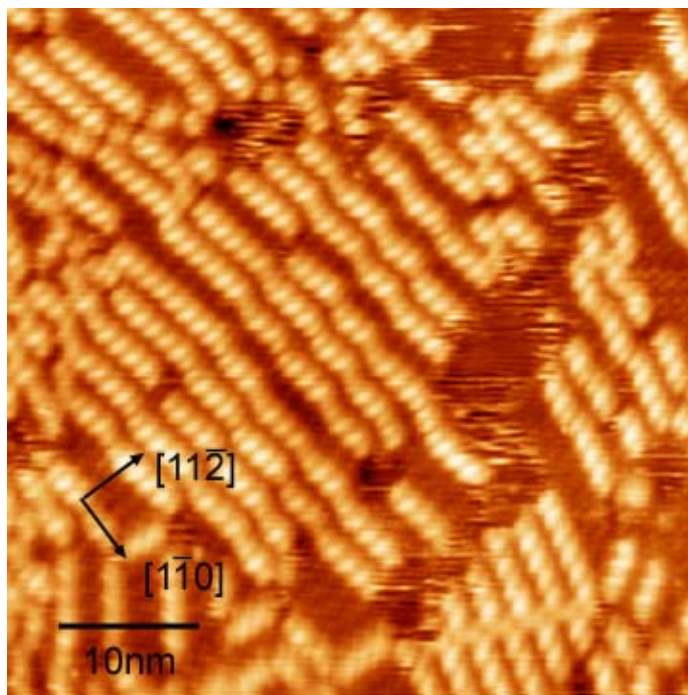


Figure 5.21 STM image of the PTCDI/melamine mixed phase on Au(111) (49.1 x 49.1 nm, 1.5 V, 0.2nA)

The unit cell of the structure has dimensions of 20.1 Å and 25.0 Å, separated by an internal angle of 80°. This phase consists of the PTCDI barriers that are only 3 molecules wide, the outer two molecules hydrogen bond to a PTCDI molecule of adjacent barriers such that 4 melamine molecules become completely encapsulated by 8 PTCDI molecules. For this reason, this phase shall be referred to as the ‘capped mixed phase’. Occasionally, barriers may be 4 PTCDI molecules wide; this permits another two melamine molecules to be contained within each enclave (a row of this is indicated by the arrow in the zoomed image of figure 5.22, below). This phase shows stability from its inception at 320K to at least 370K. Due to the inherent chirality of the hydrogen bonding structure of melamine, this structure is also chiral. Furthermore, the same enantiomeric form of melamine structures must reside on each side of the PTCDI barrier for the capped mixed phase to exist.

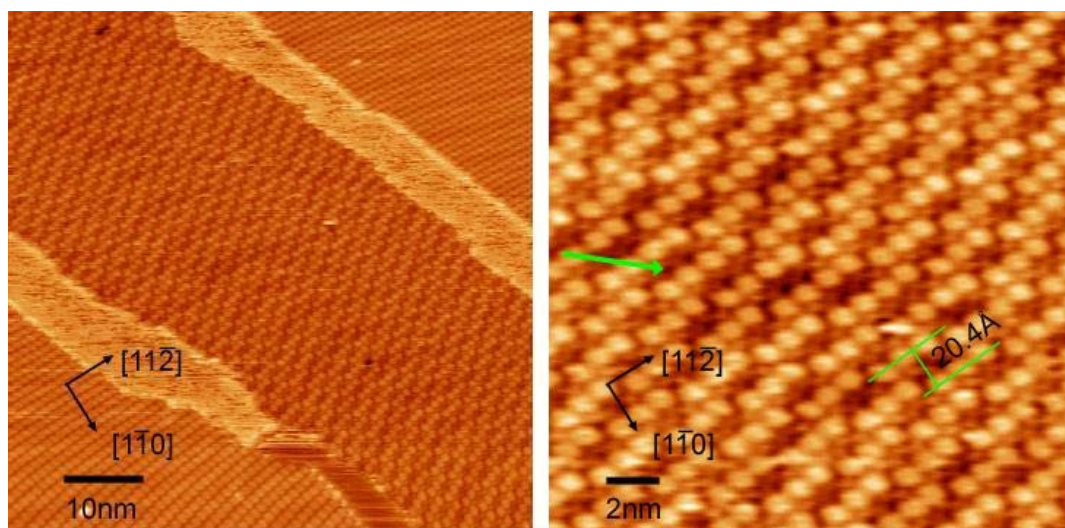


Figure 5.22 STM image showing a domain of the capped mixed phase and, right, a zoomed area of the domain (-1.5V, 0.5nA)

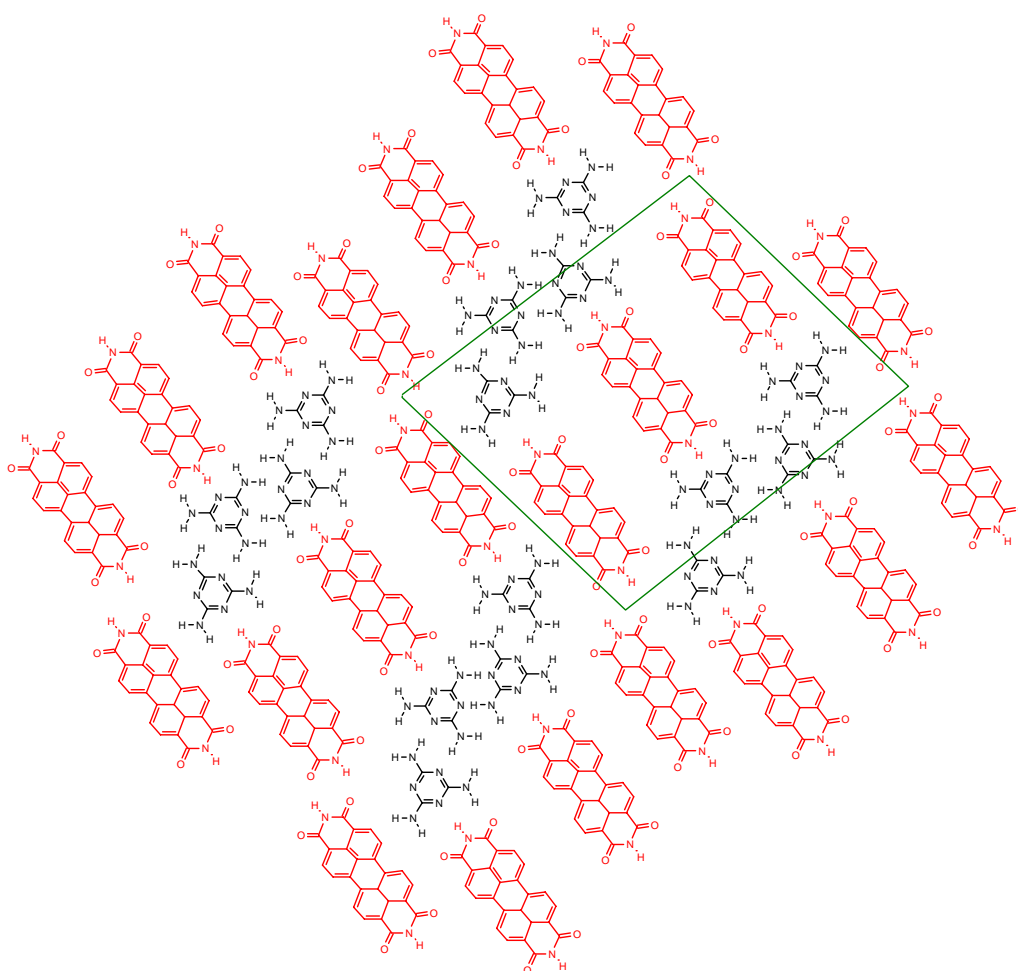


Figure 5.23 Model of the melamine-poor capped mixed phase

Analogous to the mixed phase observed by Saywell et al<sup>18</sup>, this structure can be expanded to accommodate more melamine molecules between the PTCDI barriers as is observed in figure 5.24. The melamine-rich variant still possesses PTCDI barriers that are three molecules wide, but because they are further apart they do not fully encapsulate the melamine molecules and a melamine-melamine hydrogen bonding interaction links each enclave to the next (figure 5.25). The unit cell for this structure has dimensions of 33.8 Å and 31.9 Å separated by an internal angle of 70° and is orientated at 23° to the  $\langle 11\bar{2} \rangle$  direction. This structure tends to be less abundant than the melamine-poor structure. This is due to the fact that it contains more melamine-melamine (double) hydrogen bonding junctions and these are weaker than PTCDI-melamine (triple) hydrogen bonding junctions, and it contains some melamine molecules that interact exclusively with other melamine molecules. During annealing, these molecules are most vulnerable to desorption.

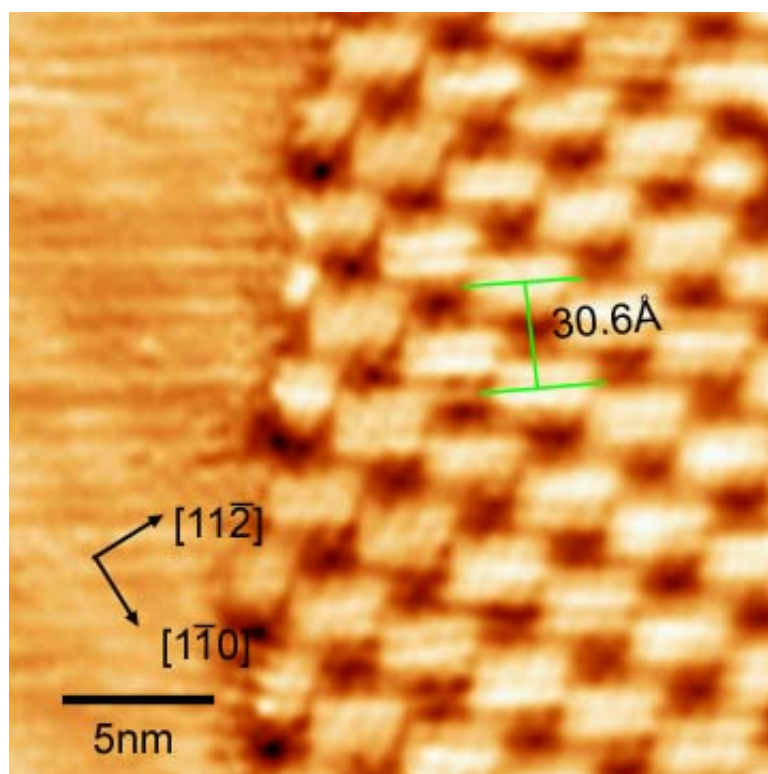


Figure 5.24 STM image of the melamine-rich capped mixed phase (25.3 x 25.3 nm, 1.5 V, 0.4 nA)

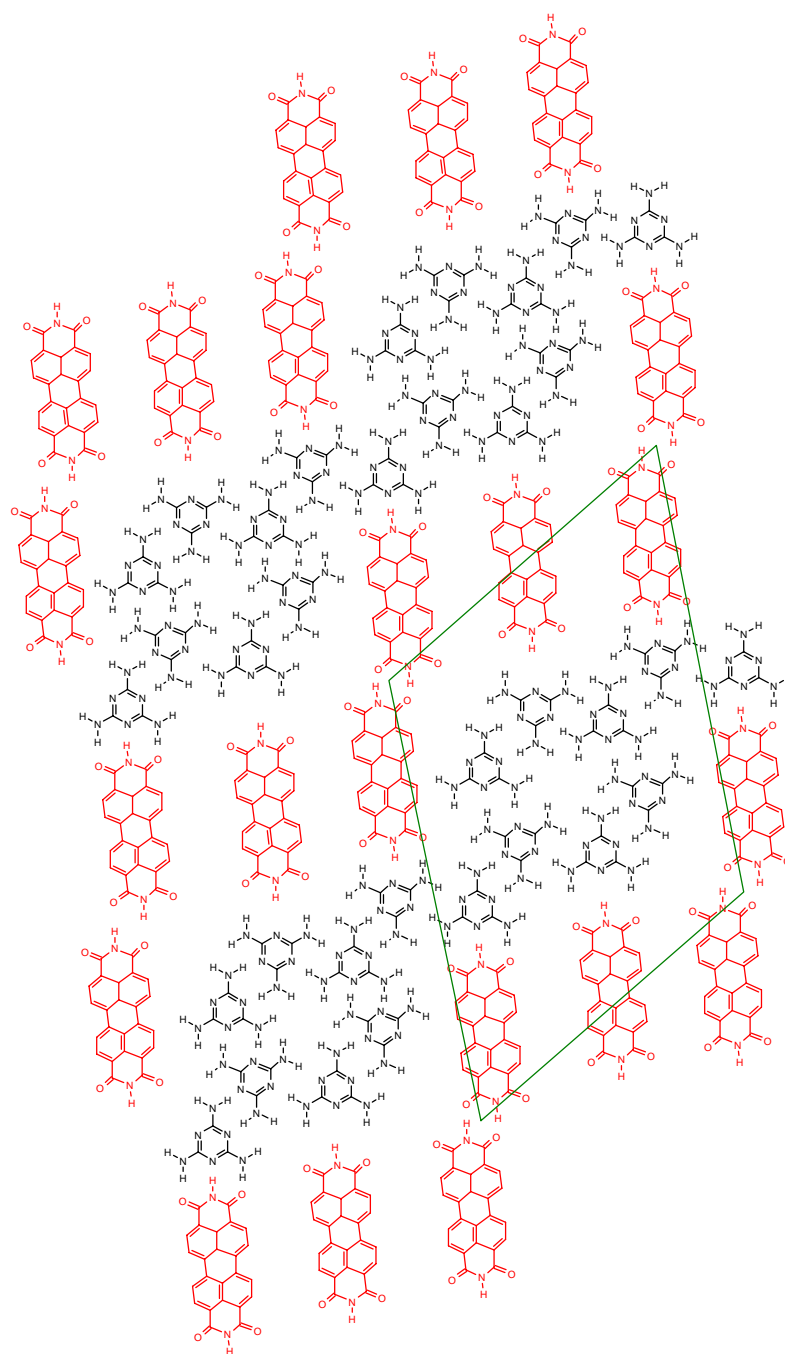


Figure 5.25 Model of melamine-rich capped mixed phase

Composite structures of these mixed phases, whose unit cell dimension are dependent on the sequencing of melamine-rich and melamine-poor enclaves, are observed. The resolution in the large scale STM image of figure 5.26 only allows PTCDI barriers of three molecules to be seen as single bright features, the sequence in this example is poor, poor, rich, poor, poor, rich... roughly along the  $\langle 11\bar{2} \rangle$  direction. There is an offsetting of the barriers and this is due to extra

pockets of melamine that continue from each melamine-rich enclave to melamine-rich enclaves in rows above and below following the same sequence (figure 5.27).

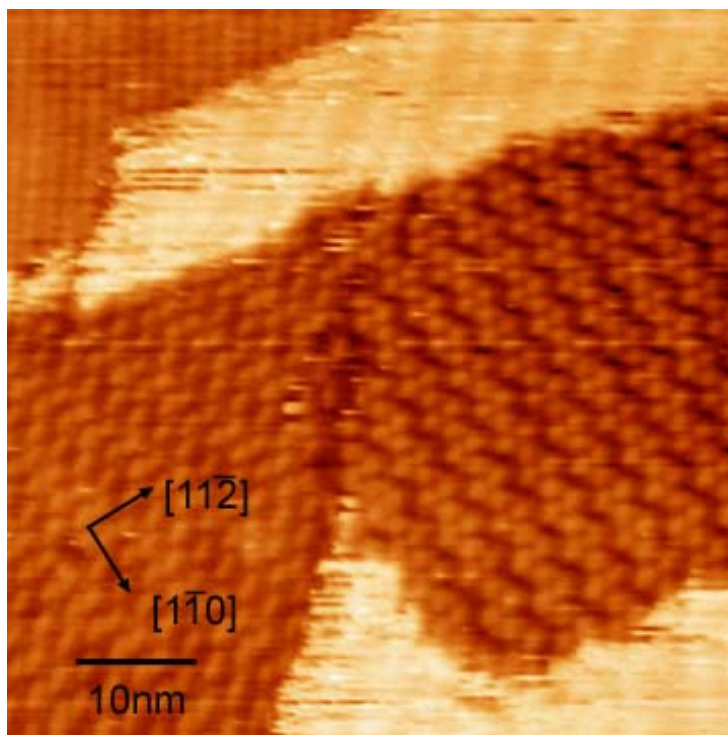


Figure 5.26 STM image showing domains of PTCDI and two mixed phases (62 nm x 62 nm, -1.8 V, 0.2 nA)

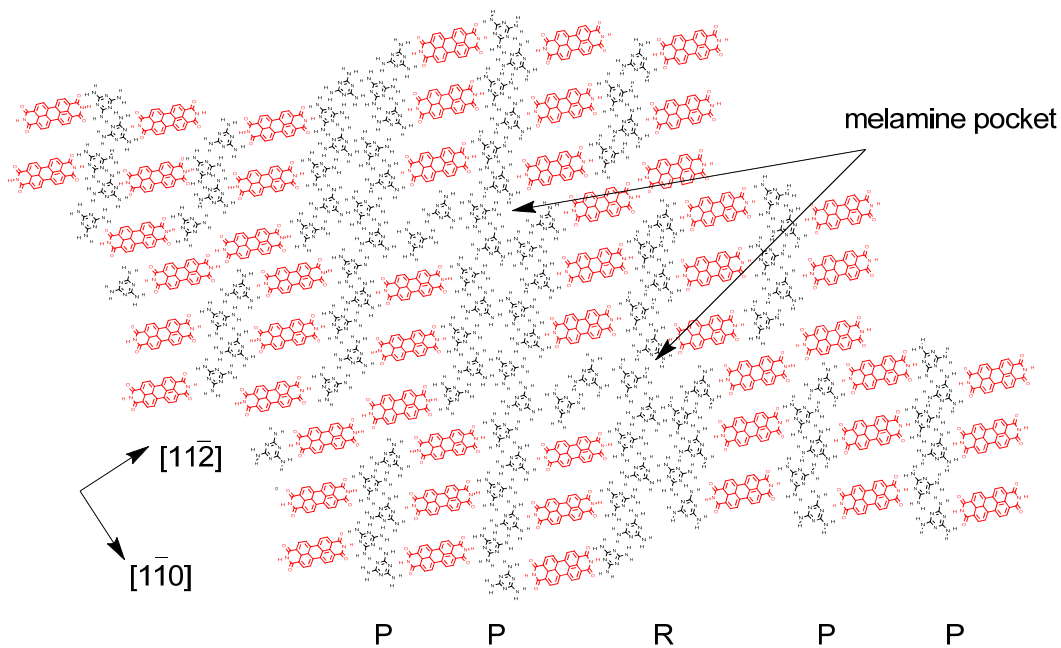


Figure 5.27 Model of the phase of the right hand domain of the image in figure 5.26. R and P indicate melamine-rich and melamine-poor enclaves, respectively

The adjacent domain in figure 5.26 is essentially the melamine-rich capped mixed phase; the variation takes the form of periodic insertions of single chains of melamine molecules to fulfil hexagons that would not be complete in standard melamine-rich capped mixed phase domains (figure 5.28).

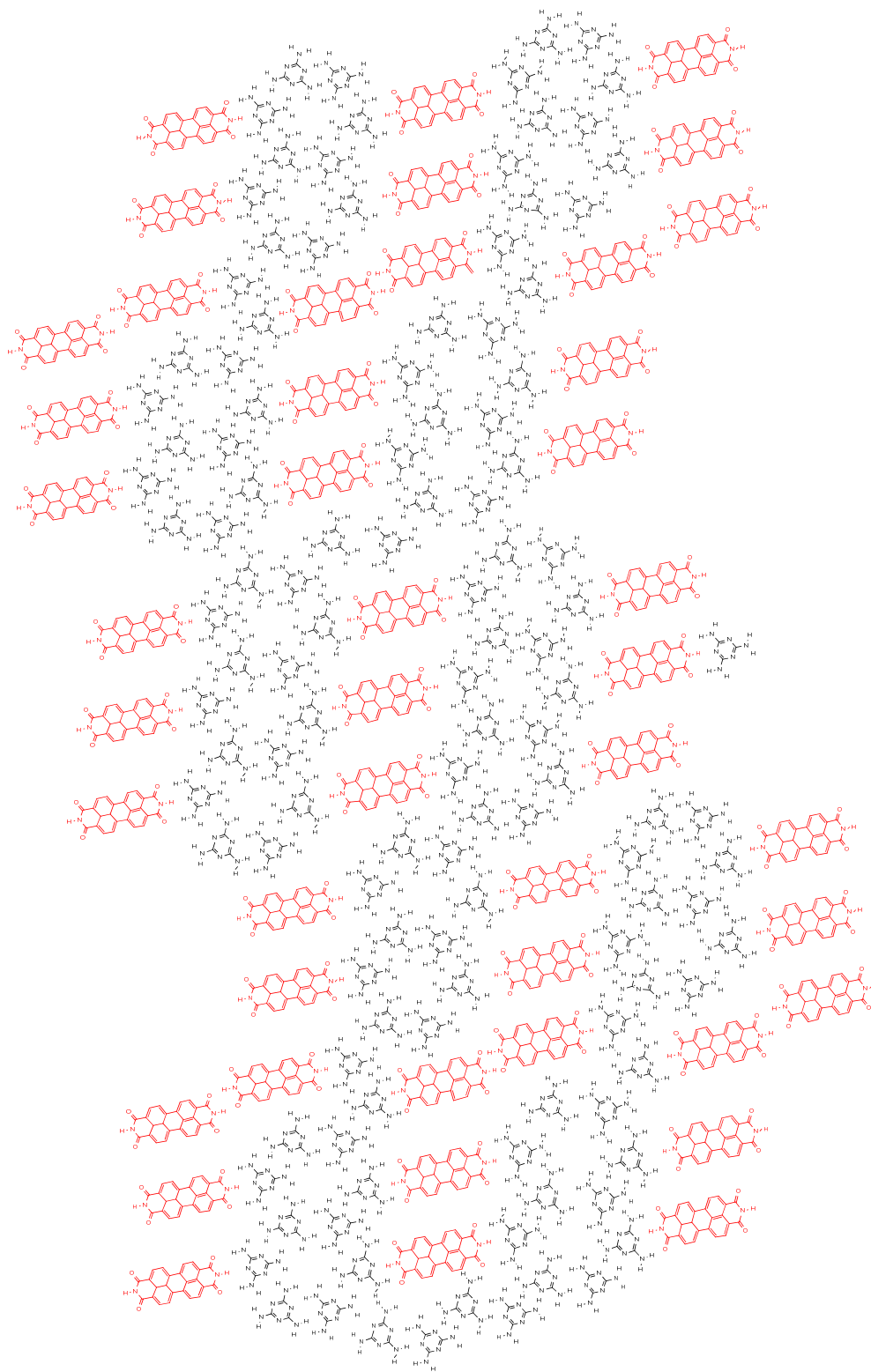


Figure 5.28 Model of the domain show left in the image of figure 5.26

Nickel Deposition

After deposition of Ni, the same ‘skimming’ effect, discussed with respect to monocomponent PTCDI domains earlier in Section 4.4.3, is evident on domains of the capped mixed phase; the PTCDI molecules of the domain interior appear much brighter than those around the edge, this is shown in figure 5.29.

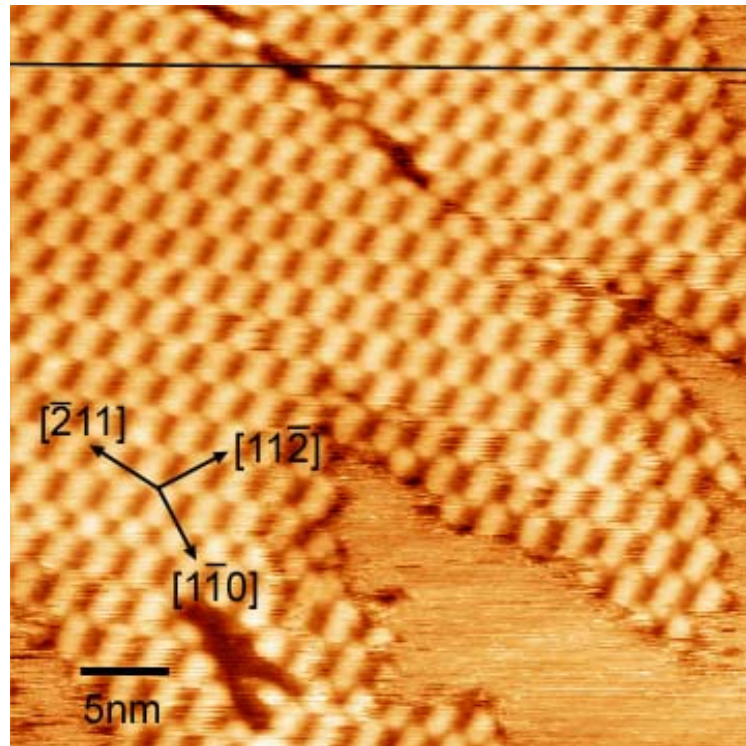


Figure 5.29 STM image of melamine-poor capped mixed phase after deposition of 0.1 ML nickel (42.0 x 42.0 nm, 1.5 V, 0.4 nA)

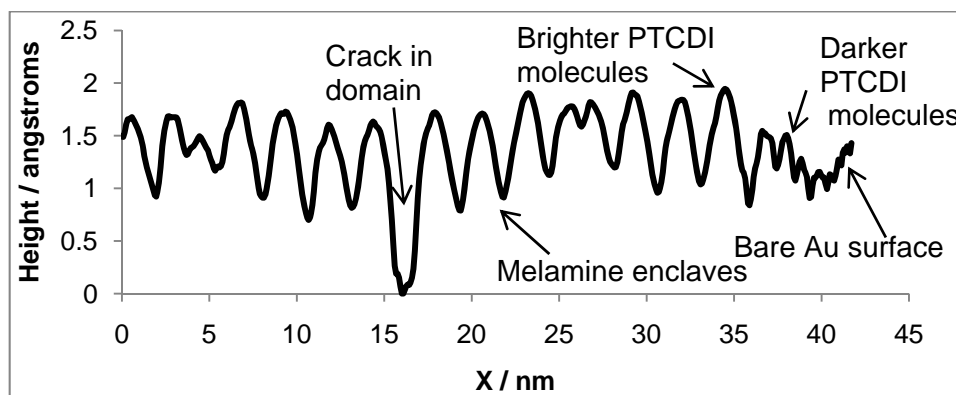


Figure 5.30 Height profile along section indicated in figure 5.29

The first changes that can be observed once this process has subsided, usually after 1-2 hours, are defects along the rows of elbow sites, and just as before, molecules can be displaced to create holes in the domain or the domains can be split along these rows.

An image of the capped mixed phase captured later after nickel deposition is shown in figure 5.31. Ni growths can possibly settle in elbow sites and lie underneath the domain but the relative contrasts of PTCDI, melamine and Ni do not allow firm conclusion to be drawn on whether this is the case. The brightness of the metal adatoms tends to eclipse that of the molecular adsorbates, but the domain does not appear to be significantly disrupted in the immediate vicinity of Ni islands which show up as bright spots in its midst. This may suggest that in some instances, after nickel atoms nucleate in elbow sites, the molecules within the domain may be able to reorganise and the domain can self-heal over the nickel island.

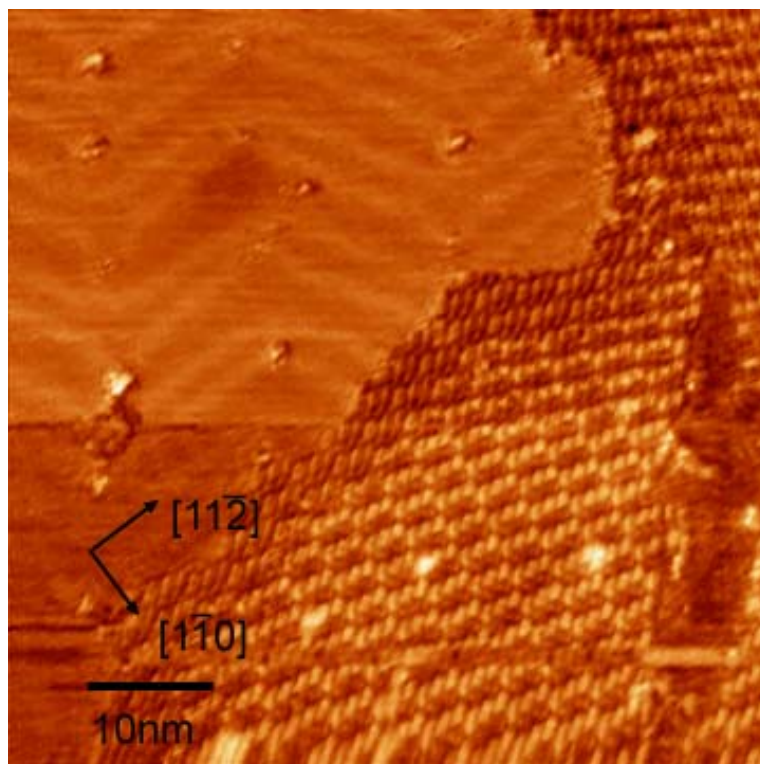


Figure 5.31 STM image of a mixed phase domain that has been altered by deposition of 0.1ML nickel (60.4 nm x 60.4 nm, 1.5 V, 0.4 nA)

The defects in the domain of figure 5.29 are thought to be created by nickel because they are above its usual nucleation sites. However, these defects appear as dark features. This is a rather strange phenomenon because other Ni features, in figure 5.31, appear as the brightest features; this may be because Ni, in the earlier image, may still be mobile within the defects that it has created or it is obscured by the mobility of molecules, particularly melamine, that it has displaced in the creation of those defects.

By the possible argument that diffusing nickel gives dark contrast to areas, the edges of the capped mixed phase domain shown in figure 5.31 may contain Ni around its edges. However, the unit cell dimensions, which have been measured based on PTCDI positions, do not seem to differ across the domain – from the bright interior to the dark exterior. In this particular image, there still remains a substantial quantity of mobile particles; around the edge of the domain and on the open surface, there is a considerable amount of streaking.

The possibility remains that these diffusive particles, Ni atoms, later become encapsulated in the enclaves of the structure closest to the edge of the domain. In figure 5.31, there is less evidence of diffusing species (the herringbone reconstruction of the surface is more visible) and it can be seen that the edges of the domain of the capped mixed phase are very different in appearance to the centre. The PTCDI molecules around the edge appear distorted, they are less vivid and the lobes have developed tails which are connected to features between the PTCDI barriers, these tails do not exist in the centre of the domain where PTCDI is certain to be interacting with melamine molecules via hydrogen bonding. The differing appearance of the PTCDI molecules may indicate a different type of supramolecular interaction around the edges of the domains. PTCDI molecules coordinated to Ni atoms might be expected to appear different to those only hydrogen bonded to melamine molecules.

### 5.4.2.2 Parallelogram Phase

The parallelogram phase of PTCDI and melamine is thought to succeed the hexagonal network. It has been reported<sup>16</sup> that after annealing a sample bearing PTCDI and melamine in the range 333 K to 353 K, the hexagonal network results (**A**), with further annealing to 363 K inducing the formation of the parallelogram structure (**B**). Whilst the results of this study tend to agree with the fact that the parallelogram structure shows greater thermal stability, it was seen to form at room temperature and co-exist with domains of the hexagonal and capped mixed (**C**) phases at 373 K (figure 5.32).

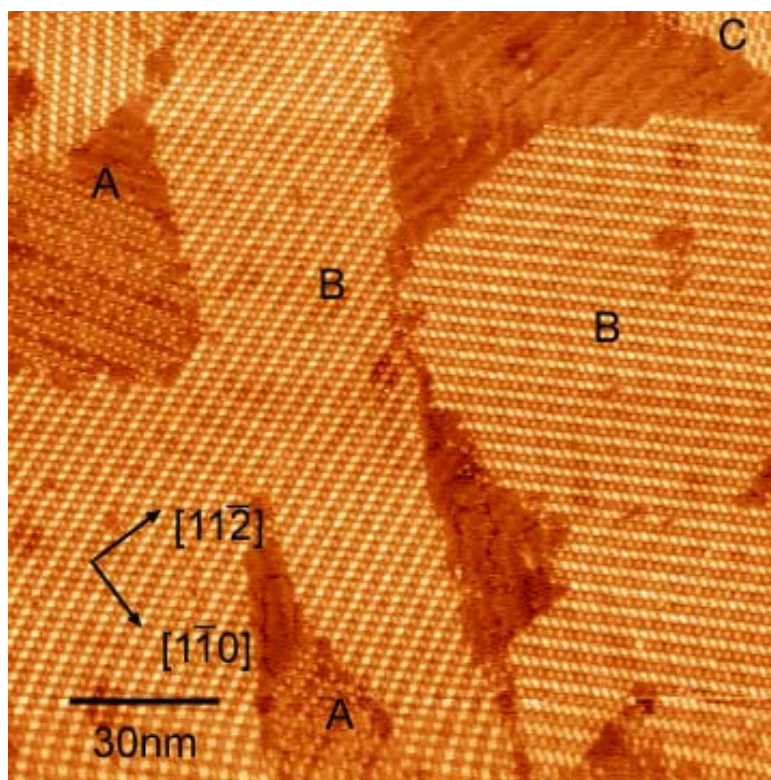


Figure 5.32 STM image of sample bearing PTCDI and melamine that has been annealed to 370K, domains of hexagonal (A), parallelogram (B) and capped mixed phase (C) structures are observed (155.4 x 155.4 nm, -1.5 V, 0.4 nA).

This phase is an open framework of parallelogram pores that have dimensions nearly equivalent to the PTCDI molecules that make up its sides. The structure is built from broader stiles that consist of pairs of PTCDI molecules interacting via double hydrogen bonds, each end of these PTCDI dimers forms a triple hydrogen bond to a melamine molecule. The PTCDI molecules that form the rungs of these

structures are stabilised at each end by triple hydrogen bonds to melamine molecules within the stiles. The unit cell vectors of dimensions 30.7 Å and 19.4 Å being separated by an internal angle of 87° and its alignment of parallel to or at 17° to the  $\langle 1\bar{1}0 \rangle$  direction declared by Staniec et al<sup>16</sup> are confirmed by the results of these experiments.

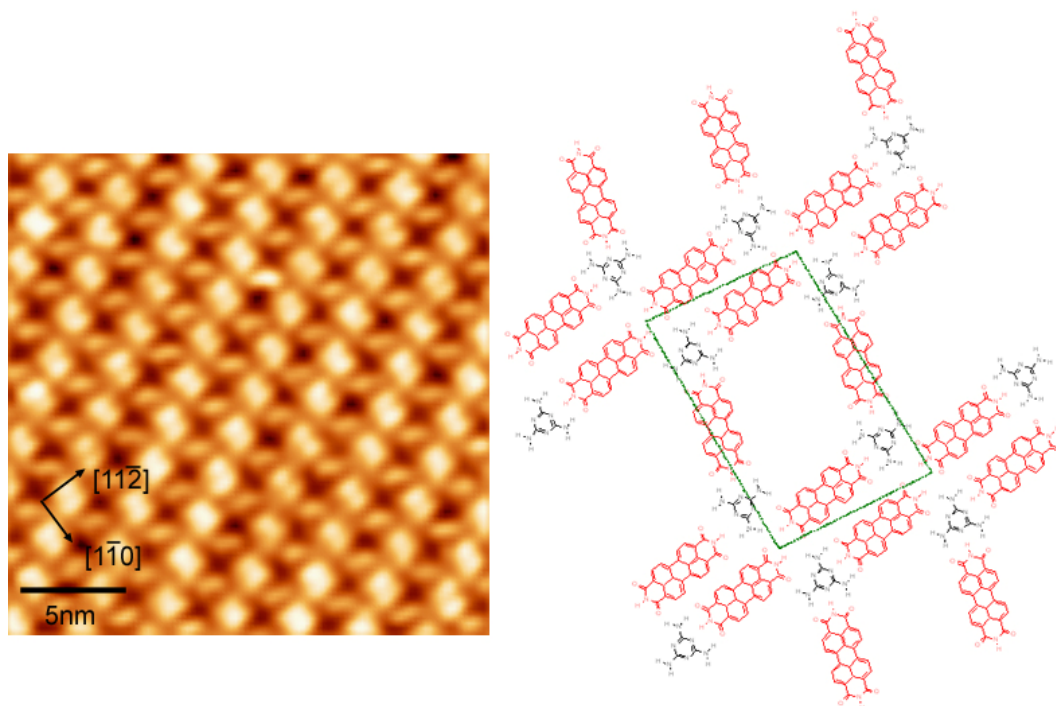


Figure 5.33 STM image (23 nm x 23 nm, -1.5 V, 0.4 nA) and model of the parallelogram phase<sup>16</sup>.

### Nickel Deposition

The main changes observed in the parallelogram phase following the deposition of nickel are thought to be a result of two different processes. Initially, it appears that deposits of Ni, where quantities equivalent to coverages below 0.1 ML are evaporated onto the surface, begin to fill some of the pores in the structure. However, on closer inspection, the obvious Ni growths are mostly in rows that correspond with rows of elbows of the surface reconstruction. In figure 5.34, the blue arrows, parallel with the  $\langle 1\bar{2}1 \rangle$  direction indicate where the rows of herringbone elbows lie and coincide with the nickel deposits within the area of the network. Where the Ni growths appear as bright features, the network continues to

exist uninterrupted above them, this is seen in the zoomed right hand image of figure 5.34.

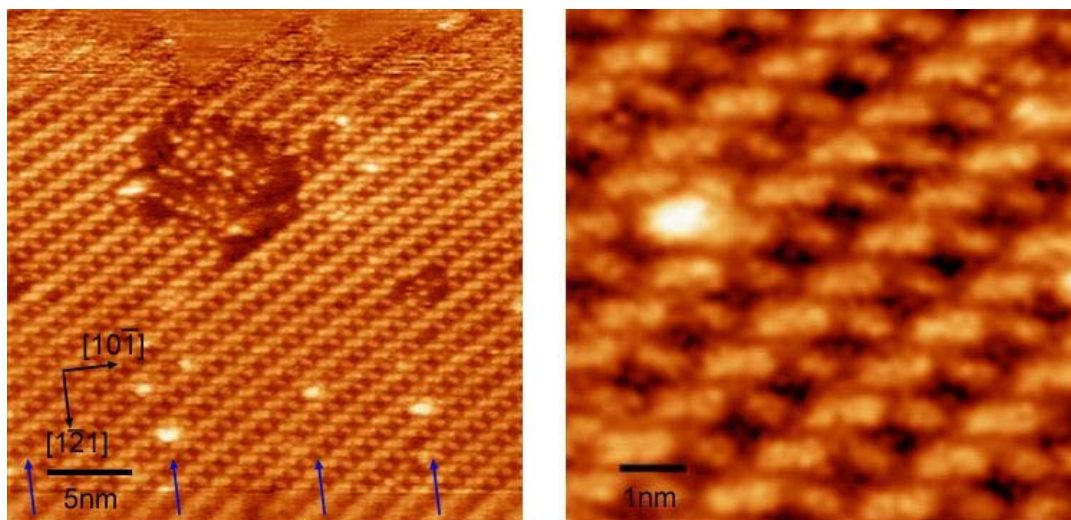


Figure 5.34 STM image of parallelogram structure after deposition of approximately 0.05 ML Ni, and zoomed area of network, right (-1.5 V, 0.4 nA)

Some of the brighter Ni growths lie away from these rows and it can be said that the network does have a limited capability to capture Ni that arrives via evaporation. The pores of the network in the zoom of figure 5.34 do not appear entirely empty, minor characters can be seen within some pores, but of course, their identity cannot be confirmed; they may be melamine molecules or metal atoms (Ni or Au).

As with the capped mixed phase, defects appear within the domain above elbow sites of the surface reconstruction, yet within the defects, no obvious Ni growth appears. It seems as the network continues uninterrupted above bright Ni features, but dark features may arise where defects have been created and the nickel is still mobile or the growth of the cluster is small (perhaps through inhibition from the presence of network molecules). Nickel cluster growth may indeed be favoured where the elbow nucleation site lies directly within the pore.

These effects are thought to be associated with the evaporation of hot, energetic Ni atoms onto the molecular domains but secondary changes may occur via a longer term diffusion process of Ni atoms that may not have found or are disturbed from their initial nucleation sites (elbows of the surface reconstruction or edges of molecular domains). This may result in the capture of Ni atoms within the parallelogram structure many hours after initial deposition. The STM image of figure 5.35 shows a domain of parallelogram structure that contains the initial defects elucidated above, including the removal of a large tract of the phase along a row of elbows, however, the main feature of the domain is the large amount of streaking within the pores. The pores closest to the edge appear to have more of the bright streaks as if to suggest that they contain more of the mobile particles within them relative to the inner pores.

To try to quantify this observation, pores were classified as being more than  $\frac{2}{3}$ ,  $\sim\frac{1}{2}$  or less than  $\frac{1}{2}$  full of brightness and the number of pore walls, (where stiles are counted as two and rungs as one; i.e. their thickness in PTCDI molecules, respectively) between the each pore and the edge of the domain (the source of diffusive particles). The average number in each classification was taken and this leads to the assertion that pores that have less than 3 PTCDI walls between them and the edge will be more than  $\frac{2}{3}$  filled, about 4-5 barriers from the edges will result in the pore being about  $\frac{1}{2}$  filled with brightness and where there are more than 6 barriers from the edge, the pore will be less than  $\frac{1}{2}$  full.

Height profiles may not provide conclusive evidence of the pores within the network as the mobility of the diffusive species may yield artefacts in the contrast across the images. The height profile selected spans a nickel cluster grown within an elbow of the surface reconstruction underneath a network pore, a bare area of the surface in network defects, the network with darker and lighter pores. The nickel cluster towards the left appears as two peaks in the height profile of figure 5.36 due to the fact that a PTCDI molecule lies across the middle of the cluster; it measures as around 2.1 Å higher than the bare surface within a defect of the

network (bounded by dashed blue lines on figure 5.36 and shown by the blue arrow in figure 5.35).

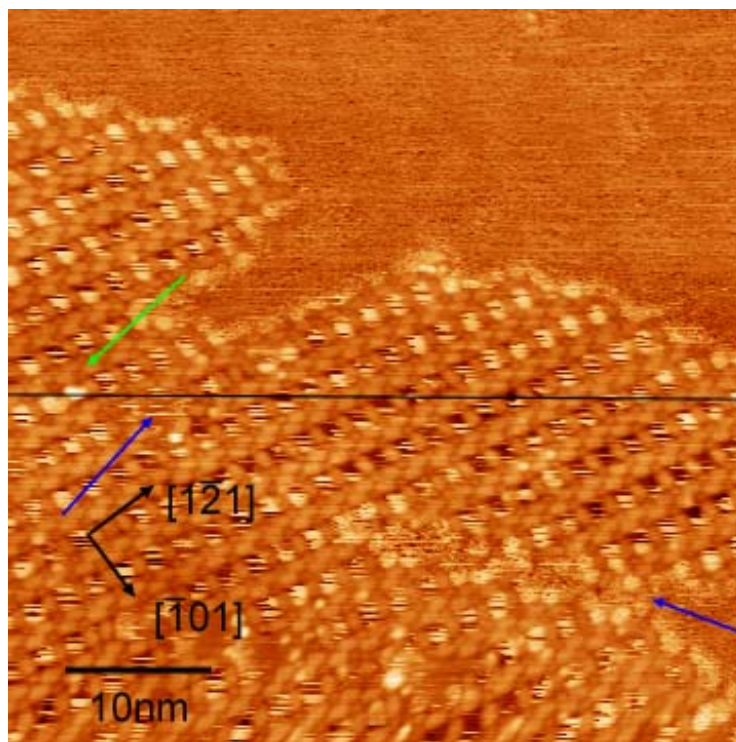


Figure 5.35 STM image of a parallelogram domain that has been left overnight after a deposition of Ni (0.1ML). Blue arrows indicate a bare tract of the surface in defects coincident with a row of herringbone elbows. The green arrow points towards a nickel cluster lying below the molecular network (50.5 nm x 50.5 nm, -2.0 V, 0.2nA).

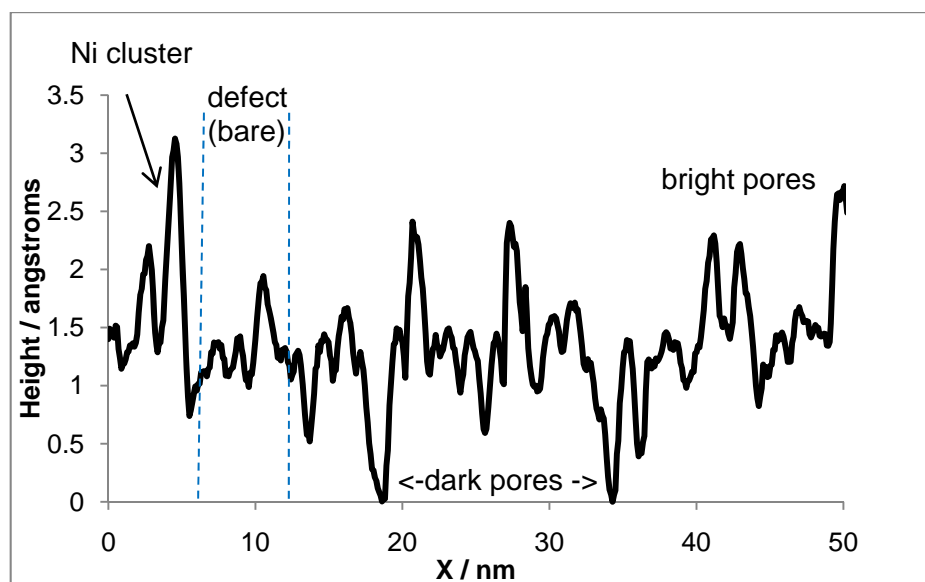


Figure 5.36 Height profile along the flat line across network of figure 5.35

A height difference of 2.4-2.6 Å is suggested between the bright pores and the dark pores; alone, the fact that the height difference between a bright pore and

dark pore is comparable with the height difference between a Ni island and the Au surface would suggest that the bright pores host Ni atoms. However, because the height profiles generated are influenced by electronic effects, this argument is not watertight and as the height difference between a Ni island and a dark pore is perhaps too large at 3.1 Å relative to the height difference between nickel islands and the gold surface previously observed<sup>5</sup> of 1.9 Å.

Certainly, it seems pores never become completely filled but there is definitely a case for stating that for Ni coverages up to 0.1 ML, Ni can be stored within the networks for a period of time. The network fails to act as a template for nickel growth as attempts to fill the pores by the deposition of further quantities of Ni lead to the destruction of the structure.

#### 5.4.2.3 Hexagonal Phase

The hexagonal network<sup>1</sup> was observed under two sets of conditions during this study. On many occasions after co-deposition of both network components, the capped mixed phase (Section 5.4.2.1) was the only phase present on the surface despite annealing in the range 323-353 K for several hours with monitoring at intervals. The capped mixed phase could be only be disrupted by annealing the surface to a higher temperature; after heating to 373 K for less than 5 minutes, most of the capped mixed phase was converted to parallelogram phase but the hexagonal phase was produced as a by-product (figure 5.32, above).

The PTCDI-melamine hexagonal phase was also seen to form after samples bearing a low coverage of PTCDI were subject to limited exposures of melamine (figure 5.37). Under these conditions no annealing of the surface was required to ensure every domain of PTCDI on the surface was either converted to the hexagonal phase or have a substantial growth of the hexagonal phase around its edges.

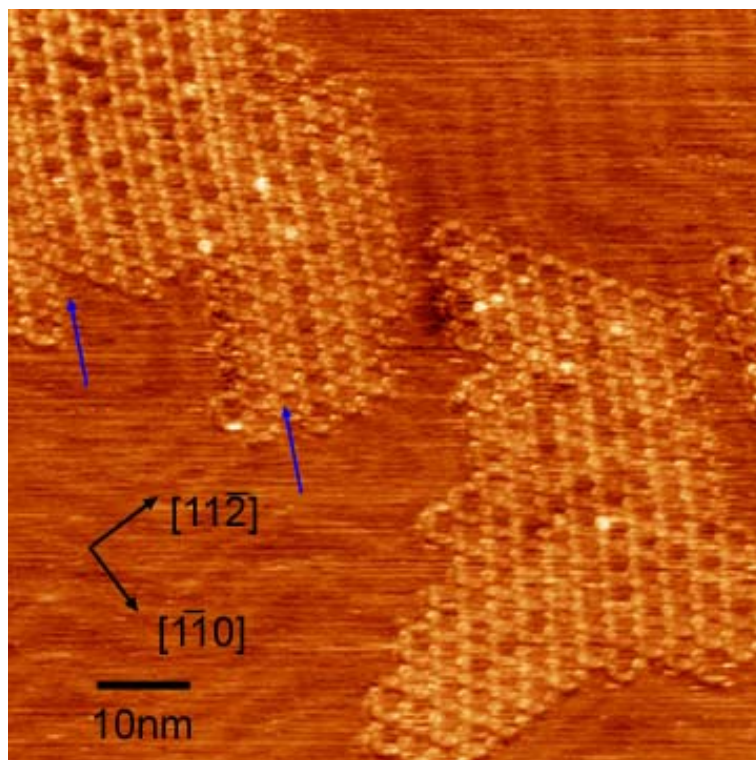
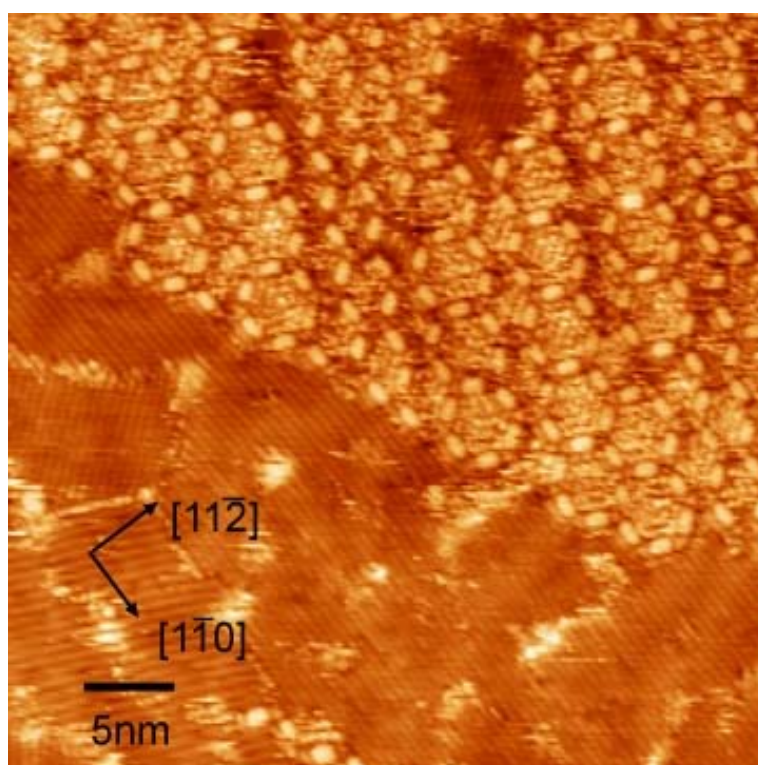


Figure 5.37 STM image of the hexagonal network formed between PTCDI and melamine. Blue arrows indicate defect rows of parallelograms (84.7 x 84.7 nm, -1.5V, 0.2 nA).

These results suggest that the annealing conditions (duration and temperature) are not as important in the formation of the hexagonal network – given that the desorption temperature of the limiting component, melamine, is not exceeded – as the coverage of the two components. The quantities of the two components have to be sufficiently large that they meet, yet be low enough to allow space on the surface for mixing via diffusion and expansion of close-packed domains.

The hexagonal structure observed here adheres closely to the dimensional parameters elucidated by Perdigão et al<sup>1</sup>, the periodicity of the network is  $\sim 34.6$  Å, centre-to-centre separation of vertex melamine molecules along the edge of a hexagon is  $\sim 20.5$  Å, the principal axes of the hexagonal structure were found to be orientated  $30^\circ$  to the  $\langle 11\bar{2} \rangle$  direction in this study.

The surface reconstruction has been shown to influence the integrity of the structure and frequently defects occur in the structure. Parallelogram pores are often seen to form between domains of hexagons, these are stabilised by more complex hydrogen bonded attractions between melamine molecules and PTCDI molecules of adjacent domains, they often lie along the crystallographic equivalent directions of the  $\langle 11\bar{2} \rangle$  direction. The study of Perdigão et al<sup>1</sup> acknowledges the occurrence of these parallelogram defects, but Silly et al<sup>16</sup> observe a regime whereby defect rows of parallelograms occur around every 6.3 nm, two hexagon rows apart, at every boundary between fcc and hcp region along equivalents of the  $\langle 11\bar{2} \rangle$  direction.



**Figure 5.38** STM image of a domain of hexagonal phase where defects are abundant. In this area, the hexagons formed by PTCDI and melamine exist as single rows and do not form a consistent honeycomb structure (42.0 x 42.0 nm, -1.5 V, 0.4 nA).

Whilst the same direction of the defect rows is found here, the strict regularity in which they appear is not. In figure 5.37, 6 rows of hexagons separate two rows of defect parallelograms, but in figure 5.38, the frequency of faults is so high that parallelogram rows alternate with single hexagon rows. The overall domain boundaries tend to be shaped by the surface reconstruction underneath, and can be

seen in figure 5.37, the edges of the domain tend to coincide with the ridged boundaries between hcp and fcc regions of the surface, thus the height difference between these areas must represent a significant barrier for expansion of the network.

### *Nickel Deposition*

Immediately, after the deposition of nickel (<0.1 ML), the contrast of the molecules is seen to vary across domains of hexagonal network and its appearance becomes blurred (figure 5.39). After the deposition, the molecules of the network rarely appear as bright features and instead the network pore walls are depicted as dark outlines.

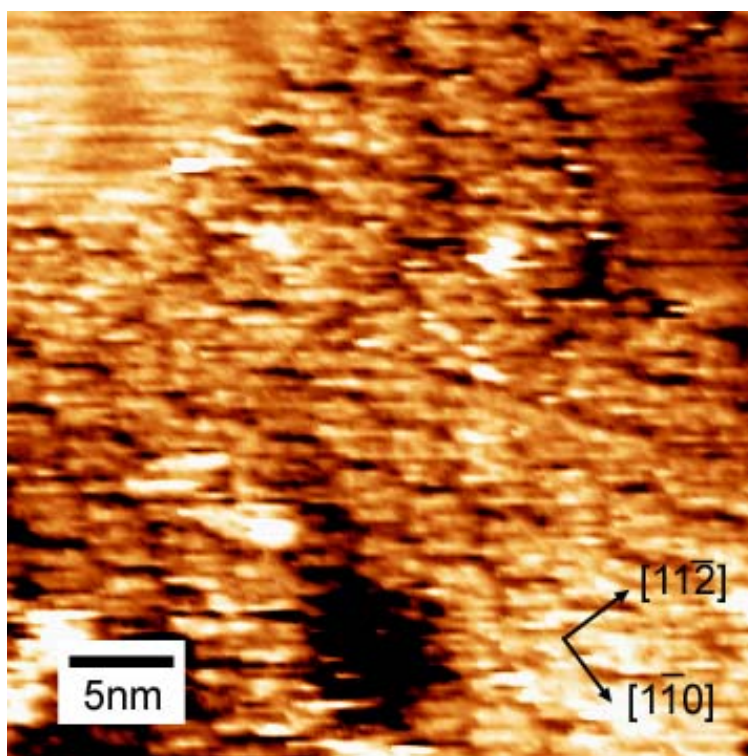


Figure 5.39 STM image of an area of PTCDI-melamine hexagonal network immediately after deposition of 0.08 ML Ni (35.8 nm x 35.8 nm, -1.5 V, 0.2 nA)

Within the pores, features resembling the ‘heptamer’ arrangements that had are formed by fullerenes when deposited into the PTCDI-melamine network, however, in this case, it would be implausible to assign ‘heptamers’ as 7 Ni atoms

given the mismatch in size between the lobes of the features ( $\sim 10 \text{ \AA}$ ) and a Ni atom ( $2.7 \text{ \AA}$ ). There may be more or less than 7 particles trapped within the pores, each with a diffusion rate greater than the rate of scanning, and as such the same particle may be imaged multiple times and as a result the STM image builds up a map showing where - highlighting the 7 positions the probability of mobile particles being located is highest.

A few hours after the deposition of nickel, the 'heptamer' features are no longer observed and the features within the network take on a different appearance. Discrete bright features are seen within and around the outside of honeycomb network, they are oval and around  $6\text{-}7 \text{ \AA}$  in length, they are always associated with the vertices of the hexagons; the pores usually contain 6 of these features. In figure 5.40, the features within the honeycomb pores are seen to resemble the minute growths of Ni that have begun to form in the elbows of the surface reconstruction.

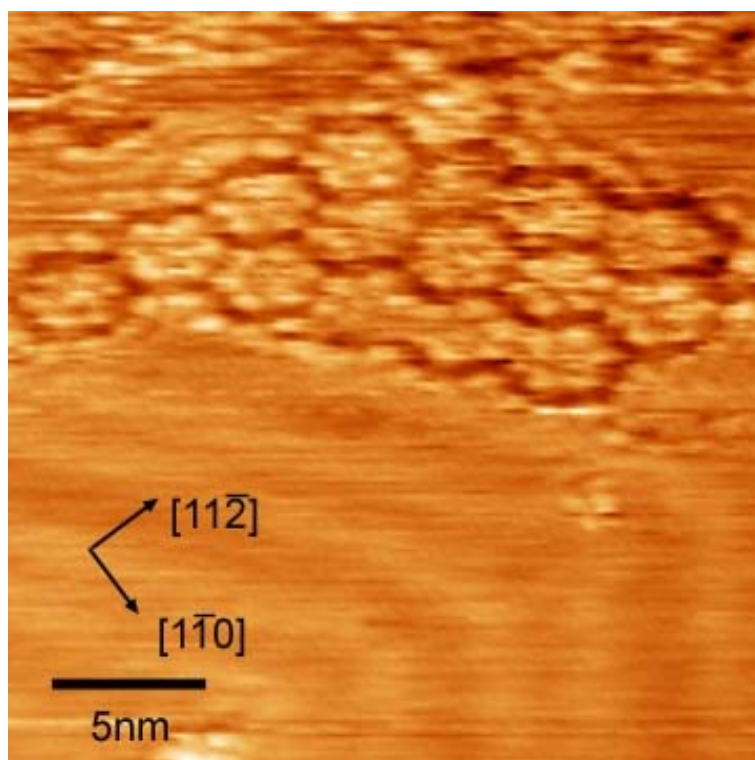


Figure 5.40 STM image of an area of PTCDI-melamine hexagonal network around two hours after deposition of 0.08 ML Ni ( $-1.5 \text{ V}$ ,  $0.2 \text{ nA}$ ).

The features are the vertices of the honeycomb pores on the inside and outside of the network may consist of two nickel atoms, each associated with one of the PTCDI molecules that converge to hydrogen bond with a vertex melamine molecule, and this proposal is illustrated in figure 5.41.

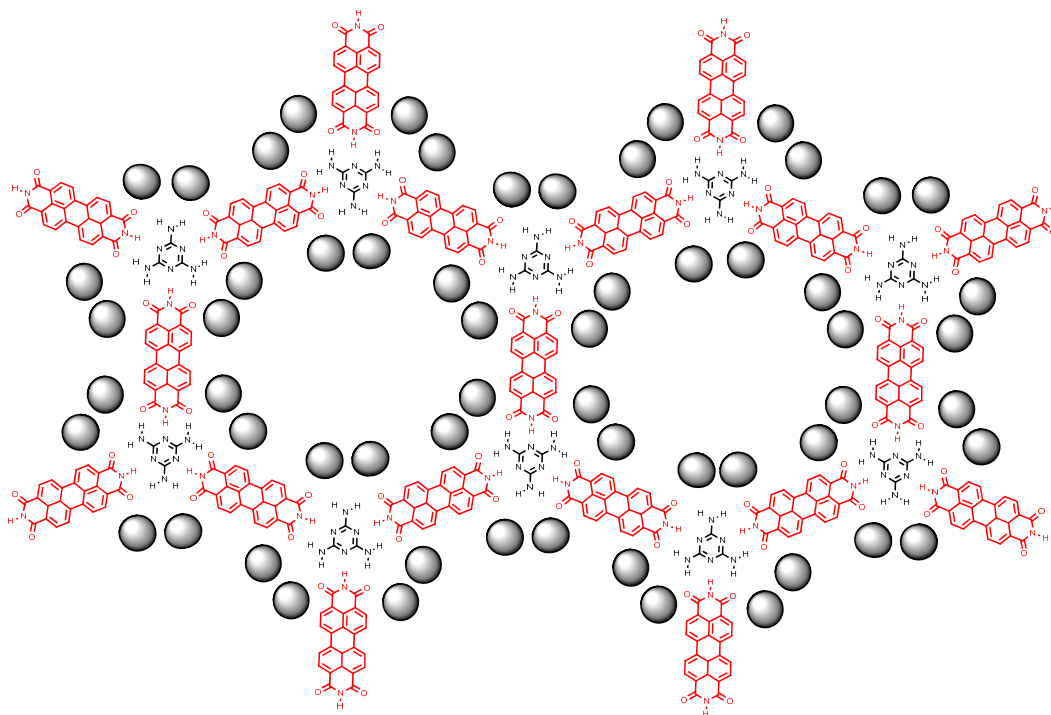


Figure 5.41 Model of honeycomb network hosting metal atoms

The parallelogram pores that form as defects within domains can be seen, in figure 5.42, to contain two bright features that are similarly sized to those in figure 5.40, this is illustrated in figure 5.43.

The smaller domains of hexagonal phase have shown discrete features within their pores. However, it is unclear how they have been filled, perpendicularly via evaporation or laterally via diffusion. The centre of one of the larger domains of hexagonal phase, in figure 5.42, appears very blurred, it is difficult to determine whether the network appears this way because those pores have been over-filled and nickel obscures pore walls or the pores are emptier and the lack of resolution is caused by greater mobility because particles have more space within which to move. If particles entered the pores via diffusion, pores in the centres of domains would be expected to have a lower occupancy of Ni atoms.

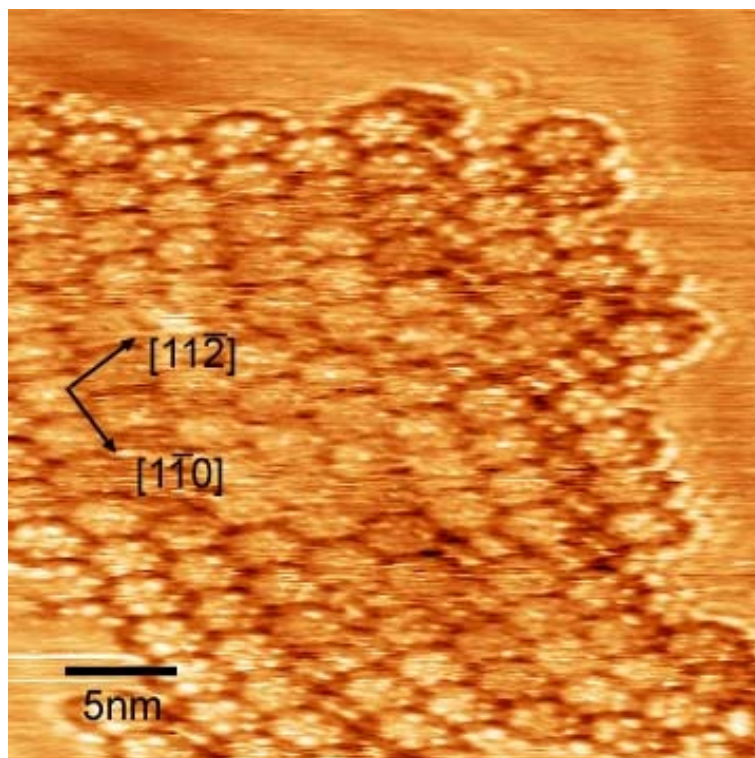


Figure 5.42 STM image of an area of PTCDI-melamine hexagonal network around two hours after deposition of 0.08 ML Ni, right, zoomed area (33.7 nm x 33.7 nm, -1.5 V, 0.2 nA).

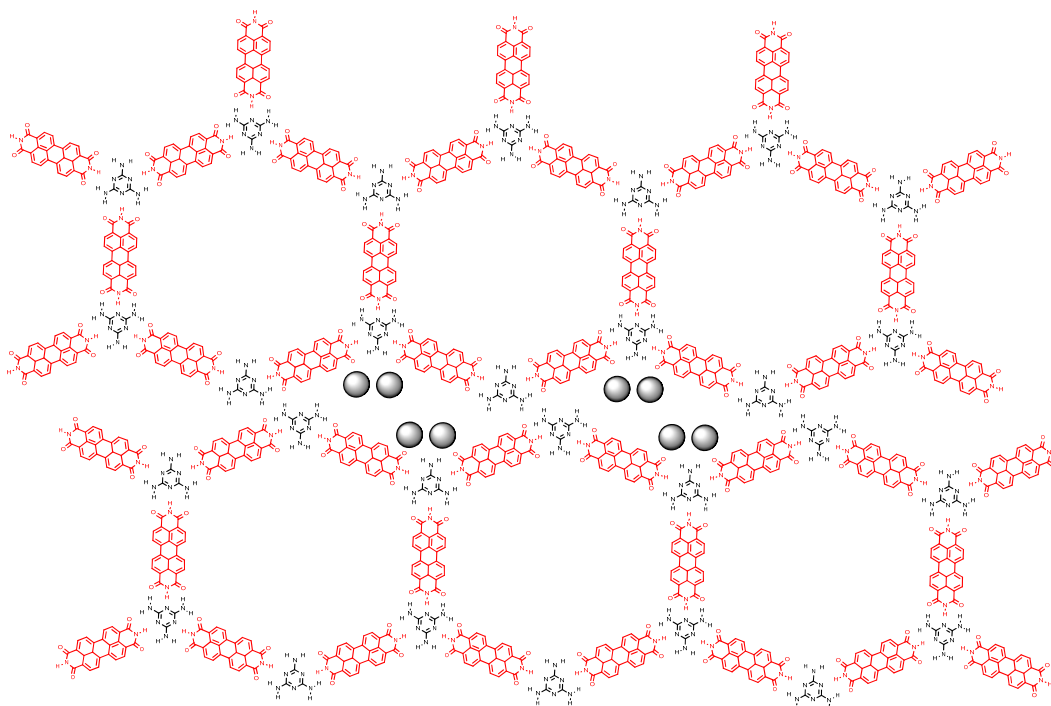


Figure 5.43 Model of the parallelogram spaces between hexagonal areas and proposed situation of Ni within them

The great hope of these experiments was to grow larger, well-defined Ni clusters – of the size and shape of the network pores - but complete obliteration of the hexagonal phase is observed either through time or by increasing the nickel coverage. Where only 0.08 ML coverage was present and networks were thought to contain small amounts of nickel, disordered structures are observed after a day. Increasing the nickel coverage, even to 0.15 ML, accelerates the attainment of the same result, although it was noted that parallelogram and capped mixed phase domain were more robust towards the presence of Ni; the edges of these domains became littered by chains and ladders similar to those previously observed after deposition of PTCDI on Ni/Au(111) surfaces, figure 5.44 shows an example of adjacent PTCDI and mixed phase domains surrounded by metal-organic chains.

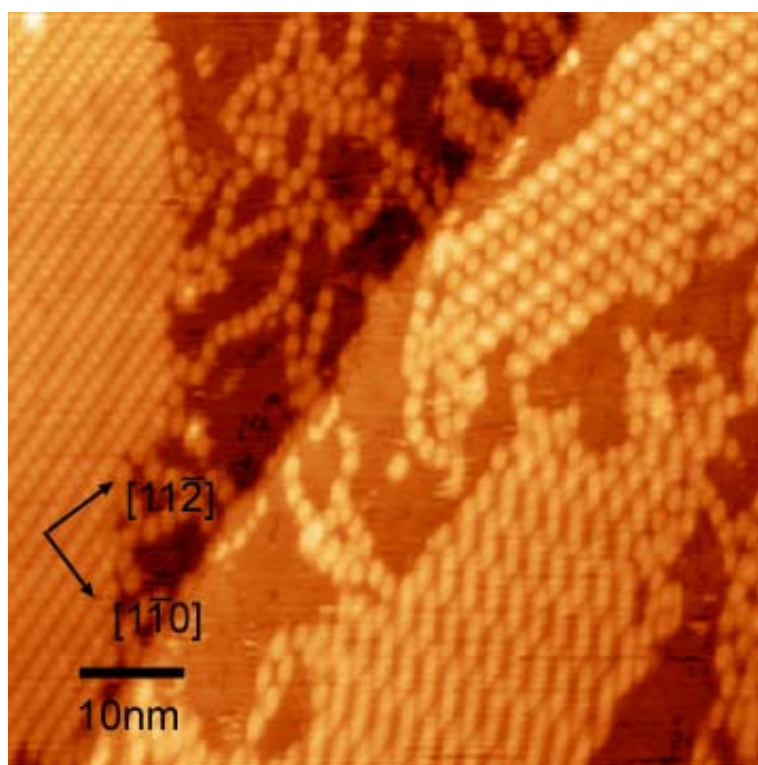


Figure 5.44 STM image showing chains incorporating nickel at the edge of domains occurring after nickel coverage is 0.15 ML. (72.3 nm x 72.3 nm, 1.5 V, 0.2 nA).

Linear chains with centre-to-centre separations in the range 16-18 Å are thought to consist of only PTCDI and Ni, with their structure as described in Chapter 4. Thinner chains of centre-to-centre separation between parts of around 8 Å are

thought to be comprised of melamine and Ni. More crooked chains where the centre-to-centre separations between their brightest features are more than 20 Å most likely result from combination of both PTCDI and melamine with nickel.

Structures consisting of pores of irregular dimensions appear are generated from the destruction of hexagonal networks, although amongst the amorphous array, a few symmetrical hydrogen-bonded hexagons can be seen to remain intact (figure 5.45). Although nickel is most likely incorporated into the pore walls of these formations, it is also probable that the nickel exists within them. The widespread disruption and lack of periodicity within these formations is not completely unexpected given the results from the experiments where melamine was deposited on Ni/Au(111) surfaces; high reactivity between nickel and melamine was evident by the abundance of new structures created.

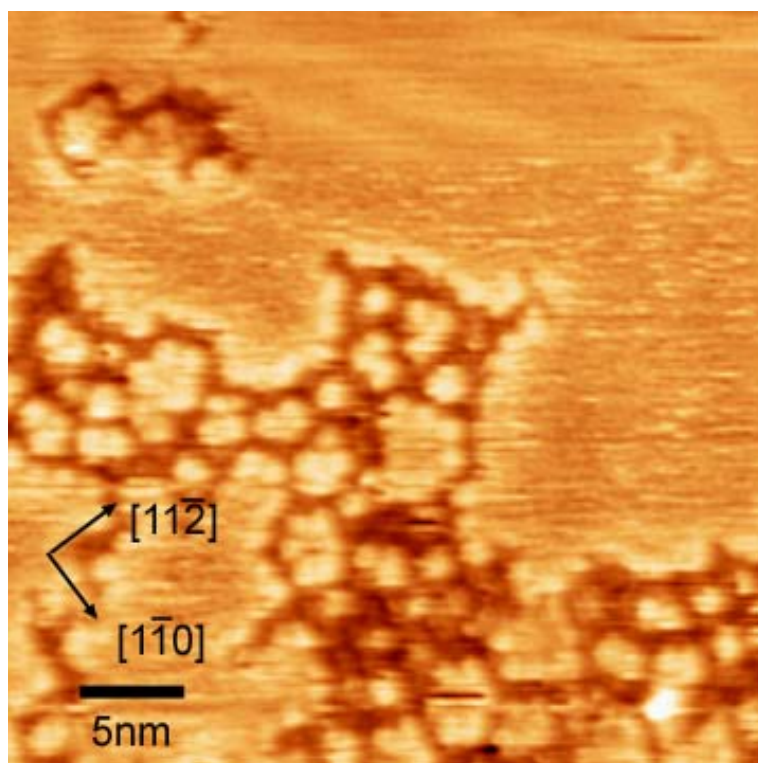


Figure 5.45 STM image taken 20 hours after 0.2 ML Ni had been deposited on a sample previously hosting hexagonal networks (36.0 nm x 36.0 nm, -2.0 V, 0.2 nA)

The differing reactivity of each phase toward metal coordination can most likely be explained by the availability of melamine. Melamine more readily undergoes

coordination with nickel. Phases where melamine molecules are more exposed to diffusing nickel atoms might be expected to be less robust. The capped mixed phase and the parallelogram phase show more resistance than the hexagonal network which has melamine present within its pore walls and adjacent to the apparent nucleation points of nickel particles in the vertices of the hexagonal pores, as the porous structure is very open, it is very easy to break apart. Although the parallelogram phase is porous, its melamine molecules are shrouded by PTCDI molecules within the stiles of the framework, whilst within the capped mixed phase, the melamine molecules are trapped in enclaves protected by PTCDI barriers.

## 5.5 Conclusions

The TPD spectra of the individual network components on Au(111) are thought to be strongly affected by hydrogen bonding. The TPD spectra, of PTCDI in particular, are characterised by broader peaks which are thought to be generated by the slow, gradual break-up of vast islands that consist of molecules in many different adsorption sites that can be assigned different activation energies of desorption based on the number of hydrogen bonding interactions experienced. Simple spreadsheet models based on each of the observed surface assemblies of PTCDI and melamine and layer-by-layer desorption from the edges of molecular islands seem to simulate experimental results fairly well.

The process of PTCDI desorption from Au(111) is very different from that observed on Ni(111). On Ni(111), the adsorbate-substrate interaction is thought to be dominant and the spectra is made up of three areas: a low T peak (molecules thought to be molecules not lying parallel to the surface), the main desorption peak of molecules with  $E_d$  ranging 100-120 kJ mol<sup>-1</sup> and a broad high T desorption of molecules thought to have formed metal-organic complexes and of  $E_d$  up to 170 kJ mol<sup>-1</sup>. On Au(111), a single broad peak is observed. Molecules were assigned  $E_d$  values ranging 84-174 kJ mol<sup>-1</sup> based on their position within

molecular islands. The most important  $E_d$  value was  $144.3 \text{ kJ mol}^{-1}$ ; this corresponded to a number of sites on the edges of PTCDI islands. The interaction between PTCDI and the Au(111) surface is thought to be very weak but the formation of intermolecular hydrogen bonds can result in the desorption activation energy of a large proportion of molecules being greater than that of molecules on Ni(111), where the adsorbate-substrate interaction is greater.

Strong adsorbate-substrate interactions are thought to dominate the behaviour of melamine on Ni(111). The desorption of melamine from Ni(111) generated a stepped low T peak which could be simulated by estimated desorption activation energy values of  $75 \text{ kJ mol}^{-1}$  and  $87 \text{ kJ mol}^{-1}$ . The spectrum features a long, slow decay through the high T range; this might be caused by molecules that have formed metal-organic complexes with adatoms (as observed for PTCDI) or molecules that form stronger bonds to the surface. Unfortunately, a high background pressure renders this area of the spectrum difficult to analyse. On Au(111), a single sharp peak in the TPD spectra was observed. Like PTCDI, this could be interpreted by assigning  $E_d$  values to different positions within hydrogen bonded melamine arrays and a layer-by-layer desorption process could be applied. The most important site in controlling the position of the simulated desorption peak was a position on the edge of molecular islands for which  $E_d$  was estimated as  $91 \text{ kJ mol}^{-1}$ . The values of  $E_d$  for melamine from each surface is comparable but the interactions which control these values are different. On Au(111), the ability to form intermolecular hydrogen bonding arrays compensates for the weak adsorbate-substrate interaction. The thermal stability of melamine on Ni(111) can mostly be attributed to adsorbate-substrate interactions as little evidence of ordered hydrogen bonded arrangements are observed using STM.

TPD experiments involving both components are difficult to control (and interpret) in the absence of STM to indicate the phases adopted by the molecules upon the surface prior to beginning the temperature ramp. The presence of melamine seems to have the effect of prolonging the existence of PTCDI on the surface to higher temperatures but the vastly different  $E_d$  between melamine and

PTCDI and the uncertainty over the surface configurations means that it is impossible to attribute this effect solely to the formation of bicomponent hydrogen bonded phases or specifically one phase, particularly, when the opposite effect is not observed in the melamine desorption spectra. The presence of PTCDI increases the sticking probability of melamine to the surface and increases its thermal stability on the surface. The bicomponent TPD spectra suggest that melamine is still on the Au(111) surface at around 440 K which is at least 50 K higher than when no PTCDI is present.

The STM experiments show that construction of the hexagonal network is not straightforward as there is a narrow range of conditions of not only temperature, but also coverage within which the hexagonal network may assemble. Intermixing of PTCDI and melamine is shown to occur readily but the parallelogram and the capped mixed phases are more prevalent. The capped mixed phases are previously unreported but their structure appears to incorporate aspects of the previously reported parallelogram and mixed phases. Similar to the reported mixed phase, this arrangement can be expanded to incorporate more melamine. Other PTCDI-melamine bicomponent phases are observed, these usually only vary slightly from the three principal phases and are present in low abundance.

The results of nickel deposition show that the PTCDI-melamine H-bonded network cannot be used to control the distribution and growth of metal atoms. Although small quantities of nickel are captured by the porous phases, nickel still tends to nucleate in the elbows of the surface reconstruction. Small groups of nickel atoms are thought to reside by the vertices of the PTCDI-melamine hexagonal network for up to 20 hours before they cause the disruption of the network and are incorporated into new, disorganised metal-organic structures. Unfortunately, the very same functional groups which allow the formation of a hydrogen bonded structure are amenable to metal coordination and these stronger interactions are favoured leading to network destruction.

Both components have been shown in the previous chapter to form metal-organic structures with nickel although melamine exhibits much higher tendency to react with Ni at room temperature ergo the destruction of the hexagonal network and the relative robustness of the parallelogram and capped mixed phase (which both show some signs of disruption) can be explained in terms of availability of melamine to nickel adatoms which are diffusing freely across the surface.

## 5.6 References

- (1) Perdigao, L. M. A.; Perkins, E. W.; Ma, J.; Staniec, P. A.; Rogers, B. L.; Champness, N. R.; Beton, P. H. *Journal of Physical Chemistry B* **2006**, *110*, 12539
- (2) Silly, F.; Shaw, A. Q.; Porfyraakis, K.; Briggs, G. A. D.; Castell, M. R. *Applied Physics Letters* **2007**, *91*, 253109 .
- (3) Perdigao, L. M. A.; Staniec, P. A.; Champness, N. R.; Beton, P. H. *Langmuir* **2009**, *25*, 2278.
- (4) Madueno, R.; Raisanen, M. T.; Silien, C.; Buck, M. *Nature* **2008**, *454*, 618
- (5) Silien, C.; Raisanen, M. T.; Buck, M. *Angewandte Chemie-International Edition* **2009**, *48*, 3349.
- (6) Silien, C.; Raisanen, M. T.; Buck, M. *Small* **2009**, *6*, 391.
- (7) Chambliss, D. D.; Wilson, R. J.; Chiang, S. *Physical Review Letters* **1991**, *66*, 1721.
- (8) Stepanow, S.; Lin, N.; Barth, J. V.; Kern, K. *Journal of Physical Chemistry B* **2006**, *110*, 23472.
- (9) Zhang, Y. F.; Zhu, N.; Komeda, T. *Surface Science* **2008**, *602*, 614.
- (10) Auwarter, W.; Weber-Bargioni, A.; Brink, S.; Riemann, A.; Schiffrin, A.; Ruben, M.; Barth, J. V. *Chemphyschem* **2007**, *8*, 250.
- (11) Flechtner, K.; Kretschmann, A.; Bradshaw, L. R.; Walz, M. M.; Steinruck, H. P.; Gottfried, J. M. *Journal of Physical Chemistry C* **2007**, *111*, 5821.
- (12) Gottfried, J. M.; Flechtner, K.; Kretschmann, A.; Lukasczyk, T.; Steinruck, H. P. *Journal of the American Chemical Society* **2006**, *128*, 5644.
- (13) Breitruck, A.; Hoster, H. E.; Meier, C.; Ziener, U.; Behm, R. J. *Surface Science* **2007**, *601*, 4200.

- (14) Schiffrin, A.; Reichert, J.; Auwarter, W.; Jahnz, G.; Pennec, Y.; Weber-Bargioni, A.; Stepanyuk, V. S.; Niebergall, L.; Bruno, P.; Barth, J. V. *Physical Review B* **2008**, *78*, 035424.
- (15) Theobald, J. A.; Oxtoby, N. S.; Phillips, M. A.; Champness, N. R.; Beton, P. H. *Nature* **2003**, *424*, 1029-1031.
- (16) Silly, F.; Shaw, A. Q.; Briggs, G. A. D.; Castell, M. R. *Applied Physics Letters* **2008**, *92*, 023102.
- (17) Staniec, P. A.; Perdigao, L. M. A.; Saywell, A.; Champness, N. R.; Beton, P. H. *Chemphyschem* **2007**, *8*, 2177.
- (18) Saywell, A.; Magnano, G.; Satterley, C. J.; Perdigao, L. M. A.; Champness, N. R.; Beton, P. H.; O'Shea, J. N. *Journal of Physical Chemistry C* **2008**, *112*, 7706-7709.
- (19) Silly, F.; Shaw, A. Q.; Castell, M. R.; Briggs, G. A. D. *Chemical Communications* **2008**, 1907.
- (20) Horcas, I.; Fernandez, R.; Gomez-Rodriguez, J. M.; Colchero, J.; Gomez-Herrero, J.; Baro, A. M. *Review of Scientific Instruments* **2007**, *78*, 013705.
- (21) Mura, M.; Gulans, A.; Thonhauser, T.; Kantorovich, L. N.; *Physical Chemistry Chemical Physics* **2010**, *12*, 4759-4767.
- (22) Sales, J. L.; Zgrablich, G. *Physical Review B* **1987**, *35*, 9520-9528.
- (23) Weber, U. K.; Burlakov, V. M.; Perdigao, L. M. A.; Fawcett, R. H. J.; Beton, P. H.; Champness, N. R.; Jefferson, J. H.; Briggs, G. A. D.; Pettifor, D. G. *Physical Review Letters* **2008**, *100*, 156101.
- (24) Canas-Ventura, M. E.; Xiao, W.; Wasserfallen, D.; Mullen, K.; Brune, H.; Barth, J. V.; Fasel, R. *Angewandte Chemie-International Edition* **2007**, *46*, 1814.
- (25) Swarbrick, J. C.; Ma, J.; Theobald, J. A.; Oxtoby, N. S.; O'Shea, J. N.; Champness, N. R.; Beton, P. H. *Journal of Physical Chemistry B* **2005**, *109*, 12167.
- (26) Mura, M.; Martsinovich, N.; Kantorovich, L. *Nanotechnology* **2008**, *19*, 14.
- (27) Syomin, D.; Kim, J.; Koel, B. E.; Ellison, G. B. *Journal of Physical Chemistry B* **2001**, *105*, 8387.
- (28) Wetterer, S. M.; Lavrich, D. J.; Cummings, T.; Bernasek, S. L.; Scoles, G. *Journal of Physical Chemistry B* **1998**, *102*, 9266.

## 6 Covalent Self-assembly

Hydrogen bonding has been utilised in the synthesis of many elegant supramolecular surface structures, the directionality of hydrogen bonds can often be relied upon to generate predictable or desirable target phases, but in some cases, a multitude of phases result upon the same surface. Of course, hydrogen bonds are only very weak interactions (the strength of a hydrogen bond<sup>1</sup> is usually in the range 8-80 kJ mol<sup>-1</sup>), thus the stabilisation energies between different hydrogen bonded phases may not vary greatly, and the steric hindrance provided by the surface or by a higher coverage of adsorbates may prevent the most stable hydrogen bonded configuration being adopted. Within the PTCDI-melamine bicomponent system, a range of phases have been reported and further phases have been observed in Chapter 5. Although modelling studies have been carried out in order to try to predict the annealing conditions that will yield porous or compact phases<sup>2</sup>, there are still too many possible arrangements of PTCDI and melamine within these two broad categories and the probability of mixtures of phases and transitions between them is too high. Stoichiometry of the components in each phase is vital; controlling overall surface coverage of each component by vapour deposition in UHV is difficult, and although the solution-based deposition in ambient conditions allows for more accurate quantification of the deposition parameters, controlling localised surface coverages which ultimately produce the stoichiometry of each phase is nearly impossible.

Not only are hydrogen bonded structures susceptible to thermally induced change, they are vulnerable towards competition from other supramolecular interactions; PTCDI molecules are reasonably large and isotropic van der Waals interactions play a part in the stabilisation of some of the less predictable phases, such as the mixed phase<sup>3</sup> or the parallelogram phase<sup>4</sup>. However, these interactions are insignificant in comparison to metal-organic interactions which render the PTCDI-melamine networks unsuitable for their intended purpose of controlling the distribution of metal particles. Unfortunately, the same functional groups

which allow hydrogen bonding networks to form are also amenable to metal coordination and responsible for their degradation, thus a new strategy has to be developed for the achievement of stable modifying overlayers upon metal surfaces.

An attractive alternative may be the fabrication of nanostructures via the formation of covalent linkages on surfaces. However, it is only very recently that covalent reactions have been employed in the formation of 2-D nanostructures on surfaces with the goal of creating extended structurally defined, periodic structures of superior robustness and rigidity and the discovery of reaction systems that yield ordered surface networks is at a very early stage. One of the advantages of self-assembly is the ability of domains of molecules held together by non-covalent interactions to ‘self-heal’, eliminate defects and create uniformity. By employing a strategy based on the formation of new covalent linkages, this benefit is lost as components may become locked in place by the formation of new bonds regardless of their position. At the outset, formation of a completely ordered covalent network may be an unattainable goal but incorporation of functionality into surface polymers may ensure that they are still able to interact with further adsorbates (potentially, prochiral reagents) in a way that is beneficial.

## 6.1 Surface-confined Covalent Reactions

Surface-confined thermally-induced polymerizations via debromination of porphyrins<sup>5</sup> or 1,3,5-tris(4-bromophenyl)benzene<sup>6</sup>, via condensation reactions between aldehydes and amines<sup>7</sup> and between anhydrides and amines<sup>8,9</sup>, via nucleophilic attack of acyl chlorides by amines<sup>10</sup> and of N-heterocyclic compounds via carbene intermediates<sup>11</sup> have recently been reported. The surface can be used to promote two-dimensional polymerization reactions as has been demonstrated by Lipton-Duffin et al<sup>12</sup> and Blake et al<sup>13</sup> who both report examples of Ullmann coupling reactions of diiodobenzene on Cu(110), whilst it is proposed

that surface may be vital to the mechanisms of other unusual reactions such as the conversion of octylamine to trioctylamine on Au(111)<sup>14</sup> and the formation of multiporphyrins on Cu(110)<sup>15</sup>.

In this study, with the use of STM in UHV and in ambient conditions, the formation of polymer networks on Au(111) are investigated. A primary aim of the work is to form 2-D covalently bonded networks with a defined functionality which can later be utilized in molecular recognition in applications such as (enantio)selective catalysis or (bio)sensors. Ideally, the covalent network created would incorporate hydrogen bond donors or acceptors to enable interaction with guest molecules. Figure 6.1 illustrates the potential hydrogen bonding interaction between a polymer containing urea groups and molecules of methyl acetoacetate, a prochiral species. Section 6.3 concentrates on the formation of polyurea networks on the Au(111) surface; to this end, a range of reactions involving both aromatic and aliphatic amines and isocyanates are carried out under various deposition conditions. Section 6.4 looks at the formation of polyamide networks: examples of two possible routes to polyamides are examined. Section 6.4.1 investigates the reaction of an isocyanate species, 1,4-phenylene diisocyanate, with a tricarboxylic acid, benzene-1,3,5-triyl-tribenzoic acid. Section 6.4.2 looks at the reaction of an acid chloride species, trimesoyl chloride, with an amine species, melamine.

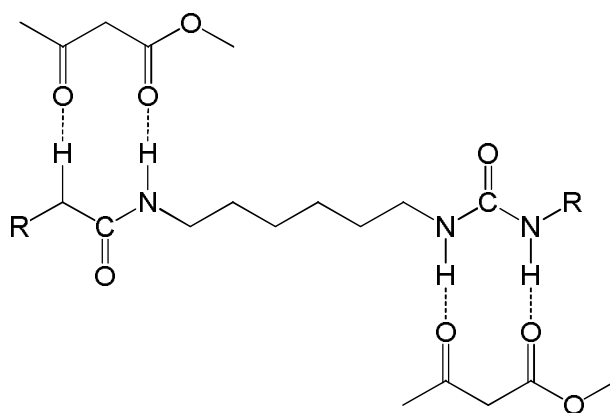


**Figure 6.1** Potential docking interaction between a polyurea network with a methyl acetoacetate, a prochiral reagent.

## 6.2 Experimental

In this chapter, the formation of surface-supported polyurea structures in both UHV and ambient conditions is investigated. As well as investigating polyurea networks, two different methods of producing polyamide networks are also explored.

### 6.2.1 Ambient Conditions

Au/mica substrates (300 nm gold, Georg Albert PVD) were flame-annealed prior to immersion in reactant solutions. Immersion times were typically between 10 s and 30 s. Melamine (Sigma-Aldrich) was deposited from a saturated solution in DMF that was diluted 1:4. Diisocyanate and amino compounds (Sigma-Aldrich) were typically dissolved in THF to give 0.1 mM solutions. All STM measurements were carried out in air at room temperature using a Molecular Imaging Picoscan STM instrument. In all cases, tips were prepared mechanically by cutting a 0.25 mm Pt/Ir alloy (8:2, Goodfellow) wire. The data were collected in constant current mode.

### 6.2.2 UHV Conditions

The STM experiments were carried out in an Omicron UHV system with a base pressure of  $1 \times 10^{-10}$  mbar. The Au(111) sample was prepared by cycles of argon ion bombardment (1 kV) and annealing to 873 K until low energy electron diffraction (LEED) and STM indicated the presence of a clean Au(111) surface exhibiting the characteristic ( $\sqrt{3} \times 22$ ) herringbone reconstruction<sup>16</sup>. Melamine (Sigma-Aldrich) was heated to 363 K and sublimed onto the Au(111) substrate which was held at 300 K. 1,4-phenylene diisocyanate (Sigma-Aldrich) was sublimed by heating to 333 K. 1,3-phenylene diisocyanate (Sigma-Aldrich) and benzene-1,3,5-tricarbonyl chloride (trimesoyl chloride) (Sigma-Aldrich) were both leaked into the chamber after heating to 310 K using a high-precision leak

valve. Tris-(4-aminophenyl)-1,3,5-benzene was exposed to the sample after heating to 450 K. Images of the surface were acquired by transferring under UHV conditions to the STM chamber where data were taken in constant current mode using an electrochemically etched W tip. All STM images were acquired at room temperature. STM images were processed using WSxM software<sup>17</sup>.

### 6.2.3 Computational Theory

Theoretical calculations were performed by Dr H A Früchtl of the EaStChem Research Computing Facility. Simulations on the isolated molecules were carried out with Gaussian 03<sup>18</sup>, employing density functional theory (DFT) using the M05-2X meta-GGA functional<sup>19</sup> and 6-311+g\* basis set<sup>20</sup>. The proposed phases on the gold surface were modelled by periodic DFT calculations using the SIESTA program<sup>21</sup>, employing the PBE functional<sup>22</sup>, a numerical split-valence PAO (pseudo-atomic orbital<sup>23</sup>) basis set with polarization functions (SVP) and Troullier-Martin pseudopotentials<sup>24</sup> as available from the SIESTA web site. Based on the assumption that the geometry of the adsorbate layer is predominantly determined by the H-bond network and other intermolecular interactions rather than chemical interactions with the gold atoms, only the molecular layer was incorporated into the calculations. The effect of the Au surface was simulated by constraining all carbon atoms into a plane. This allowed the optimisation of the cell geometries based on the intermolecular interactions. The unit cell length orthogonal to plane of the molecular network was kept at 20 Å; all other lattice parameters were optimised.

## 6.3 Formation of surface-supported polyurea networks

Isocyanates are an important class of compounds, they are key to the formation of polyurethanes and polyureas, two types of polymer that have huge ranges of applications such as foams, coatings and adhesives. The isocyanate group (-N=C=O) is particularly reactive to compounds that contain a mobile hydrogen

atom of the type X-H and addition reactions typically occur at the N=C bond<sup>25</sup> (Figure 6.2). Amine groups react with isocyanate groups to produce urea compounds, these reactions often take place readily in solution at room temperature; furthermore, it is well-established that a diisocyanate can react with a polyamine to produce a polyurea. The urea linkage (-NH-CO-NH-), itself, is highly useful; because it contains three bonds amenable to hydrogen bonding, it is vital in many systems that rely upon molecular recognition<sup>26</sup>.

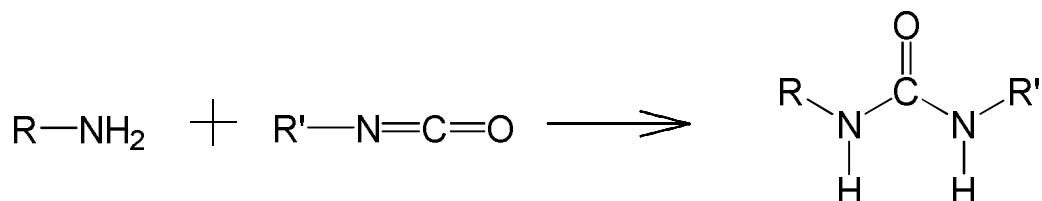


Figure 6.2 Coupling reaction between an amine and an isocyanate to form a urea

Studies of isocyanate/amine-coupling reactions at surfaces have been carried out at or near to room temperature, in both UHV<sup>-27</sup> and solution<sup>28-30</sup>-based environments with the aim of producing 3-D urea structures, but in this study, the possibility of creating extended 2-D networks is explored by co-deposition of a series of potential reactants.

## Results and Discussion

### 6.3.1 Melamine and 1,4-phenylene diisocyanate

The reaction between melamine and 1,4-phenylene diisocyanate (1,4-PDI) was carried out in both ambient and UHV conditions; initial experiments in ambient conditions indicated significant change, the reaction was repeated in UHV to take advantage of better imaging conditions to better understand the stages of the reaction and obtain improved images of the end products.

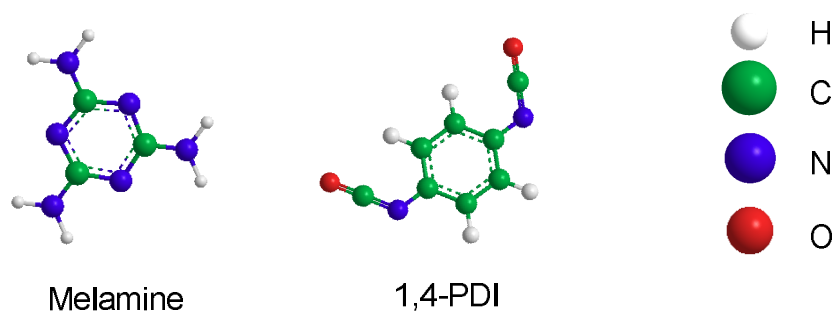


Figure 6.3 Components of the surface-confined reaction: melamine and 1,4-phenylene diisocyanate

Based upon the three-fold symmetry of melamine, the idealised product of the surface-confined reaction would be a hexagonal structure of fully covalent pore walls, as illustrated in figure 6.4.

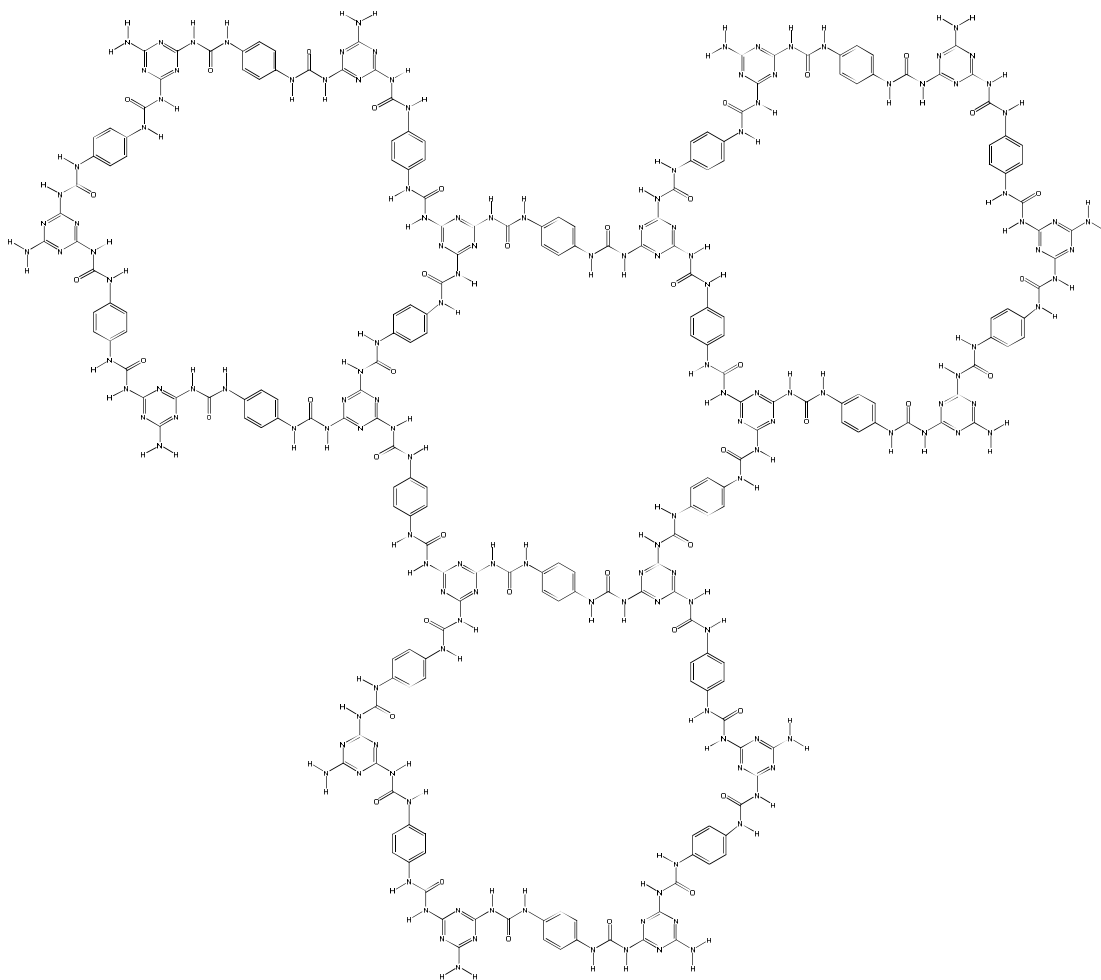


Figure 6.4 Model showing a small area of the ideal network formed by the trisubstitution of melamine units

### 6.3.3.1 Deposition of melamine and 1,4-PDI on Au(111) in ambient conditions

The initial situation after co-deposition of melamine and 1,4-PDI is shown in figure 6.5, two distinct types of feature are observed: brighter features similar to the amorphous stack features sometimes observed when 1,4-PDI is deposited separately on Au/mica from solution but also darker areas; these darker areas appear to have a degree of order. There are three main candidates for features in this area; melamine, which typically appear as darker features on Au(111), monolayer 1,4-PDI formations or new covalent structures. The domains appear as a series of rows but the lack of resolution does not allow further understanding as to the packing of the rows; the centre-to-centre separation across rows is approximately 9-10 Å, which is consistent with the unit cell lengths of the melamine two-dimensional assembly.

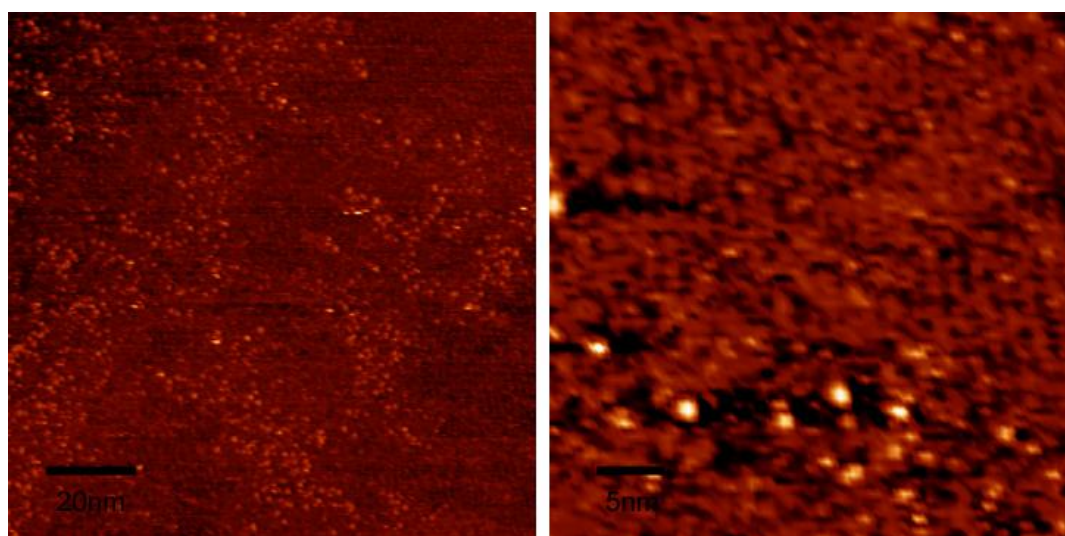


Figure 6.5 Initial STM image of the Au surface after co-deposition of melamine and 1,4-PDI, melamine is thought to form the ordered domains in the dark areas of the left hand image (117.2 nm x 117.2 nm, -1.5 V, 0.1 nA), this is shown in a zoom, right (38.4 nm x 38.4 nm)

These areas of ordered arrangements gradually disappear as scanning progresses which might suggest that they are consumed by the reaction. Covalent structures would be expected to be more robust and resistant to being ‘brushed’ by the STM tip, thus these domains can most likely be attributed to melamine. Although, the hexagonal packing arrangements are not immediately apparent, the features might

be thought of as rows of the pores within the hexagonal assemblies. The contrast is inconsistent across the domain shown in the zoomed image of figure 6.5 and this may be indicative of the intermixing and the beginning of a reaction.

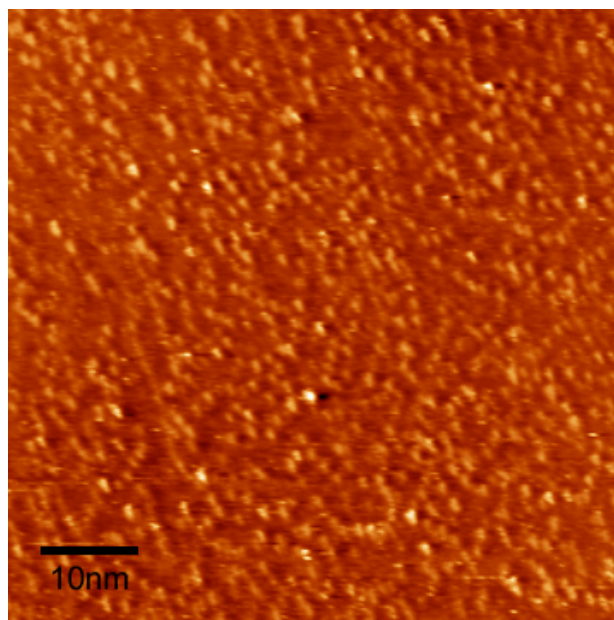


Figure 6.6 STM image two days after co-deposition of melamine and 1,4-PDI (63.1 nm x 63.1 nm, -1.5 V, 0.1 nA)

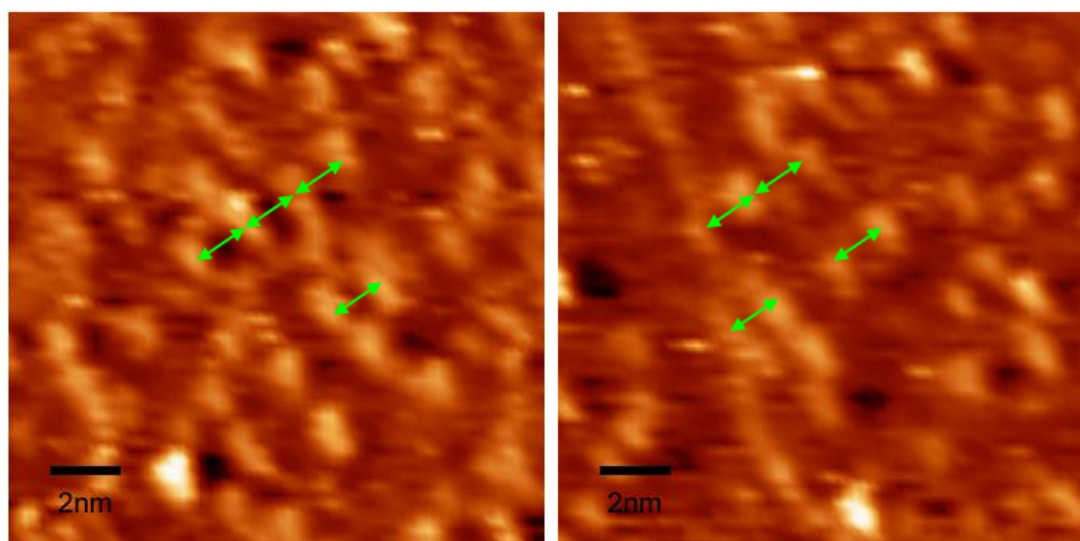


Figure 6.7 Zoomed sections of the STM image of figure 6.6 (left, 17 nm x 17 nm, right, 15 nm x 15 nm), green distances are equivalent to 15 Å.

Two days after co-deposition of the reactants, the ordered domains have completely disappeared and the surface is characterised by a population of bright features, mostly either tubular or triangular and sized about 2-3 nm, however, some larger strands exist, this is seen in figure 6.6. On closer analysis, a common

separation of 15 Å between some of the features can be measured, this is indicated by the green lengths in figure 6.7. This distance takes on more relevance when compared to the end result of the UHV study where it corresponds to the diameter of pores.

Furthermore, these surfaces can be exposed to a solution of C<sub>60</sub> fullerenes in toluene in attempt to yield a clearer impression of the surface topography; C<sub>60</sub> fullerenes would be expected to fill suitable pores and form densely packed islands on areas of bare surface. C<sub>60</sub> fullerenes is known to form close packed structures on the clean Au(111) surface<sup>31</sup>, where the centre-to-centre spacing between molecules is 1.0 nm. Figure 6.8 shows the surface after deposition of C<sub>60</sub>. The bright features can be attributed to C<sub>60</sub> fullerenes and it is assumed that darker area is completely occupied by molecular features. Some dense islands of fullerenes are visible and this probably corresponds to bare areas of the surface, but mostly, the fullerenes exist individually or in pairs and this may be fullerenes filling the pores within the polymeric networks, the fullerenes are not ordered upon the surface which indicates that the networks themselves are not regular and perhaps consist of aggregates of oligomers of different sizes, this is discussed later with respect to the better quality images captured in UHV.

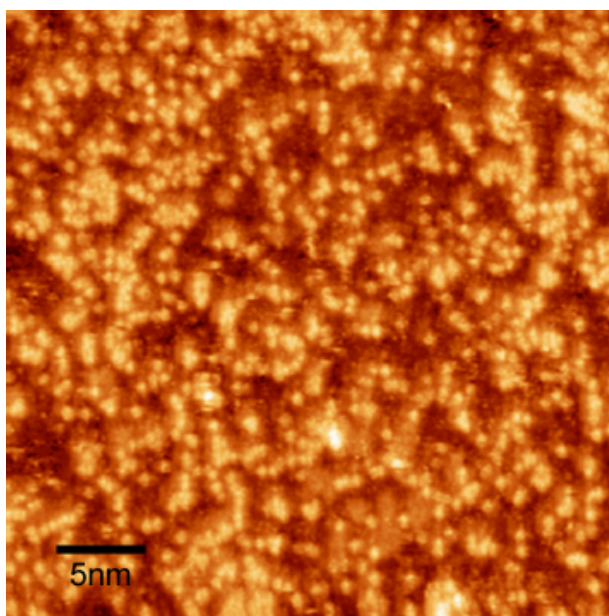


Figure 6.8 STM image taken after C<sub>60</sub> is deposited onto sample bearing melamine and 1,4-PDI (35 nm x 35 nm, -0.2 V, 0.1 nA)

### 6.3.1.2 Deposition of melamine and 1,4-PDI to Au(111) in UHV Conditions

Following the deposition of melamine and subsequently, 1,4-PDI, onto the clean Au(111) surface, initially held at room temperature, only the characteristic hexagonal melamine arrangement, which will be referred to as Phase I, is observed (Figure 2a), each melamine molecule is typically observed, under conditions of good resolution, as a single triangular feature due to the location and shape of its molecular orbitals<sup>32</sup>. This arrangement is stabilized by double hydrogen bonds between adjacent molecules, as discussed in Section 1.1.1.3 and reported in more detail elsewhere<sup>33,34</sup>.

Definitive single component arrangements of 1,4-PDI on Au(111) are not observed under these conditions. This may be explained by a high diffusion rate rendering the species invisible to STM at room temperature or the species may exhibit too low a sticking probability on Au(111) at 300 K. In order to enhance the sticking probability of 1,4-PDI, melamine was first deposited on the surface. Subsequent changes in the appearance of melamine domains after a few hours were the only indication of the presence of 1,4-PDI on the surface.

Figure 6.9 shows that striped features are observed between domains of pure melamine. The features within these stripes appear brighter than melamine molecules and the features are less densely packed than in the typical misfit domain boundaries identified by Silly et al<sup>33</sup>. A distance of 29.4 Å is measured between the centres of molecules in equivalent positions within the two hexagonal arrangements on either side of the boundary (figure 6.9). The analogous distance across the boundaries discussed by Silly et al is only 17.69 Å<sup>33</sup>. This additional distance may be explained by the formation of a mixed, unreacted domain of melamine and 1,4-PDI, the new features appear bolder than the bulk of the melamine domain and the shortest centre-to-centre distance between the bright regions of the features is 8.5 Å which is longer than the typical centre-to-centre separation between melamine molecules of 6.1 Å<sup>34</sup>.

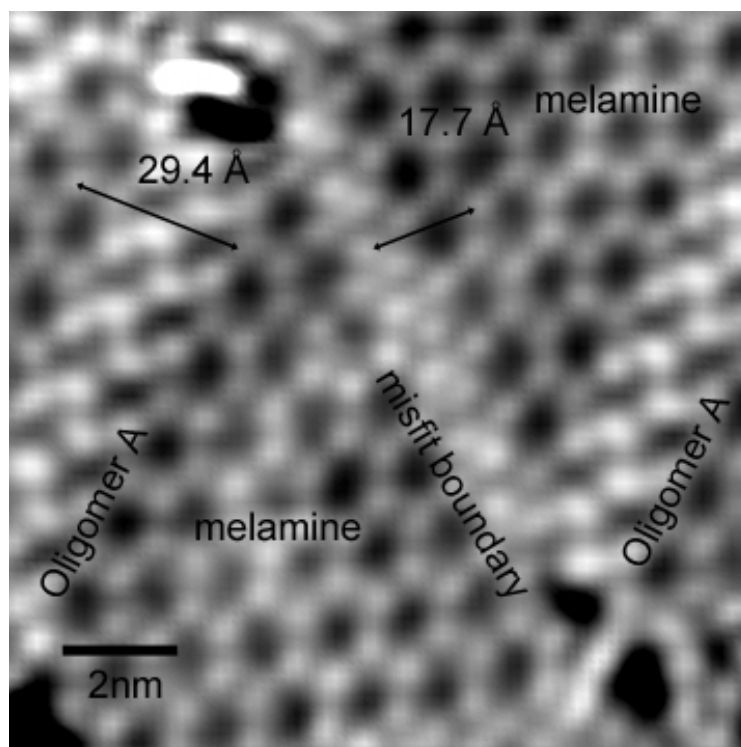


Figure 6.9 STM image comparing the misfit boundaries in melamine domains with those caused by the incorporation of 1,4-PDI and possible formation of Oligomer A (12.9 nm x 12.9 nm, 1.5 V, 0.2 nA)

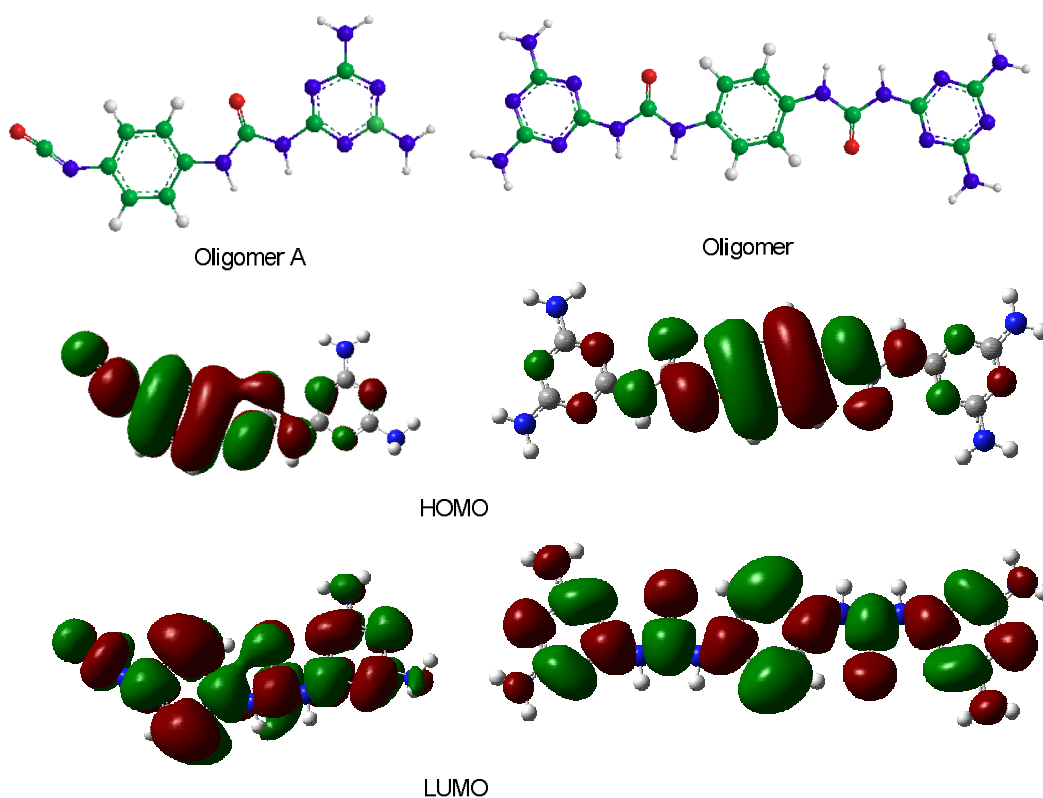
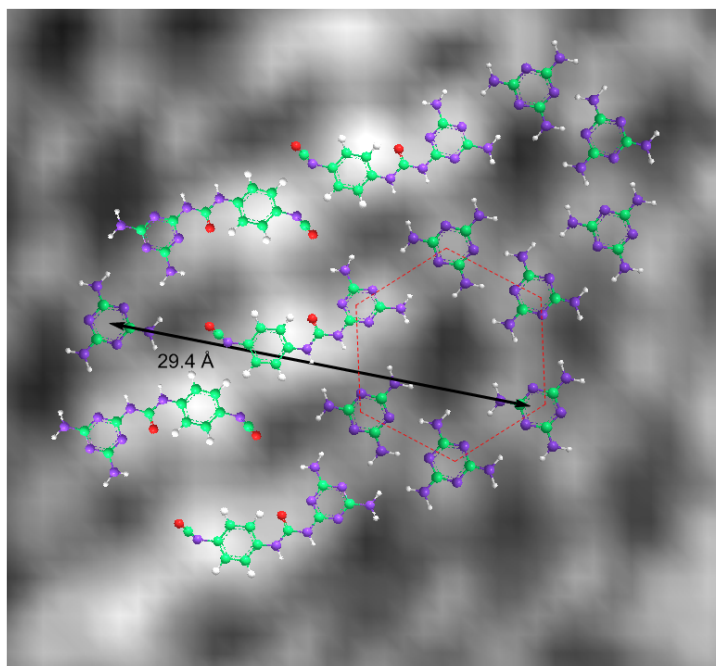


Figure 6.10 Two short oligomer products, A and B, are shown with calculated HOMOs and LUMOs (Gaussian 03, density functional theory using M05-2X functional with 6-311+g\* basis set) below the respective oligomer product



**Figure 6.11 Model showing the proposed packing of Oligomer A species at the boundary of two domains of melamine on Au(111)**

The new feature could also be explained by the incorporation of Oligomer A (Figure 6.10), created by the reaction of a single melamine with a single 1,4-PDI molecule to produce mono-substituted melamine units consisting of two aromatic rings (IUPAC nomenclature: 1-(4,6-diamino-1,3,5-triazin-2-yl)-3-(4-isocyanatophenyl) urea). The total distance across the two bright features, that give rise to the aforementioned 8.5 Å centre-to-centre separation, is measured as 15.2 Å which is comparable with the length of Oligomer A of 15.3 Å calculated using DFT (B3LYP/6-311g\*) by Dr H. A. Früchtl. The triazine part of Oligomer A retains two amino substituents and can thus be incorporated as part of a melamine hexagon. The remainder of the molecule, with its isocyanate terminus, is seen to interlock with like molecules protruding from the other side of the boundary and the arrangement may be stabilized by hydrogen bonds between the isocyanate C=O bonds and the N-H bonds on adjacent species. A model of this assembly is shown in figure 6.11. Similarly, wider domain boundaries are sometimes observed. The species linking the two domains may be a second oligomer (IUPAC name: 1,1-(1,4-phenylene)bis(3-(4,6-diamino-1,3,5-triazin-2-yl) ), Oligomer B (Figure 1, to be discussed later), which contains two urea functionalities and can participate in the formation of melamine-type hydrogen

bonding hexagons and hydrogen bond to the simple melamine-phenylene isocyanate urea oligomers at each terminus. Hence, like Oligomer A, it is readily understandable how Oligomer B is also capable of undergoing incorporation into the melamine domains.

Once certain that 1,4-PDI is present as an adsorbate, the surface may be annealed to accelerate polymerization; it is thought the main purpose of the annealing treatments is to create space for reactions to occur by perturbation of dense supramolecular arrangements rather than to activate the addition reaction. Figure 6.12 shows a new porous phase, Phase II, of which domains (100 nm x 100 nm) are observed after annealing the surface to 345 K. The new phase has a rectangular unit cell with lattice constants of 40.8 Å x 46.4 Å, where the longer side is orientated at 40° to the  $\overline{112}$  direction. A high resolution image is shown in figure 6.13.

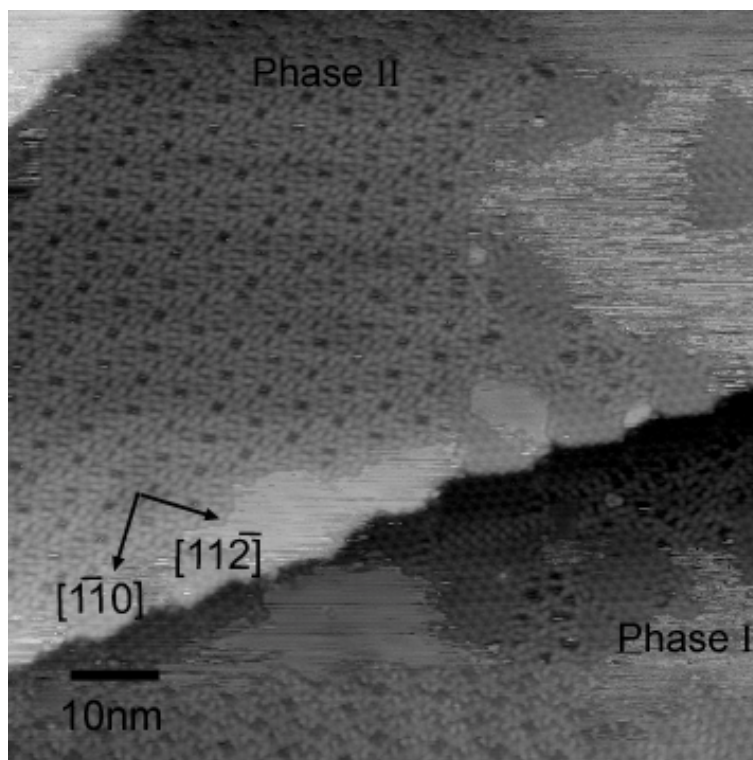
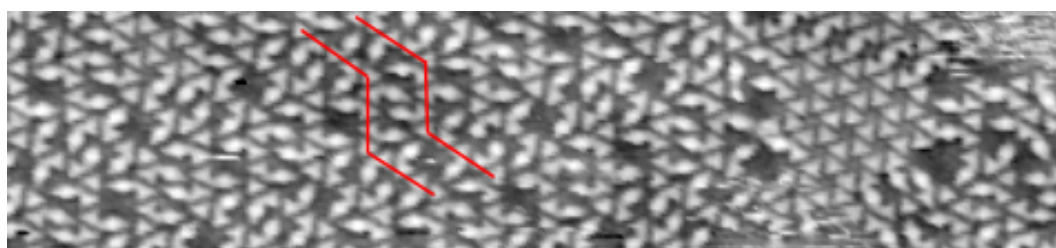


Figure 6.12 STM image of Phase II consisting of melamine and Oligomer A created after the surface is annealed to 345 K (60 nm x 60 nm, 1.5 V, 0.35 nA).

Phase II consists of Oligomer A and melamine in a 3:1 ratio. Spatial distribution of highest occupied molecular orbitals (HOMO) and lowest occupied molecular orbitals (LUMO) of Oligomer A and B, as shown in figure 6.10, were calculated using Gaussian 03 software by Dr H. A. Früchtl. Molecules may be expected to have a comparable shape in STM images. On this basis, it is believed that the features, which measure 15.2 Å in length and appear as two connected lobes correspond to Oligomer A, whilst, as aforementioned, melamine appears as singular triangular features.



**Figure 6.13** Small section of an STM image showing the shapes of melamine and oligomers A and B at high resolution (54.2 nm x 8.2 nm, 1.5 V, 0.35 nA)

Under these imaging conditions, the triazine moiety of Oligomer A is observed as triangular, the features narrow close to the middle where the urea linkage exists, and it is presumed that elongated lozenge part of the STM features represent the aromatic isocyanate fixed to melamine via a urea linkage. The triangular shape is consistent with the appearance of melamine, whilst the lozenge shape is similar to the orbitals of the aromatic isocyanate moiety.

The structure is constructed from a series of parallel zig-zags running approximately along the  $\langle 211 \rangle$  type directions of the surface. The structure is interpreted as containing an unreacted melamine molecule at the vertex of each zig-zag. The  $120^\circ$  rotation in the alignment of features along the zig-zag is caused by the 3-fold symmetry of the melamine molecule. Between two vertices of the zig-zag, two elbow-located melamine features are separated by three features of similar appearance.

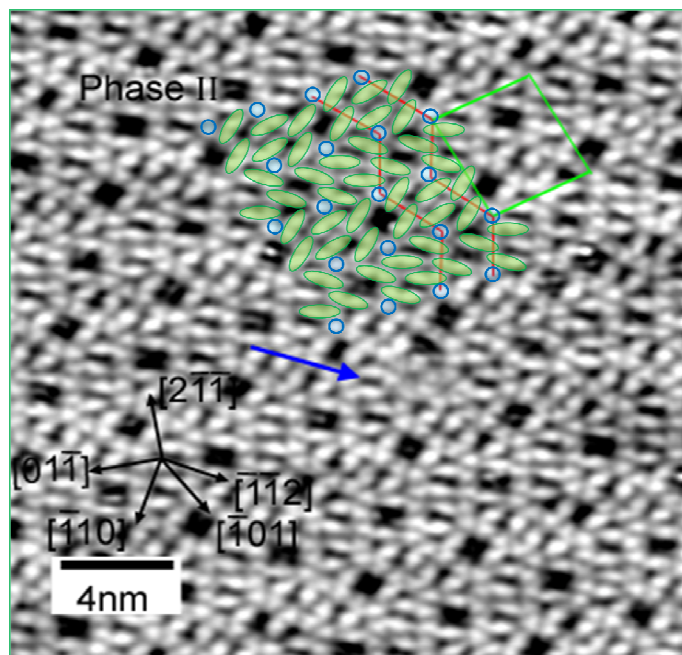


Figure 6.14 STM image of Phase II consisting of melamine and Oligomer A created after the surface is annealed to 345 K (23 nm x 23 nm, 1.5 V, 0.35 nA). The red zigzags highlight the zigzag pattern made up of triazine moieties that runs throughout the phase. The blue arrow points at one of the many defects: two complete hexagonal arrangements of unreacted melamine molecules.

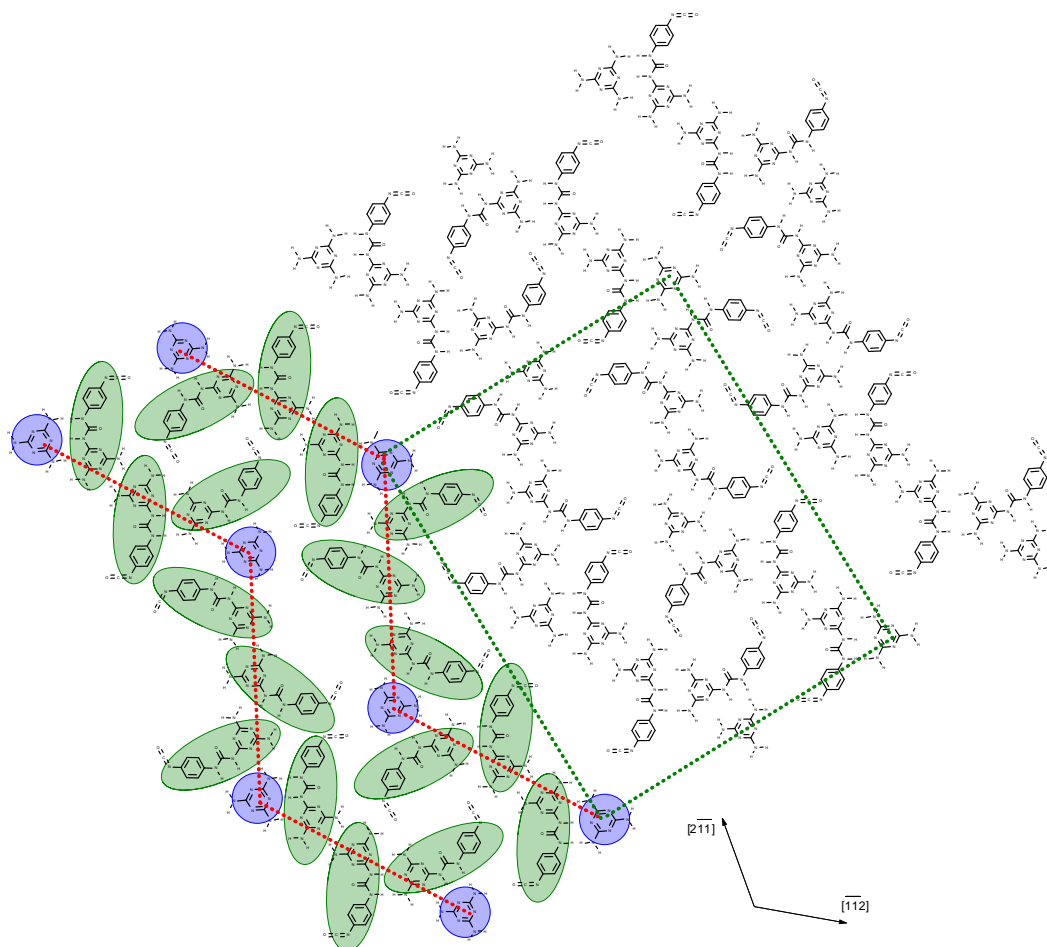


Figure 6.15 Schematic diagram showing the molecular packing in the porous Oligomer A:melamine network, Phase II

The length of the line segment of the zig-zag is 24.6 Å which is equivalent to four times the centre-to-centre spacing in the typical melamine monolayer arrangement. The three features connecting the two isolated melamine molecules at each vertex are thought to be the triazine units of Oligomer A species connected via typical melamine-melamine N-H---N hydrogen-bonds. The phenyl isocyanate moieties of each of these species extend into the interim space like branches. It appears that adjacent zigzags interlock with each other via several different types of hydrogen bonding arrangements between isocyanate groups and amine groups of neighbouring zigzags. The steric hindrance associated with the phenylisocyanato moieties of Oligomers A disfavors the formation of a third H-bonding interaction with a triazine unit, instead, the isolated melamine species form the corners of rectangular pores of approximate dimensions 10 Å x 8 Å. There are frequently defects in domains of Phase II, close to the centre of Figure 6.14, a defect in the domain which consists of two adjacent hexagons of melamine units is indicated by an arrow. In other areas the rectangular porous structure is lost, however, despite the number of defects, the zigzag pattern retains its integrity to stabilise these domains. A model of the Phase II is shown in figure 6.15.

Annealing the surface to 360 K results in the formation of a new phase (Phase III, Figure 6.16) consisting exclusively of Oligomer A in an ordered arrangement. Once formed, Phase III, is dominant up to 420 K, although it must be noted that as the temperature is increased throughout this range, the abundance of features caused by the presence of larger oligomers also increases. Figure 6.17 displays a more detailed image of Phase III on which is superimposed the energy minimized structure. Phase III has a rectangular unit cell, of sides ~23.8 Å and ~18.0 Å, with the longer side orientated at 40° to the  $\overline{\langle 112 \rangle}$  direction or its equivalents, the unit cell matches the values, 23.12 Å and 16.74 Å, for the model calculated within reasonable error.

Within Phase III, pairs of Oligomer A align to promote the formation of a number of intermolecular hydrogen bonds. Each Oligomer A species forms four H-bonds

with the parallel oligomer. In the energy minimized structure each of these N-H...N distances fall in the range 2.8 to 3.0 Å – i.e. consistent with H-bond lengths. Two of these involve N-H...N interactions between the urea N-H bonds and the triazine. In the energy minimized model a further two H-bonds are possible between urea N-H and one of the unreacted –NH<sub>2</sub> functionalities of the triazine of the neighbouring molecule. In the latter case, these two H-bonds require the two N-H bonds of the NH<sub>2</sub> functionality to rotate out of the plane of the molecule. Additional stabilization is achieved via H-bonds between the –NCO functionality and –NH<sub>2</sub> groups on neighbouring molecules. Alternate rows are almost related by mirror symmetry giving the phase a ‘herringbone’ appearance. There is a small offset which breaks the mirror symmetry. The offset allows the optimization of intermolecular H-bonding interactions.

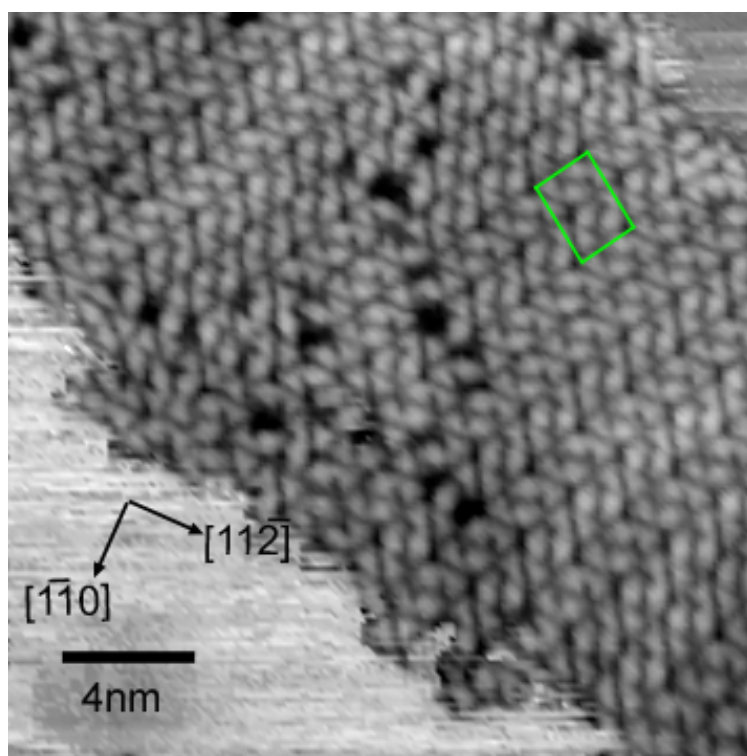


Figure 6.16 STM image of Phase III, consisting of Oligomer A (21 nm x 21 nm, 1.5 V, 0.35 nA)

The energy minimized structure of an isolated Oligomer A molecule is found not to be perfectly planar. The energy cost associated with the molecule adopting a planar geometry and thereby optimizing inter-molecular interactions and

substrate-molecule interactions is, however, only  $\sim 0.03$  eV. The calculated 2-D structure is stabilized by 0.76 eV per molecule compared with the isolated planar molecule. Additional stabilization of a similar magnitude might be expected if the interaction between the molecule and the surface were also considered in the calculations.

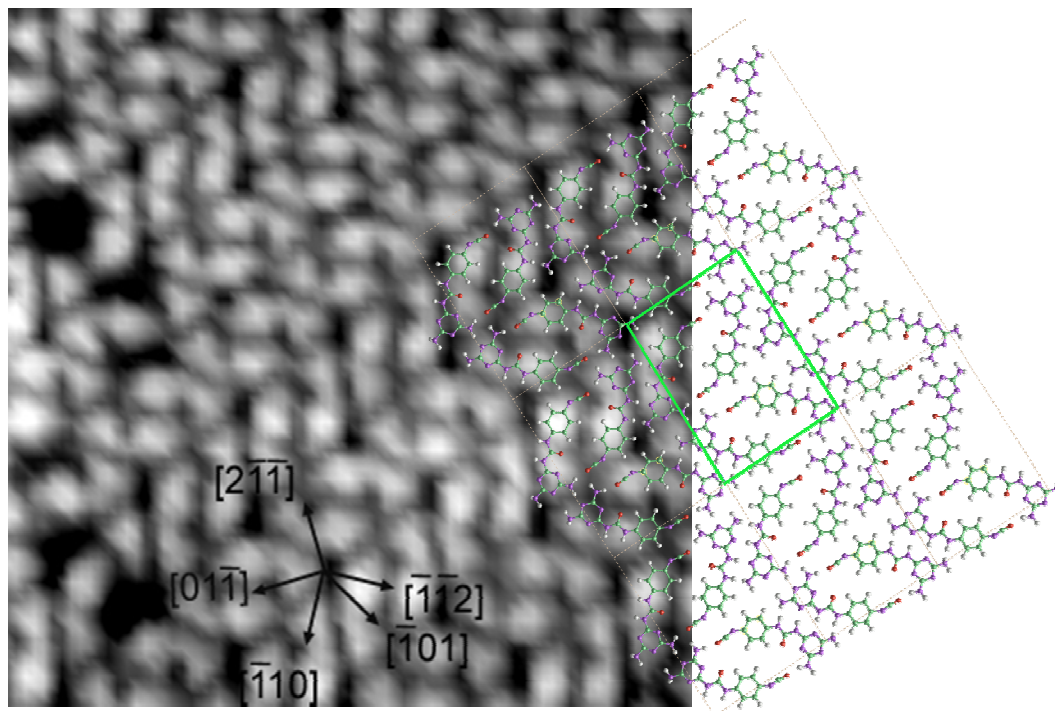


Figure 6.17 The energy-minimised arrangement of Oligomer A in Phase III overlaid on a zoomed section of an STM image

This phase shows remarkable stability in light of the fact that reactive groups are still abundant within its arrangement and in very close proximity on the surface. The slow rate of reaction can be attributed not only to the steric hindrance provided by the substrate which inhibits nucleophilic attack but also to the close-packing, aided by the formation of a large number of intermolecular H-bonds, in the initial melamine phase and subsequently in the Phases II and III, both of which presumably prevent molecules that possess amine and isocyanate groups from adopting favourable positions for reaction.

Double addition to 1,4-PDI by two melamine molecules leads to the formation of diurea oligomers, Oligomer B, containing three aromatic rings and including two urea linkages (IUPAC nomenclature: 1,1'-(1,4-phenylene)bis(3-(4,6-diamino-1,3,5-triazin-2-yl)urea)). These oligomers can assemble into porous formations such as those observed in Figure 6.18 and Figure 6.20 (Phase IV). Oligomer B is observed as features of three connected lobes, as with Oligomer A and the comparable HOMO and LUMO models of figure 6.10, the triazine moieties appear as triangular lobes, the features are narrower close to the urea linkages either side of the middle phenyl ring which, due to a higher electron density, typically appears brighter than the triazine rings. Throughout the temperature range at which Phase III is stable ( $360 \text{ K} \leq T \leq 420 \text{ K}$ ), smaller domains of these molecules are observed, they are often present at the outermost edge of Phase III; this is consistent with the concept of close-packed domains on the surface hindering the urea-forming reaction; these structures are still observed after annealing to around 520 K.

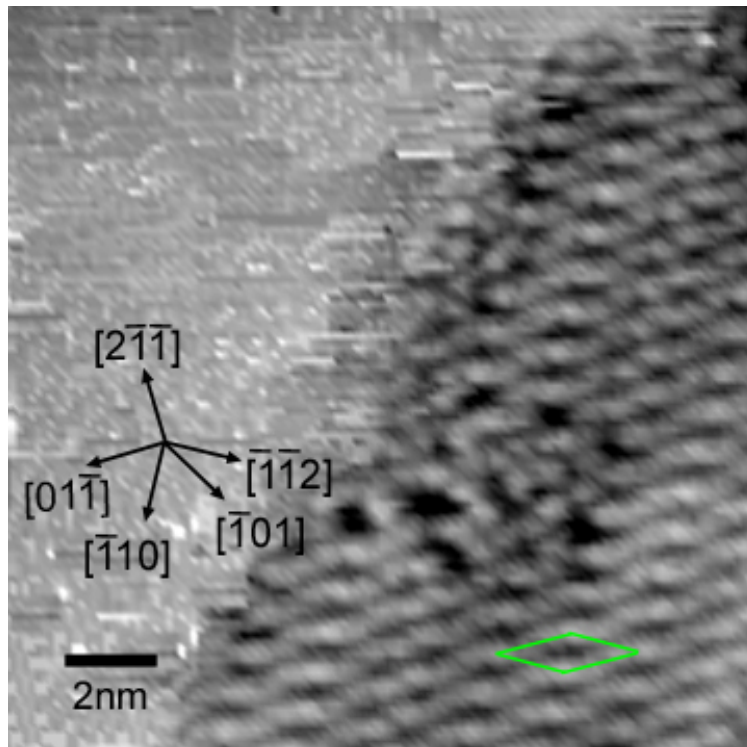
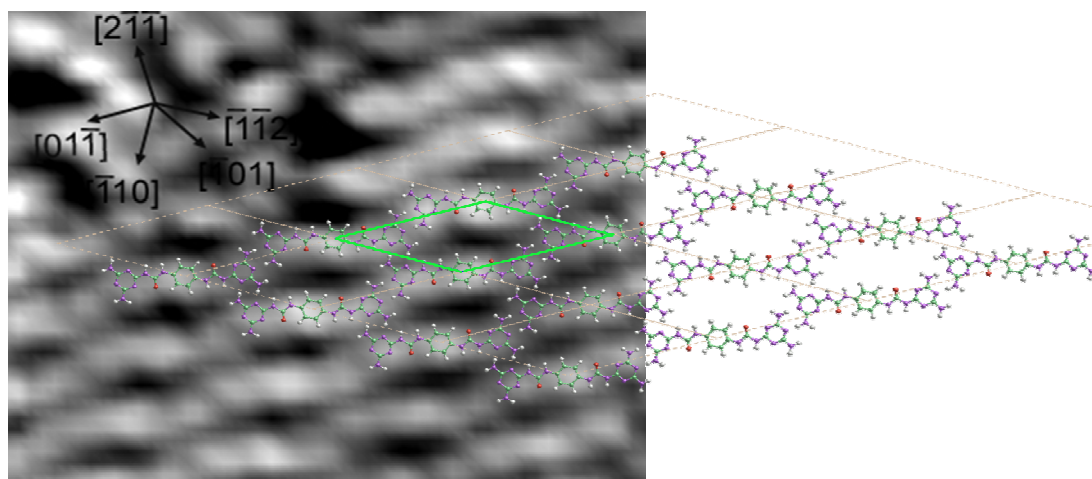


Figure 6.18 STM image showing porous rectangular Phase IV formed from Oligomer B at the edge of a domain after annealing to 350 K (16.3 nm x 16.3 nm, 1.5 V, 0.35 nA)



**Figure 6.19** The energy-minimised arrangement of Oligomer B in the porous rectangular Phase IV

Figure 6.19 shows a model of the porous arrangement formed by these oligomers. The measured unit cell for this structure has sides separated by an angle of  $\sim 30^\circ$ , of  $19.9 \text{ \AA}$  and  $16.7 \text{ \AA}$ , this is in close agreement with the calculated dimensions of  $20.15 \text{ \AA}$  and  $17.18 \text{ \AA}$  for the model of Phase IV generated, this is shown superimposed on a zoomed STM image in Figure 6.19. The shorter side of the unit cell can be seen to be closely aligned with the  $\langle \overline{11} 2 \rangle$  direction or its equivalents. The measured centre-to-centre spacing between triazine rings at the junctions is  $\sim 6.2 \text{ \AA}$  which is consistent with the melamine-melamine-type stabilization by hydrogen bonding at the junctions where the equivalent distance is  $6.1 \text{ \AA}$ . The rhombus-shaped pores are measured to be around  $4 \text{ \AA}$  wide.

Figure 6.20 shows Phase V, a Kagomé lattice formed from Oligomer B near the edges of a compact domain of Oligomer A after annealing the surface to  $420 \text{ K}$ . Shown in more detail in Figure 6.21, this feature is observed quite frequently between  $420 \text{ K}$  and  $490 \text{ K}$ , a temperature range where widespread disruption of Phase III and formation of greater oligomers is observed. Based on prior knowledge of the stabilization of the melamine arrangement on Au(111), the Kagomé lattice can be explained simply as follows. The arrangements are based on a hexagonal centre which consists of the diamino triazine moieties of six Oligomer B molecules in an arrangement structurally identical to the hexagonal

arrangement formed by six melamine molecules within their typical hydrogen bonding arrangement<sup>33</sup>. It is noteworthy that, as such, the Kagomé lattice formed here is inherently chiral. A given hexagon is linked to six other hexagons via two new urea linkages either side of phenyl moieties. The unit cell of this arrangement has sides  $\sim 27.1 \text{ \AA}$  separated by an angle of  $60^\circ$  and parallel to the  $\langle \bar{1}12 \rangle$  direction or its equivalents, the measurements are in good agreement with the calculated values of  $26.85 \text{ \AA}$  and  $60^\circ$  respectively in our energy minimized model. Pores with a triangular shape are produced of side  $\sim 1 \text{ nm}$ . Each pore contains three urea functionalities. Ordered regions of Phase V of  $\sim 20 \text{ nm} \times 10 \text{ nm}$  were typically identified at the edges of Phase III domains, other larger oligomers are seen to surround these domains and sometimes create distortions within them.

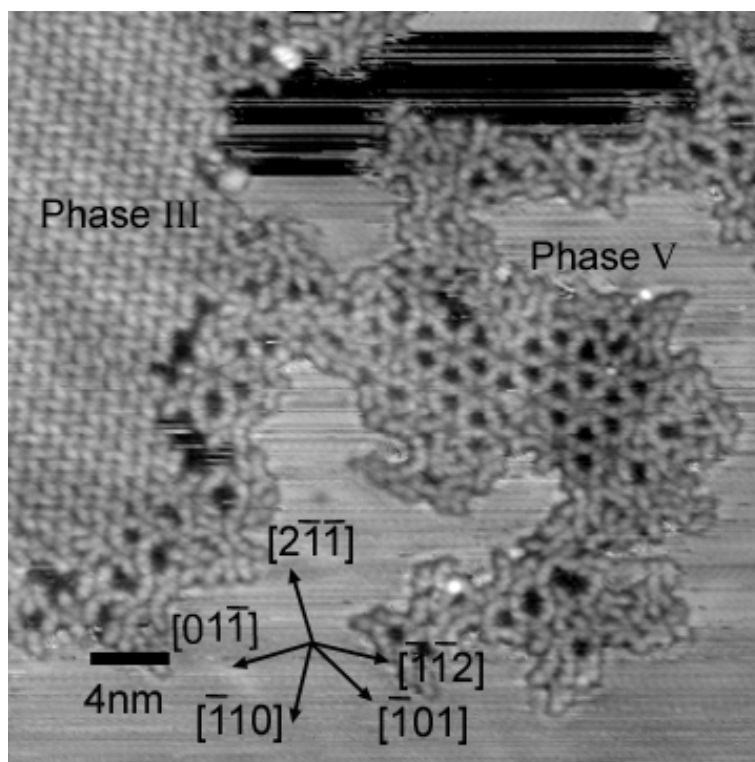
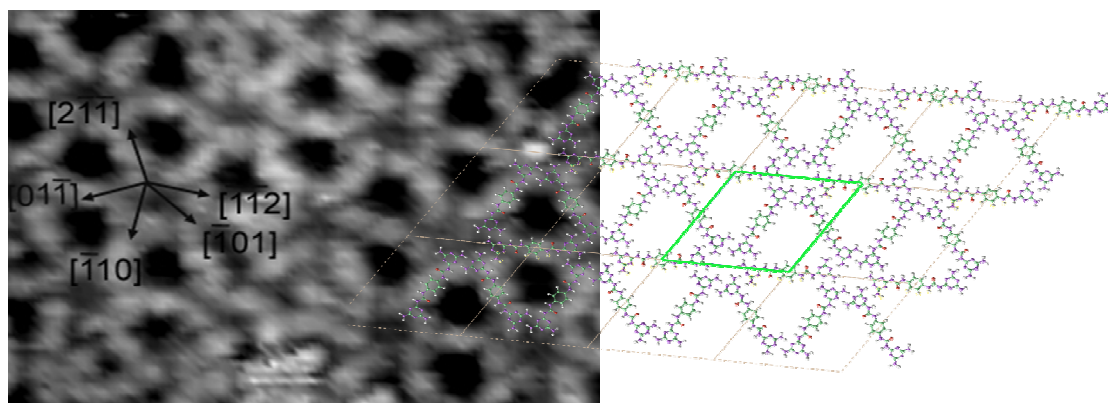


Figure 6.20 STM image showing the Kagome arrangement of Oligomer B, Phase V, beside a domain of Phase III after the surface was annealed to 420 K (38.3 nm x 38.3 nm, 1.5 V, 0.5 nA)



**Figure 6.21** The energy-minimised arrangement of Oligomer B, Phase V (Kagome lattice) overlaid on the zoomed STM image.

Figure 6.22 shows that the surface after annealing to 520 K is largely characterized by larger molecular weight oligomers. Either through desorption of the smallest oligomers or reaction, complete disappearance of Phase III is realized after annealing to 470 K. The resultant surface arrangements are, on the whole, not well-ordered, apart from areas of Phase VI which often bound domains of larger oligomers. These larger oligomers are mostly snake-like chains with each melamine unit in the oligomers having been disubstituted. Hydrogen bonding between the remaining free amine groups and triazine rings along these longer oligomers is most likely responsible for their positioning within these domains, pores that are  $\sim 15$  Å wide are regularly observed. The target network of tri-substituted melamine molecules is shown in Figure 6.4, this would contain pores  $\sim 25$  Å wide; twelve molecules (six of each reactant) would have to bond with the appropriate orientation in order to form a single pore of this ideal structure. Although some instances of ‘half pores’ (semicircular arrangements of oligomers of six molecules linked as in the ideal structure) are observed, the pores most frequently observed consist of walls consisting of up to 9 urea linkages; two nearby oligomers are seen to align such that the pore becomes closed only by two melamine-melamine-type hydrogen bonding interactions on opposite sides of the pore. One of the advantages of self-assembly is the ability of domains of molecules held together by non-covalent interactions to be able to ‘self-heal’, eliminate defects and create uniformity; these domains, although controlled

largely by hydrogen bonding, are unable to do so largely because of the variation in the sizes of the oligomers that have conglomerated.

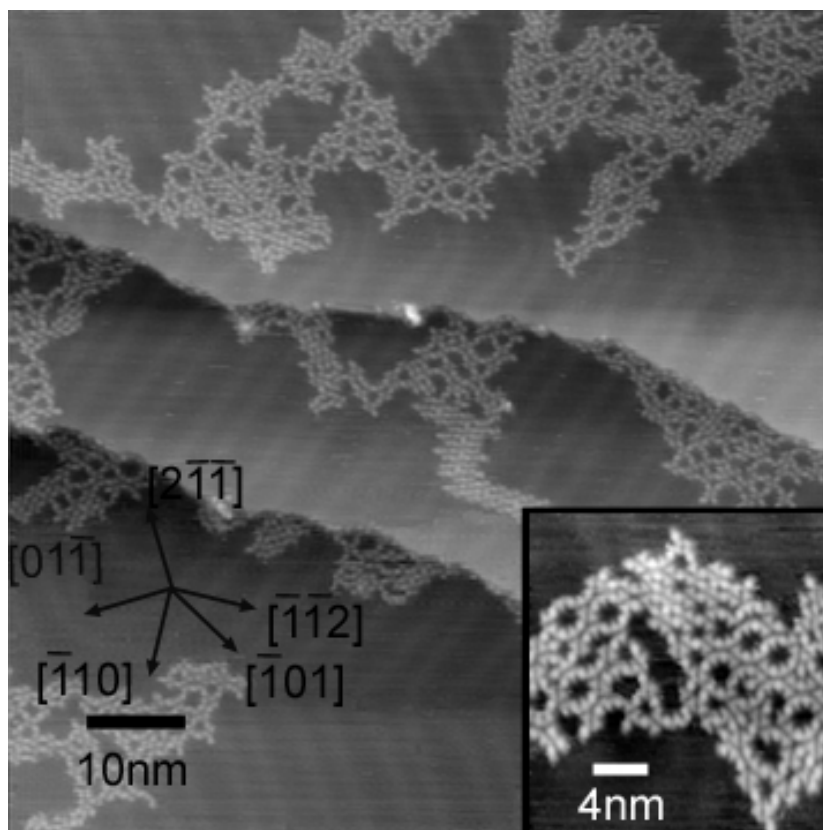


Figure 6.22 STM image of the surface after annealing to 520 K (90 nm x 90 nm, 1.5 V, 0.3 nA). Domains of Phase IV occasionally emanate from aggregates of polymeric chains.

The production of fully covalent pores appears to be hindered by the inability of melamine to undergo trisubstitution via reaction with three isocyanate species. In principle, a single covalent pore would be produced by the reaction of six melamine molecules and six 1,4-PDI species whereby each melamine undergoes only two coupling reactions and the twelve molecules arrange in a hexagonal configuration. No examples of this type of structure were observed and, instead, snake-like chains containing twelve aromatic rings were widespread. One strategy to promote the formation of further urea linkages may involve dosing further 1,4-PDI once long oligomer chains are observed. In principle, the additional 1,4-PDI could replace the melamine-melamine-type hydrogen bonds that are present in the arrangements represented in Figure 6.23.

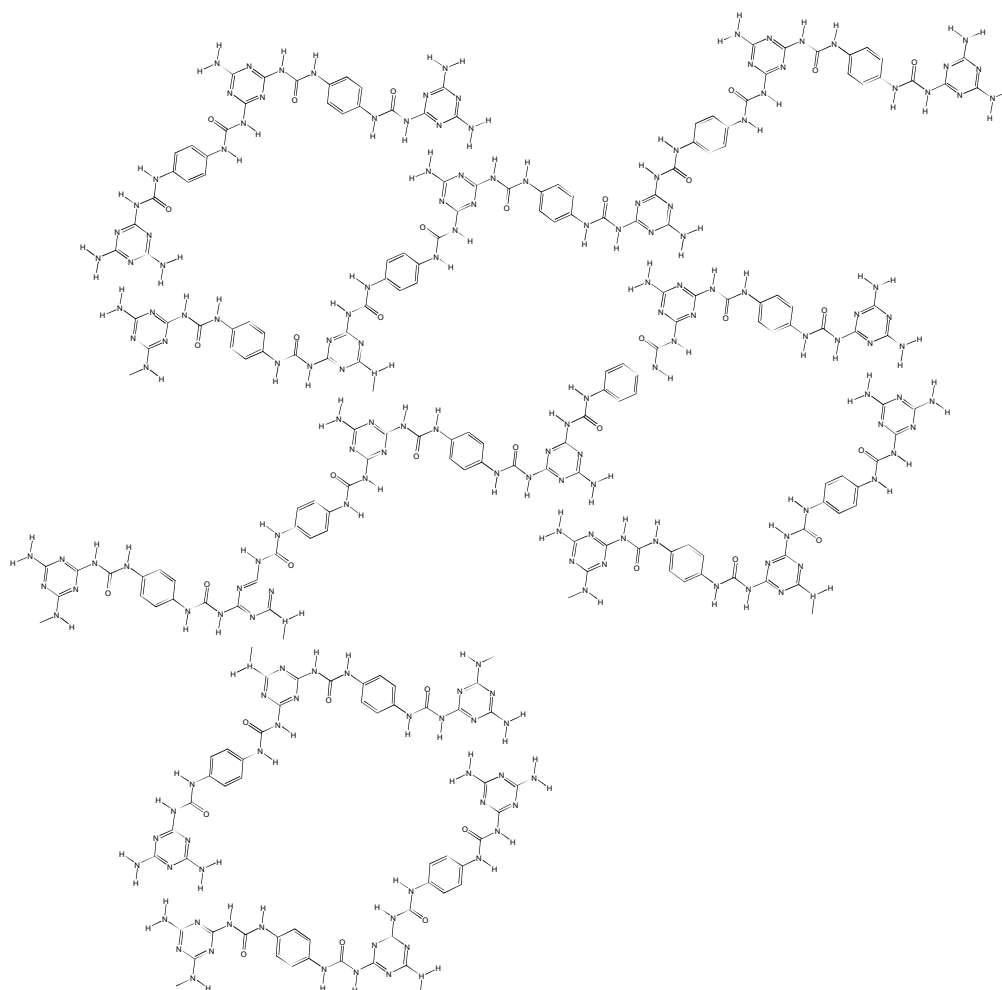


Figure 6.23 Model showing how longer oligomer chains can interact to create pores.

Initial experiments involving dosing further 1,4-PDI were carried out, but change was not observed in the snake-like structures. Optimisation of concentration and annealing conditions is almost certainly required for such a strategy to be successful. Annealing to higher temperatures may aid the trisubstitution of melamine, however, the surface was only ever annealed to a maximum of 520 K throughout this series of experiments because the surface coverage was seen to be reduced dramatically after 490 K, and it must be noted that there is sufficient evidence, as the formation of Oligomer A and the domain break features in Fig 6.9 show, that the urea coupling between an amine and an isocyanate occurs readily at room temperature.

From these observations, it can be deduced that trisubstitution of melamine by aromatic isocyanate molecules (in this case, often larger oligomers) is unfavourable presumably for either (or both) steric or electronic reasons. As substitution of amino groups for urea substituents occurs on melamine molecules, their remaining amine groups must be progressively deactivated towards reaction, monosubstitution to form Oligomers A and B is observed at lower temperatures whilst larger oligomers are only observed more regularly as the temperature is increased above 420 K. Formation of large ordered domains of melamine in its close-packed hydrogen bonding formation further inhibits trisubstitution by blocking the access of 1,4-PDI to the amine functionalities of melamine. Annealing the surface is required to accelerate the reaction and there is considerable evidence that reaction initially only occurs at the edges of ordered H-bonded domains. The initial introduction of order to the surface via the self-assembly of melamine into its hexagonal formation may be key to the formation of subsequent ordered domains such as the porous Phase II observed at 350 K and the compact Phase III observed from 360 K to 470 K, it may be expected that if melamine was less ordered in the initial stages then polymeric features, that begin to be observed from 440 K, would be formed at much lower temperatures.

As aforementioned, the highest annealing temperature tested in this series was 520 K, and although some of the smallest oligomers, Oligomer A, may have desorbed from the surface by this temperature, it can be concluded that structures of greater thermal stability on Au(111) than the starting material, melamine, which is known to desorb at around 370 K, were generated by these reactions. The goal of these experiments was to create covalent structures, and although these have been generated, it is remarkable to see that the same hydrogen bonding interactions, two N-H...N bonds at each junction, that exist within the two-dimensional melamine array are still largely responsible for the spatial distribution of the much larger oligomers formed during these experiments. Despite the lack of order and the inability to form porous structures of fully covalent pore walls from melamine and 1,4-PDI, the final products of these polymerization reactions may still be capable of performing some tasks where molecular recognition is key due to the presence of the urea linkages and their hydrogen bonding capabilities.

## 6.3.1.2.1 Nickel Deposition onto Polyurea Networks on Au(111)

Nickel is seen to behave in a number of different ways after evaporation onto an Au(111) surface bearing the polyurea aggregates. After initial deposition of 0.1 ML Ni, islands of average diameter  $\sim 3$  nm can be seen in most of the elbows of the herringbone reconstruction, this happens fairly reliably in bare areas of the surface (figure 6.24).

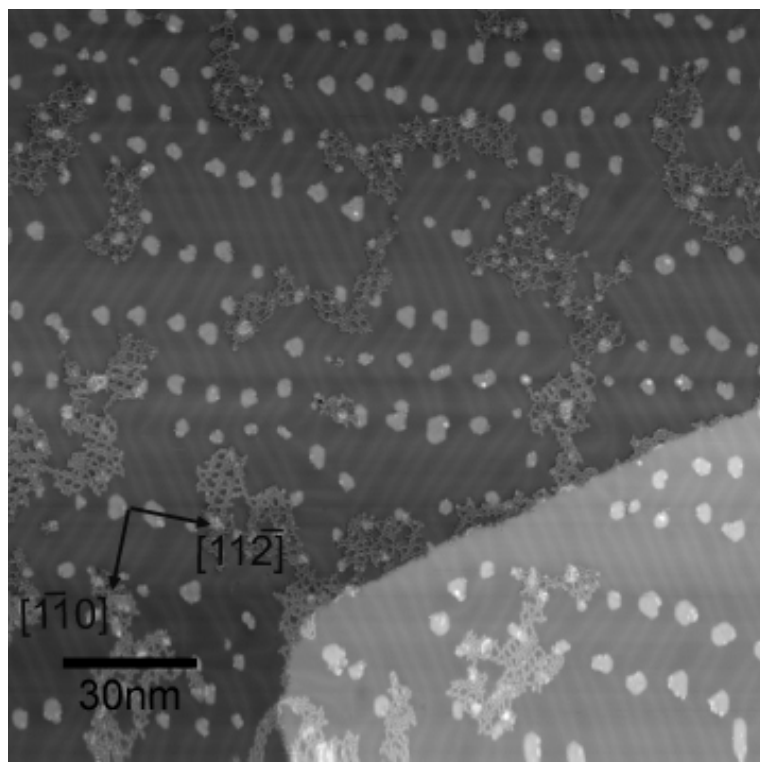


Figure 6.24 STM image of the Au(111) surface bearing polymeric aggregates after subsequent deposition of 0.1 ML Ni(111) (170 nm x 170 nm, 15. V, 0.3 nA)

When areas are covered by the organic domains, as shown in figure 6.25, the molecules appear brighter as they cross the elevated island but it appears that this does not affect either their structure (covalent bonds are not broken) or their relative position within the domain (supramolecular arrangements are relatively unperturbed). Sometimes these islands under the organic domain grow to the same size as those grown on uncovered sites. However, it seems that the occurrence of the molecular domain over the elbow site can hinder island growth and islands of

only 1-2 nm width result. In some cases, the presence of the polymeric aggregates means that islands do not form at all in the elbow sites. Figure 6.26 shows an area of the surface where growth of nickel in an elbow site has been inhibited causing nucleation in small pores within the polyurea network.

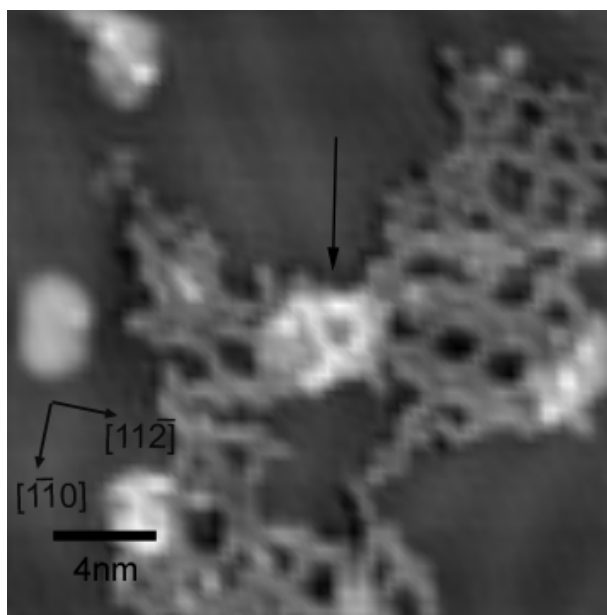
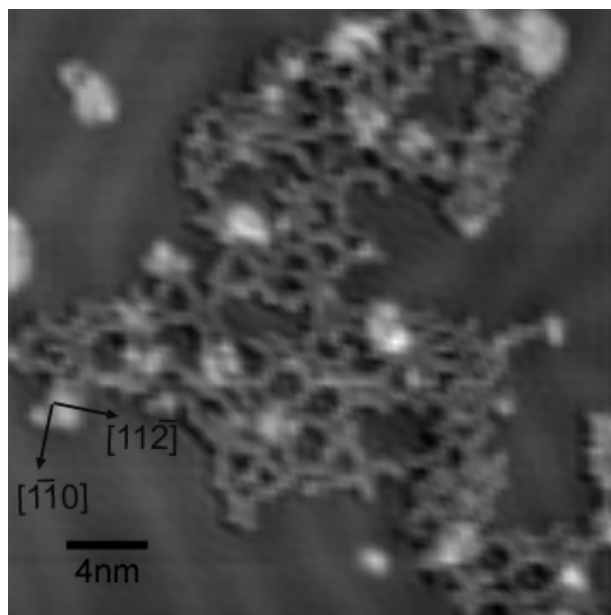


Figure 6.25 Zoomed STM image showing polymers crossing an Ni island (23.6 nm x 23.6 nm, 1.5 V, 0.3 nA)

The polymeric aggregates themselves can act as nucleation points for nickel deposition and small growths (up to 2 nm) form inside the pores, around the edges and under the organic domain away from the elbow sites, this is also seen in figure 6.26.

As the nickel coverage is increased, all nickel deposits (at or away from elbow sites) are seen to grow accordingly and other new deposits are seen to form in the same fashion as for the initial 0.1 ML addition. Thus as the Ni coverage builds, a greater proportion of the polyurea domains are situated above the Ni adlayer and as such progressively more of the pores and gaps in the polymeric array have the new Ni surface inside them.



**Figure 6.26** Zoomed STM image showing the inhibited formation of Ni island at an elbow site and the polymeric domain acting as a nucleation point for several smaller Ni clusters (30.2 nm x 30.2 nm, 1.5 V, 0.3 nA)

As 0.4-0.5 ML Ni coverage is reached (figure 6.27), individual clusters begin to coalesce. By this stage, the surface coverage of the organic adsorbate is slightly diminished. Some of the molecular domains appear to desorb during the deposition of Ni. The remaining adsorbate follows the ongoing trend of having an increased proportion of the organic domain above a nickel island and where the organic domains is not atop an island, more nickel is nucleated along the edges of the polymer chains, and small nickel particles are thought to line the inside of some of the pores that are present within the domain.

Achievement of an ordered molecular adlayer of defined functionality upon a nickel or a catalytic surface is a major aim of this project. Previously, in Chapter 3, it has been shown that the PTCDI-melamine hydrogen bonding system which reliably assembles on  $\text{Ag-Si}(111)-\sqrt{3} \times \sqrt{3}R30^{035}$  and  $\text{Au}(111)^{34}$  cannot be formed on  $\text{Ni}(111)$ , then it was shown that the introduction of Ni onto the PTCDI-melamine hydrogen bonding schemes on  $\text{Au}(111)$  result in disordered metal-organic structures on the surface.

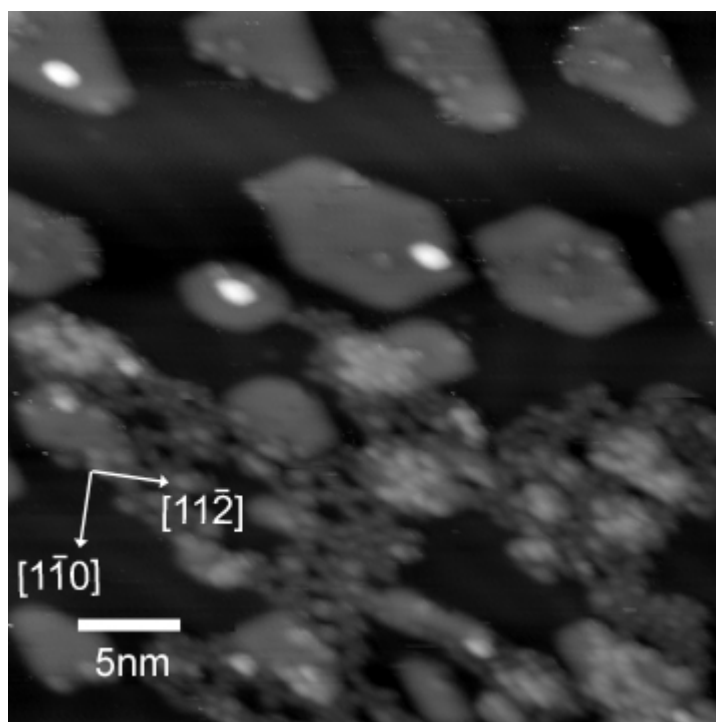


Figure 6.27 STM image of Au(111)/polyurea surface after 0.5 ML Ni is deposited (35 nm x 35 nm, 1.5 V, 0.3 nA)

The molecular arrangements formed here from the polyurea chains contain only a small degree of order but they do display significantly more robustness towards nickel deposition. The polyurea domains are disorganised prior to nickel deposition so it is difficult to detect if there are local effects on their arrangements due to metal-organic coordination, although it would seem that if nickel atoms have become coordinated to available functional groups amongst the polymeric aggregates then the polyurea chain units are unable to manoeuvre into position to form extended metal coordination polymers that can be defined with some certainty from STM evidence alone. Spectroscopic analysis might be required to quantify the extent to which this occurs.

The nickel is seen to grow under the organic domain which goes some way to meeting the objective of introducing an ordered porous structure onto a catalytic surface. Again, it is difficult to determine exactly how nickel nucleates around the polymeric units, it seems that covalent polymers (key for hydrogen bonding to further adsorbates) do remain intact and that the urea linkages along them should be available to hydrogen bond to further adsorbates unless blocked by metal

coordination. Nickel may simply be nucleating along the polymeric aggregates as if they were step edges or elbow sites (barriers to diffusion) in a similar way to the growth of Ni on the PTCDI/melamine network reported in Chapter 5. Opportunities for nucleation via coordination are available not just from the urea groups, but from the triazine N atoms and unreacted amine and isocyanate groups along the polymers.

The ability to put a Ni surface under some of the pores in the arrangements as outlined in figure 5.1 with respect to PTCDI and melamine is observed successfully here but a major problem is the removal of surface coverage with the addition of Ni to the polyurea bearing surface. The incidence of hot Ni atoms on the surface may increase the surface temperature sufficiently at the local scale to desorb the organic adsorbate. A new way of introducing nickel (possibly from a volatile inorganic complex, e.g.  $\text{Ni}(\text{CO})_4$ ) should be sought in order to preserve the polyurea networks or loss of a proportion of networks should be anticipated and accounted for by increasing the initial surface coverage in order that a sizeable coverage remains after the deposition of nickel. The method of evaporation may well become irrelevant as focus is moved to preparing samples in ambient conditions from amine and isocyanate solutions, but the introduction of Ni to samples in UHV via a volatile and labile inorganic complex may need to be considered.

The domains made up of the polyurea molecules are more stable in the presence of Ni because there are fewer junctions that can be interrupted. The most commonly observed types of pores within the domains of grouped polymers are composed completely of covalent walls except for the two melamine-melamine-type hydrogen bonding junctions at opposite ends, whereas the pores of the PTCDI-melamine networks have twelve hydrogen bonding junctions that can be replaced by metal-organic interactions.

### 6.3.1.3 Comparison of Ambient and UHV reactions

The major difference between the two experiments apart from the obvious change between UHV and ambient conditions is that annealing was carried out in the UHV experiments and that this has a significant effect upon surface coverage.

1,4-PDI is definitely present in both cases, although it is only visible in the ambient situation where it seems to form amorphous stacks after deposition from solution whereas it remains invisible and diffusive in UHV, thus solvent molecules may be vital in contributing to the nucleation and stabilisation of the 1,4-PDI surface growths.

The melamine coverage is much lower in the ambient experiment; it forms domains that are much smaller hence more easily diminished through reaction as molecules are more easily accessed. The 1,4-PDI stacks also inhibit large domains of melamine from forming. As the initial degree of surface order from melamine domains disappears quickly, some of the intermediate phases made up of the small oligomers A and B, which result from diffusion into and transformation of melamine domains, are not observed.

Although the quality of the STM images in ambient conditions means that the results are not conclusive, it appears that the same outcome may be reached, the C<sub>60</sub> fullerene distribution features many pairs or individual units and these could arguably be ascribed to molecules filling pores similar to those observed after annealing to 520 K in UHV. Annealing in the UHV experiments is thought not only to hasten the reaction but desorb the starting reactants or small oligomers, thus the disordered layout of fullerenes may also be due to nucleation around the species observed at the start of the UHV experiment which may still be present if not removed via desorption or reaction. If small oligomers are present they might be likely to form ordered, porous domains by themselves like in UHV, these might be capable of hosting C<sub>60</sub> fullerenes (if the pores are not large enough, dark

areas corresponding to the domain size should be seen) or, more likely, aggregate alongside the larger polymer chains.

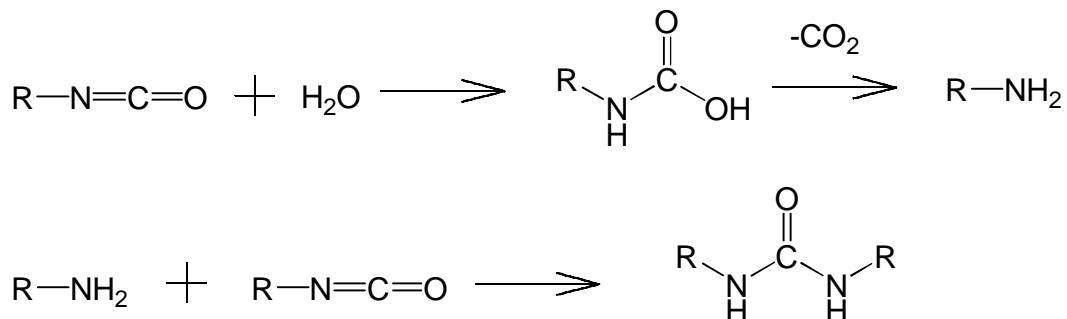


Figure 6.28 Self-polymerisation of an isocyanate in the presence of water

With respect to the contrast between UHV and ambient conditions, the major difference that might be anticipated in the behaviour of the chemicals is the potential of isocyanates to self-polymerise in the presence of water vapour via the reaction scheme shown in figure 6.28. Whilst the resolution of the UHV images is good enough to distinguish between triazine and phenyl aromatic rings along the polymer chains, the ambient images are not sufficiently clear to do so. Therefore it is difficult to judge if the presence of water vapour in the atmosphere whilst scanning has an effect on the surface composition.

#### 6.3.1.4 Conclusion

The reaction between melamine and 1,4-phenylene diisocyanate to produce urea linkages is observed directly via STM. The reaction occurs at room temperature although annealing can accelerate break up of the compact domains of molecules in order for coupling reactions to occur. Small oligomers form organised domains, stabilised by hydrogen bonding, which are observed as intermediate phases. Melamine is incapable of undergoing trisubstitution ergo further reaction leads to production of longer polymer chains; these chains aggregate in a reasonably controlled fashion with the formation of large pores of nearly fully covalent walls.

Nickel grows under the polyurea structures on Au(111) when deposited without disruption of the overlying molecular formations thus growth of a covalent network on an Au surface followed by deposition of nickel might be the best method of developing a successful chiral modifier upon a catalytic surface. Fullerene deposition alludes to the same polyurea network being formed from melamine and 1,4-phenylene diisocyanate under ambient conditions.

### 6.3.2 1,3,5-tris-(4-aminophenyl)-benzene and 1,4-phenylene diisocyanate

Melamine only undergoes disubstitution by 1,4-PDI, thus the surface-confined reaction can only proceed as far as the production of snake-like chains, shown in figure 6.23. As discussed, the reasons for this may be the progressive deactivation of the amino groups as the reaction proceeds or steric hindrance around the triazine centres. Replacement of melamine by a triamine species whose reactive groups are all available and well-spaced might allow production of better-developed polyurea networks. To this end, 1,3,5-tris-(4-aminophenyl)-benzene (TAPB) was tested in a surface-confined reaction with 1,4-PDI on Au(111) in UHV (figure 6.29).

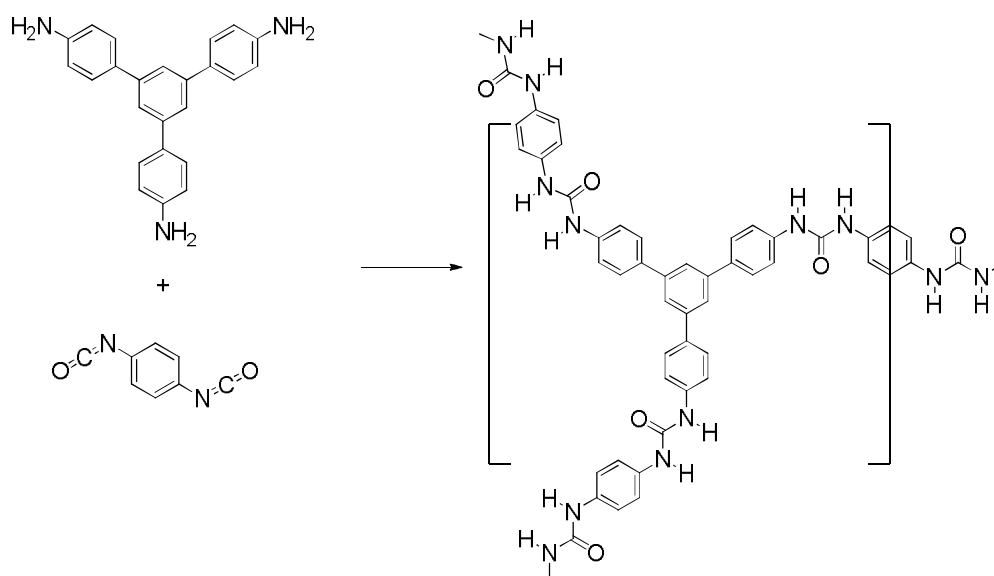


Figure 6.29 Structures of TAPB and 1,4-PDI and the potential polyurea network

The reaction did not take place as expected and STM images were not obtained. From the observations of the reaction of 1,4-PDI and melamine, it was known that 1,4-PDI is too mobile on the surface at room temperature to image and its presence could only be determined by the changes detected to the melamine domains. In this case, TAPB could not be visualised upon the surface which suggest that, from vapour deposition, its sticking probability is too low or that it is similarly too mobile upon the surface to image.

Saturating the surface upon which TAPB might be present with 1,4-PDI might be expected to generate polyurea oligomer molecules. These oligomers might then assemble into ordered domains due to the presence of newly formed urea groups that allow stabilisation via hydrogen bonding between urea groups and unreacted amine groups or isocyanate functionalities. Formation of molecular domains would allow for easier STM analysis and characterisation of the surface processes to take place. The high rate of diffusion of both species may ensure that they do not take part in enough collisions which result in reactions and formation of new oligomers.

Low temperature STM might be required to detect the presence of each of the species upon the surface. It may be expected that van der Waals interactions would control the organisation of TAPB on the surface. TAPB may eventually pack upon the surface in a fashion similar to that adopted by 4,4',4''-benzene-1,3,5-triyl-tribenzoic acid on Ag(111) after annealing to 420 K<sup>36</sup>. Such a formation would ensure that the amino groups are pointing away from those on neighbouring molecules thus reducing electrostatic repulsion (figure 6.30).

Some x-ray crystal structures of isocyanate species indicate ordering which is induced via the formation of dipole-dipole stabilising interaction between  $\delta^+C\equiv N\delta^-$  bonds on adjacent molecules. Low temperature STM might allow analysis of 1,4-PDI arrangements on the Au(111) surface and information about

the type of supramolecular interactions which are formed between 1,4-PDI molecules.

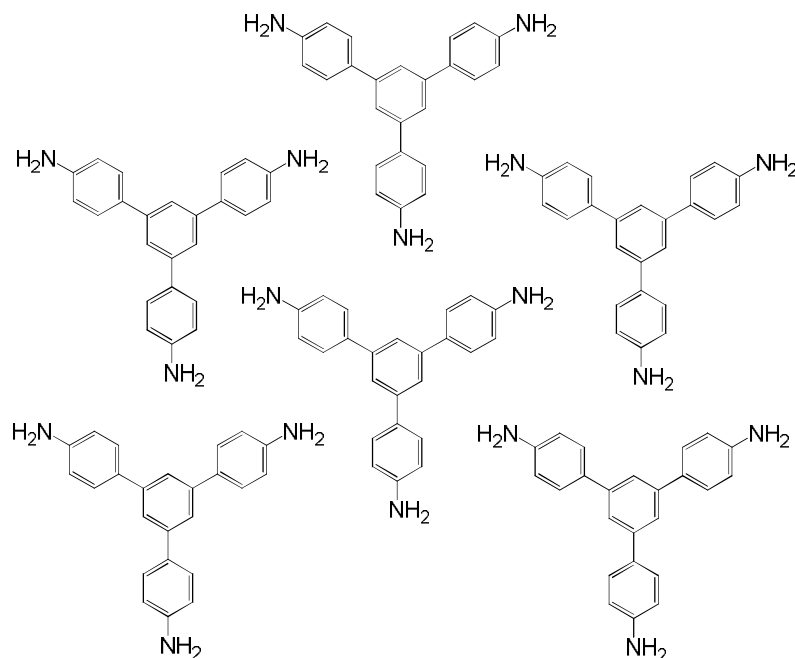


**Figure 6.30** A potential monolayer arrangement of TAPB on Au(111) which would avoid electrostatic repulsion between amino groups.

Although it has previously been stated that organised close-packed domains slow the rate of surface-confined reactions by preventing molecules adopting positions for reaction; the formation of such domains may ultimately be required to increase the sticking probability of further reactants being deposited from vapour. The monocomponent deposition of 2,4,6-tris(4-aminophenyl)-1,3,5-triazine on Au(111) was not reported by Treier et al<sup>8,9</sup> in their study of its reaction with PTCDA. However, it might be anticipated that the presence of a triazine ring in the centre of the molecule might aid the self-assembly of the triamine molecules by the formation of N-H...N hydrogen bonds between amine groups and triazine N atoms, this is illustrated in figure 6.31.

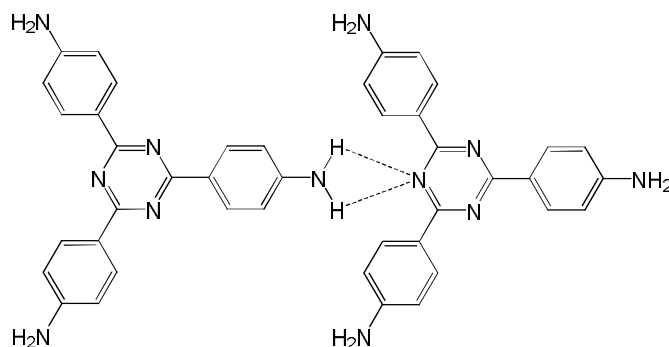


**Figure 6.31 Potential hydrogen bonding interaction between 2,4,6-tris(4-aminophenyl)-1,3,5-triazine molecules**

The reaction may have a better chance of success if carried out at the liquid-solid interface, where solvent molecules may be able to stabilise TAPB upon the surface or co-deposition of both TAPB and 1,4-PDI could be performed by mixing solutions of both species. In UHV, simultaneous co-deposition may bring about deposition of polyurea molecules on the Au(111) surface although significant alterations to the UHV STM apparatus would have to be undertaken. A situation where oligomers may form in the liquid or gaseous phase around the sample before adsorption might be more favourable for the formation of extended polyurea molecules. From vapour deposition, simultaneous co-deposition methods might allow the surface to be bombarded with high concentrations of both species, annealing the surface during this exposure may activate the reaction. A downside to these approaches where the reactions are promoted might be the loss of pre-organisation. Once covalent bonds are formed, the structure is set and organised hydrogen bonded assemblies of smaller oligomers which might still serve purposes as host templates may be bypassed. Co-deposition from solution may allow for some degree of pre-organisation of both reactants and subsequently new oligomers in the environment at the interface, however, this is less likely to occur whilst dosing both species to a sample held within a UHV chamber.

### 6.3.3 Melamine and 1,3-phenylene diisocyanate

The co-deposition of melamine with 1,3-phenylene diisocyanate (1,3-PDI) on Au(111) was performed in UHV in order to observe the potential surface-confined reaction between the two species. As before, melamine is deposited upon the surface first in order to increase the sticking probability of the isocyanate species.

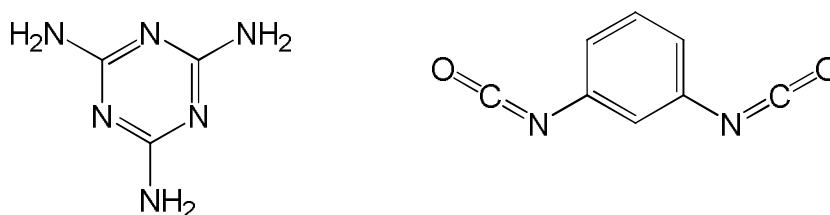


Figure 6.32 Melamine and 1,3-phenylene diisocyanate

At room temperature, it is noted that no change is observed to the melamine domains for the first day despite allowing the sample to experience long exposures to relatively high pressure doses ( $\sim 10^{-6}$  mbar) of 1,3-PDI. In this experiment, the melamine domains were considerably smaller, ergo the molecules within them would presumably be more easily accessed by reactive 1,3-PDI molecules. The initial signs of change are in the form of larger particles on the edge of melamine domains, this is evident in the STM image of figure 6.33 (after Step 1). These new molecules appear as symmetrical features of three lobes in a bent conformation. These have been assigned as diurea molecules and labelled Oligomer D. This species is analogous to Oligomer B of the previous experiment (Section 6.4.2) since it has also been formed from the reaction of a diisocyanate species with two melamine molecules. The end features of Oligomer D are triangular, these correspond to the triazine moieties whilst the phenyl ring of 1,3-PDI is represented by the rounder centre features. These features seen by STM match the shape of the lowest energy conformation of Oligomer D in the gas phase, shown in figure 6.34. This was obtained by DFT calculations using Gaussian 09 (M05-2X/6-311+g\*) by Dr H A Früchtl. This conformation of Oligomer D is almost planar and is presumably stabilised by intramolecular

hydrogen bond formation between the N-H bonds of its urea groups and the N atoms in its triazine rings.

Despite annealing the sample for short periods of time to low temperatures, below the estimated desorption temperatures of both species (<350 K), the formation of larger urea molecules is not observed. The diurea Oligomer D species on the edges of melamine domains become surrounded by melamine molecules, which are still diffusing across the surface. As illustrated by Step 2 in figure 6.33, melamine molecules hydrogen bond to Oligomer D molecules, further melamine molecules join these islands and the diurea molecules become embedded in the domain interior. Both species, melamine and 1,3-PDI, must be mobile upon the surface, thus it can be deduced that formation of hydrogen bonded melamine arrays is easier and quicker than urea forming reactions or formation of any mixed phase domains.

As shown in figure 6.33, after Step 2, the chirality of the melamine arrangements on each side of Oligomer D molecules is maintained. In order to comply with the chiral hydrogen bonding motif of melamine domains, the triazine rings at either end of Oligomer D must be orientated as shown in figure 6.33 (after Step 2) and 6.35 – as reflections of each other.

In figure 6.36, the diurea molecules embedded within the melamine domains appear linear and different from the initial features seen on the edges of the domains after Step 1. In this linear conformation, the central phenyl ring is possibly twisted out of plane in order that Oligomer D molecules are stabilised within the hydrogen bonding domain. This conformation of Oligomer D must be higher in energy than that adopted after Step 1. Presumably, this is offset by the stabilisation energy gained from incorporation into the centre of melamine islands.

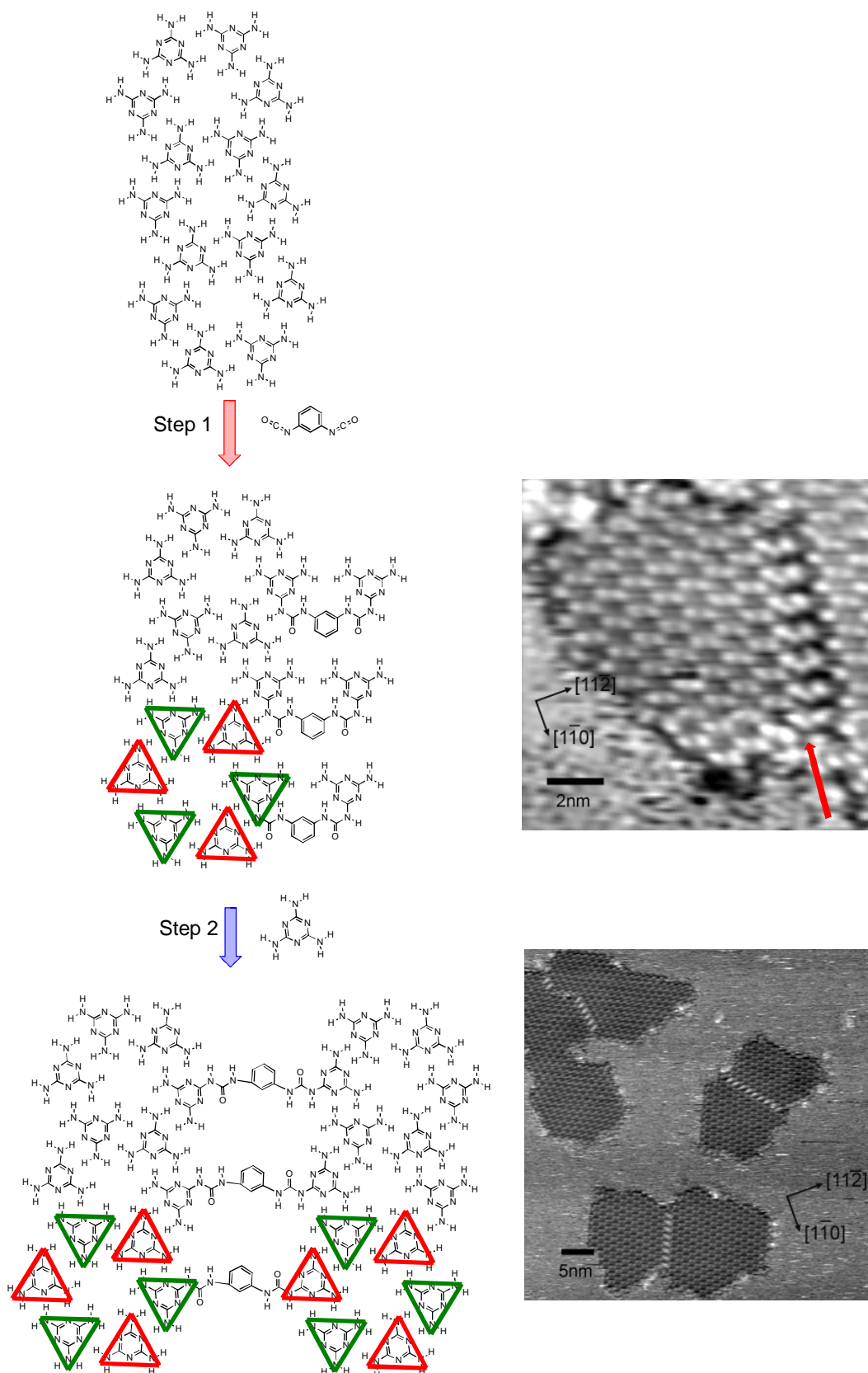


Figure 6.33 Schematic showing how diurea species Oligomer D is incorporated into melamine domains

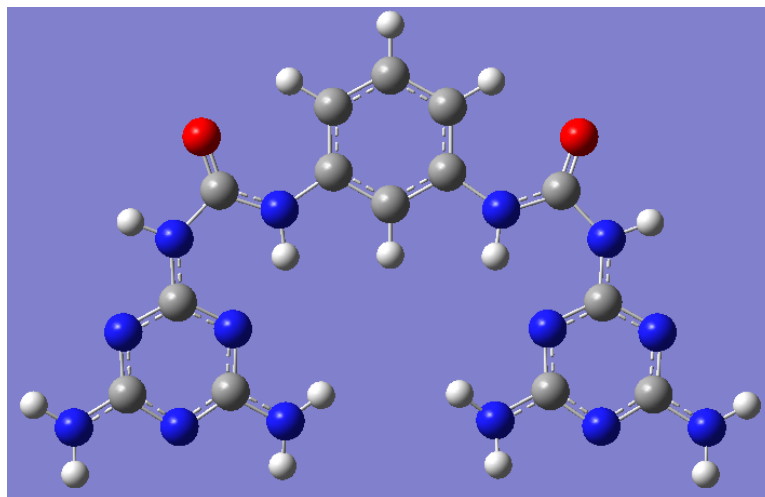


Figure 6.34 Optimised gas-phase structure of Oligomer D, as acquired by calculation in Gaussian 09. Carbon atoms appear as grey, hydrogen white, oxygen red and nitrogen blue.

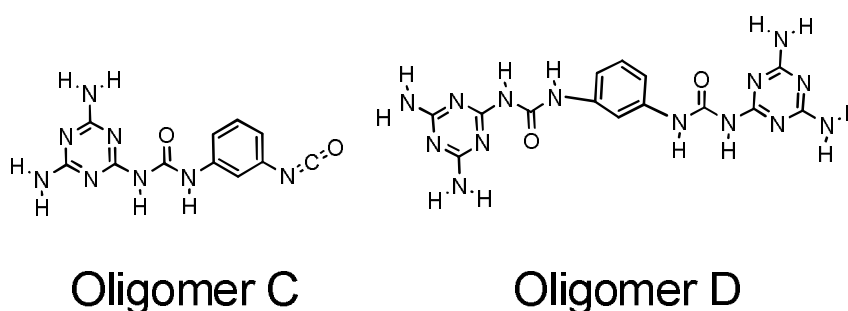


Figure 6.35 Possible urea species formed in the reaction of 1,3-PDI and melamine. Oligomer D, in figure 6.36, is most likely linear with its middle aromatic ring pointing out of plane.

Annealing the sample for a greater length of time only serves to slightly increase the number of the stripes within melamine domains that are caused by the formation of Oligomer D. Hence, this experiment was discontinued. 1,3-PDI seems to react more slowly than 1,4-PDI and this might be attributed to the fact that the two isocyanate groups are closer to each other and one may sterically hinder the other during an addition reaction. The low desorption temperature of both species limits the aggressiveness with which the sample can be annealed and in order to see more urea species on the surface, it may be best to allow the molecules to react upon the sample at room temperature over a period of days; from these observations, a period over a week may be necessary to see significant development.

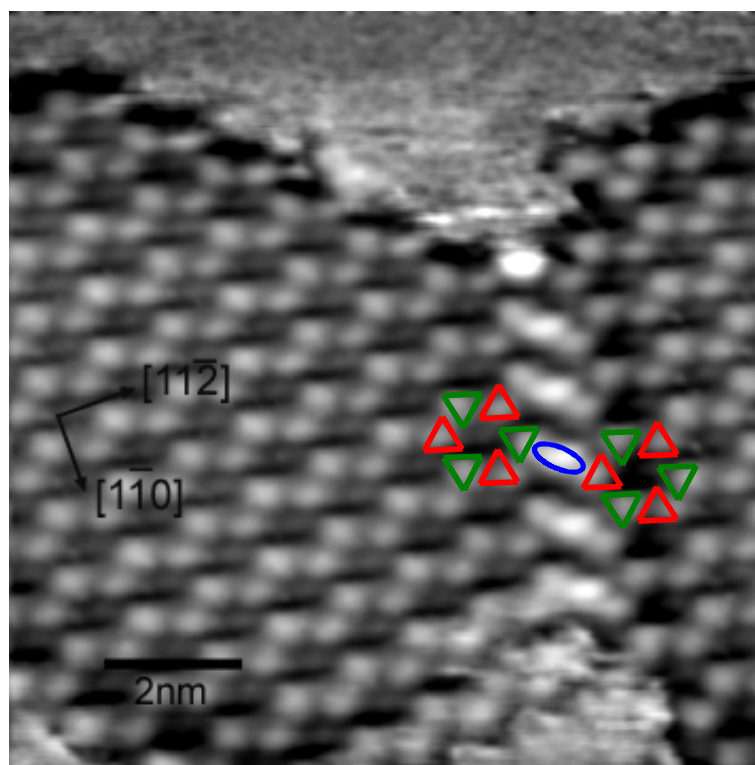


Figure 6.36 STM image showing complete stripes caused by diurea molecules being incorporated into melamine domains (11 nm x 11 nm, 0.8 V, 0.2 nA)

One striking difference between 1,3-PDI and 1,4-PDI in the reaction with melamine is the production of the diurea species, Oligomer D, consisting one diisocyanate and two melamine molecules which is analogous to Oligomer B, without any build up in concentration of monourea molecules consisting of only one melamine molecule and a diisocyanate molecule (Oligomer C, figure 6.35). These results suggest that although 1,3-PDI is less reactive than 1,4-PDI, Oligomer C, the urea with just one melamine unit, must be more reactive than the analogous Oligomer A species formed in the reaction of 1,4-PDI. The reason for this may be that the transition state of Oligomer C during the reaction with melamine is better stabilised by delocalisation of electrons around the phenyl ring. The analogous reaction between Oligomer A and melamine may have higher activation energy causing the continued observation of Oligomer A through a large range of annealing temperatures during the previous experiment. The diurea molecule, Oligomer D, is considered a relatively unreactive species, it contains no isocyanate groups thus further reaction is dependent upon the incident concentration of 1,3-PDI at the edges of molecular domains. Presumably, if the experiment was allowed to continue, there would be a larger population of

Oligomer D on the surface and these would assemble into organised porous phases that are stabilised by hydrogen bonding before being converted to larger oligomers by reaction with further 1,3-PDI molecules.

### 6.3.3.1 Summary

The reaction of melamine and 1,3-PDI on Au(111) results in the production of diurea molecules which are incorporated into melamine domains and seen as stripes. Despite annealing the surface bearing both species for 3-4 days, no larger polyurea molecules are observed. The temperature at which the surface can be annealed is limited by the desorption temperature of melamine and 1,3-PDI (although TPD experiments have yet to be performed to confirm). The experiment would likely yield more urea products if left for a longer period but limitations of apparatus availability meant that the reaction was curtailed.

### 6.3.4 Melamine and 1,6-hexamethylene diisocyanate

The reaction of melamine with 1,6-hexamethylene diisocyanate (1,6-HDI) upon Au/mica was carried out under ambient conditions.

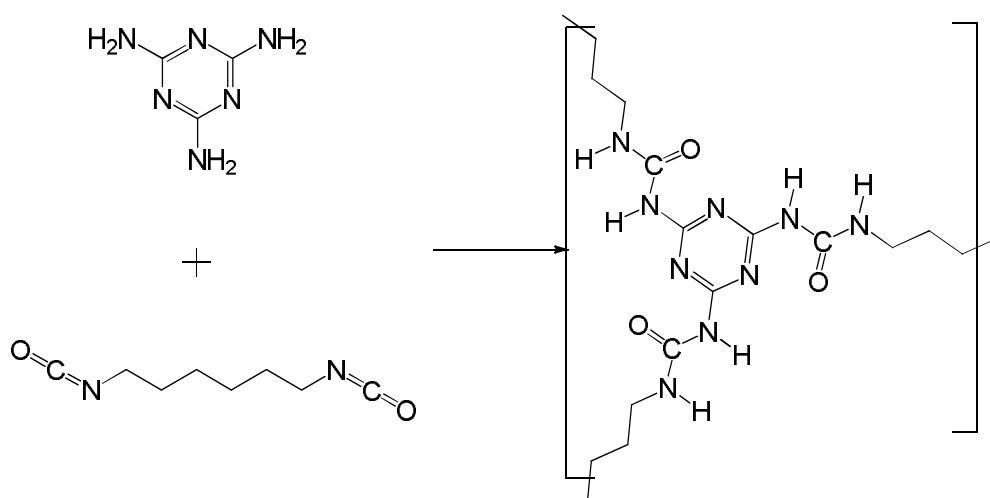
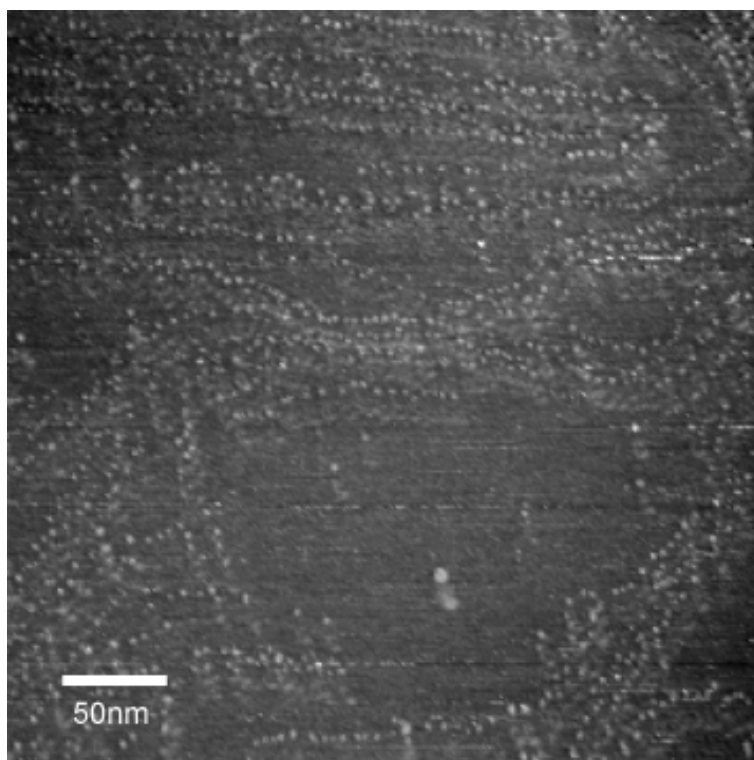


Figure 6.37 Reaction of melamine and 1,6-hexamethylene diisocyanate and the potential polyurea product

After the deposition of melamine from DMF solution, dark patches appear on the surface and from previous experience of STM analysis of melamine on Au(111), these are assigned as melamine domains. A few hours after the deposition of 1,6-HDI from THF solution, the compact domains of melamine are no longer observed upon the surface, and instead, a new structure stretches over wide expanses of the surface (figure 6.38).



**Figure 6.38** STM image showing widespread network formation after the reaction of melamine and 1,6-HDI on Au/mica (350 nm x 350 nm, 0.5 V, 0.2 nA)

The features do seem to have some repeating units, they appear porous (measuring 2-3.5 nm) and often have several inlets around their edges. The structure appears blurred which may be symptomatic of the aliphatic linkers within polymeric chains. These may give the chains a degree of flexibility which could contribute to the STM appearance of the new structures. The lack of a strong interaction between the polymers and the Au surface might further enhance the hazy appearance of the new surface. Polymer chains might be expected to line up with each other and pack closely to maximise van der Waals stabilisation interactions; this could be another possible explanation why these structures contain ‘walls’ which appear thicker than the actual diameter of a single aliphatic

chain. As reported in section 6.3.1, it may be expected that melamine will only undergo double addition, however, there is a possibility that, with reduced steric hindrance of an aliphatic chain relative to a phenyl ring, trisubstitution might be slightly more favourable. In proposing models for how these polymer chains might pack, the melamine-melamine hydrogen bond also has to be considered; examples of how small oligomer chains might aggregate to yield the type of features observed in figure 6.39 are shown in figure 6.40.

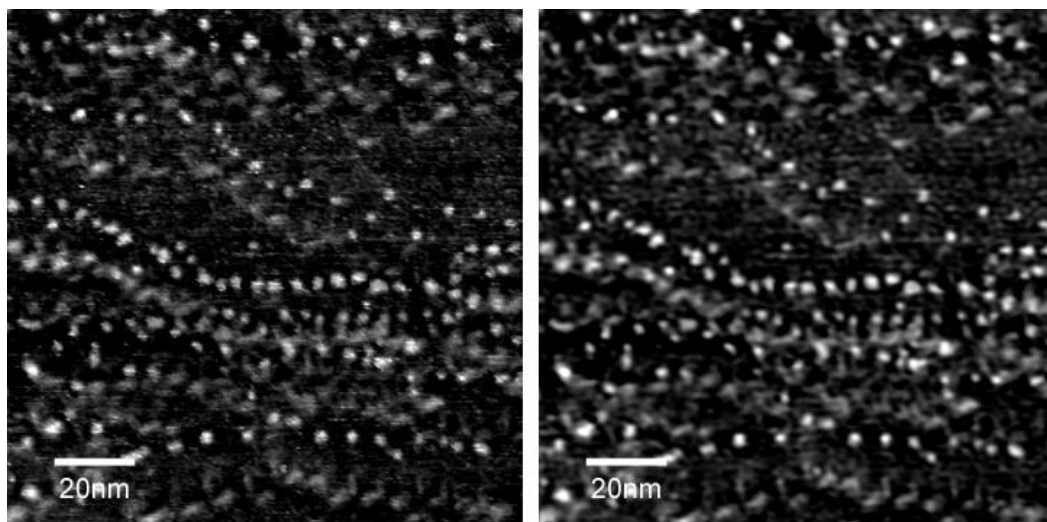


**Figure 6.39** STM images of the structures formed after the co-deposition of melamine and 1,6-HDI on Au/mica, the right hand image has undergone Fourier transform to enhance the appearance of the surface features (129.2 nm x 129.2 nm, 0.5 V, 0.2 nA)

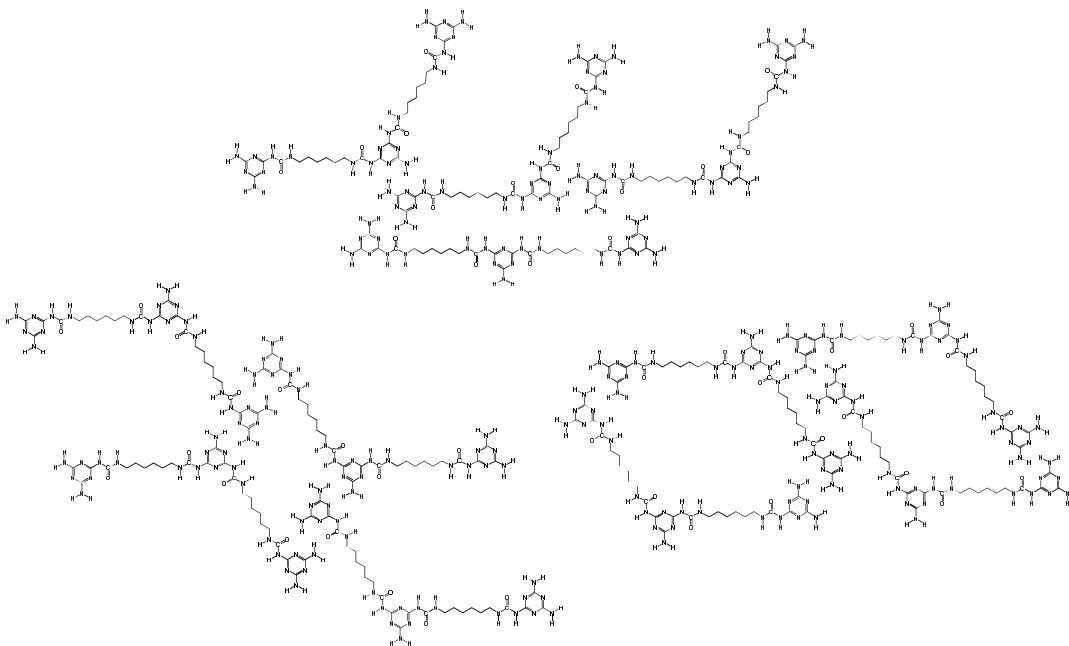


**Figure 6.40** Model showing how molecules formed from disubstitution of melamine by 1,6-HDI might arrange to form the pores and inlets in the networks seen in above STM images

The possibility of further hydrogen bonding of amino group hydrogen atoms to the carbonyl of urea linkages might also stabilise the interaction between chains. It may be possible to form both straight and bent polymer chains depending on the orientation of the urea groups about the triazine moieties. 1,6-HDI molecules measure approximately 16 Å thus it is not unreasonable to suggest, with the added distance across triazine moieties and hydrogen bonding distances between separate oligomer units, that the 2-3 nm pores within the image shown could be created by the possible arrangements shown in figure 6.40. Straight chain features are seen running left to right in figure 6.41, a model of aligned chains stabilised by hydrogen bonding interactions between amine and urea groups is proposed in figure 6.42.

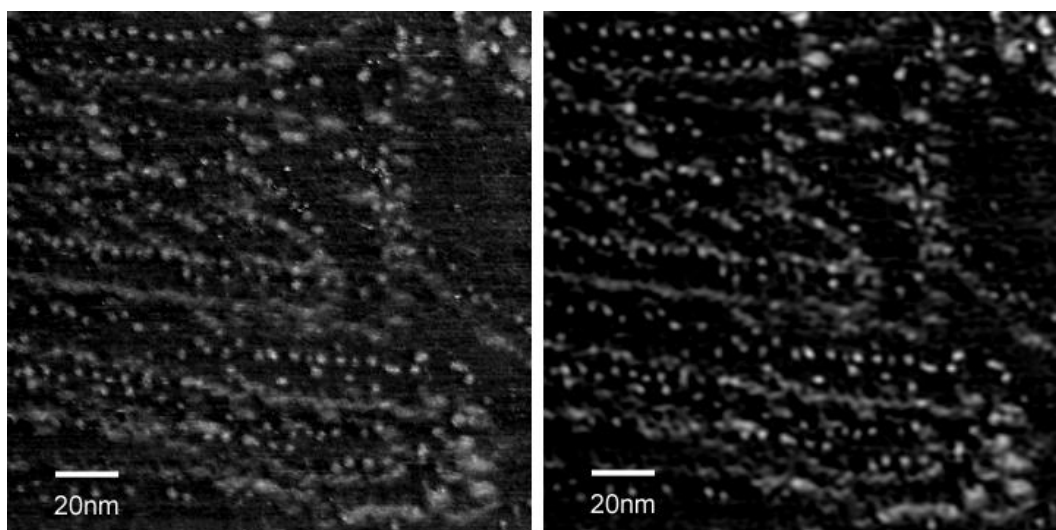


**Figure 6.41** STM showing an area of the surface characterised by chains, seen running left to right, rather than porous compact networks. Both images show the same area, the image on the right has been processed to enhance the appearance of the molecular arrangements (170 nm x 170 nm, 0.5 V, 0.2 nA)

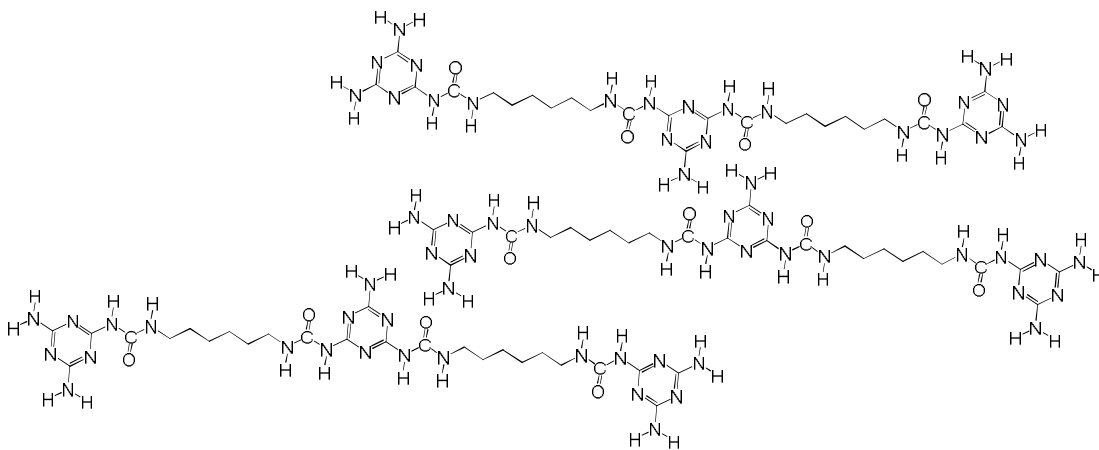


**Figure 6.42** Proposed packing of straight chains to produce chains seen in STM images.

A number of bright round features seem to mark some of the edges of the structures. These features are around 3 nm wide so cannot be assigned to either component, aliphatic or triazine linkers, of the polymer molecules. These might be explained by excess reactants piled up around the edges of the structures, possibly hydrogen bonded to whatever the protruding functional group (amino or isocyanate) is the termini of the polymer molecules. However, Richardson et al<sup>8</sup> remark that bright features are observed via STM as bond formation occurs during the surface-confined polyimide reaction studied.

#### 6.3.4.1 Summary

On this occasion, no further adsorbates were deposited, although the addition of C<sub>60</sub> fullerenes or a thiol species to the surface might have helped to characterise the new surface structures by occupying the pores and inlets within them. The appearance of the new surface structure is quite hazy, this may be characteristic of aliphatic chains upon metal surfaces or it may be symptomatic of a weak interaction between the polymer structure and the Au surface. The reaction of melamine and 1,4-phenylene diisocyanate on Au(111) only leads to two urea linkages being formed by each melamine unit, analysing the co-deposition of melamine and 1,6-hexamethylene diisocyanate on a highly-oriented pyrolytic graphite (HOPG) surface, where the adhesion of the polymeric units to the surface might be greater and better STM images may be obtained, may allow the likely products of a surface-confined reaction to be observed and permit better understanding of the obscure products witnessed upon Au/mica.

#### 6.3.5 1,4-phenylene diisocyanate and 1,6-diaminohexane

Similarly, the reaction of 1,4-phenylene diisocyanate (1,4-PDI) and 1,6-diaminohexane (figure 6.43) was carried out under ambient conditions using sequential deposition of each component from THF solutions onto a Au/mica sample.

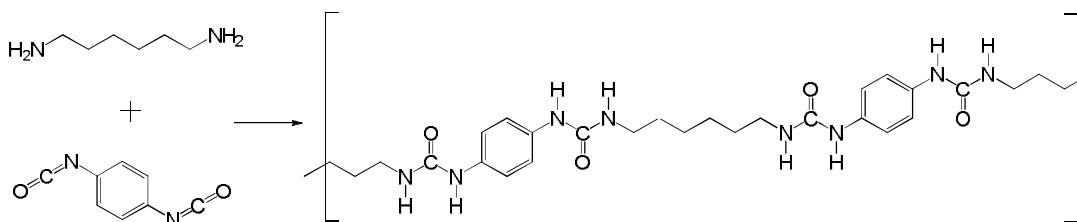


Figure 6.43 Potential reaction between 1,6-diaminohexane and 1,4-PDI

As previously observed, the deposition of 1,4-PDI from solution leads to amorphous piles that are perhaps stabilised by solvent molecules during their initial nucleation and growth, as seen in figure 6.44. Features around 10 nm wide and of apparent height 1-2 nm are seen distributed randomly across the surface. The stabilisation afforded by  $\pi$ - $\pi$  stacking must exceed any benefit gained by the formation of monolayer structures which might be destabilised by repulsive electrostatic interactions between isocyanate groups pointing towards each other in the same plane.

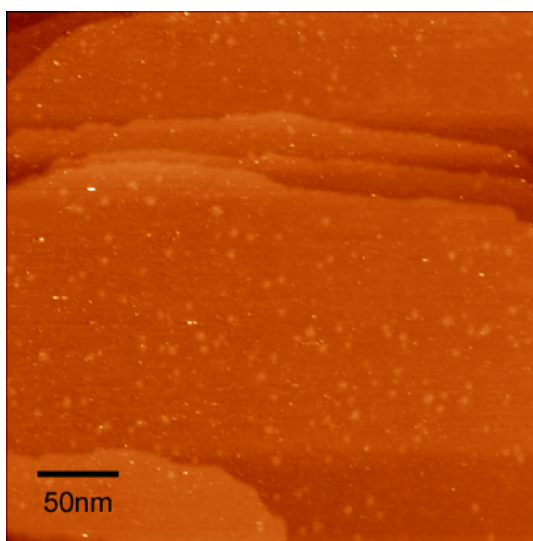


Figure 6.44 STM image showing multilayer deposits of 1,4-PDI on the Au/mica surface (330 nm x 330 nm, 0.5 V, 0.2 nA)

Exposure of surfaces bearing these 1,4-PDI formations to a 1 mM 1,6-diaminohexane (DAH) in THF solution leads to two different types of features. The first may be the ultimate product of the reaction, straight chains are seen in figure 6.45; rounded features of ~6 nm wide are separated by 7-8 nm. The fact that the features appear close together and linked as opposed to randomly spread across the surface suggest that reaction has occurred between the DAH solution

and the 1,4-PDI stacks. However, the width of these features means that they are likely to be agglomerates of many polymeric chains or multilayer chains where structures are stabilised as before by  $\pi$ - $\pi$  stacking of chains on top of each other.

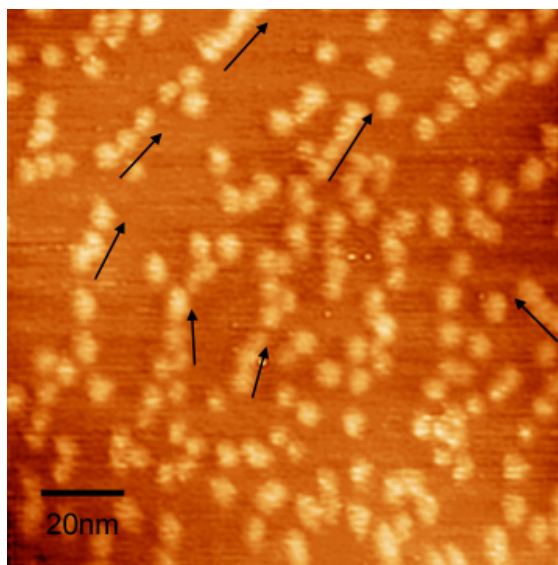


Figure 6.45 STM image showing the alignment of molecular features following the deposition of 1,6-diaminohexane onto the surface bearing 1,4-PDI (134.5 nm x 134.5 nm, 0.5 V, 0.2 nA)

The second type of feature observed, in figure 6.46, consists of circular features being accompanied by cloudy rectangular formations (7 nm long). Based on some of the intermediate stages witnessed during some of the other urea forming reactions, it may be that these features are DAH molecules attacking 1,4-PDI molecules within the circular stacks, as discussed, the aliphatic chains seem to cause blurred features when analysed by STM. The other possibility is that these features are artefacts and a result of a ‘double tip’, a problem that results in features being represented twice (best STM images are obtained when tunnelling occurs through a single atom but if tunnelling occurs through multiple atoms, the acquired image is a convolution of multiple images<sup>37</sup>), but the terrace edges appear to be imaged accurately thus the features must be caused by the behaviour of the molecular components present. Although the reaction is instantaneous in solution, the surface may inhibit the angle of nucleophilic attack and slow the progress of the reaction thus enabling the images of incomplete reactions to be captured.

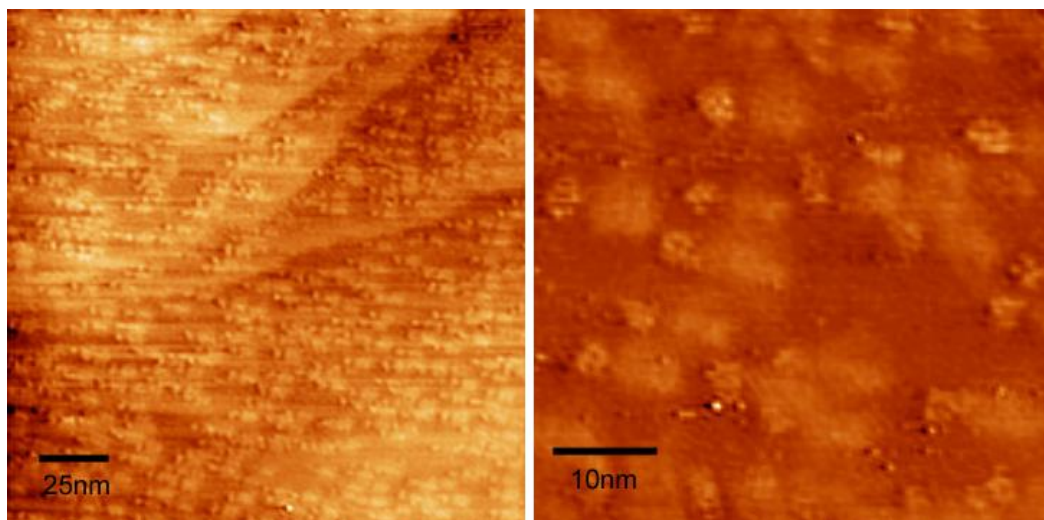


Figure 6.46 STM images showing 1,6-diaminohexane groups reacting with 1,4-phenylene diisocyanate aggregates (left, 190 nm x 190 nm, right, 75 nm x 75 nm, 0.05 nA, -0.5V)

In order to obtain better images depicting monolayer structures, the reaction between 1,4-PDI and DAH was carried out in solution by combining equal volumes of 1 mM solutions of each in THF, a cloudy layer is instantaneously observed in the solution. The mixture was then diluted 20-fold before briefly exposing to an Au/mica sample; this results in chains of circular features of only 1-2 nm diameter which are separated by only ~2-3 nm. It is likely that the image of figure 6.47 may depict structures that are mostly monolayer polymers where the bright features along the chain are actually the aromatic parts of the polyurea chains.

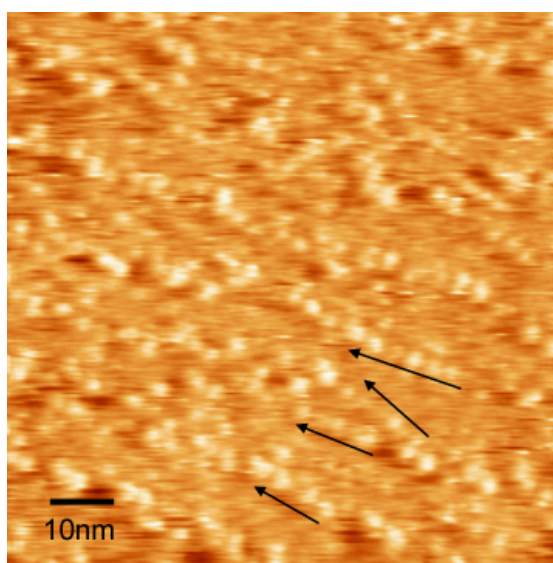


Figure 6.47 STM image of the polymeric structure formed between 1,4-phenylene diisocyanate and 1,6-diaminohexane, arrows highlight some of the proposed polymer chains (87 nm x 87 nm, 0.05 nA, -0.4V)

### 6.3.6 1,3-phenylene diisocyanate and 1,6-diaminohexane

The reaction of 1,3-phenylene diisocyanate (1,3-PDI) and 1,6-diaminohexane (1,6-DAH) was carried out under ambient conditions using sequential deposition of each component from solution onto a Au/mica sample. Surface coverage, in this case, is higher after the deposition of 1,6-DAH than for the previous example. Like 1,4-PDI, 1,3-PDI is initially to be seen forming stacks across the Au surface after deposition from 0.1 mM solutions in THF (figure 6.49).

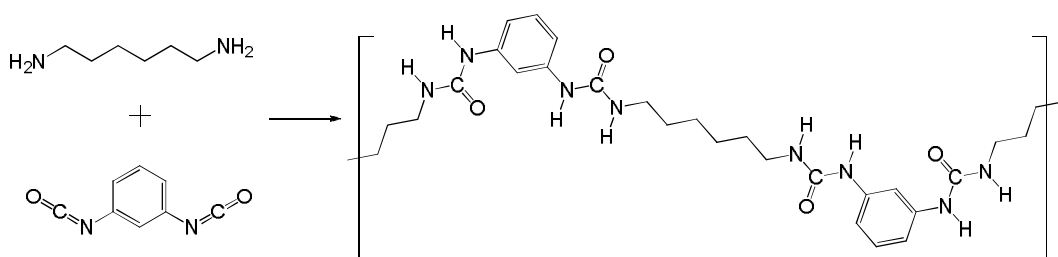


Figure 6.48 Potential reaction between 1,6-diaminohexane and 1,3-phenylene diisocyanate

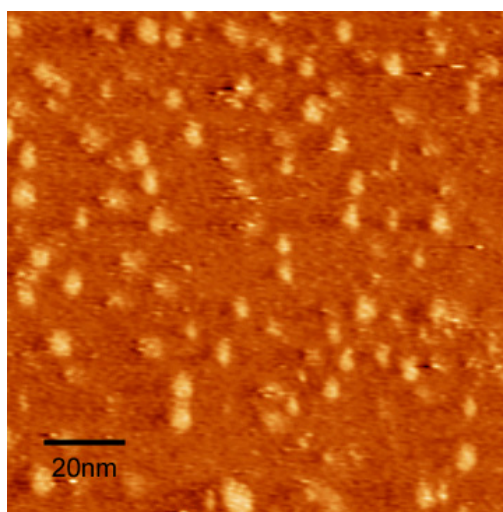


Figure 6.49 STM image of the amorphous features observed when 1,3-PDI is deposited from THF (120 nm x 120 nm, 0.5 V, 0.15 nA)

After exposure to 1mM DAH solution, the stacks are first seen to diminish in quantity, with the occurrence of disorganised chain-like features sprawling across the surface. The main characteristics of these chains are bright characters spaced by less than 2 nm. This is in accordance with the separation between aromatic

rings along the target polymer. It is difficult to deduce the length of the chains, although it is certainly possible to identify particles of 3-4 linked aromatic units. However, the chains may undoubtedly be much longer. Figure 6.50, with the use of arrows, indicates the direction of growth of some of the straight linked units.

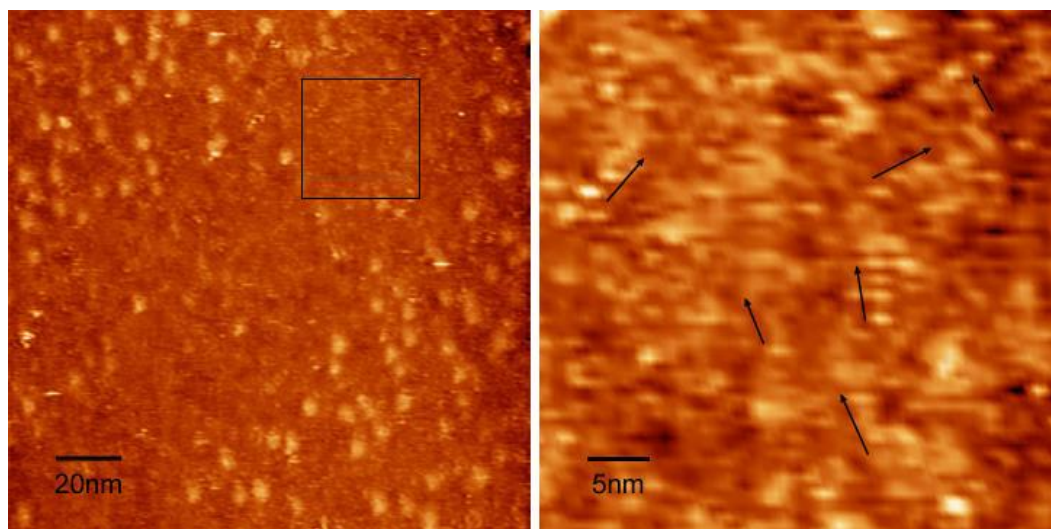


Figure 6.50 Right, STM image showing the progressive diminution of 1,3-PDI features after deposition of 1,6-diaminohexane (140 nm x 140 nm, 0.5 V, 0.15 nA), left, zoomed area of STM image showing smaller features and possible chains (42 nm x 42 nm)

Once all of the stacks are consumed, the surface is then thought to be completely covered with polymeric material (figure 6.51). As stated before, the aliphatic moieties may cause structures to appear blurred if they do not interact strongly with the Au(111) surface. Irregular shaped gaps appear in the molecular layer. It is thought that this must consist of agglomerated polymeric chains, the 1,3-positions of the substituents on the aromatic rings means that the polymeric chains do not order as neatly relative to the polymeric chains built from 1,4-PDI units. One of the other explanations for the disorder may be the ability of polyureas to cross-link, as illustrated in figure 6.52; such a possibility applies to all of the polyureas formed over this set of experiments. Lone pairs of electrons on the urea groups can attack free isocyanate groups to form branched structures, should these form, the chances of tighter packing of chains is decreased. The manoeuvrability of larger polymeric units into positions necessary for reaction may hamper such a

reaction, ureas are much less reactive towards isocyanates and require heat to activate the reaction<sup>38</sup>.

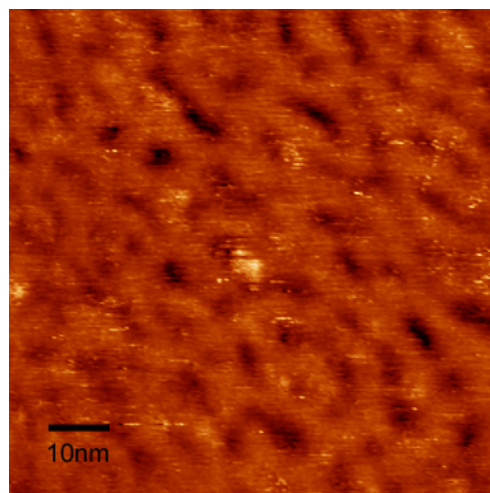


Figure 6.51 STM image showing the surface after removal of all 1,3-PDI features (80 nm x 80 nm, 0.5 V, 0.15 nA)

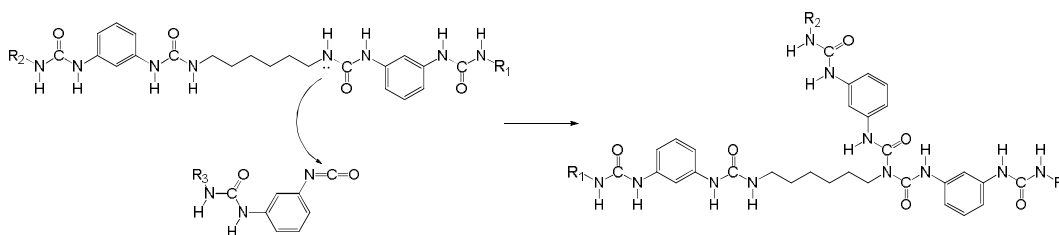


Figure 6.52 Possible cross-linking caused by reaction of urea groups with isocyanates

## 6.4 Formation of surface-supported polyamide networks

Amides are a class of compounds that consist of a nitrogen atom linked to a carbonyl group. In this study the formation of surface-supported covalent networks incorporating secondary amides ( $\text{RC(O)NHR}$ ) is investigated. Like urea groups, secondary amides possess electronegative bonds that are potentially useful for molecular recognition applications involving hydrogen bonding<sup>39,40</sup>. Here, examples of amide formation from the reaction of carboxylic acid and isocyanate species (Section 6.4.1) and the reaction of acyl chloride and amine species (Section 6.4.2) are examined.

## Results and Discussion

### 6.4.1 1,4-phenylene diisocyanate and Benzene-1,3,5-triyl-tribenzoic acid

The co-deposition of 1,4-PDI and benzene-1,3,5-triyl-tribenzoic acid (BTA) was carried out on Au/mica to determine if a surface-confined reaction could occur. Carboxylic acids and isocyanates react to form mixed carbamic-carboxylic anhydrides (I) that are, in most cases, unstable<sup>41</sup>, this is illustrated in figure 6.53. These species decompose by two paths (A) to either an amide (II) or (B) to a mixture of symmetrical ureas (III) and anhydrides (IV). Under normal circumstances (in non-polymerisation reactions), the mixture of urea and anhydride products can be converted to the amide (II) by heating the solution of reactants.

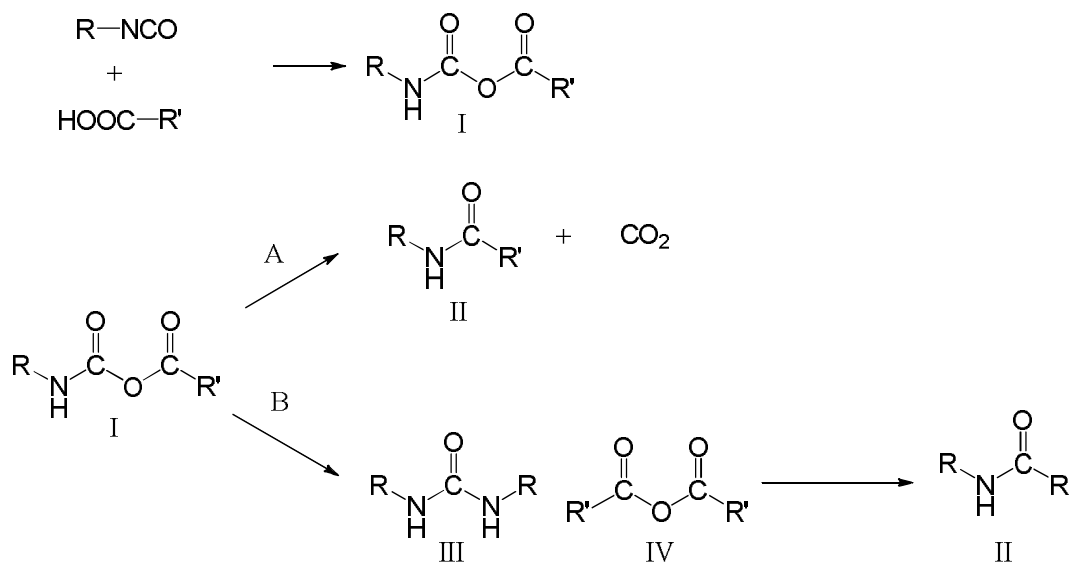
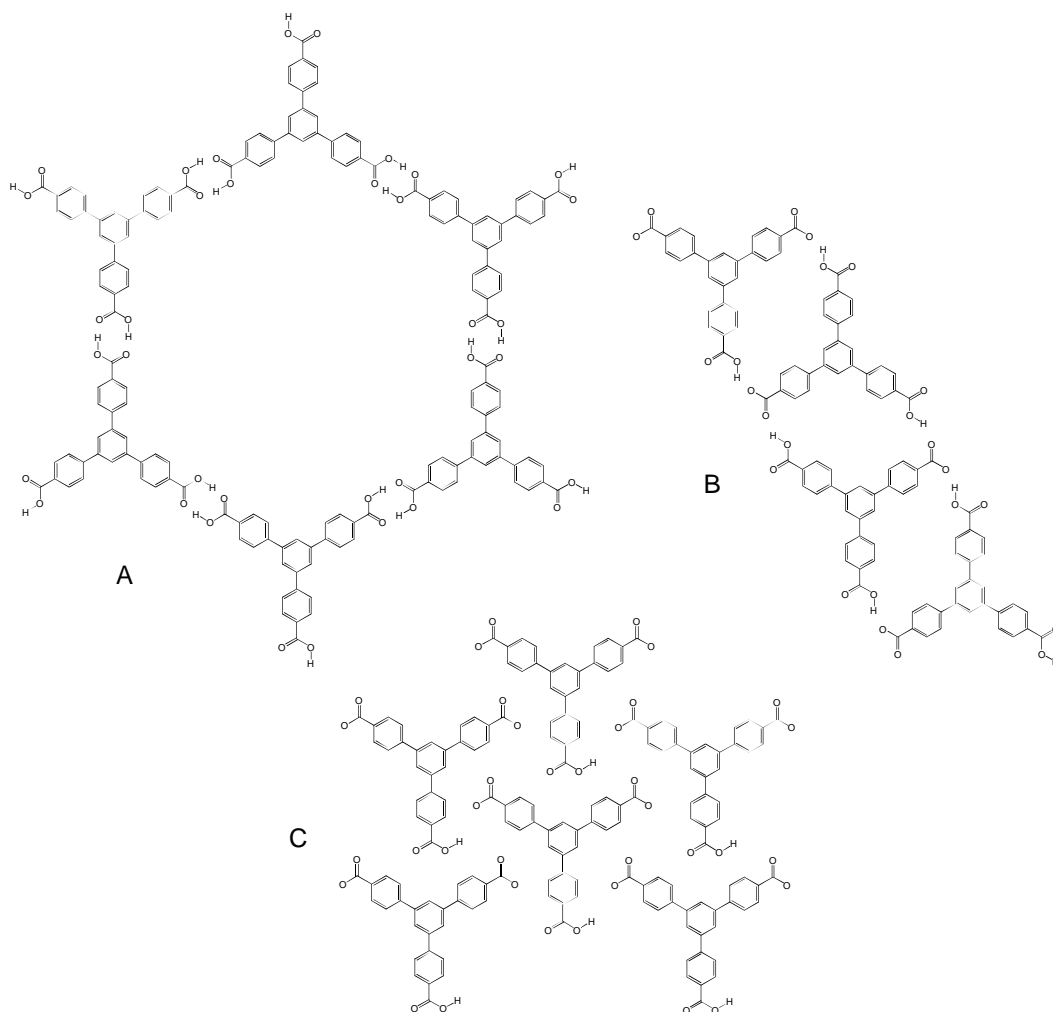


Figure 6.53 Scheme illustrating possibilities of a reaction between an isocyanate and a carboxylic acid

Melamine is shown to only form two urea linkages when reacted with 1,4-PDI<sup>42</sup>, although the amino groups of melamine become progressively deactivated towards reaction with the formation of each urea linkage, the reaction might also be disfavoured by steric hindrance around the triazine moieties. Addition of three aromatic molecules may occur around a larger three-fold molecule. To this end, 1,4-PDI was co-deposited with benzene-1,3,5-triyl-tribenzoic acid with the intention of forming polyamide structures upon the Au surface.

The self-assembly of trimesic acid<sup>43-48</sup> into 2-D hydrogen bonding networks on surfaces has been studied extensively, its carboxylic acid groups align to form two O-H...O hydrogen bonds and its three-fold symmetry lends itself to the formation of hexagonal arrangements. Benzene-1,3,5-triyl-tribenzoic acid (BTA) can be considered a larger analogue of trimesic acid, possessing the same symmetry and functional groups; its adsorption on Ag(111) has been studied, however, three temperature-dependent phases are observed<sup>36</sup> (figure 6.54).



**Figure 6.54** Models of the three phases formed by BTA on Ag(111)<sup>36</sup>: honeycomb (A), ribbon (B) and close-packed (C)

The hexagonal phase which is observed at room temperature on Ag(111) could potentially be transformed into an ordered covalent network by templating reactive co-adsorbents in a similar way to the macrocyclic guest molecules

reported<sup>36</sup>. Addition reactions could then possibly be activated through annealing treatments. This potential mechanism is shown in figure 6.55.

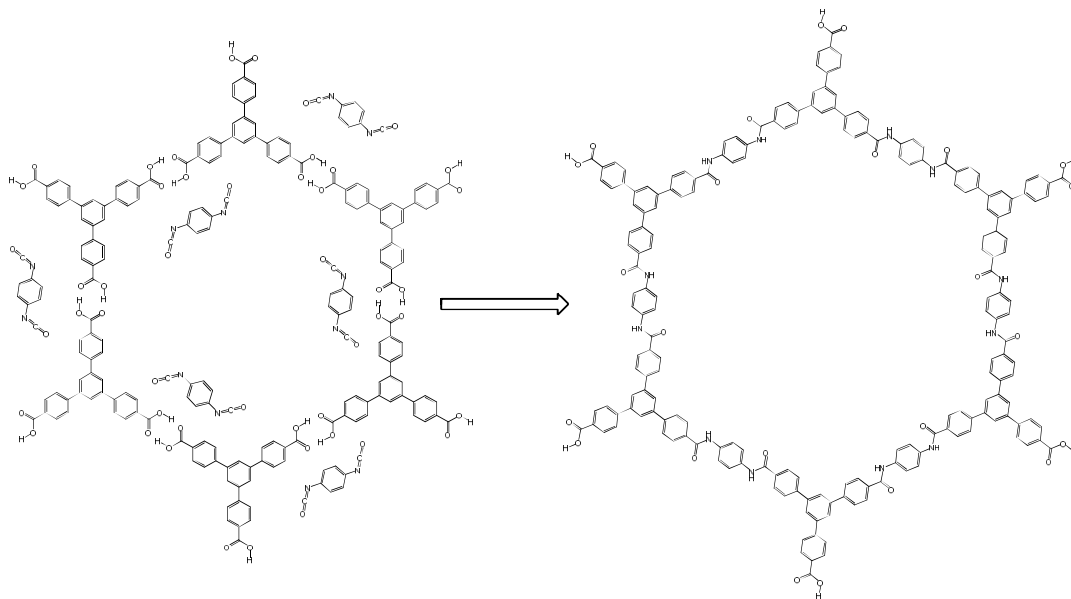


Figure 6.55 Potential mechanism for templating reactants prior to polyamide network formation

#### 6.4.1.1 Benzene-1,3,5-tri(4-tribenzyloxyphenyl)carboxylic acid on Au/mica in ambient conditions

The resolution allowed by the STM in ambient conditions makes it difficult to define the observed arrangements formed by BTA on Au/mica. At high coverage, ordered and disordered areas of the sample are observed. The ordered structures consist of rows of features measuring 15 Å, variably spaced between 15 Å and 20 Å apart, molecular resolution is not attained in the STM images of figures 6.56. A ribbon feature consisting of pairs of molecules is observed on Ag(111) (arrangement B in figure 6.54), but although resolution is poor, it is unlikely that the ribbon feature is observed here although it appears as the most similar of the phases previously reported; the rows do not measure two BTA molecules wide and the features with them do not appear in pairs. The honeycomb arrangement observed on Ag(111) does not appear to have formed in this case either. Another possibility may be the formation of chains where pairs of BTA molecules hydrogen bonded by the typical junction line up with each other perhaps via weaker, non-aligned O-H...O interactions, a potential chain arrangement is shown in figure 6.57.

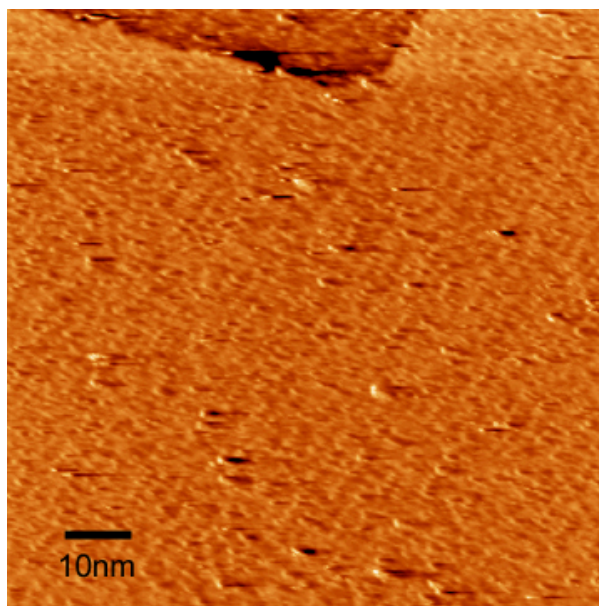


Figure 6.56 STM image showing linear rows of BTA on Au/mica after deposition from THF solution (124.4 nm x 124.4 nm, 1.2 V, 0.15 nA)

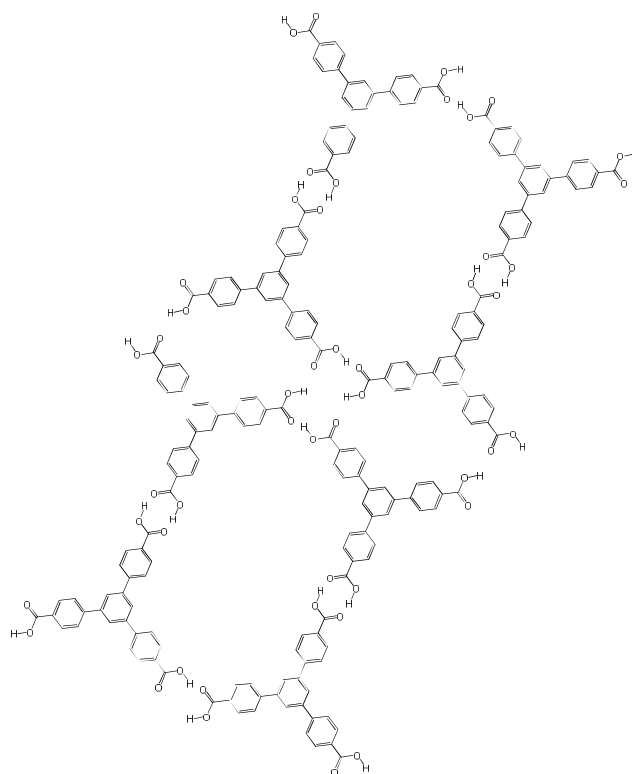
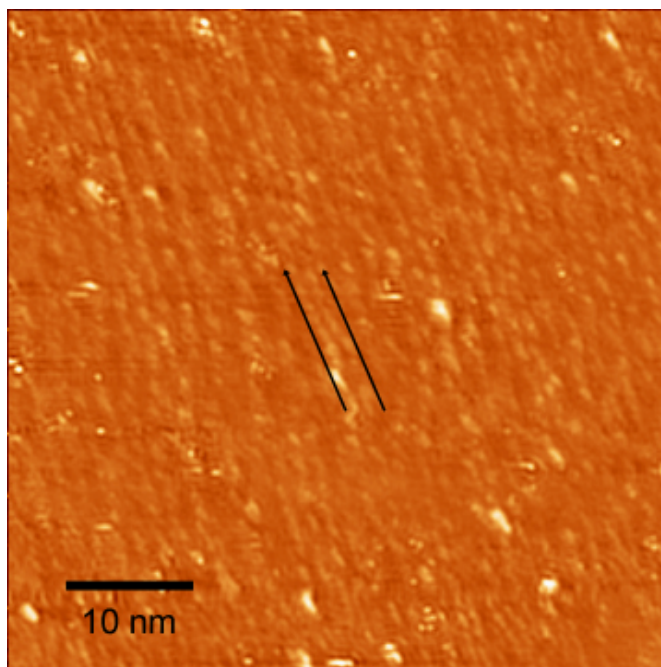


Figure 6.57 Model of how single molecule-wide chains might be interconnected and align to give the row features observed in figure 6.56

The disordered structures observed at high coverage (figure 6.58) might be localised areas of molecules interacting with each other due to a mixture of interactions. The more closely-packed arrangements that are observed most

closely resemble the close-packed BTA phase formed at 420 K on Ag(111) (C), with contributions from the ribbon phase, which was observed at 320 K (B) on Ag(111).



**Figure 6.58** STM image showing a more disordered arrangement of BTA on Au/mica after deposition from THF solution. Most of the molecules appear to be in a compact arrangement but some, indicated by the two arrows seem to be in a ribbon formation (60 nm x 60 nm, -1.3 V, 0.1 nA)

At lower coverages, the surface, shown in figure 6.59, is characterised by chains  $\sim 19$  Å and apparently two molecules in width, the periodicity along the rows is  $\sim 16$  Å thus they may be analogous to the ribbon phase formed on Ag(111). Conversely, the study of BTA on Ag(111)<sup>36</sup> suggests that different levels of thermal deprotonation can explain the conversion between phases, but the formations observed here were observed at room temperature and warming samples did not induce noticeable change. There are several factors which may be responsible for the differences in behaviour: the change of substrate (Ag(111) to Au(111)), different environments (in UHV and in air) and means of deposition (evaporation and solvent deposition). THF is a commonly used solvent for deposition of molecules, self-assembled monolayers and polymeric thin films. It is not strongly basic and was chosen here for its anticipated inertness towards isocyanates. Hydrogen bonded chains are proposed in figure 6.60 which may form from fully protonated BTA molecules.

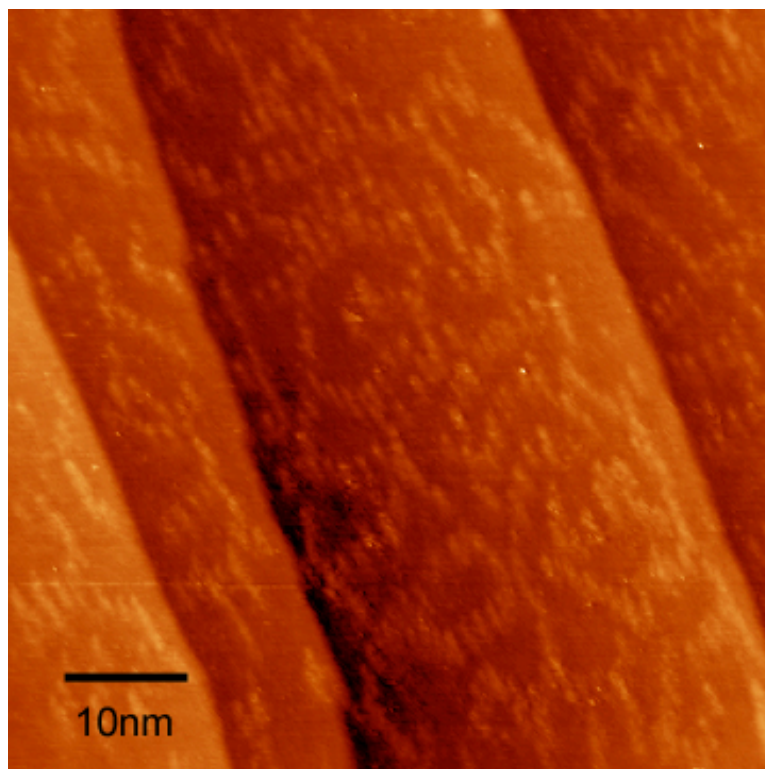


Figure 6.59 STM image of a low coverage of BTA upon Au/mica (62.4 nm x 62.4 nm, 1.2 V, 0.15 nA)

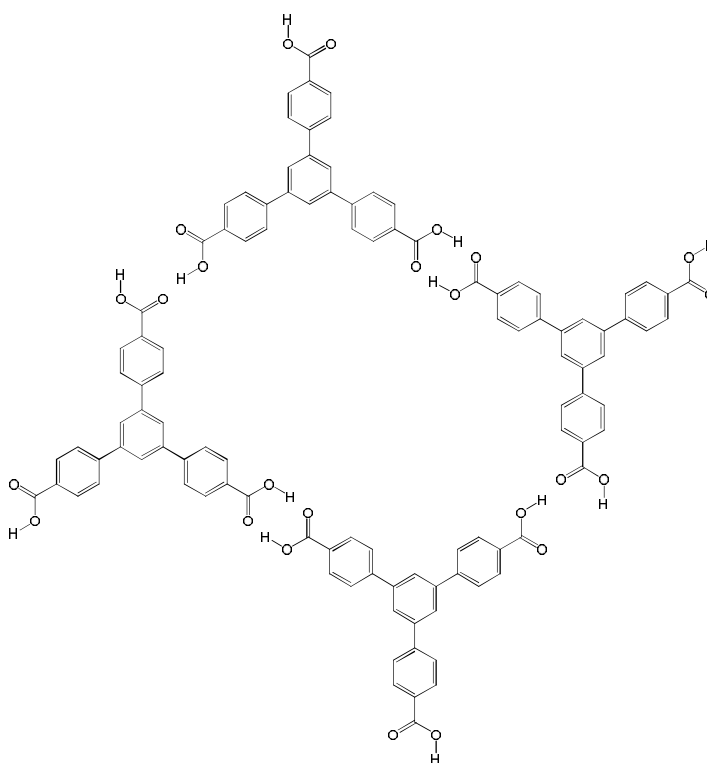
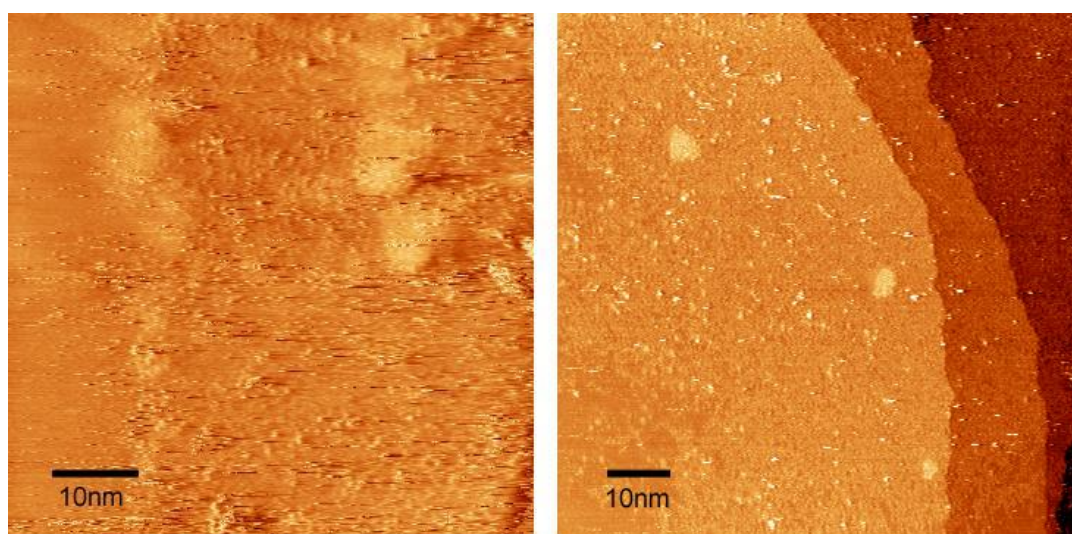


Figure 6.60 Proposed arrangement of BTA molecules to explain the ‘ribbon’ features observed on Au(111)

### 6.4.1.2 Co-deposition of BTA and 1,4-PDI

Etching of the Au surface by BTA and by 1,4-PDI is occasionally observed; in extreme cases, it can make analysis of the organic adsorbate impossible. Roughening of gold surfaces after exposure to THF has been reported<sup>49</sup>. However this effect generates a different type of morphology change that occurs over 3-4 hours, whereas sample immersion times in this system are in the order of minutes. Although, the initial idea was to template the deposition of the reactive 1,4-PDI species into the BTA network (figure 6.55), to avoid deterioration of substrate and any influence this has upon adsorbate distribution (by the creation of nucleation points), the approach of swift exposure to 1,4-PDI after deposition of BTA, without time-consuming prior STM analysis of the arrangements of BTA upon the surface, is used such that both species become occupied in reactions with each other rather than etch the surface.



**Figure 6.61** STM images showing the surface after the deposition of 1,4-PDI and BTA before and after annealing. The left hand image is captured immediately after deposition and shows a disordered and rough surface (60.8 nm x 60.8 nm, 1.0 V, 0.05 nA). The right hand image shows densely packed monolayer arrangements of molecules towards the step edges after heating up to 390 K (83.1 nm x 83.1 nm, 0.9 V, 0.1nA)

The reaction between amines and isocyanates seems to occur more quickly<sup>38</sup>, or at least, the surface-confined reaction between melamine and 1,4-PDI takes place more readily than BTA and 1,4-PDI. At room temperature, the surface is disorganised and annealing is required to allow monolayer arrangements to be observed (figure 6.61). After annealing to 390 K, dense areas of molecules are

seen despite overall coverage being far from a saturated monolayer. Despite the aforementioned problem of poor resolution, it may be possible to argue that reaction has occurred with the outcome most likely being decomposition of an unstable mixed carbamic-carboxylic anhydride to a mixture of ureas and anhydrides rather than amides. On closer analysis of the features that make up the densely-packed areas, in figure 6.62, larger features are seen to be surrounded by thin chains, which appear to line up alongside each other (examples are highlighted by arrows).

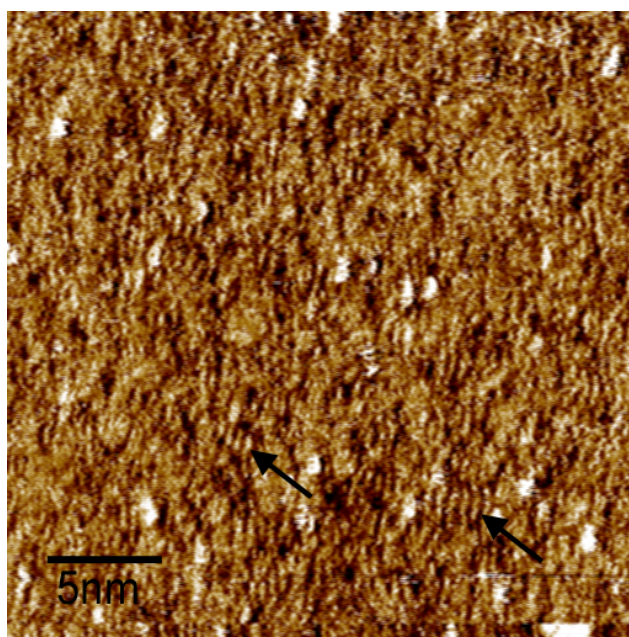


Figure 6.62 STM image of BTA and 1,4-PDI after annealing the Au/mica substrate to 390 K (27.5 nm x 27.5 nm, 0.9 V, 0.15 nA)

With reference to the reaction possibilities in figure 6.53, these straight chain features measure around 55 Å across and are up to 24 Å long thus can reasonably be attributed to ureas (III) based upon 1,4-PDI of various lengths, with chains of 2 or 3 aromatic rings most common. Hydrogen bonding between the urea groups, as shown in figure 6.63, likely stabilises the surface arrangements of the urea chains and cause them to align with each other. The larger molecular features appear less discrete.

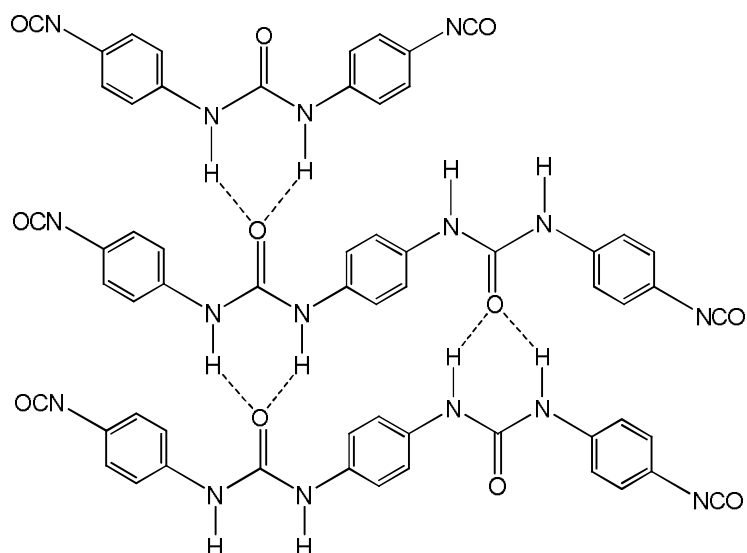


Figure 6.63 Model showing two different small urea products and how hydrogen bonds might be formed between urea groups on adjacent chains

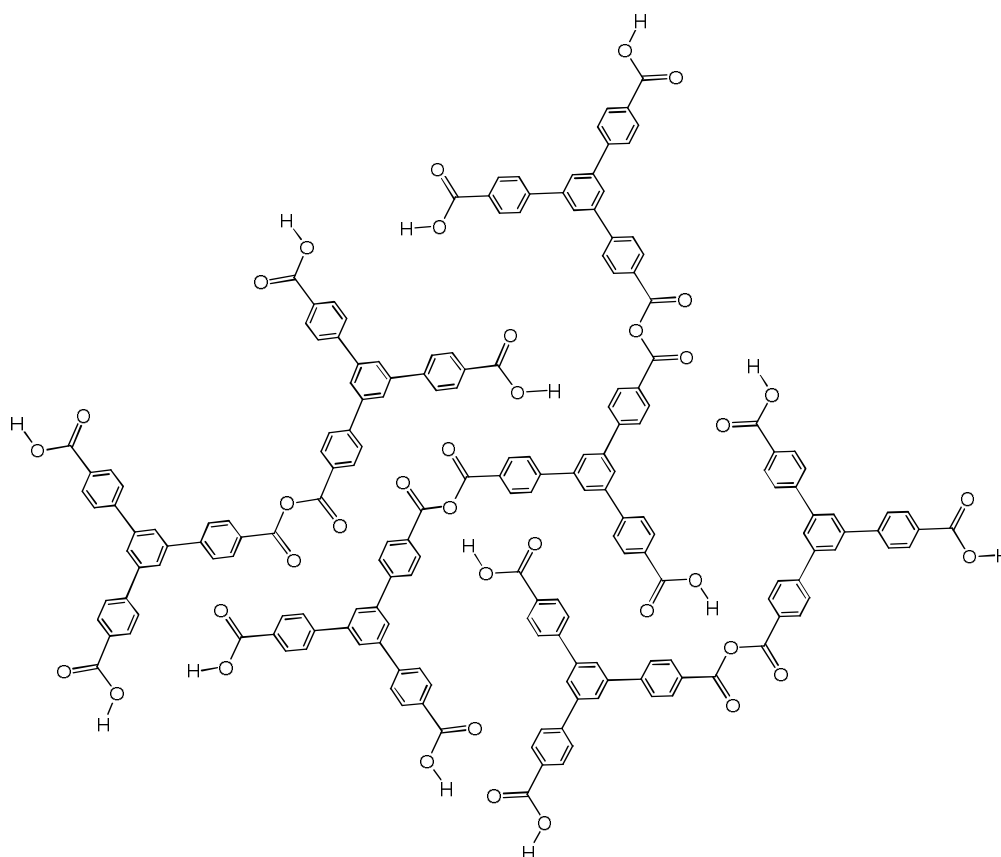


Figure 6.64 Model showing two different anhydride products based upon BTA and how disordered close-packing of these molecules might yield the obscure, dense, amorphous features observed in STM images

With reference to the possible outcomes of the reaction, if ureas are formed, then so to must anhydrides (IV). It is difficult to attribute the sizes of these features in the STM images to discrete molecules and estimate a chain length but anhydride molecules made from BTA contain multiple aromatic rings thus can be expected

to be seen as broader features. These units will still retain some hydrogen bonding capability through unreacted carboxylic acid groups (figure 6.64). However, the bulk of these units might cause their stabilisation upon the surface to be controlled by van der Waals interactions and lack directionality, resulting in amorphous agglomerates like those shown in figure 6.62. Alternatively, anhydride oligomers form porous arrangements which are filled by smaller unreacted 1,4-PDI or BTA molecules, causing these domains to be observed as solid features.

No discernible change is observed after heating to 420K, but upon annealing to 470 K, the molecular arrangement appears much more porous (figure 6.65). The thin chain features are no longer apparent upon the surface. The gaps in the molecular formation vary from 7 Å to 15 Å. A zone where the features appear to have some sort of periodicity is marked on the STM image. In the solution-based reaction of carboxylic acids and isocyanates, the mixture of urea and anhydride products are converted to amides upon heating but in the surface-confined polymerisation reaction of carboxylic acids and isocyanates, the surface might be expected to block this conversion by hindering the rearrangement of the short urea and anhydride oligomers into suitable positions for further reaction.

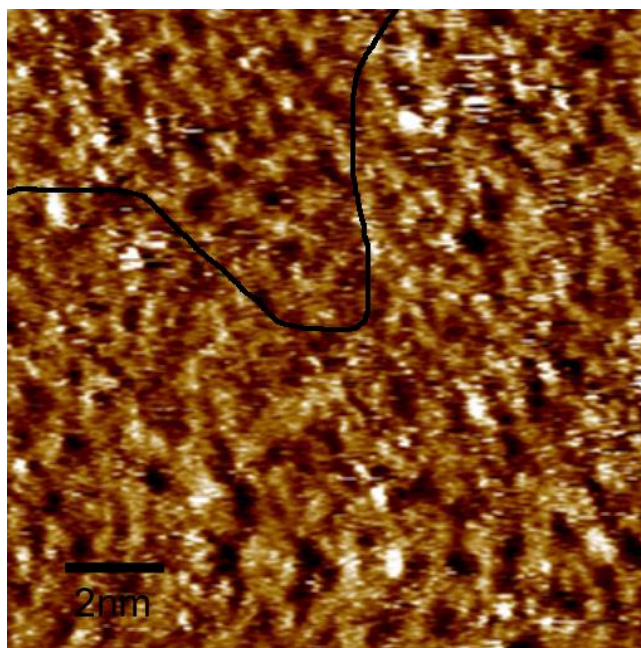
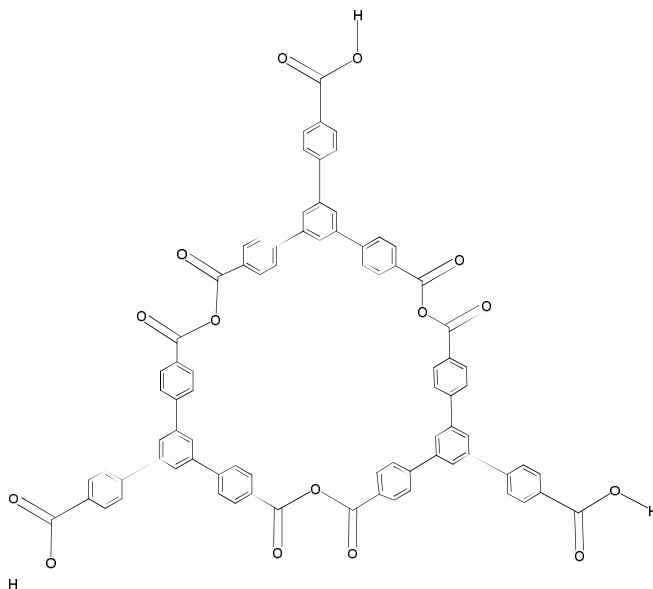


Figure 6.65 STM image of BTA and 1,4-PDI after annealing the sample to 470 K. A fairly well-ordered region is marked off in the top left corner (15 nm x 15 nm, 0.9 V, 0.15 nA)

The tubular features assigned as ureas disappear but it is unlikely that they have combined with the other features identified as anhydrides and their removal may be due to desorption at elevated temperatures, removal of other smaller molecules (1,4-PDI and BTA) may be the reason why more gaps are present in the molecular overlayer. Remaining upon the surface must be the larger anhydride molecules. The reasonably well-ordered region indicated does not contain pores wide enough to constitute the target polyamide network shown in figure 6.46.



**Figure 6.66** A potential macrocycle based upon the formation of anhydride linkages between BTA molecules

There is perhaps too much ring strain involved in the creation of fully covalent pores based upon anhydride linkages between BTA starting units (figure 6.66) thus a porous network of anhydride oligomers stabilised by hydrogen bonding between carboxylic acid group H atoms and anhydride carbonyl O atoms may have been formed (figure 6.67). This structure may seem contradictory with respect to what was proposed for these molecules at lower temperatures (figure 6.64) and it might be expected that as the surface temperature was increased then clustering of molecules into denser domains might be accelerated<sup>2</sup> but in this case, the removal of molecules from the surface may have emptied pores which existed even after annealing to 390 K and as such, the argument for van der Waals forces causing close packing of anhydride oligomers (shown in figure 6.64) may be discounted, models of potential porous arrangements based upon two different oligomers are shown in figures 6.67 and 6.68; small molecules such as 1,4-PDI or

part of BTA molecules can be envisaged as possible guests within the pores and inlets of these formations.

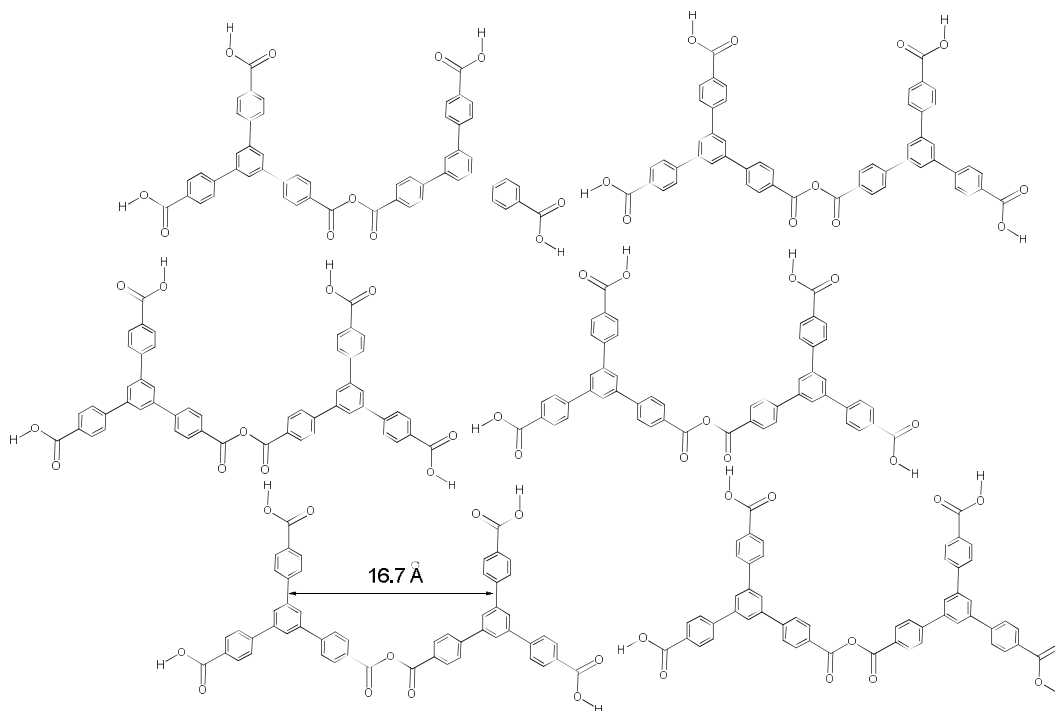


Figure 6.67 A model of a porous network stabilised by hydrogen bond between anhydride oligomers

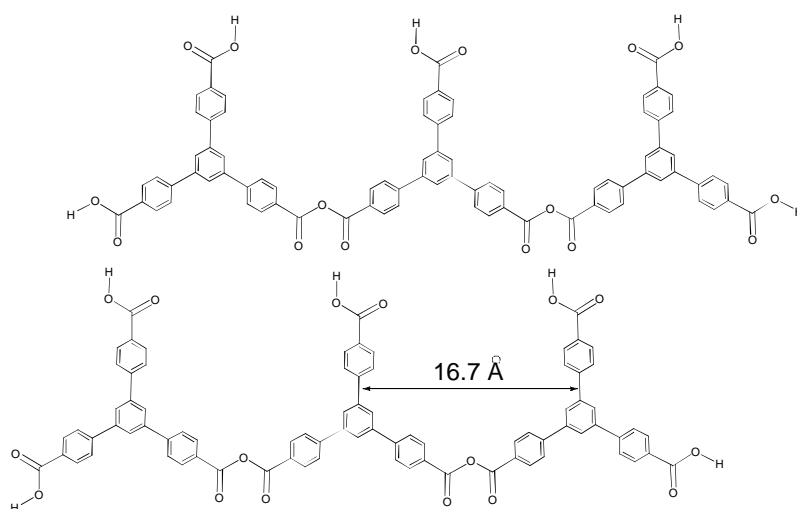


Figure 6.68 A possible hydrogen bonded network assembled from polyanhydride molecules

### 6.4.1.3 Conclusion

In summary, the surface-confined reaction between BTA and 1,4-PDI likely leads to a mixture of polyureas based upon 1,4-PDI and polyanhydrides based upon BTA after annealing to 390 K. Due to the resolution of the STM images, it is

difficult to confirm or deny the formation of polyamides from decomposition of the initial mixed carbamic-carboxylic anhydride product (figure 6.53, I) but on the evidence gathered, it seems that decomposition path B is favoured. Conversion to polyamides by heating of the polyurea/polyanhydride mixture seems like a reaction step that is limited to the solution environment as desorption from Au/mica surface removes oligomer ureas by desorption. Formation of surface polymers consisting of amide linkages might best be carried out by co-deposition of acid chlorides and amines, this has already proved a successful method for production of poly(*p*-phenylene-terephthalamide) upon the Ag(111) surface<sup>10</sup>.

### 6.4.2 Melamine and Trimesoyl Chloride

Observation of polyamides on an Ag(111) was reported after the co-deposition of *p*-phenylene diamine and terephthaloyl chloride<sup>10</sup>. Polymeric chains are seen to thread through domains of *p*-phenylene diamine shortly after the deposition of the acyl chloride reactant. Annealing the surface results in the aggregation of aligned polyamide chains after desorption of unreacted molecules.

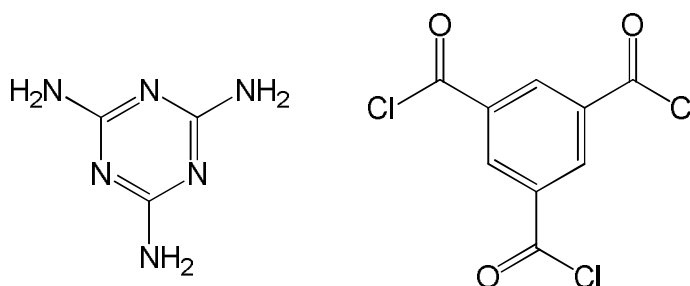


Figure 6.69 Melamine and trimesoyl chloride

#### 6.4.2.1 Reaction of acyl chlorides with amines

Acyl chlorides are susceptible to reaction with a range of nucleophiles to produce carboxylic acid derivatives. Amides are produced by the reaction of acyl chlorides with amines (figure 6.70). The desire to incorporate hydrogen bonding functional groups into networks has previously been discussed. Like urea groups, the R-NH-CO-R amide linkage has N-H and C=O bonds which guest species might be capable of docking with via hydrogen bonding interactions.

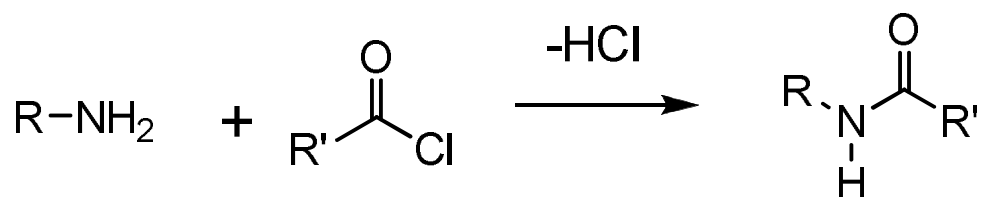


Figure 6.70 Reaction of an amine with an acyl chloride to form an amide

#### 6.4.2.2 Co-deposition of melamine and trimesoyl chloride on Au(111) in UHV

Co-deposition of melamine with trimesoyl chloride on Au(111) in UHV was performed in order to observe possible surface-confined reactions and the formation of polyamide networks. Combining two species of three-fold symmetry would ideally result in hexagonal structures. The idealised network is shown in figure 6.71. However, from previous results, it might be expected that only two of melamine's amino groups would undergo reaction<sup>42</sup>.

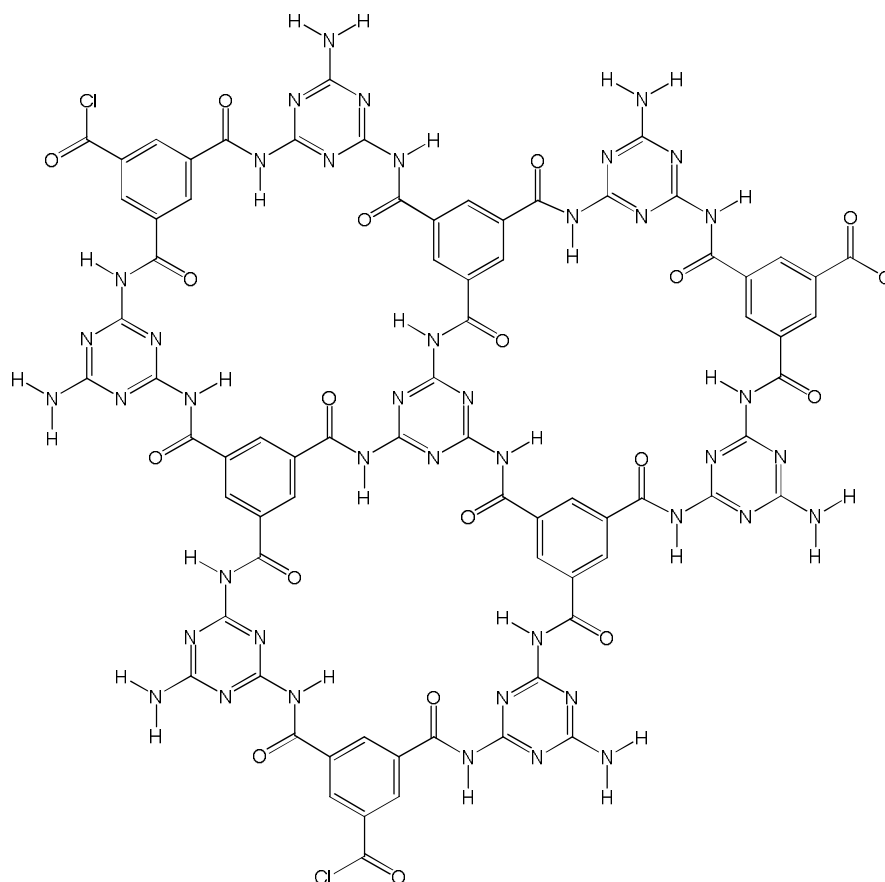
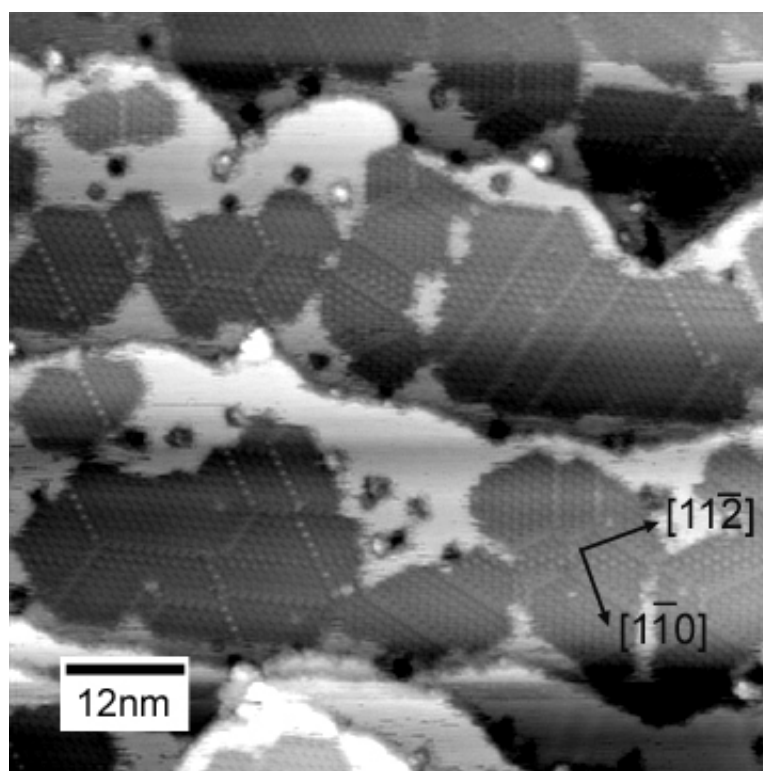


Figure 6.71 Section of idealised polyamide network formed from melamine and trimesoyl chloride

As in previous experiments, melamine was deposited prior to the second reactant in order to boost the sticking probability of trimesoyl chloride on the Au(111) surface. Immediately after depositing trimesoyl chloride, change can be seen in the melamine domains of figure 6.72. The Au(111) surface is also considerably etched by the adsorption of trimesoyl chloride. The terraces become much smaller and often small flower-shaped islands are observed upon the corroded surface. Etch pits are visible upon these terraces. Obtaining STM images becomes a very difficult task during the initial stages of reactions because the molecular arrangement is undergoing constant change; a characteristic cloudiness is often seen over domains as this happens.



**Figure 6.72** Melamine domains featuring diamide particles on the Au(111) surface after the deposition of trimesoyl chloride. The step edges have been re-shaped and etch pits have been created by the presence of trimesoyl chloride (77.5 nm x 77.5 nm, 1.5 V, 0.2 nA)

Initially, stripes are seen through domains, in figure 6.73, and, as in the reaction of 1,3-phenylene diisocyanate with melamine. These can be attributed to the formation of molecules consisting of three aromatic rings. In this case, diamides are formed from reaction of trimesoyl chloride molecules with two melamine molecules; their incorporation into the melamine domains is modelled in figure 6.74. The lowest energy conformation, as derived from DFT calculations using

Gaussian (M05-2X/6-311+g\*), of the diamide species in the gas phase is also shown. In this conformation, the molecule is nearly planar and non-linear. However, the molecular features observed in figure 6.73 are linear and the chirality of the melamine domains on either side of the stripes of diamide molecules is maintained.

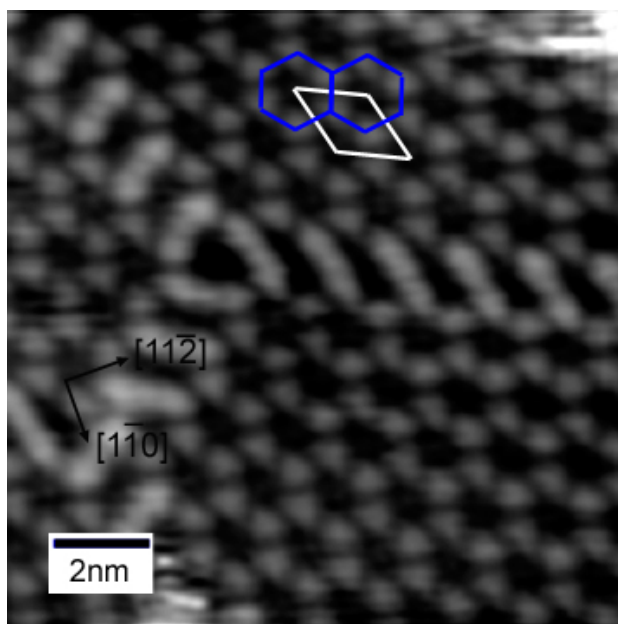


**Figure 6.73** STM image showing the incorporation of diamide molecules into a melamine domain (10 nm x 10 nm, 1.5 V, 0.2 nA)

Similar to the behaviour of diurea species in the surface-confined reaction of melamine and 1,3-PDI in Section 6.6, the two triazine rings have to be reflections of each other in order to comply with the chiral hydrogen bonding motif of the entire domain. In the study of Schmitz et al<sup>10</sup>, they suggest that every adjacent aromatic ring along the polyamide chain - formed by the reaction of p-phenylene diamine and terephthaloyl chloride - is perpendicular to its neighbour in order to limit the electrostatic repulsion between N-H bonds amide groups and hydrogens on adjacent aromatic rings. The central aromatic ring of the linear diamide molecules formed in this case may be orientated differently to the terminal triazine rings, which presumably remain flat with respect to the surface in order to form hydrogen bonds with the surrounding melamine molecules.

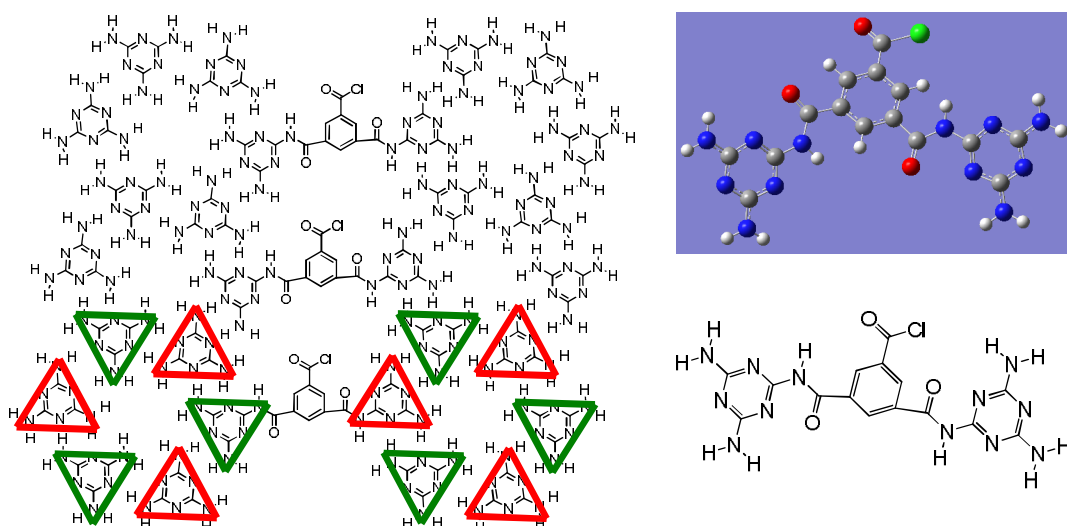


**Figure 6.74** Model showing the incorporation of diamide molecules into melamine domains. The optimised conformation of the diamide species in the gas phase is shown, top right, with a comparison to the conformation adopted within the melamine domains.

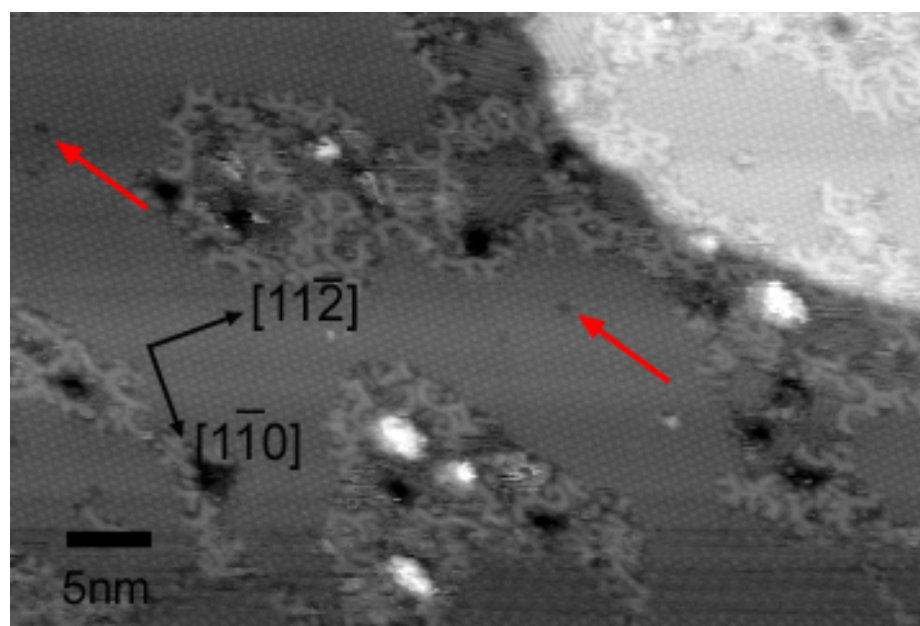


**Figure 6.75** STM image showing polyamide molecules conglomerated around the edges of melamine domains after annealing to 350 K. The melamine has formed a new phase which incorporates guest molecules into pores of the hexagonal arrangement. Red arrows indicate empty pores (54.4 nm x 36.7 nm, 1.5 V, 0.35 nA)

After annealing the surface to 350 K, these stripes are removed as the molecular domains undergo a reorganisation involving the segregation of the diamide molecules from the melamine domains. Presumably, they migrate to the edge of the melamine domains where they undergo further reaction to produce larger polyamide molecules, seen in figure 6.75. The polyamide molecules bound the

melamine domains and cluster around the etch pits. They do not form ordered domains and they are varied in shape and length. A propensity for the polyamides to curl and form 'horseshoe' structures is frequently observed.

Molecules which feature three branches from a single aromatic ring are sometimes observed, these are highlighted in the zoomed STM images of figure 6.76. From previous observations of melamine reactions, these are most probably phenyl centres of trimesoyl chloride molecules that have undergone reaction with three melamine molecules. Chloride is a good leaving group and each acyl chloride group remains reactive despite reaction of neighbouring groups of the same aromatic ring. The formation of 'horseshoe' structures (figure 6.77) rather than enclosed rings can most likely be attributed to the sequential deactivation of melamine after reaction of its first and second amino groups. Failure of melamine molecules to form three amide linkages leads to an incomplete network and, as seen previously<sup>42</sup>, elongated snake-like chains rather than macrocycles result.

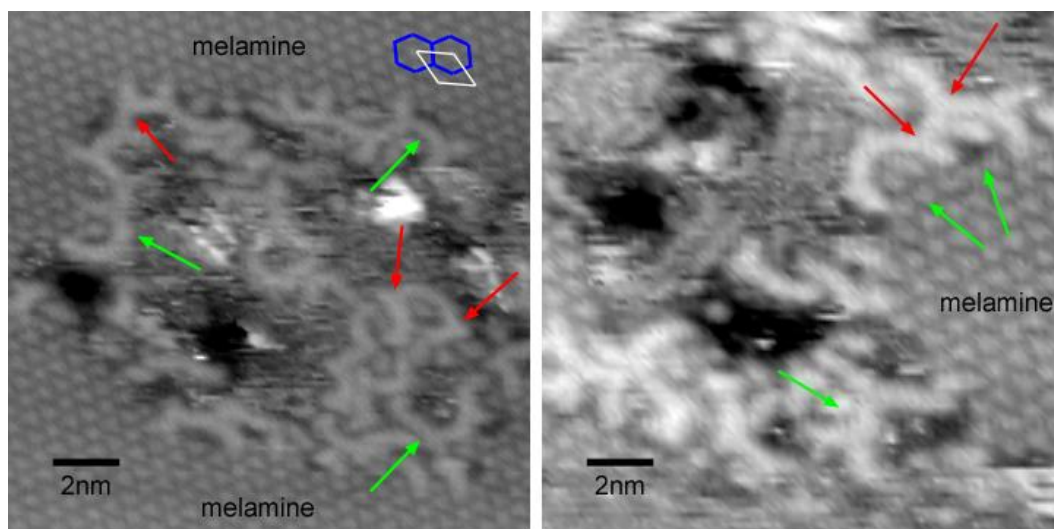


**Figure 6.76** Zoomed STM images showing the polyamide molecules around the edges of melamine domains. Green arrows point towards molecules that have formed in a 'horseshoe' shape. Red arrows indicate aromatic molecules that have reacted completely to form three amide linkages.

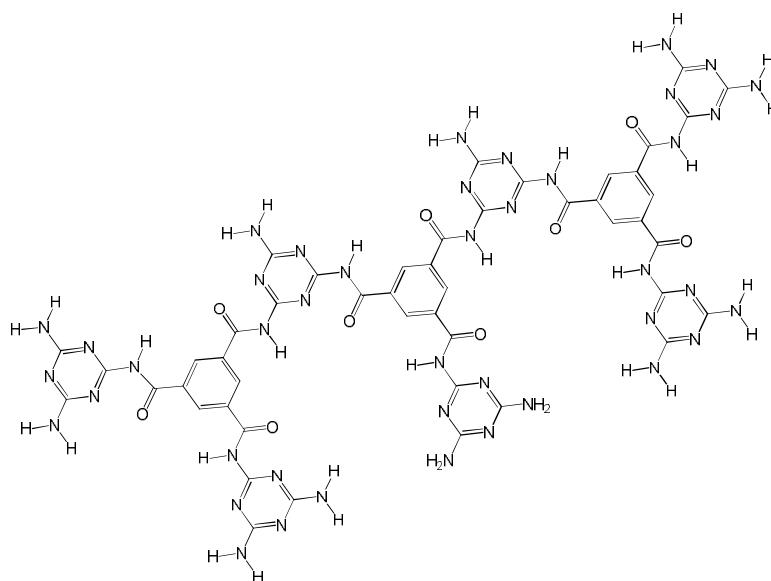


**Figure 6.77** Model showing a polyamide molecule with horseshoe inlets caused by branching of the polymer. The branches are all terminated by a melamine unit so enclosed pores are not formed.

The branched sections of the amide oligomers are mostly embedded within the melamine domain edges. The ends of the branches probably consist of unreacted melamine moieties, which can be incorporated within the melamine hydrogen bonded array, thereby stabilizing the arrangements at the melamine domain boundaries. The aggregates of polymers around the melamine domains may be occasionally three-dimensional and mixed with material that has been etched from the surface. Annealing the surface to around 370 K seems to promote the monolayer arrangements.

After annealing to 350 K and the segregation of diamide molecules to the boundaries, the melamine domains image differently in the STM experiment. The black features at the centre of the pores within the hexagonal arrangements, as observed in figure 6.73, are rarely seen in the melamine domains of figures 6.75 or 6.76. The melamine appears to have undergone a phase transformation.

Close-packed arrangements of melamine co-existent with the typical hexagonal phase on Au(111) was reported by Silly et al.<sup>33</sup>. They performed calculations on the melamine ordering and found for the close-packed structure some of the hydrogen bonds are weaker with respect to the hexagonal phase. They concluded

that the close-packed structure is less stable than the hexagonal phase but is denser, allowing for a more efficient packing of the melamine molecules. The close-packing of melamine in the study by Silly et al<sup>33</sup> was instigated by a high coverage causing a compression of the melamine phase to optimise the stability. In this investigation, the transition from the hexagonal ordering to close-packing of melamine is not the result of an increase in melamine coverage. Instead, the compression is brought about by thermal energy, driving the process of Ostwald ripening. The polyamide molecules act as a barrier to the expansion of the islands; hence, in order to accommodate the extra melamine molecules, the domain becomes a close-packed structure.

The unit cell dimensions of the new melamine structure observed after annealing to 350 K do not differ from the initial hexagonal arrangement. The bright centres of the melamine pores may be indicative of a phenomenon observed by Zhang et al<sup>50</sup>. In their study, in ambient conditions, melamine deposited from solutions in water onto Au/mica was seen to form the typical hexagonal arrangement. However, a mixture of dark and bright features was observed at the centre of the pores. They interpret the bright features as pores which have been filled by extra melamine and the dark features as pores which remain empty. The observed hexagonal structure is reported as having unit cell vectors of length 10.2 Å separated by an angle of 60°. Despite the presence of extra melamine molecules in the pores, the dimensions of the hexagonal structure do not vary significantly from the typical unfilled hexagonal arrangement. This structure is reported<sup>34</sup> to possess unit cell vectors of length 10.9 Å separated by an angle of 66.5°. The similarity in the unit cell dimensions between the filled<sup>50</sup> and empty<sup>34</sup> structures suggests that the melamine on the surface could have undergone a phase transformation without any significant change to the unit cell of the melamine arrangement. In this study, the unit cell vector lengths of ~10.5 Å are maintained despite annealing and the apparent phase change.

The melamine arrangements observed in figures 6.75 and 6.76 exhibit similarities to those observed by Zhang et al<sup>50</sup>. They measure the pore diameter between six

melamine molecules in the hexagonal arrangement as  $\sim 5 \text{ \AA}$ . This is in good agreement with the pore size measured here. This distance is too small to enable a guest melamine molecule to lie flat within the pore. Hence, the bright features within the centres of the pores must represent melamine molecules adsorbed at an orientation pointing out from the Au(111) surface. Of course, the possibility of the pores being filled by trimesyl chloride molecules cannot be ruled out. However, the high reactivity between melamine and trimesoyl chloride suggests that the likelihood of this occurring is very small.

The proportion of empty pores observed after ripening is far smaller than that reported by Zhang et al<sup>50</sup>. Red arrows in figure 6.75 point to dark features within the melamine domains; these are believed to be empty pores. The fact that there are fewer empty pores in this case than seen in the results of Zhang et al suggest that the driving force for compression of the melamine domains and the filling of the pores is greater. The restricted expansion of the melamine domains into the empty hexagonal arrangement by the presence of polyamide oligomers at the domain edges may explain the widespread occurrence of the filled arrangement after annealing.

There is no discernable change as the surface is annealed incrementally up to 390 K. Throughout the temperature range 300 K to 390 K, polyamide molecule are seen to bound the edges of melamine islands. STM studies<sup>34</sup> have stated that melamine begins to desorb from the Au(111) surface when annealing in the range 333 K to 353 K. TPD experiments in Section 5.4.2 have shown that melamine begins to desorb from the Au(111) surface around 350 K. Annealing above 380 K should completely remove melamine from the surface. However, the presence of polyamide molecules on the surface seems to prevent the desorption of melamine.

The layer-by-layer desorption mechanism proposed in Section 5, whereby molecules on the edges of domains are desorbed first, is seemingly blocked. For desorption of melamine to occur, the temperature has to be substantially higher. In

this case, molecules from the centres of domains may be removed first although these are usually party to the strongest supramolecular interactions; each molecule will form two hydrogen bonds to each of the three adjacent molecules and will be subject to the associated van der Waals forces from being surrounded by molecules on every side.

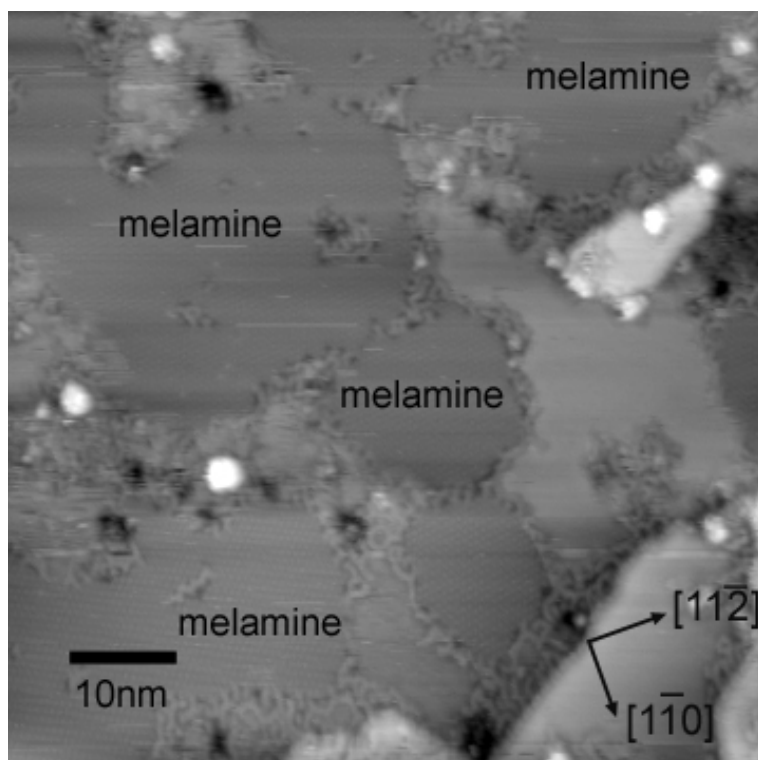


Figure 6.78 STM image showing the surface after annealing to 410 K (70.7 nm x 70.7 nm, 1.5 V, 0.25 nA)

The islands are seen to shrink after the surface is annealed to 410 K (figure 6.78). Complete removal of melamine only takes place after the surface is annealed to 450 K (figure 6.79). The polyamide molecules remaining on the surface are seen to nucleate around the numerous surface defects that were created upon deposition of trimesoyl chloride. The arrangements of these polyamide molecules differ from those of the polyurea molecules (of figure 6.22) within the aggregates. The polyamide species show no order whereas the polyurea moieties formed from melamine and 1,4-PDI often align with adjacent molecules to promote hydrogen bonding, producing small areas of ordered porous networks within the aggregates. The polyamide molecules are most likely melamine-terminated, these bear amino groups which can act as hydrogen bond donors and similarly contain triazine

moieties that are capable of acting as hydrogen bond acceptors but ordered hydrogen bonding arrays of polyamide chains are not observed.

The complete lack of order may be attributed to the larger variation in shape of the polyamide molecules formed; this can, in turn, be attributed to the 1,3,5-positions of the acyl chloride groups on the phenyl rings of trimesoyl chloride, these cause the polyamide molecules to be shaped haphazardly – more curled and branched relative to the polyurea molecules formed from melamine and 1,4-PDI. The branches tend to interlock as polyamide molecules agglomerate, filling the spaces within the ‘horsehoes’ observed earlier. This may cause some of the amide functional groups along these covalent networks to be blocked off to the further guest molecules, preventing docking interactions.

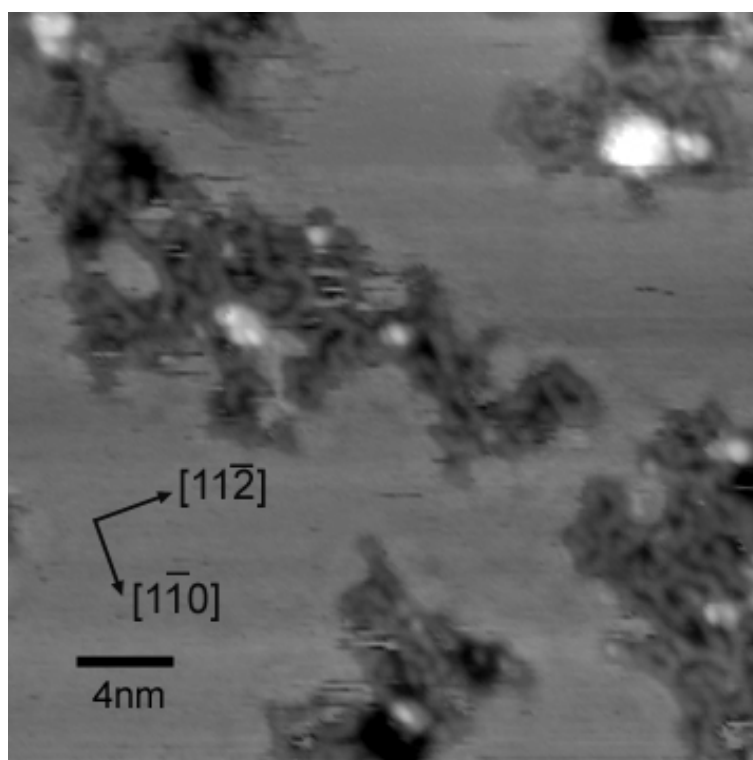


Figure 6.79 STM image of polyamide particles left on the surface after desorption of melamine above 450 K (31.3 nm x 31.3 nm, 1.5 V, 0.3 nA)

The extent to which the reaction occurs is again limited; perhaps less than a tenth of the initial melamine coverage is consumed by reaction. Access to melamine is

not only hindered by the assembly of compact domains but also by the initial reaction products. The formation of polyamide molecules first occurs around the edges of these domains but this then precludes further reaction. As discussed, the polyamide oligomers bound the edges of melamine domains and form a physical barrier between melamine molecules and trimesoyl chloride molecules that are mobile upon the surface. The reaction may benefit from simultaneous deposition of both species in order for better mixing on the surface, amide bond formation may also occur in the gas phase before adsorption of oligomers onto the surface and aid the formation of extended polyamide structures.

#### 6.4.2.3 Summary

The surface-confined reaction between melamine and trimesoyl chloride is observed on Au(111) following co-deposition from vapour in UHV. The formation of polyamide molecules takes place at the edges of melamine domains which they subsequently bound. The polyamide molecules play two major roles: they delay desorption of melamine by blocking the layer-by-layer break up of melamine islands and they prevent further reaction of melamine molecules by containing them behind a physical barrier. The reaction occurs readily at room temperature but by improving methods of deposition or better controlling surface coverage, greater covalent networks might be produced. Experiments in ambient environment have yet to be carried out; similar to isocyanates, acyl chlorides are reactive with water so precaution would have to be taken against contamination.

### 6.5 Conclusions

Creation of covalent molecular networks on surfaces was investigated by carrying out co-deposition of reactive species on Au(111) surfaces in UHV and ambient environments. Functionalising surface networks is necessary to enable interaction with guest species; here, networks have been designed to promote hydrogen bonding associations with prochiral reagents.

The formation of urea and amide linkages was observed by carrying out surface-confined reactions of amines with isocyanates and acyl chlorides, respectively. The formation of polyureas is particularly attractive due to the possibility of hydrogen bonding docking interactions between the network and methyl acetoacetate, an important prochiral reagent. The two N-H bonds of the urea linkage should align with C=O bonds of methyl acetoacetate, optimisation of these hydrogen bonds should ensure that the prochiral reactant molecules adopt a specific orientation during hydrogenation reactions. Isocyanate and amine molecules have been shown to react at room temperature on the Au(111) surface, although annealing the surface can accelerate reactions. Small oligomers have been shown to form ordered hydrogen bonding networks. Different species exhibit different degrees of reactivity and the shape and size of resultant polyurea networks varies. The polyurea networks are generally disordered; the ability of molecules to self-assemble into uniform arrays is sacrificed for the benefits of covalent structures. For use as a chiral modifier upon a catalytic surface, these networks may not necessarily need to be vast or exhibit a great degree of order, in theory, docking interactions with guest species should still take place as long as the urea or amide functionalities are available.

The ability to deposit nickel onto the Au(111) without disruption to the network demonstrates the improved robustness of covalent networks relative to hydrogen bonded structures. Nickel is seen to nucleate in the elbows of the surface reconstruction and grow underneath the network, this situation can be thought of as analogous to chiral modifiers (for example, amino acids) adsorbed upon a catalytic surface.

Obtaining STM images during surface-confined reactions and of covalent networks is relatively difficult. Maintaining the tip in good condition in the presence of reactive molecules on the surface requires constant attention. Whilst scanning, molecules may become adsorbed onto the tip; as scanning progresses,

the tip inevitably encounters molecules capable of undergoing reaction with those adsorbed on it, thus the tip constantly changes in shape as it becomes gradually coated in growing polymers. UHV offers a better environment in which to acquire better quality STM images of covalent reactions on surface but of course, does not incorporate factors such as moisture in the ambient environment which may inhibit or deactivate reactants. The STM images obtained in ambient environment are not particularly informative with respect to characterisation of surface-confined reaction products but as an analytical tool, it can, at least, be used to indicate changes before and after a reaction. Pairs of molecules which are thought to react after analysis in ambient conditions can then be analysed further in UHV to try to understand the potential products of the potential reaction. Other analytical techniques might be useful in characterising the products from surface-confined reactions; reflection absorption infrared spectroscopy (RAIRS) might be able to detect new bonds within the molecules adsorbed on the surface.

## 6.6 References

- (1) Prins, L. J.; Reinhoudt, D. N.; Timmerman, P. *Angewandte Chemie-International Edition* **2001**, *40*, 2383.
- (2) Weber, U. K.; Burlakov, V. M.; Perdigao, L. M. A.; Fawcett, R. H. J.; Beton, P. H.; Champness, N. R.; Jefferson, J. H.; Briggs, G. A. D.; Pettifor, D. G. *Physical Review Letters* **2008**, *100*, 156101.
- (3) Saywell, A.; Magnano, G.; Satterley, C. J.; Perdigao, L. M. A.; Champness, N. R.; Beton, P. H.; O'Shea, J. N. *Journal of Physical Chemistry C* **2008**, *112*, 7706.
- (4) Staniec, P. A.; Perdigao, L. M. A.; Saywell, A.; Champness, N. R.; Beton, P. H. *Chemphyschem* **2007**, *8*, 2177.
- (5) Grill, L.; Dyer, M.; Lafferentz, L.; Persson, M.; Peters, M. V.; Hecht, S. *Nature Nanotechnology* **2007**, *2*, 687.
- (6) Gutzler, R.; Walch, H.; Eder, G.; Kloft, S.; Heckl, W. M.; Lackinger, M. *Chemical Communications* **2009**, 4456.

- (7) Weigelt, S.; Busse, C.; Bombis, C.; Knudsen, M. M.; Gothelf, K. V.; Strunskus, T.; Woll, C.; Dahlbom, M.; Hammer, B.; Laegsgaard, E.; Besenbacher, F.; Linderoth, T. R. *Angewandte Chemie-International Edition* **2007**, *46*, 9227.
- (8) Treier, M.; Fasel, R.; Champness, N. R.; Argent, S.; Richardson, N. V. *Physical Chemistry Chemical Physics* **2009**, *11*, 1209.
- (9) Treier, M.; Richardson, N. V.; Fasel, R. *Journal of the American Chemical Society* **2008**, *130*, 14054.
- (10) Schmitz, C. H.; Ikononov, J.; Sokolowski, M. *Journal of Physical Chemistry C* **2009**, *113*, 11984.
- (11) Matena, M.; Riehm, T.; Stohr, M.; Jung, T. A.; Gade, L. H. *Angewandte Chemie-International Edition* **2008**, *47*, 2414.
- (12) Lipton-Duffin, J. A.; Ivasenko, O.; Perepichka, D. F.; Rosei, F. *Small* **2009**, *5*, 592.
- (13) Blake, M. M.; Nanayakkara, S. U.; Claridge, S. A.; Fernandez-Torres, L. C.; Sykes, E. C. H.; Weiss, P. S. *Journal of Physical Chemistry A* **2009**, *113*, 13167.
- (14) Weigelt, S.; Schnadt, J.; Tuxen, A. K.; Masini, F.; Bombis, C.; Busse, C.; Isvoranu, C.; Ataman, E.; Laegsgaard, E.; Besenbacher, F.; Linderoth, T. R. *Journal of the American Chemical Society* **2008**, *130*, 5388.
- (15) Veld, M. I.; Iavicoli, P.; Haq, S.; Amabilino, D. B.; Raval, R. *Chemical Communications* **2008**, 1536.
- (16) Barth, J. V.; Brune, H.; Ertl, G.; Behm, R. J. *Physical Review B* **1990**, *42*, 9307.
- (17) Horcas, I.; Fernandez, R.; Gomez-Rodriguez, J. M.; Colchero, J.; Gomez-Herrero, J.; Baro, A. M. *Review of Scientific Instruments* **2007**, *78*, 8.
- (18) Frisch, M. J.; Trucks, G. W.; Schlegel, H. B.; Scuseria, G. E.; Robb, M. A.; Cheeseman, J. R.; Montgomery, J., J. A.; Vreven, T.; Kudin, K. N.; Burant, J. C.; Milliam, J. M.; Iyengar, S. S.; Tomasi, J.; Barone, V.; Mennucci, B.; Cossi, M.; Scalmani, G.; Rega, N.; Petersson, G. A.; Nakatsuji, H.; Hada, M.; Ehara, M.; Toyota, K.; Fukuda, R.; Hasegawa, J.; Ishida, M.; Nakajima, T.; Honda, Y.; Kitao, O.; Nakai, H.; Klene, M.; Li, X.; Knox, J. E.; Hratchian, H. P.; Cross, J. B.; Bakken, V.; Adamo, C.; Jaramillo, J.; Gomperts, R.; Stratmann, R. E.; Yazyev, O.; Austin, A. J.; Cammi, R.; Pomelli, C.; Ochterski, J. W.; Ayala, P. Y.; Morokuma, K.; Voth, G. A.; Salvador, P.; Dannenberg, J. J.; Zakrzewski, V. G.;

Dapprich, S.; Daniels, A. D.; Strain, M. C.; Farkas, O.; Malick, D. K.; Rabuck, A. D.; Raghavachari, K.; Foresman, J. B.; Ortiz, J. V.; Cui, O.; Baboul, A. G.; Clifford, S.; Cioslowski, J.; Stefanov, B. B.; Liu, G.; Liashenko, A.; Piskorz, P.; Komaromi, I.; Martin, R. L.; Fox, D. J.; Keith, T.; Al-Laham, M. A.; Peng, C. Y.; Nanayakkara, A.; Challacombe, M.; Gill, P. M. W.; Johnson, B.; Chen, W.; Wong, M. W.; Gonzalez, C.; Pople, J. A. Gaussian 03, revision E.01; Gaussian, Inc.: Wallingford, CT, 2004.

(19) Zhao, Y.; Schultz, N. E.; Truhler, D. G. J. *Journal of Chemical Theory and Computation* **2006**, *2*, 364.

(20) Krishnan, R.; Binkley, J. S.; Seeger, R.; Pople, J. A. *Journal of Chemical Physics* **1980**, *72*, 650.

(21) Soler, J. M.; Artacho, E.; Gale, J. D.; Garcia, A.; Junquera, J.; Ordejon, P.; Sanchez-Portal, P. *Journal of Physics - Condensed Matter* **2002**, *14*, 2745.

(22) Perdew, J. P.; Burke, K.; Ernzerhof, M. *Physical Review Letters* **1996**, *77*, 3865.

(23) Sankey, O. F.; Niklewski, D. J. *Physical Review B* **1989**, *40*, 3979.

(24) Troullier, N.; Martins, J. L. *Physical Review B* **1991**, *43*, 1993.

(25) Caraculacu, A. A.; Coseri, S. *Progress in Polymer Science* **2001**, *26*, 799.

(26) Etter, M. C.; Urbanczyklipkowska, Z.; Ziaebrahimi, M.; Panunto, T. W. *Journal of the American Chemical Society* **1990**, *112*, 8415.

(27) Kim, A.; Filler, M. A.; Kim, S.; Bent, S. F. *Journal of the American Chemical Society* **2005**, *127*, 6123.

(28) Kohli, P.; Blanchard, G. J. *Langmuir* **2000**, *16*, 4655.

(29) Vogel, B. M.; DeLongchamp, M.; Mahoney, C. M.; Lucas, L. A.; Fischer, D. A.; Lin, E. K. *Applied Surface Science* **2008**, *254*, 1789.

(30) van Gorp, J. J.; Vekemans, J.; Meijer, E. W. *Journal of the American Chemical Society* **2002**, *124*, 14759.

(31) Altman, E. I.; Colton, R. J. *Physical Review B* **1993**, *48*, 18244.

(32) Chis, V.; Mile, G.; Stiuftuc, R.; Leopold, N.; Oltean, M. *Journal of Molecular Structure* **2008**, *924-926*, 47.

(33) Silly, F.; Shaw, A. Q.; Castell, M. R.; Briggs, G. A. D.; Mura, M.; Martsinovich, N.; Kantorovich, L. *Journal of Physical Chemistry C* **2008**, *112*, 11476.

- (34) Perdigao, L. M. A.; Perkins, E. W.; Ma, J.; Staniec, P. A.; Rogers, B. L.; Champness, N. R.; Beton, P. H. *Journal of Physical Chemistry B* **2006**, *110*, 12539.
- (35) Theobald, J. A.; Oxtoby, N. S.; Phillips, M. A.; Champness, N. R.; Beton, P. H. *Nature* **2003**, *424*, 1029.
- (36) Ruben, M.; Payer, D.; Landa, A.; Comisso, A.; Gattinoni, C.; Lin, N.; Collin, J. P.; Sauvage, J. P.; De Vita, A.; Kern, K. *Journal of the American Chemical Society* **2006**, *128*, 15644.
- (37) Stroschio, J. A.; Kaiser, W. J. *Scanning Tunnelling Microscopy*; Academic Press, Inc.: San Diego, 1993.
- (38) Ionescu, M. *Chemistry and Technology of Polyols for Polyurethanes*; Rapra Technology Limited: Shawbury, 2005.
- (39) Yu, C.; Mosbach, K. *Journal of Organic Chemistry* **1997**, *62*, 4057.
- (40) Garciatellado, F.; Geib, S. J.; Goswami, S.; Hamilton, A. D. *Journal of the American Chemical Society* **1991**, *113*, 9265.
- (41) Sorenson, W. R. *Journal of Organic Chemistry* **1959**, *24*, 978.
- (42) Jensen, S.; Fruchtl, H.; Baddeley, C. J. *Journal of the American Chemical Society* **2009**.
- (43) Dmitriev, A.; Lin, N.; Weckesser, J.; Barth, J. V.; Kern, K. *Journal of Physical Chemistry B* **2002**, *106*, 6907.
- (44) Griessl, S. J. H.; Lackinger, M.; Jamitzky, F.; Markert, T.; Hietschold, M.; Heckl, W. A. *Langmuir* **2004**, *20*, 9403.
- (45) Ishikawa, Y.; Ohira, A.; Sakata, M.; Hirayama, C.; Kunitake, M. *Chemical Communications* **2002**, 2652.
- (46) Kudernac, T.; Lei, S. B.; Elemans, J.; De Feyter, S. *Chemical Society Reviews* **2009**, *38*, 402.
- (47) Lackinger, M.; Griessl, S.; Heckl, W. A.; Hietschold, M.; Flynn, G. W. *Langmuir* **2005**, *21*, 4984.
- (48) Sheerin, G.; Cafolla, A. A. *Surface Science* **2005**, *577*, 211.
- (49) Barden, W. R. T.; Singh, S.; Kruse, P. *Langmuir* **2008**, *24*, 2452.
- (50) Zhang, H. M.; Xie, Z. X.; Long, L. S.; Zhong, H. P.; Zhao, W.; Mao, B. W.; Xu, X.; Zheng, L. S. *Journal of Physical Chemistry C* **2008**, *112*, 4209.

## 7 Conclusions and Outlook

The self-assembly of molecules upon surfaces, and therefore the governing of supramolecular interactions, may be vital to the development of many new nanotechnology devices; in this study, a hydrogen bonding network was probed for use in the generation of enantioselective heterogeneous catalysts. In enantioselective heterogeneous catalysis, the orientation of adsorbed prochiral reagents upon the reactive metal surface has to be controlled. Successful examples of enantioselective heterogeneous catalysts have involved the adsorption of chiral modifier species, such as amino acids, onto reactive metals prior to reaction<sup>1-3</sup>. Although there are competing theories over the mechanism of the catalysed reaction, promotion of interactions such as hydrogen bonds, between chiral modifiers and prochiral reagents and, to a lesser extent, the distribution of chiral modifier molecules upon the surface are important to the fabrication of effective enantioselective catalysts.

Hydrogen bonding has been used to create many interesting molecular networks on surfaces. The PTCDI-melamine honeycomb network presented itself as an outstanding example to further develop. On the Ag-Si(111)- $\sqrt{3}\times\sqrt{3}R30^\circ$ <sup>4</sup> and Au(111)<sup>5</sup> surfaces, PTCDI and melamine were shown to form vast networks capable of hosting guest molecules, the ability to customise the network by functionalising the component molecules is an attractive possibility. Initial work of this thesis concentrated on testing the PTCDI-melamine network for use as a template which could be developed for use in enantioselective catalysis.

### 7.1 Conclusions

The adsorbate-substrate interaction between both PTCDI and melamine on Ni(111) is too strong to permit the formation of ordered hydrogen bonded arrangements. Once deposited on the surface, the molecules are effectively pinned in place and diffusion into organised arrays does not occur. STM images also indicate the formation of metal-organic complexes from PTCDI molecules and surface adatoms.

The interaction of both PTCDI and melamine with nickel was explored by co-deposition on Au(111). Ordered arrays of nickel islands are produced on the Au(111) surface following nucleation in the elbows of the herringbone surface reconstruction. These islands can be leached by PTCDI to produce a range of metal-organic structures. Porous and compact phases or 1-D chains are formed depending on the nickel coverage, the PTCDI coverage and the temperature to which the surface is annealed. Melamine is much more reactive and completely corrodes the nickel islands resulting in disorganised chains or dense, amorphous structures. After nickel was deposited onto the Au(111) surface bearing PTCDI, nickel islands are seen to grow in the elbows of the surface reconstruction under the molecular domains. The nickel islands initially leave the domains unperturbed, but if the nickel coverage is increased, the islands in the elbows may grow large enough to cause the splitting of PTCDI domains.

The hexagonal PTCDI-melamine network was formed on Au(111) after co-deposition of both components. Several other mixed phases were observed. Low coverages of both PTCDI and melamine is most favourable for the formation of the porous hexagonal network. The hexagonal network was shown to host a small quantity of nickel atoms, nucleation of a few atoms occurs at the vertices of the pores after entering vertically via evaporation deposition and laterally via diffusion. Using the network to create ordered array of metal clusters upon on the Au(111) surface, which would have many other applications as well as catalysis, is impossible as degradation of the network template occurs over a few hours where a low coverage of nickel is present or more rapidly if the nickel coverage is increased. Disorganised metal organic structures are formed in place of the hydrogen bonded network.

The possibility of replacing chiral modifiers with covalent networks was investigated. Functionalised surface polymers, designed to promote interactions with prochiral reagents may serve as a more robust form of chiral modifiers upon catalyst surfaces. Polyurea species were produced on Au(111) after the reaction of melamine and 1,4-phenylene diisocyanate. The reaction between the absorbed species is observed at room temperature although annealing accelerates the number of reactions and increase of oligomer size. Small oligomers are capable of ordering into hydrogen bonded networks. Larger oligomers were formed upon

annealing. These formed porous aggregates which displayed a small degree of order. Nickel was deposited onto these and was seen to nucleate in the elbows of the surface reconstruction. The nickel islands were seen to grow outwards and underneath the polyurea domains. The polymers exhibit a greater stability in terms of reactivity towards nickel than hydrogen bonded networks; a greater loading of nickel could be applied to the surface and the molecular domains were seen to be unchanged by the presence of the large nickel islands for several hours. A number of other surface-confined reactions were also studied in both UHV and ambient conditions. STM images in ambient conditions are of poor quality but the changes in appearance of the molecular arrangements suggest that surface-confined reactions and polymer generation may be occurring as in UHV.

## **7.2 Future Work**

Successful heterogeneous catalysts have relied upon the adsorption of ‘chiral modifiers’ onto reactive metal surfaces such as Ni or Pt. This procedure has failed to transfer into the industrial process due to displacement of the modifiers during reaction cycles. The findings of this study point towards surface-supported porous, covalent networks as the most suitable replacements of traditional chiral modifiers.

Self-assembled hydrogen bonded networks may offer uniformity on gold and other inert substrates but the inability to assemble networks on reactive metals is a major problem. The network components which are adsorbed strongly in haphazard arrangements have no benefit over traditional modifiers. The chemical stability of hydrogen bonded networks is insufficient on Au(111) to allow Ni to be added to the surface retrospectively. An inert substrate such as Au seems necessary to permit diffusion of molecules into self-assembled networks. Presumably, covalent networks formed by surface-confined reactions can only take place on substrates which allow reactants to mix. The enhanced robustness of covalent networks against metal-organic coordination allows Ni to be added to the Au surface after formation.

The ability to transfer the process from UHV to ambient conditions is a major step and would require some optimisation due to the contrasting substrates and deposition techniques. The UHV results suggest that in ambient conditions enantioselective heterogeneous catalysts would be prepared by first growing gold nanoparticles upon an appropriate support. The gold surface would then be exposed to solutions of the reactants needed to produce the desired network. The solutions or the gold surface could be heated to produce more developed polymeric networks. The surface may then be washed to remove excess reactants. Nickel would then be deposited onto the gold surface by immersion in appropriate solutions.

Formation of covalent networks on other surfaces should also be considered. Surface-confined polymerisation reactions seem to require an inert surface to allow mixing of components. Alloys which afford diffusion and also catalytic activity should be investigated.

There are various other aspects of catalyst fabrication procedure that require attentions. Formation of polymers in solution may allow direct adsorption onto a reactive metal surface. Controlling the surface coverage may be more difficult using this method. Allowing network components to react in solution would allow the molecules more freedom and may produce polymeric structures that are more three-dimensional. Large or growing three-dimensional polymers or multilayer adsorption may reduce the accessibility of reactants to the catalyst surface, thus careful control of solution concentration would be required.

More work is required to attain better characterisation of covalent networks in ambient conditions, the difficulties of imaging polymers by STM have already been discussed. Better sample preparation (reducing surface coverage through lower concentration deposition solutions or removal of excess reactants through washing) may alleviate some of the problems.

Different reaction types may be utilised in constructing surface networks. Polymer linkages other than ureas and amides possess polar bonds which are capable of interacting with guest molecules. The reactions of amines with isocyanates and acid chlorides occurs quite quickly;

slower reactions may afford more time for pre-organisation of network components and produce more ordered networks. The possibility of incorporating a catalyst into the deposition solutions may expand the range of viable reactions available.

The formation of completely ordered covalent networks on the surface may not be strictly necessary for creation of a successful catalyst if docking interactions with guest molecules ensure a consistent adsorption geometry. The urea group is particularly attractive due to the potential hydrogen bonding interactions it may form. Host-guest interactions need to be investigated; STM or RAIRS analysis would indicate docking interactions between the fabricated networks and prochiral reagents. Characterisation of this interaction may allow more efficient design of networks, the component parts of the covalent networks could be customised for the reactions to be performed. Synthetic organic chemistry may need to be utilised to incorporate chirality into one of the two reactants.

Ultimately, the success of covalent networks as chiral modifiers will be judged by reaction performance. If reasonably well-ordered, porous covalent networks can be formed on a gold surface, a satisfactory method of introducing a reactive metal onto the surface is found and a docking interaction between the networks and prochiral reagents can be observed, then trials of model catalysts in reactions should be planned.

### 7.3 References

- (1) Izumi, Y. *Advances in Catalysis* **1983**, 32, 215.
- (2) Orito, Y.; Imai, S.; Niwa, S. *Nippon Kagaku Kaishi* **1979**, 1118.
- (3) Webb, G.; Wells, P. B. *Catalysis Today* **1992**, 12, 319.
- (4) Theobald, J. A.; Oxtoby, N. S.; Phillips, M. A.; Champness, N. R.; Beton, P. H. *Nature* **2003**, 424, 1029.
- (5) Perdigo, L. M. A.; Perkins, E. W.; Ma, J.; Staniec, P. A.; Rogers, B. L.; Champness, N. R.; Beton, P. H. *Journal of Physical Chemistry B* **2006**, 110, 12539.